Fall 2012

Surface expressions of discontinuities, and the estimation of their 3-D orientations using combined LiDAR and optical imaging

James Nii Aboh Otoo

Department: Geosciences and Geological and Petroleum Engineering

Recommended Citation

Otoo, James Nii Aboh, "Surface expressions of discontinuities, and the estimation of their 3-D orientations using combined LiDAR and optical imaging" (2012). *Doctoral Dissertations*. 1975.
https://scholarsmine.mst.edu/doctoral_dissertations/1975

SURFACE EXPRESSIONS OF DISCONTINUITIES, AND THE ESTIMATION OF THEIR 3-D ORIENTATIONS USING COMBINED LIDAR AND OPTICAL IMAGING

by

JAMES NII ABOH OTOO

A DISSERTATION

Presented to the Faculty of the Graduate School of the

MISSOURI UNIVERSITY OF SCIENCE AND TECHNOLOGY

In Partial fulfillment of the Requirements for the Degree

DOCTOR OF PHILOSOPHY

in

GEOLOGICAL ENGINEERING

2012

Approved by

Norbert H. Maerz
David J. Rogers
Leslie Gertsch
Jeffrey Cawlfield
Kwame Awuah-Offei

ABSTRACT

The importance of the collection and analysis of data on discontinuities cannot be overemphasized. Problems which include sampling difficulties, risks, limited access to rock faces and exposures, and the delay in data collection has led to a high need for data collection tools and analysis techniques that can overcome these problems.

Discontinuities manifest themselves as either traces or as facets. Traces are linear features that intersect with both the discontinuity and the rock cut. Facets are the actual discontinuity surfaces that are exposed in the rock cut. Facets can be natural or induced. Identifying a facet as either natural or induced can sometimes be very difficult and can affect analytical results. The orientation of facets can be estimated from LiDAR point cloud. The orientation of traces can be estimated from optical imaging methods. LiDAR scanning alone cannot measure traces, neither can optical imaging methods measure facets. This is complicated by the fact that both facets and 'traces' are often present in the same rock cut, making the selection of an appropriate methodology or tool very difficult if not impossible. The set of traces in a rock mass usually belong to a set of facets of the same rock mass. These set of traces and facets can be combined either by the use of stereonets or by the equation of the angle between two lines.

This research has provided a simple method by which the orientation of facets can be estimated from LiDAR point cloud. It has also provided a simple method by which the orientation of traces could be estimated from 2-D images. Additionally, this research has provided a reasonable way by which professionals could differentiate between traces, natural, and induced facets. Finally, this research has provided a methodology by which traces from optical images can be combined to facets from point cloud data.

ACKNOWLEDGMENTS

I would like to thank God for his guidance and protection throughout my life. I am very grateful to Dr. Norbert Maerz, my advisor and program head, for his tremendous support, encouragement, and advice throughout my studies at the Missouri University of Science and Technology. I would like to thank him for his constructive criticism in the preparation of this dissertation. This work would not have been possible without his help. I would also like to thank the National Science Foundation (NSF) for funding this research.

I would like to thank Dr. David J. Rogers, Dr. Leslie Gertsch, Dr. Jeffrey Cawlfield, and Dr. Kwame Awuah-Offei for accepting to be part of my dissertation committee, and also for their contributions to this work. My sincere thanks also go to Dr. Ye Duan for his collaboration on this work, and to Dr. Paul N. Worsey for his discussion on rock blasting. I would also like to thank the faculty and staff of both the department of geological science and engineering, and the rock mechanics and explosives research center, especially Paula Cochran, Patricia Robertson, Diane Henke, and Leanne Nuckolls for all their advice and help throughout my studies at the Missouri University of Science and Technology. I would also like to thank all friends and colleagues at the Missouri University of Science and Technology, especially my office mates Travis Kassebaum and Ken Boyko.

Lastly, I would like to thank my entire family for their prayers and support. Special thanks go to my wife, Dr. Fatima Ellis, and my daughter, Edna Naa Tiakwah Otoo, for allowing me to spend most of my “family time” in the office.

TABLE OF CONTENTS

APPENDICES

LIST OF ILLUSTRATIONS

Page

LIST OF TABLES

Page

1. INTRODUCTION

1.1 DISCONTINUITIES IN ROCKS

Joint, fracture, fault, and discontinuity are the four common terms used to describe breaks in a rock mass. Discontinuity, likely the most general among these terms, suggests a break in the continuity of a rock mass, without an implied genetic origin (Maerz, 1990). The term discontinuity however makes no distinction concerning either the age, the geometry, or the mode of origin of the feature (Priest, 1993). The term joint is commonly used to describe a discontinuity caused by a natural geological process. The term fracture is a more inclusive term that includes joints, faults, cracks, and breaks induced by blasting (Maerz, 1990). The term fault applies only to natural breaks along which some displacement has occurred. Discontinuity in a rock is a significant mechanical break or fracture of negligible tensile strength, low shear strength, and high fluid conductivity when compared to the rock itself (Priest, 1993). Naturally breaks or cracks occur in every rock mass (Scheideger, 1979). In fact, both Yucca Mountain, Nevada, and Hanford, Washington, two of the three sites selected as candidates for the United States of America’s nuclear waste repository, are extensively jointed (Pollard and Aydin, 1988).

Discontinuities influence all the engineering properties and rock behaviors (Hudson, 1993). The properties of discontinuities become of prime importance when dealing with discontinuous rock masses. These discontinuities to a large extent determine the mechanical behavior of the rock mass (Bieniawski, 1989). The presence of discontinuities in a rock mass can affect both engineering designs and projects, which include the stability of slopes in rock masses, the stability and behavior of excavations in rock masses and their surroundings, the behavior of foundations in rock masses (settlement), the type of support, the strength of a rock, and the hydraulic conductivity of a rock, which is responsible for the transportation of groundwater and contaminants (Zhou, 2001). Thus, the importance of the analysis and the characterization of discontinuities cannot be overemphasized. Properties of discontinuity can be grouped as geometric and non-geometric. Geometric properties include position, orientation, persistence, aperture, spacing, and roughness (Figure 1.1). These properties can be measured directly from the discontinuity if the rock face is readily accessible. Non-geometric properties include wall strength, filling, and seepage (Figure 1.1).

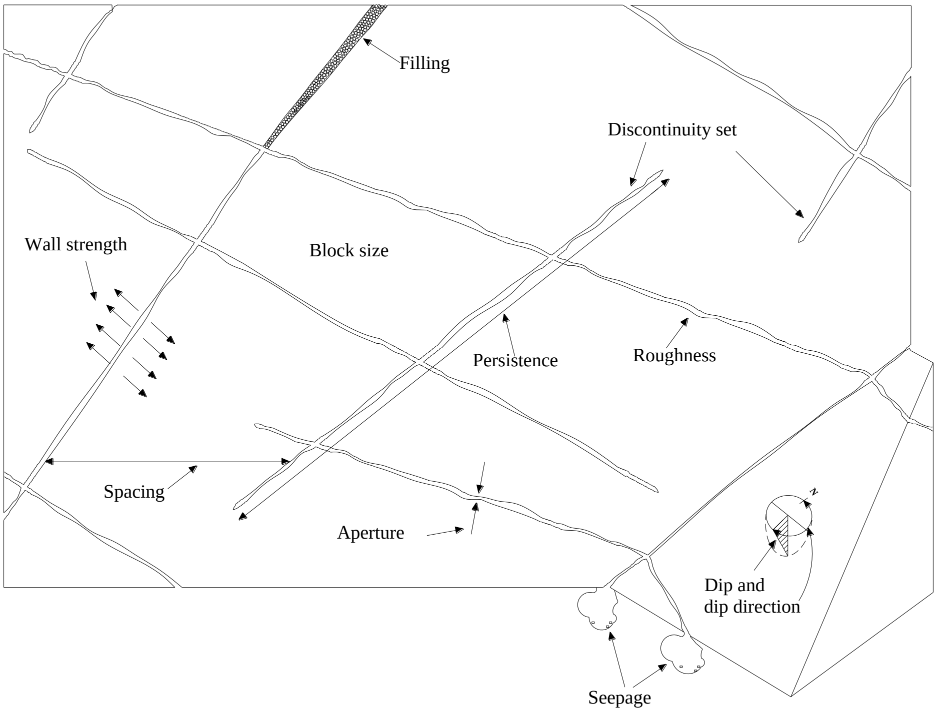

Figure 1.1. Schematic drawing of a rock mass illustrating the properties of discontinuities (Modified from Hudson, 1989).

The position of a discontinuity generally refers to the location of the discontinuity within the rock mass. Orientation is defined as the discontinuity's attitude in space. It is assumed to be planar for the purpose of analysis. Orientation is measured with either a compass or clinometer (Maerz, 1990). Persistence is the measure of the continuous length, or area, of the discontinuity. It defines both the size of the blocks and the length of potential sliding surfaces (Wyllie and Mah, 2004, Figure 1.1). An aperture is the perpendicular distance separating the adjacent rock walls of an open discontinuity. The intervening space is filled with either air or water (Wyllie and Mah, 2004, Figure 1.1a). Spacing is the distance between two discontinuities (Figure 1.1). Roughness is essentially a measure of how rough the discontinuity's surface is. Roughness is often an important component of the shear strength, especially where the discontinuity is undisplaced and interlocked (Wyllie and Mah, 2004, Figure 1.1). Roughness measuring can be very tedious and time consuming, hence a simple and time saving method was presented by Maerz et al., (1990). Wall strength refers to the strength of the rocks forming the discontinuity (Figure 1.1). Discontinuity wall strength is generally characterized by grades using a classification table (ISRM, 1981b). Filling refers to the material separating the walls of the discontinuity (Figure 1.1). The ability of the discontinuity to allow water to seep through is referred to as its seepage. Seepage conditions in a discontinuity could range from dry to continuous flow.

The most important discontinuity property is orientation (dip and dip direction). Orientation influences the potential of the rock mass to move, the direction of movement, and the volume of material to be moved (Donovan et al, 2005). Orientation is so important that it is ultimately used in every kind of analysis, both numerical and non-numerical modeling. Orientations are the easiest and the most reliable discontinuity property to measure. They can be measured at the surface from mapping and at depth from oriented core.

Discontinuities which are planar and parallel or sub-parallel are known as systematic discontinuities (Figure 1.2). Systematic discontinuities form sets in a rock mass. Irregular or curved discontinuities are known as non-systematic; and do not usually form sets.

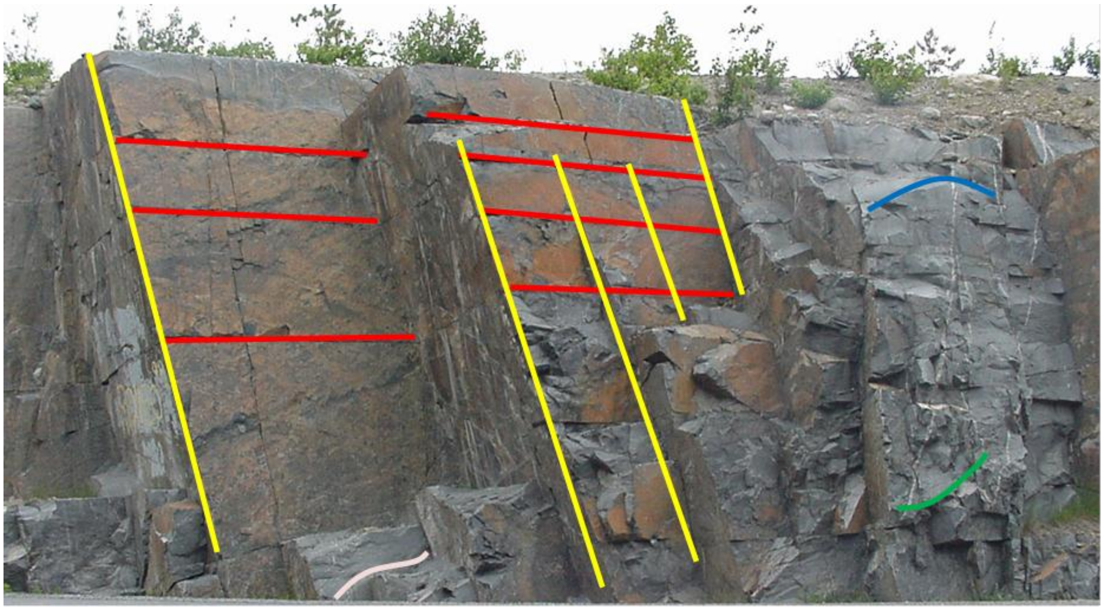

Figure 1.2. Image of a rock cut showing systematic (yellow and red) and non-systematic (almond, blue, and green) discontinuities.

1.2 ORIGIN OF DISCONTINUITIES

Some common terms used to describe discontinuities indicate their dominant mode of formation and geological history. These terms include faults, joints, fractures, and bedding. A fault is a plane of a shear failure that exhibits clear signs of differential movement of the rock mass on either sides of the plane (Price, 1966). A fault is assumed to be caused when changing tectonic stresses produce a shear stress that exceeds the shear strength on a particular plane in the rock mass (Kersten, 1990). Joints are cracks and fractures in rocks along which there has been extremely little or no movement (Price, 1966). Joints are more frequent than faults. The origin of certain joints is clearly related to simple mechanisms. Examples include columnar jointing formed by stresses induced during the cooling of basalts, and the slabbing joints caused by diurnal temperature changes on exposed rock faces (Priest, 1993). The ubiquitous nature of other joints suggests that their formation is related to some other, more common, geological process (Price, 1966). A fracture is a discrete break in a rock which is not parallel with a visible fabric (Bridges, 1975). The term fracture is used by rock mechanics engineers to describe the cracks generated during rock material testing, blasting and brittle rock failure (Priest, 1993). Bedding is a surface created by a change in such factors as grain size, grain orientation, mineralogy or chemistry during the deposition of a sedimentary rock (Priest, 1993). It is worth to note that bedding does not always create discontinuities in rocks, however they form some of the most extensive discontinuities in sedimentary rock mass (Priest, 1993). Bedding features generally run parallel to one another.

Terms such as foliation, cleavage, and schistosity, though not very common, are also used to describe discontinuities. Foliation exists primarily in metamorphic rocks.

Foliation can be defined as parallel orientations of platy minerals or mineral bands. Cleavage refers to parallel discontinuities formed in incompetent layers in a series of beds of varying degrees of competency. Rock cleavage planes are not controlled by mineral particles in parallel orientation (Wyllie and Mah, 2004). Schistosity is primarily a property of schist. Schistosity refers to foliations in either schist or other coarse grained crystalline rock, due to the parallel arrangement of mineral grains of platy or prismatic type, such as mica (Wyllie and Mah, 2004).

Earlier researchers, such as Becker (1893), and Van Hise (1896), both suggested that jointing in rocks is caused by either tensile or compressive stresses. As a matter of fact, joints are now widely accepted to be caused by three main stresses; compressive, tensile, and shear. However, geologists and engineers believe that joints (discontinuities) caused by shearing should strictly be referred to as faults. Joints formed by compression are known as compressional cracks or pressure cracks, whiles those formed by tension are known as tension cracks. After examining thousands of joints in a multitude of outcrops all over the world and making statistical evaluations of their orientations, Scheidegger (1978), found the following six general facts about joints:

1. At a single outcrop, one typically finds three joint systems. These systems are usually very definite. One system is near-horizontal (dips 0^o to 40^o), corresponding to some lithological factor. The two remaining systems are near-vertical and almost orthogonal to each other.
2. The non-lithological joints in fresh outcrops appear to cut clear across joint systems of obviously older age. These joints are, therefore, interpreted as tectonic joints.

3. Several outcrops near each other (within a few kilometers) usually show preferential joint orientations that are consistent with each other.
4. Outcrops within a region (10-20 km radius) commonly show, if treated together, definite preferential "tectonic" joint orientations. When the outcrops are considered singly, however, one often finds that approximately a quarter show "anomalous" tectonic joint orientations. These orientations are rotated up to approximately 30^o with regard to the "regionally" preferential orientations. The anomalous outcrops are not randomized but rather show a consistency amongst one another.
5. Rotated joints may "come through" as secondary, weak maxima in a regional joint diagram. The latter then has the following features: one strong lithological maximum, two strong maxima, corresponding to two near-orthogonal regional orientations, and two further but weak, near-orthogonal maxima, corresponding to the tectonic joints in the anomalous outcrop.
6. The well develop-regional joint system can commonly be explained interms of global plate tectonics if the bisectrices of the regional joint strikes are taken as principal horizontal tectonic stress directions.

In a triaxial stress state, two groups of theories exist regarding the origination of joints; the first group predicts jointing to occur at some intermediate angle ($30^o – 45^o$) to the maximum pressure direction. The second group, which only occurs under very special cases, predicts jointing to occur either parallel (tension, pressure cracks) or normal (slaty cleavage) to a principal stress direction (Scheidegger, 1978).

1.3 COLLECTION AND ANALYSIS OF DISCONTINUITY DATA

Methods of obtaining discontinuity data in a rock mass include:

- Cell mapping,
- Scanline mapping,
- Fracture set mapping, and
- Oriented core (Donavan et al., 2005, Priest and Hudson, 1981, Nicholas and Sim, 2001, Handy et al., 2004).

Cell mapping involves first dividing either the rock face or the outcrop into cells and then measuring the properties of all discontinuities within each cell that is longer than a pre-selected minimum. Scan-line mapping involves first stretching a measuring tape along either a rock face or an outcrop and then measuring both the properties of the discontinuities as well as their points of intersection with the tape line. Fracture set mapping involves identifying and measuring the properties of the discontinuities during geological mapping. Oriented core is similar to scan-line mapping. It is used when the rock types of interest are not exposed (Hustrulid, 2000, Donovan et al, 2005). The above mentioned manual methods all share common disadvantages (Kemeny and Post, 2003). These disadvantages include:

- An introduction of erroneous data due to sampling difficulties and human bias,
- Considerable safety risks, as measurements are conducted at either the base of existing slopes, or during quarrying, tunneling, or mining operations, or along busy highways,
- Difficult or impossible direct access to rock faces,
- Time consuming and labor intensive costly endeavors.

The use of laser scanners to measure discontinuities is on the increase in order to overcome these problems. Laser scanning can be used as a cheaper, more objective, more precise, and more accurate, than the manual methods to determine discontinuity orientations (Kemeny et al., 2003, Nasrallah et al., 2004, Slob et al., 2005, Otoo et al., 2011). Different types of laser scanners exist. The following section (1.4) and a section of chapter 2 elaborates on laser scanning, also a section of chapter 3 elaborates on the Leica ScanStation 2 laser scanner, the laser scanner used for this research.

The analysis of discontinuity data is very important. It basically involves building statistical models that represent the discontinuities. These statistical models are in most cases based on the fact that geological processes usually generate one or more clusters of nearly parallel discontinuities in a rock mass (Priest 1983). Thus, methods of analysis of discontinuity focus on systematic discontinuity.

1.4 LASER SCANNING AND DIGITAL PHOTOGRAPHY

The use of laser scanners and digital images is becoming increasingly useful in geology and engineering, in order to overcome some of the problems encountered when traditional methods, such as the Brunton compass is used to determine orientation of discontinuities. 3-D Laser scanning and digital photography are the two dominating imaging technologies (Nasrallah et al., 2004).

A LiDAR (Light Detection and Ranging or Light Radar) scanner uses either a time of flight or phase shift sensors to generate a 3-D image of a surface. It basically involves the emission of light pulse from a source onto a surface. The surface of the object is reflected, returning the pulse back to the source, which then receives and measures it. Laser light pulses are primarily used in LiDAR scanners because of their strong signals and narrow beams. A high precision counter measures the travel time and intensity of the returned pulse. The pulse source also measures the angle at which the light pulse is emitted and received, these enables the spatial location of a point on a surface to be calculated (Nasrallah et al, 2004). The result is millions of points reflected from the surface. The points are represented by xyz coordinates, known as a “point cloud”.

The two main common types of LiDAR systems used are the terrestrial and the airborne systems. As the names suggest, terrestrial systems are stationed and used on land to identify and study features of interest. Airborne systems however are primarily stationed or used in the air to identify and study features of interest. The bathymetric LiDAR is an example of an airborne system. This system is used over water to determine the depth of its floor. Airborne LiDAR systems require stronger laser signals than terrestrial LiDAR systems. According to the United States Geological Survey (United States Geological Survey, 2012), terrestrial LiDAR units possess significant advantages over traditional surveying techniques and airborne instruments. With regards to airborne systems, terrestrial LiDAR units are;

- Less expensive to deploy, schedule, and operate,
- Able to provide a significant increase in spatial resolutions,
- Able to map features otherwise obscured from the air, such as overhanging cliff faces, caves, and forest understory,
- Optimal for rapid damage assessments, long-term geomorphic change monitoring, and precision modeling (United States Geological Survey, 2012).

Terrestrial LiDAR units or systems possess different qualities. Some systems have better beam divergence, better range, and better data collection rate than others. Systems with smaller beam divergence, a higher range, and higher data collection rates, are mostly preferred and hence, are more expensive when compared to other systems.

As previously mentioned, LiDAR scanners use either time of flight or phase shift sensors to generate a 3-D image of a surface. Time of flight sensors determine displacement and distance by measuring the time it takes light to travel from an instrument to a target and back. Time of flight sensors, on average scan between a few thousands to several hundreds of thousands of pulses per second. The time required for each pulse to travel to the target and back to the sensor places a limitation on the scanning range (displacement or distance). Figure 1.3 is an illustration of the distance measurement from a time of flight sensor. Phase shift sensors send out modulated light, and measures its reflection on the target. The reflected signal is mixed with the originating signal to obtain the phase shift. The shift is then translated into a measurement of distance between the sensor and the target. An advantage of the phase shift sensors over the time of flight sensors is the ability to measure both the direction and the velocity of a moving target in addition to its range. Figure 1.4 is an illustration of the distance measurement from a phase shift sensor.

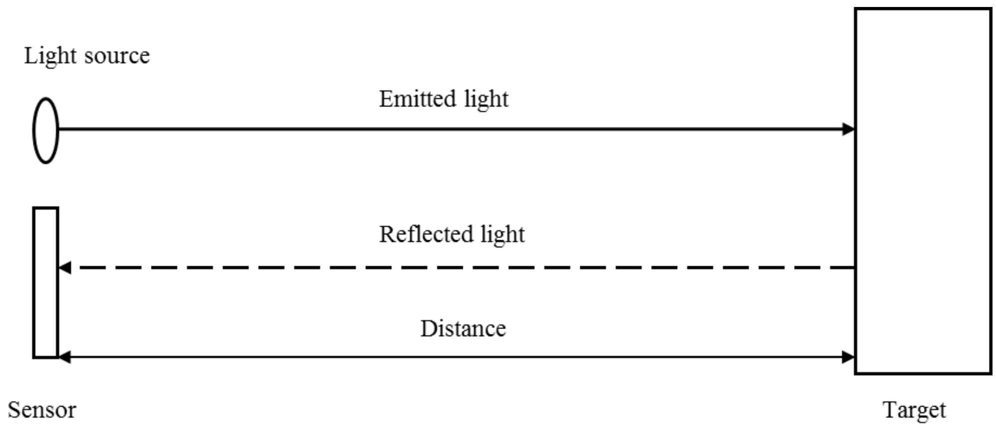

Figure 1.3. Schematic of a time of flight sensor and a target.

The distance expressed as a function of time and speed of light is,

$$D = \frac{T\ x\ c}{2} \tag{1.0}$$

where D is the distance, T is the elapsed time, and c is the speed of light.

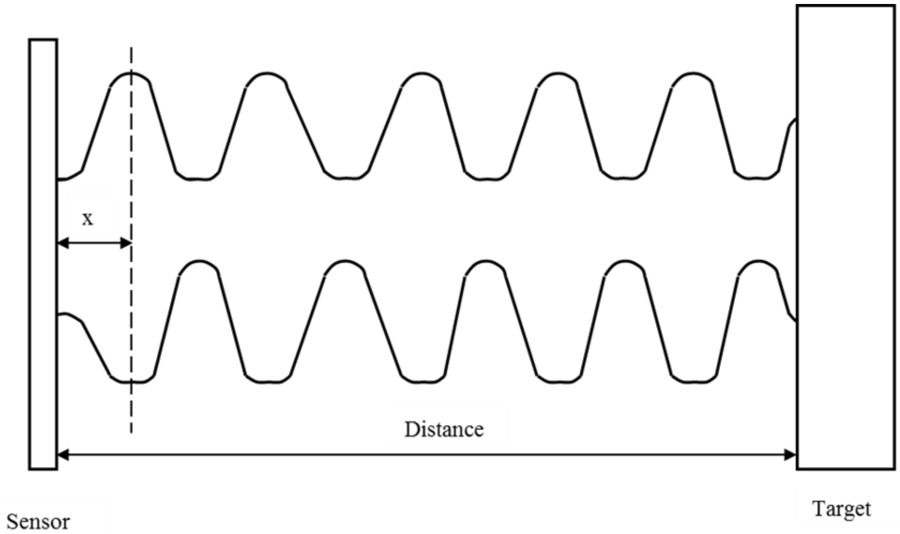

Figure 1.4. Schematic of a phase shift sensor and a target, x is the distance corresponding to the differential phase (modified from Woodbury et al., 1993).

The relative phase shift expressed as a function of distance to the reflecting target surface is;

$$\phi = \frac{4\pi D}{\lambda}, \qquad \text{Hence, } D = \frac{\phi\lambda}{4\pi} = \frac{\phi c}{4\pi f} \tag{1.1}$$

where ϕ is the phase shift, D is the distance to target, λ is the modulation wavelength, c is the speed of light, and f is the modulation frequency (Woodbury et al., 1993).

Unlike LiDAR, digital photography makes images using a digital technology (camera). The image produced is primarily 2-D. Digital cameras use a sensor array of millions of tiny pixels to produce a final image. Digital cameras can be grouped as either compact or single lens reflex (SLR) cameras. This grouping is based on the camera's viewfinder mechanism, lens, or sensor size. The viewfinder mechanism defines the light that reaches the camera sensor when the shutter button is pressed. In a compact camera, the light that reaches the sensor is estimated by the viewfinder mechanism. In the SLR camera, however, the light seen through the view finder is the same light seen at the sensor when the shutter button is pressed (Figure 1.5). An additional difference between the two cameras includes changing the lenses. In SLR cameras, the lenses can be changed, whilst, lenses in compact cameras are fixed. Finally, compact cameras have much smaller lenses when compared to SLR cameras (Cambridge in Color, 2012).

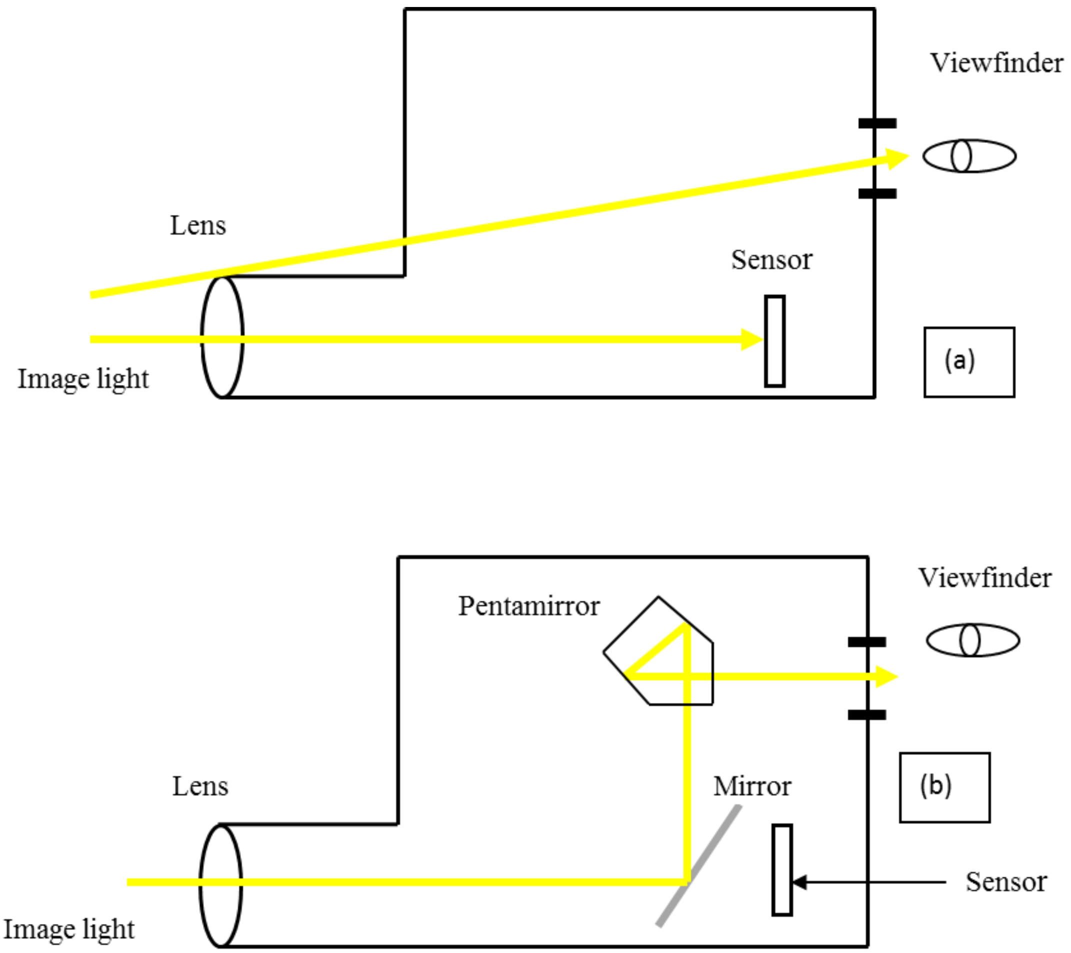

Figure 1.5. Schematic of (a) compact camera (b) SLR camera (modified from Cambridge in color, 2012)

Digital images are excellent for observing traces on smooth rock faces (Nasralla et al., 2004). Digital images contain a great deal of information, their application in the field, such as rock engineering, that depends heavily on visual data and analysis cannot be underestimated (Handy et al., 2004). Digital images can be processed and scaled to suit one's need using different image processing techniques, providing information on trace lengths, spacing and roughness (Post et al., 2001; Nasralla et al., 2004). Handy et al. (2004) argued that there are other features in digital images of rocks in addition to the presence of fractures that can provide rock characterization information. Color, a very common characteristic of digital images can be used to extract additional rock information, such as fracture fill and changes in rock types. Texture can also be used to obtain information on the weathering of an intact rock, condition of the fractures, differentiate rocks from other materials, and to classify different types of rocks (Patio et al., 2002, Lepist, 2004). Kemeny et al., (2002), demonstrated a correlation between digital rock mass rating (from digital images) method, and actual geologic strength index and rock mass rating measurements made in the field.

1.5 SURFACE EXPRESSION OF DISCONTINUITIES

Discontinuities or cracks in the rock mass, when exposed in an outcrop or cut manifest themselves in one of two ways, often in both ways on the same exposure.

- On flat planar rock cuts, the intersection of the plane of the discontinuity and the rock cut results in a visible line "fracture trace" that lies on both planes (Figure 1.6).
- On rock cuts that are irregular, the actual faces of the discontinuities can be exposed. These fracture surfaces can be considered to be like "facets" on a cut precious stone (Figure 1.6).

Figure 1.6. A rock cut containing both fracture traces (red line) and facets (cyan polygon) (Otoo et al., 2011)

1.6 STATEMENT OF RESEARCH

Data on discontinuities is necessary for the design, characterization, and analysis of rock structures. The use of laser scanners and optical images is necessary to overcome the problems and disadvantages of the manual or traditional method. Great strides have been made towards automated measurements using both optical imaging and LIDAR scanning methods. The difficulty is that discontinuities manifest themselves on outcrops in two different ways, either as facets that can be measured by LIDAR or as traces that can be measured, at least in 2-D, by optical imaging (Fig.1.6). Traces are linear features that intersect with the discontinuity and the rock cut, whilst facets are the actual discontinuity surfaces that are exposed in the rock. It is rather unfortunate that LIDAR scanning cannot measure traces nor can optical imaging measure facets. This is complicated by the fact that both facets and traces are often present in the same rock. Thus, selecting a measuring tool to fit the type of exposure is not possible. Additionally, the traces and facets in a discontinuous rock mass could be either natural or induced (Fig.1.7). A natural discontinuity is primarily caused by a geological process or processes while an induced discontinuity is primarily caused by human activities. In most cases, identifying a discontinuity as either natural or induced can be difficult, especially in situations where the rock face has undergone some weathering. Results of discontinuity analysis can be very misleading if natural discontinuities are treated as induced, and vice versa.

This research is in two areas, the first is to determine the differences between traces, natural, and induced facets. The second is to develop an integrated approach to combine optical and LIDAR imaging techniques to determine 3-D discontinuity orientations.

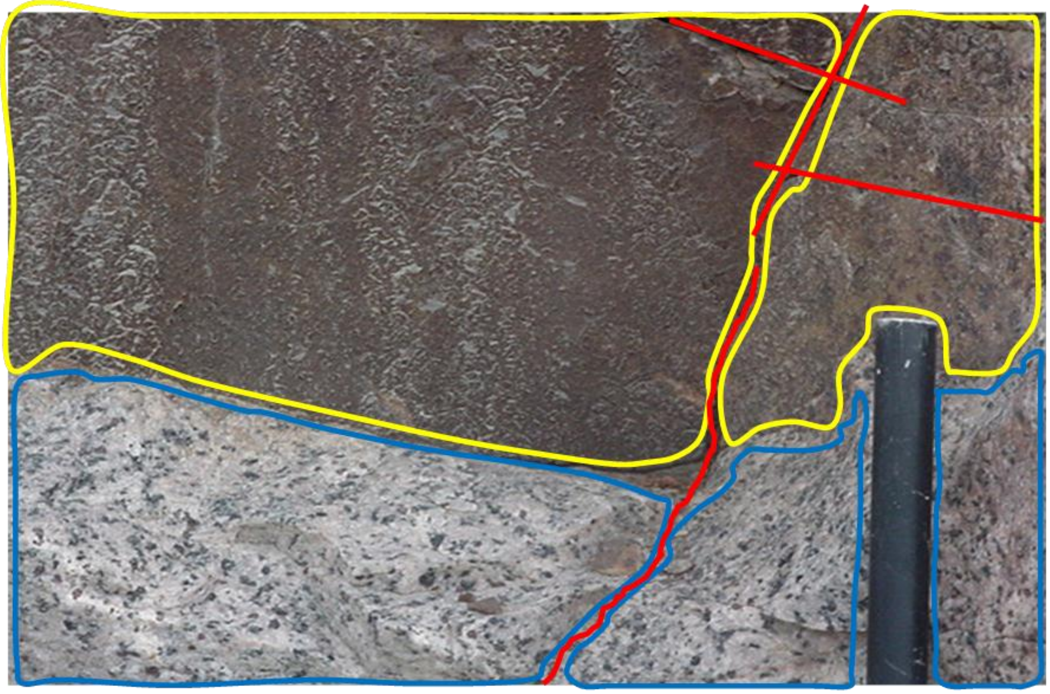

Figure 1.7. Image of a rock cut showing natural facets (joint surface, yellow polygons), joint traces (red lines) and induced facets (blasted surface, blue polygons).

1.7 OBJECTIVES AND SCOPE

This research sought to determine the differences between traces, and natural versus induced facets. This research also sought to develop an integrated approach that combines optical and LIDAR imaging techniques to estimate 3-D discontinuity orientations. The part of the research that dealt with the differences between traces, natural, and induced facets, was an observational research, involving field observations as well as a detailed study of both 2-D and 3-D rock images. The part of the research that dealt with the combination of optical images and LiDAR techniques was achieved by the collection and analyses of field data on discontinuities in rock masses, and the development of rigorous automated codes. Accepted engineering standards were obeyed and followed in the course of this research.

1.8 STRUCTURE OF DISSERTATION

Chapter 2 presents background and comprehensive literature review on the analysis of discontinuity data, optical imaging, and LiDAR techniques. Chapter 3 contains both description of the research materials and methodology. Chapter 4 analyzes the differences between traces, natural, and induced facets. Chapter 5 elaborates on how 3-D discontinuity orientations could be determined from optical imaging and LiDAR technology. Chapter 6 contains the conclusion and recommendations for future work, followed by appendices, and references.

2. BACKGROUND AND PREVIOUS WORK

Digital and LiDAR images are becoming increasingly useful in geological sciences and engineering. Though great developments have been made with regards to automated measurements using both optical imaging and LiDAR scanning methods, room for improvement still exist. The use of imaging and scanning provides the following advantages:

- Fast and time saving
- Reduces risk
- Increase in data quality and reliability
- Images and scans can be stored for future reference

This chapter covers both a comprehensive background and a review of the geological applications of digital images and LiDAR technologies, the three point problem in geology, and natural and induced fractures. In addition, this chapter reviews the analysis of discontinuity data.

2.1 PHOTOGRAMMETRY AND LiDAR TECHNOLOGY: STATE OF THE ART

The imaging industry has surprisingly grown from the use of Pin-hole cameras to the development of 3-D laser scanners, such as the LiDAR. Cameras are now everywhere, even on our mobile phones. 3-D laser scanners will likely become available on our mobile phones someday as well.

2.1.1. Image Acquisition and Formation in Photogrammetry. The pinhole camera is the earliest image acquisition tool known to mankind. This camera has no lens. Instead, in its most basic form, it consists of a box with a hole on one of its sides and a photographic plate on the opposite side. Images from the pinhole camera are created through the rectilinear propagation of light. Light rays travel in a straight line from the 3D scene facing the box onto the photographic plate. The image is formed by the principle of perspective projection, also known as either the “pinhole perspective” or the “central perspective” projection model (Forsyth and Ponce, 2003). Images formed by perspective projection are inverted. Figure 2.1 is an illustration of both the pinhole camera, and the perspective projection model.

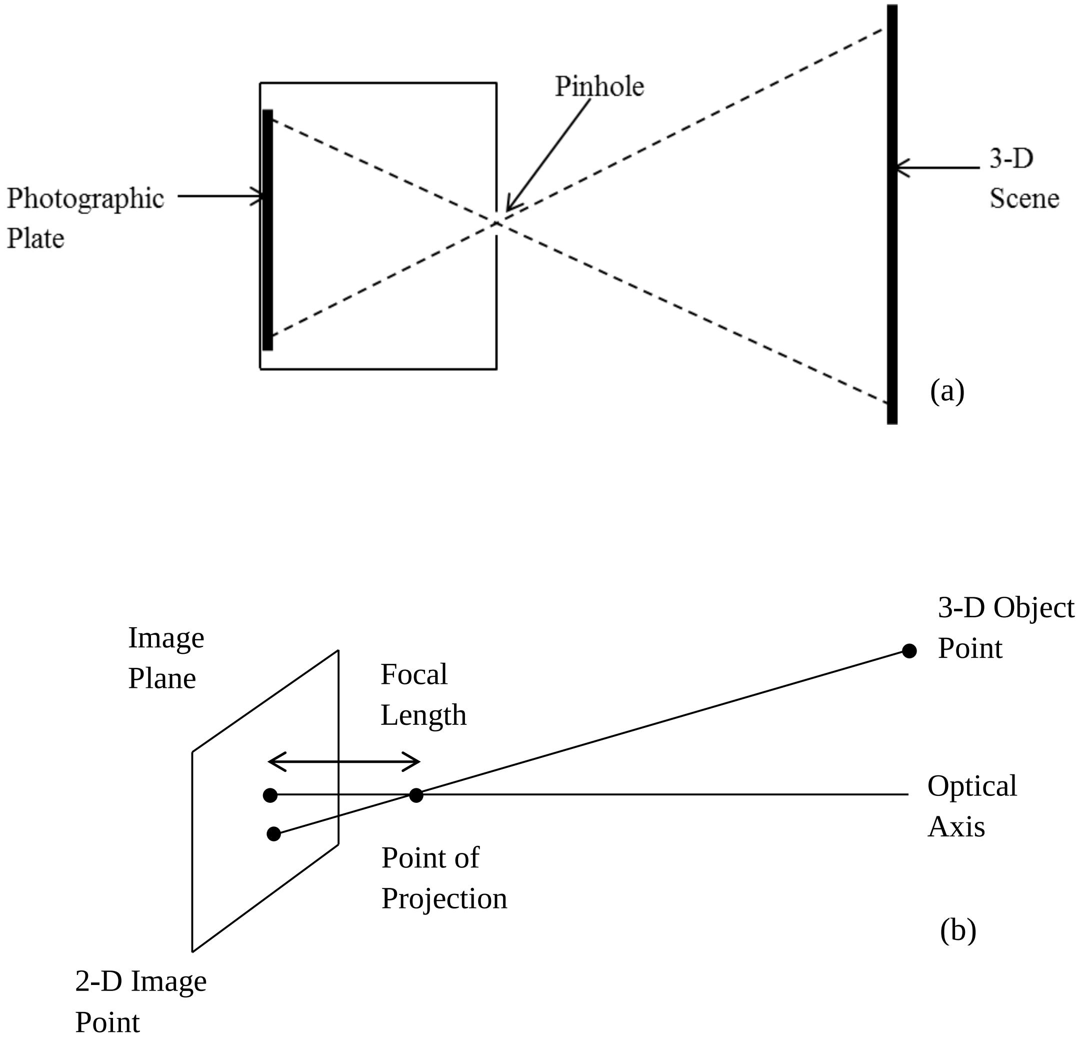

Figure 2.1. Schematic illustration of a (a) pinhole camera, (b) perspective projection model (Forsyth and Ponce, 2003).

Most of today's cameras have lenses, and are referred to as digital cameras. These lenses allow the gathering of more light than just a single array, as in the pinhole camera. Light is first focused by the lens, and then converted by a sensor array of millions of tiny pixels to produce a final image. Common sensor sizes used in today's digital cameras are presented in Table 2.1. "Type" refers to the commonly used type designation for sensors. "Aspect ratio" refers to the ratio of width to height. "Diameter" refers to the diameter of the tube size. "Diagonal" refers to the diagonal of the sensor's image-producing area. "Width" represents the width of the sensor's image-producing area. "Height" represents the height of the sensor's image-producing area. Figure 2.2 illustrates the general imaging mechanism for digital cameras. The image produced by a digital camera is primarily 2-D. In recent years, developments have been made in the area of 3-D image production by digital cameras. More research is still needed, however, as most of the 3-D images produced by digital cameras on the market could be improved.

Table 2.1. Common sensor parameters (Deb et al., 2007)

Type	Aspect ratio	Diameter (mm)	Diagonal (mm)	Width (mm)	Height (mm)
1/3.6"	4:03	7.056	5	4	3
1/3"	4:03	8.467	6	4.8	3.6
1/2.7"	4:03	9.407	6.592	5.27	3.96
1/2"	4:03	12.7	8	6.4	4.8
1/1.8"	4:03	14.111	8.933	7.176	5.319
2/3"	4:03	16.933	11	8.8	6.6

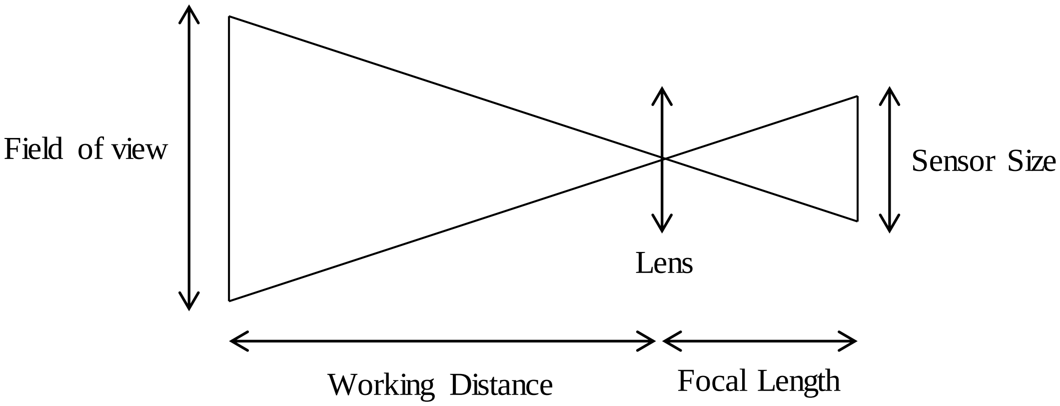

Figure 2.2. Imaging mechanism for digital cameras (Deb et al., 2007).

The image's field of view is estimated using:

$$FOV = \frac{s\ x\ d}{f} \tag{2.0}$$

where s is the sensor size (mm), d is the working distance (mm), and f is the focal length (mm).

2.1.2. Digital Image Representation and Processing Operations. Generally, any two-dimensional function that bears information can be considered an image. Thus, an image has a two-dimensional array of intensity values. Elements in the array are known as pixels. A pixel can be defined as the smallest unit of an image that can be either represented or controlled. Each pixel represents spatial coordinates in the scene. Image representation is basically the presentation of pixels with color. Images may be produced in either black and white or colored. A black and white image consists of pixels holding single numbers. These numbers correspond to the gray level of the image at a particular location**.** A color image consists of pixels holding three numbers. These numbers correspond to the red, green, and blue levels of the image at a particular location.

Image processing, in general terms, refers to the manipulation and analysis of pictorial information. Pictorial information can be defined as any two-dimensional visual image. Any operation that acts to improve, correct, analyze, or in some way change an image is called image processing (Baxes, 1994). Image processing has been applied in several fields, including geological science and engineering. The four most common image processing operations include the following:

- Smoothing
- Thresholding
- Edge Detection
- Thinning

Smoothing, also known as either blurring or noise reduction, involves the removal of texture or noise that may mask features of interest. Additionally, it involves the replacement of dead or defected pixels with pixel values of the weighted average value of their neighbors. This is based on the fact that the value of a pixel in an image is usually similar to that of its neighbor. Images with only two pixel values are termed binary images. The two pixel values are 0 and 1, and are represented with white and black, respectively. The process of converting a grey scale image to a binary image is known as thresholding.

Edge detection is also referred to as edge enhancement in some literatures. Image edge enhancement reduces an image to show only its edge details (Baxes, 1994). The enhancement process does not increase the inherent information content in the data. It simply emphasizes certain specified image characteristics. The goal is to accentuate certain image features for either subsequent analysis or image display (Jain, 1989).

Thinning is the process of reducing the width of an image element to just one pixel. Thinning is done to in order make subsequent operations easier and more accurate.

2.1.3 Discontinuity Enhancement on a Rock Face. Discontinuities in a rock mass sometimes need to be enhanced before images are acquired. Enhancement of discontinuities can help simplify subsequent image processing and analysis stages. Methods by which discontinuities on a rock can be enhanced include:

- Spraying the rock face with water;
- Inducing the rock face with florescent dye;
- Subjecting the rock face to a low angled lighting (Harvey, 1987; Maerz, 1990).

Harvey (1987) demonstrated enhancing discontinuities by spraying water on a gneissic road cut. Doing so allows water to enter the joints. After allowing the excess water on the rock face to dry, he observed that small cracks were enhanced the most. He also found that either black and white or false color infrared film produced the best increase in discontinuity visibility.

In another test, Harvey (1987) demonstrated an additional method by which discontinuities can be enhanced by inducing florescent dye on cracked concrete slab. He found equal results using either black and white, or color photography. “Low angle lighting can make joint traces more visible or discernible” (Maerz, 1990). This is because joint traces typically appear as shallow and narrow depressions in the rock face (Maerz, 1990).

2.1.4 Photogrammetry and Digital Imaging in Geological Science and Engineering. The primary rationale behind the use of digital images in geological science and engineering is to acquire information unavailable from traditional methods, and to also speed up the geological analysis process. Field data collection can be time consuming, expensive, and risky. It can also be very difficult due to the fact that features of interest could be inaccessible. Digital images can be easily acquired with a digital camera, without either special skills or training. These images can then be processed either manually or automatically.

McCarter (1976) believed that the difficulties encountered in open pit mapping can be substantially reduced by utilizing a modified form of a plane table photogrammetry. McCarter (1976) developed a technique by which photographs of rock slopes in an open pit mine could be used to locate major geological structures. The technique used photographs taken from the ground as the base upon which details were recorded. The information was later transferred to plan maps using the plane table principle of location by intersection. McCarter (1976) accommodated changes in topography by taking additional photographs. The technique proved to be a practical tool for the detailed investigation of both potentially unstable areas and routine geological mapping (Zavodni and McCarter, 1976; Richardson, 1975).

Hagan (1980) mapped the orientation of rock fractures with photographic measurement. He used a camera with the highest flash synchronized speed available, loaded with fast black and white film. He accomplished the interpretation of his photos by viewing the stereo-pair of photographs from slightly different angles. Hagan (1980) found the method to be particularly useful in areas where either natural or mining-induced fracture density is high or of a complex nature. He stressed the advantages of photogrammetry, which include time saving, efficiency and accuracy, unbiased sampling, and the provision for permanent record.

Franklin et al. (1988) measured rock fragmentation with digital photoanalysis. This method determined the sizes of both overlapping and non-overlapping fragments to reconstruct a true size distribution. Franklin et al. (1988) took photographs of the fragmental rock, and digitized the block outlines. They measured the area of both whole and partially obscured blocks by counting pixels. They obtained a true 3-D distribution of fragment volumes or weights, and converted it from a frequency histogram which expresses the number of particles in each volume class into a cumulative weight distribution.

Tsoutrelis et al. (1990) used photoanalysis to evaluate geometric characteristics, such as discontinuity orientation, trace length, discontinuity spacing, and joint roughness coefficient on jointed rock masses. They collected black and white photographs of underground locations of interest. These images were digitized, converted into an array of pixels, stored, displayed, and processed, all with the aid of a microcomputer. Tsoutrelis et al. (1990) stated that the ability to take many measurements of geometric discontinuity parameters when using imaging techniques is an important advantage over other possible techniques.

Using both a light sectioning method and digital image processing, Maerz et al. (1996) developed a new method to measure both underbreak and overbreak in underground openings. They measured a tunnel profile using a radial sheet of light (light sectioning method). They then acquired and digitized an image of the final profile, and superimposed it over the design profile. Doing so allowed them to identify, quantify, and graphically present zones of both overbreak and underbreak.

Crosta (1997) built discontinuity maps from images, focusing on simple photographic techniques and their implementation from computer aided analyses for the characterization of rock mass fracturing features. He emphasized on scale problems and reconstruction fracture density stereoplots on the basis of data collected from images according to different lithologies and outcropping conditions. Crosta (1997) implemented the analyses on planar density, spacing, frequency, and terminations in solid rock or against other discontinuities and spatial correlation in software to yield a more complete rock mass characterization.

A semi-automatic methodology for discontinuity trace detection in digital images of rock mass exposures was presented by Reid and Harrison (2000). Their methodology detected discontinuity traces as individual objects. It initially considered a rock mass exposure’s digital image as a discrete surface, with elevations given by the brightness levels of the pixels. Discontinuity traces were then related to a topographic ravine, which allowed some pixels within a discontinuity trace to be found by locating the ravine pixels. These ravine pixels were grouped and transformed into linear structures through processing techniques. The linear structures were then linked together in order to achieve the discontinuity trace detection.

Lemy and Hadjigeorgiou (2003) developed a procedure that uses a series of photographs of a rock face taken under symmetrical lighting orientations to construct discontinuity trace maps. Pictures were digitized and loaded into developed software, where subsequent analysis was optimized by pre-processing. Discontinuity traces were then extracted from the enhanced images using both edge and line detection algorithms. The result was a binary image, where black pixels corresponded to the detected features. The nature of the features were identified using artificial neural networks. These networks made it possible to distinguish between segments in the image that were due to the presence of a discontinuity and those due to other phenomena.

Using a computer based approach, Kemeny and Post (2003) developed a technique for estimating 3-D fracture orientations from 2-D trace information gathered from digital images of exposed rock faces. They clustered the fractures into sets, and represented each set by both the mean orientation and a measure of the scatter about the mean. They verified the technique on a number of case studies, concluding that it had great potential for rock mass characterization.

Using digital cameras and stereo photogrammetry, Gaich et al. (2004, 2006) measured the position, dip, and dip direction of discontinuities as well as distances and areas, by overlaying images on digital terrain models of rock surfaces which were generated by triangulation. Surface normals at given positions were computed from the mean orientation of neighboring surface elements. Planes whose orientations corresponded to the spatial orientations of marked discontinuities were automatically fitted based on 3-D polylines drawn on the traces in the image, and measured.

Chandler et al (2005) demonstrated that cheaper, consumer-grade digital cameras have the potential for routine surface measurement provided modeling is considered. Using feature based matching methods, they extracted digital elevation models and compared accuracies among three low-cost consumer grade digital cameras. They concluded that cheaper, consumer-grade digital cameras can even be successfully used for surface measurements when modeling is considered.

Tonon and Kottenstette (2006) compared field measurement to automated measurement. Their results concluded that digital photogrammetry yields reliable and reproducible results when applied to rock mass characterization. In addition to their conclusion, they stated that “digital photogrammetry is a matured enough technology that can be used with confidence by the industry” (Tonon and Kottenstette, 2006).

Deb et al. (2007) detected and analyzed discontinuity geometry of rock mass from digital images. They developed a transformation function that converts a line segment from an image coordinate system to a physical coordinate system. Their transformation additionally detects both lines as well as curves in the multilinear form. Objects which do not correspond to discontinuities in the image were classified as noise. These noises were removed by the “Hough transform”, a technique that can be used to isolate the features of a particular shape within an edge detected image (Parker, 1997).

2.1.5 3-D LiDAR Technology. 3-D laser scanners are becoming very popular in the marketplace. This popularity has led to competition among manufacturers to continuously enhance both their product offering and associated software. In fact, most current 3-D scanners are integrated with GPS systems. Rotating mirrors, a common property of 3-D laser scanners, allow measurements to be made over a scene. Major manufacturers of 3-D laser scanners include Optech, Trimble, Leica Geosystems, Riegl, Faro, Isite, Zoller+Frohlich, and InteliSum.

2.1.6 3-D LiDAR Data. The result of a LiDAR scan is millions of points reflected from a surface. These points are represented by xyz coordinates, basically known as a Point cloud. Light colored objects and closer objects give a higher reflection than darker objects and objects farther away. Generally, the data collected by a LiDAR system depends on the system's design and its components. The three basic LiDAR data options are:

- Point data (XYZ)
- Point and intensity (XYZI)
- Point, intensity, and mapped color (XYZRGB)

The point data (xyz) is the least demanding form of point cloud data with respect to computational requirements and data storage, however it is the most challenging to visualize with the human eye (Lato, 2010). The xyz values are the coordinates of the point. The point and intensity data (xyzi) consists of intensity values which are directly related to the reflectivity of the scanned object. Intensity is the percentage of the light returned in terms of light emitted. Intensity introduces a photographic quality into the point cloud, making the data relatively easier to visualize with the human eye. The point, intensity, and mapped color data (xyzrgb) consists of points and colors matching the red, green, and blue properties of a colored digital image. This data is the easiest to visualize with the human eye. LiDAR systems with internal digital cameras allow automatic association of the point data with colors from a corresponding optical image.

In a 3-D coordinate file, the point cloud is represented in a comma or tab-separated format as follows:

X1, Y1, Z1, intensity 1 ………………………………………… Line 1
X2, Y2, Z2, intensity 2 ………………………………………… Line 2
.

.

.

Xn, Yn, Zn, intensity n ………………………………………… Line n

Each line represents a point. Intensity values range from 0 to 255. Figure 2.3 shows the three basic point cloud data. Visualization of point cloud data also depends on the resolution of the data: the higher the resolution (greater number of points) the better the viewability (Figure 2.4).

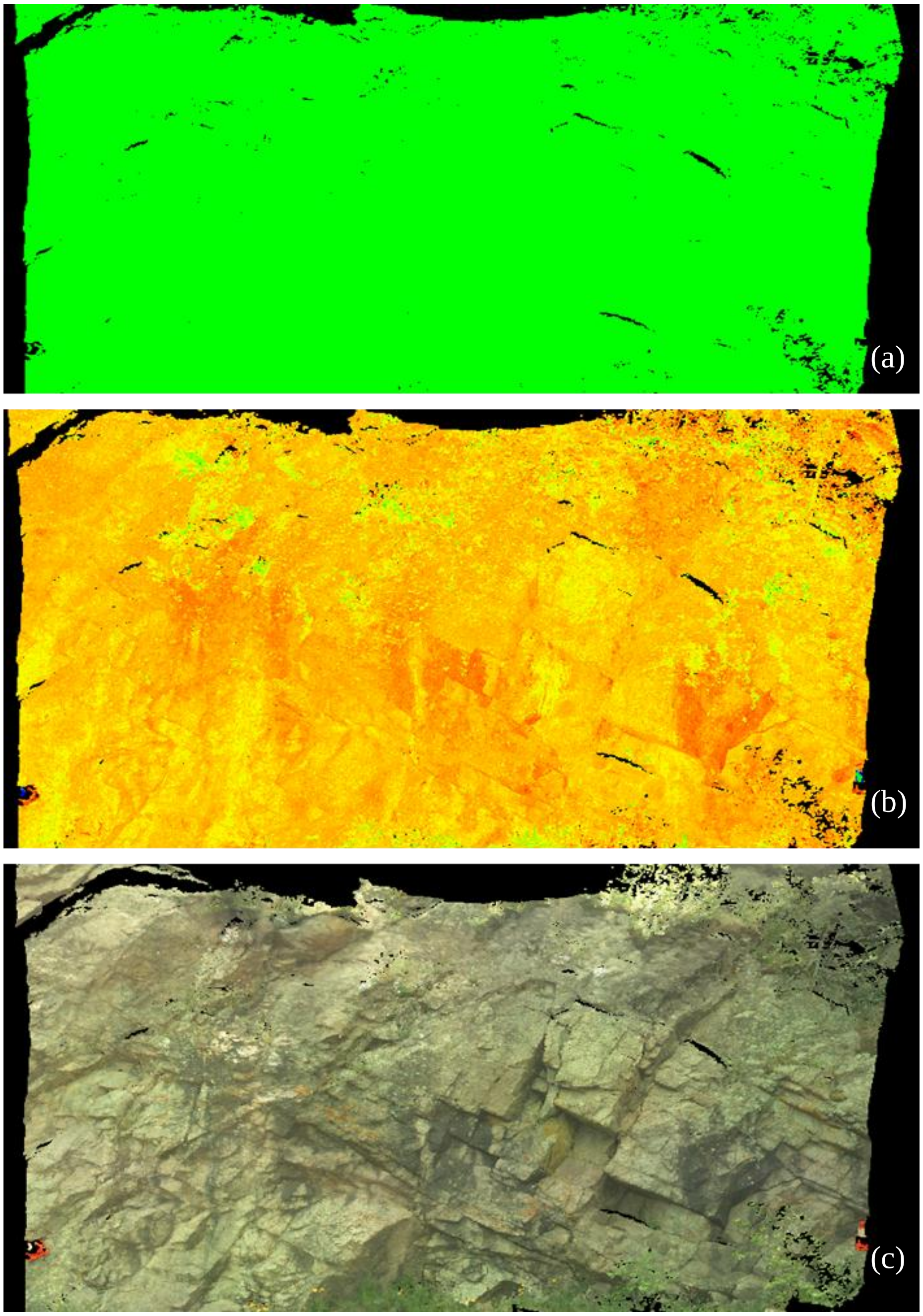

Figure 2.3. Three basic point cloud data of a rock cut in Colorado, (a) point data, (b) point and intensity, (c) point, intensity, and mapped color.

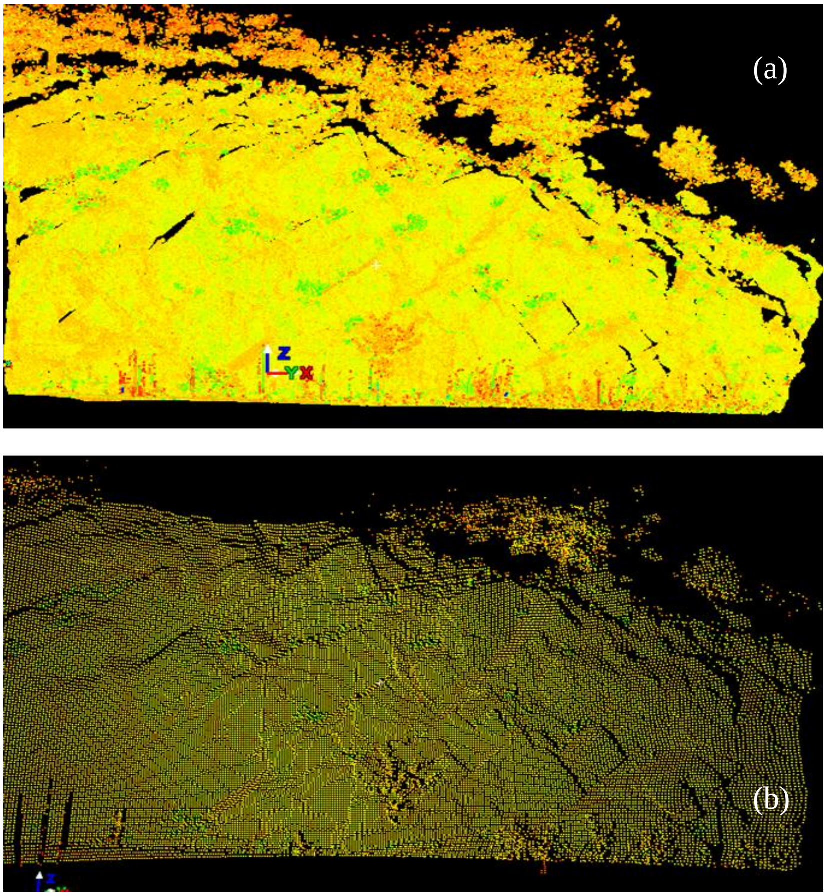

Figure 2.4. Image of a rock cut in Colorado scanned at two different resolutions, (a) resolution of 4x4mm, has more points hence a better viewability when compared to (b), (b) resolution of 8x8, and has fewer points.

2.1.7 LiDAR Data Processing. Point cloud data collected from the field must be processed in order to extract the needed measurements or information. A number of commercially available software packages for point cloud processing exist today. Most of these software tools, however, were developed by scanner manufacturers for general projects. LiDAR processing software packages currently on the market include “Cyclone and Cyclone Cloudworx” Leica geosystems, “Polyworks” by Innovmetric, “Riscan Pro” by Riegl, “Isite Studio” by Isite, “LFM Software” by Zoller+Frohlich, “RealWorks Survey” by Trimble and “Split Fx” by Split Engineering (Kemeny, 2008). Of these, “Split Fx” happens to be the only package developed for geological applications (discipline specific software). Hence, a need exists for more discipline specific software, especially for geologically related applications. A user’s choice of software depends primarily on factors such as budget, needs, experience, and data size.

Typically, most of the LiDAR software on the market performs operations which include:

- Visualization
- Segmentation
- Classification
- Filtering
- Transformation and
- Gridding (Fernandez et al., 2007)

Visualization is what allows the user to access the quality of the dataset. Visualization enables the planning and control of different processing schemes and also provides the presentation of the final product (Fernandez et al. 2007). Visualization functions usually include point selection tools, which allow the user to manually select single points from the point cloud data. According to Fernandez et al. (2007), segmentation refers to the operation that will segment or segregate points into different groups based on scan characteristics, without a prior knowledge of what they really are. Point cloud data can be separated into low, medium, or high based on their intensity.

The separation of points into different groups of classes defined by an intrinsic or natural characteristic is termed Classification (Fernandez et al. 2007). Separation of points into vegetation, broken rock, and fresh rock is an example of classification.

Filtering is the removal of a set of points from the point cloud based on either segmentation or a classification pattern. An example of filtering is the removal of vegetation points from the point cloud of a rock face. Transformation primarily means to change in either form or appearance. The transformation of a point cloud includes the rotation of the point cloud about one of its axes, cropping the point cloud to only points that fall within the space of interest, and the merging of several points together. A special form of transformation, which converts the coordinate systems of point clouds to other coordinate systems, is known as geo-referencing. The process of converting a point cloud into a regular spaced data set by means of interpolation is known as gridding (Fernandez et al., 2007).

2.1.8 3-D LiDAR Scanning in Geological Science and Engineering. Just like the case in generic digital images use, the main rationale behind the use of LiDAR images in geological science and engineering is to acquire information unavailable from traditional methods, and to speed up geological analyses. LiDAR can easily be used to collect geological information in the field. The technology is fast, provides a 3-D image, helps reduce human error, and can help collect data from inaccessible rock cuts or research areas.

Slob et al. (2004) presented a computer approach to identify and calculate different discontinuity sets on a virtual rock surface based on a terrestrial laser scan data. The point cloud of the rock face was reconstructed by triangulation. The reconstructed face was then visualized using 3-D visualization techniques. The discontinuity sets of the rock face were then identified using clustering techniques. Slob et al. (2004) concluded that “the automation of the identification and characterization of discontinuities in outcropping rock masses with the aid of 3-D terrestrial laser scan survey technique seems very promising”.

Mikos et al. (2005) used a medium range high performance, handheld non-reflective laser measurement system to monitor ground surface changes in rock fall sources areas. He also evaluated morphological changes by measuring distances from fixed points using the same system. Data was collected using both a laser scanner and a pocket computer from a serial port. The collected data was handled with a Qbasic computer program. Mikos et al. (2005) concluded that the laser measurement system provided a good replacement for the classical terrestrial geodetic survey equipment, especially when performing remote monitoring or morphological changes in a rock fall hazard zone.

Kemeny et al. (2005) demonstrated that LiDAR can be used to characterize rock masses. They made several scans using an Optech 3-D LiDAR scanner. They then compared analyzed results using the Split FX program to measurements obtained from the field. Results obtained from the LiDAR data was very close to results obtained from the manual measurements.

Donovan et al. (2005) demonstrated the use of 3-D imaging to characterize discontinuities in a rock mass. They reoriented point cloud data into a known coordinate system, triangulated the unstructured point cloud, and created polygon models from it. They then grouped elemental triangles with similar orientations into fracture patches. These patched orientations were then outputted and displayed on a stereonet. Donovan et al. (2005) concluded that 3-D laser scanners can be used to estimate the orientations of discontinuities in a rock mass. Additionally, they concluded that a larger data set is obtained when 3-D laser scanners and “fracture finder” algorithms are used to estimate discontinuity orientations.

Roncella and Forlani (2005) used an automated approach to extract the dip and dip directions from a dense digital surface model of a rock face obtained by laser scanning. In their approach, they generated a multi-resolution digital surface model (DSM) pyramid from an original DSM. This DSM was then segmented into planes at each level of the pyramid. The segmentation of the planes and the accuracy of the surfaces were then balanced with one another through clustering. The dip and the dip directions were then computed from the normal vector of each plane. Roncella and Forlani (2005) concluded that the laser technique can be used to estimate the dip and the dip directions of discontinuities in a rock mass. Additionally, they concluded that the technique can be used to determine discontinuity properties such as persistence, dilation, and roughness.

Voyat et al. (2006) computed discontinuity orientations and their positions on a rock face from dense point cloud data. In their work, they segmented the point cloud into discontinuity planes, in order to be able to single out the planes. Both dips and dip directions were then determined for the planes using the equation of a 3-D plane.

Enge et al. (2007) demonstrated the usefulness of LiDAR as a data collection technique for building accurate outcrop-based geocellular models by studying petroleum reservoir analogues using terrestrial LiDAR. They generated 3-D information using ground based laser scanning of an outcrop believed to be similar to a subsurface reservoir, and built virtual outcrops and geocellular models using industry standard reservoir modeling software. Enge et al. (2007) then collected important information from the built models into their subsurface model.

Preliminary results obtained by Otoo et al. (2011) in their research to determine 3-D discontinuity orientations from combined LiDAR and optical imaging, concluded that discontinuity orientations can be accurately extracted from point cloud data. They estimated discontinuity orientations from the point cloud data of selected sites and compared the results to manually obtained orientation measurements.

Mah et al. (2011) in their 3-D imaging for joint orientation analysis research concluded that 3-D imaging can successfully be used to estimate the orientation of joints in rocks. Additionally, they found that image resolution has minimal effect on the accuracy of measurements.

Maerz et al. (2012) presented a simple method by which discontinuity orientations can be measured from terrestrial LiDAR images. Terrestrial images were reoriented with the orientation of a sub-vertical joint. The orientations of discontinuity facets were then computed by picking three non-collinear points on the facets. Discontinuity orientation results obtained from this method were almost the same as the measurements they obtained from the field.

The fact is that, most of the work done in terms of discontinuity orientations using digital images are on traces (lineaments). Those done using LiDAR are on facets (planes). Since discontinuities exist as both traces and facets, the need still exists to determine methods by which orientations of both facets and traces can be determined with a single tool that combines digital images and point cloud data. This is another solid justification for this research. Several geological problems have also been solved with the assistance of LiDAR data. These projects include reservoir, channel, and terrain modeling in order to extract accurate 3-D lines and surfaces of geological features. LiDAR has helped in the understanding of several geological processes and activities by providing a means of collecting accurate and detailed geological data. Table 2.2 presents a summary of some major projects and geological problems that have benefited from the use of LiDAR.

Table 2.2. Examples of known projects, and geological problems that have benefited from the use of LiDAR (modified from Buckley, et al. 2008)

Project Location	Study Aim	Size of Area (km)	Number of Scans	Maximum Range (m)	Data Extracted	Benefit Conferred by LiDAR
Ferron Sandstone Utah, USA	Effect on small-scale clinoform geometry on reservoir models	1.5 x 1.5 x 1.5	18	650	3D lines representing Clinoform contacts; creation of surfaces and volumes	Allowed study of detailed features, where high internal accuracy is needed to track surfaces across outcrop
Woodside Canyon, Utah, USA	Modelling of channel bodies in reservoir models	1.5 x 1.5 x 0.3	18	500	3D lines representing channel bodies and sedimentary structures; facies contacts	Abillity to correlate channel geometry between arms of a canyon; integration of data at different scales
Canyonlands, Utah, USA	Structural reconstruction of ralay ramps for flow simulation study	0.6 x 0.3 x 0.1	13	400	Planes, meshes, cross-sections representing fault surfaces, lines representing fractures	Accurate geometry of ramp surfaces, faults and fracture network possible
Apricena Quarry, Gargano, Italy	Reconstruction of fracture network in carbonate reservoir analogue	0.3 x 0.3 x 0.05	17	250	Detailed fracture analysis: density, orientation, length, etc.; delineation of fill-in features	Integration of imagery, 3D data and geological measurements for micro-scale (cm to tens of metres) analysis
Roda Sandstone, Northern, Spain	Reservoir modelling of sedimentary environment	2 x .7 x .3	33	700	Stratigraphic horizons and faults; local sedimentary features (eg. tital bundles)	Correlation of and modelling of stratigraphy over a wide area, where exposure was sporadic
Hartley Steps, Northumberland, UK	Analysis of fault damage zone in sedimentary rock	0.1 x 0.05 x 0.05	4	100	Lines representing faults, strike and dip measurements	Accurate strike and dip measurements on otherwise inaccesible planes
Spitbergen, Norway	Terrain modelling and change detection in avalanche risk area	0.5 x 0.5 x 0.2	7	650	Detailed DEM for use in avalanche modelling and prediction	Collection of accurate DEM in polar area where no high-resolution data is available; repeat measurement at future epoch

2.1.9 Advantages of LiDAR over Photogrammetry. The four main advantages of LiDAR over photogrammetry include the following:

- LiDAR has the ability to conduct scans in the dark because it emits its own light. Photogrammetry, however, does not emit its own light. It relies on external light, such as the sun or the flash system, which can make it difficult to conduct survey in the dark. Additionally, shadows which are variable because of the direction of the sun, can affect the results of photogrammetry.
- LiDAR can determine the 3-D coordinates of features from a single scan. Photogrammetry, however, does not have this capability.
- LiDAR surveys generally require less time to process than an equivalent photogrammetry survey requires.
- LiDAR surveys (point cloud) allow for more digital data analysis than an equivalent photogrammetry survey allows.

2.2. THE 3-POINT PROBLEM

The 3-point problem is not new in geology. In geology, the 3-point problem is usually combined with topographic base maps. This allows the insertion of outcrop patterns. A plane can be defined by three non-collinear points. Thus, outcrop and structural geological features such as dips and strike can be estimated from three points of known locations and elevations. 3-point methods used in geology are either graphical or non-graphical.

2.3. NATURAL AND INDUCED FRACTURES

Most of the work done on distinguishing natural from induced fractures is primarily on image logs and core. Differences between natural and induced fractures are primarily in terms of fracture surface morphology and the geometric relationships between the core and the fracture shape. The fact is that, natural and induced fractures have geometries relative to a borehole. The author is yet to find any work that differentiates natural and induced fractures found on the surface.

2.4. ANALYSIS OF DISCONTINUITY DATA

Measurements of the orientation of facets are recorded in terms of dip direction and dip angle. Traces, however, are better represented with trend and plunge. Trend is the geographical azimuth measured in a clockwise rotation from the north of a vertical plane containing the trace (Priest, 1993). Plunge is the downward acute angle between a given trace and the horizontal plane measured in a vertical plane (Priest, 1993). For a given plane, the trend and the downward plunge of the line of maximum dip are referred to as the dip direction and the dip angle, respectively (Priest, 1993).

Another common parameter of interest for the orientation of planar features, known as the strike, is defined as the trend direction of a horizontal line in a given plane. Using the right hand rule, given dip directions (DD) and dip angles (DA) of a plane, The strike (α_s) is obtained from the relationship:

$$Strike\ (\alpha s) = DD - 90 \tag{2.1}$$

Discontinuity data are commonly analyzed by geostatistical methods. These methods are based on the fact that geological processes typically generate discontinuities in a given rock mass in one or more clusters of usually near parallel or parallel attitudes (Priest, 1993). Miller (1979) was the first to apply statistical methods to discontinuity analysis. His work was primarily on spacing. Miller (1979) considered three alternative methods for obtaining a sample of discontinuity spacing at each location: discontinuity spacing by sequence, discontinuity spacing by distance, and mean discontinuity spacing by distance.

Geostatistical methods were also applied by La Pointe and Hudson (1985) in their characterization and interpretation of jointing patterns in the Niagara dolomite, Wisconsin. Lamas (1986) also applied geostatistical methods in his analysis of the stability of rock faces. Based on Miller's (1979) methods, Villaescuya and Brown (1990) investigated the spatial correlation in joint spacing and joint locations for the most prominent sets at selected sites. Recently, geostatistics have been used by Zhou and Maerz (2002) to characterize discontinuity data from scanlines and oriented boreholes. Coli et al. (2012) found a strong link between geostatistical model parameters and the content, size, and spatial variability of rock fragments.

More emphasis was placed on discontinuity orientation data, as it is the most important discontinuity property, and also the primary focus of this research.

2.4.1 Representation of Orientation data. Orientation data of discontinuities can be represented graphically by means of either a rose diagram or a stereographic projection. The rose diagram is the simplest way to graphically represent discontinuity orientation data. The rose diagram is in the form of a circle, divided into convenient class intervals depending on the sample size. Dip direction values of the classes are counted and noted. The dip directions are then plotted in the circle as wedges. These wedges have their radial extents proportional to the frequency of each class interval. The rose diagram approach is typically suited when most of the discontinuities under consideration have dip angles greater than 60^o (Priest, 1993). The main disadvantage of the rose diagram is the fact that it does not contain information on the dip angle. However, this disadvantage can be overcome by plotting a histogram of dip angles of the class intervals. Presented in Figure 2.5 is a rose diagram, and a corresponding histogram of 101 discontinuity orientations collected from one of our research sites in Southeastern Missouri.

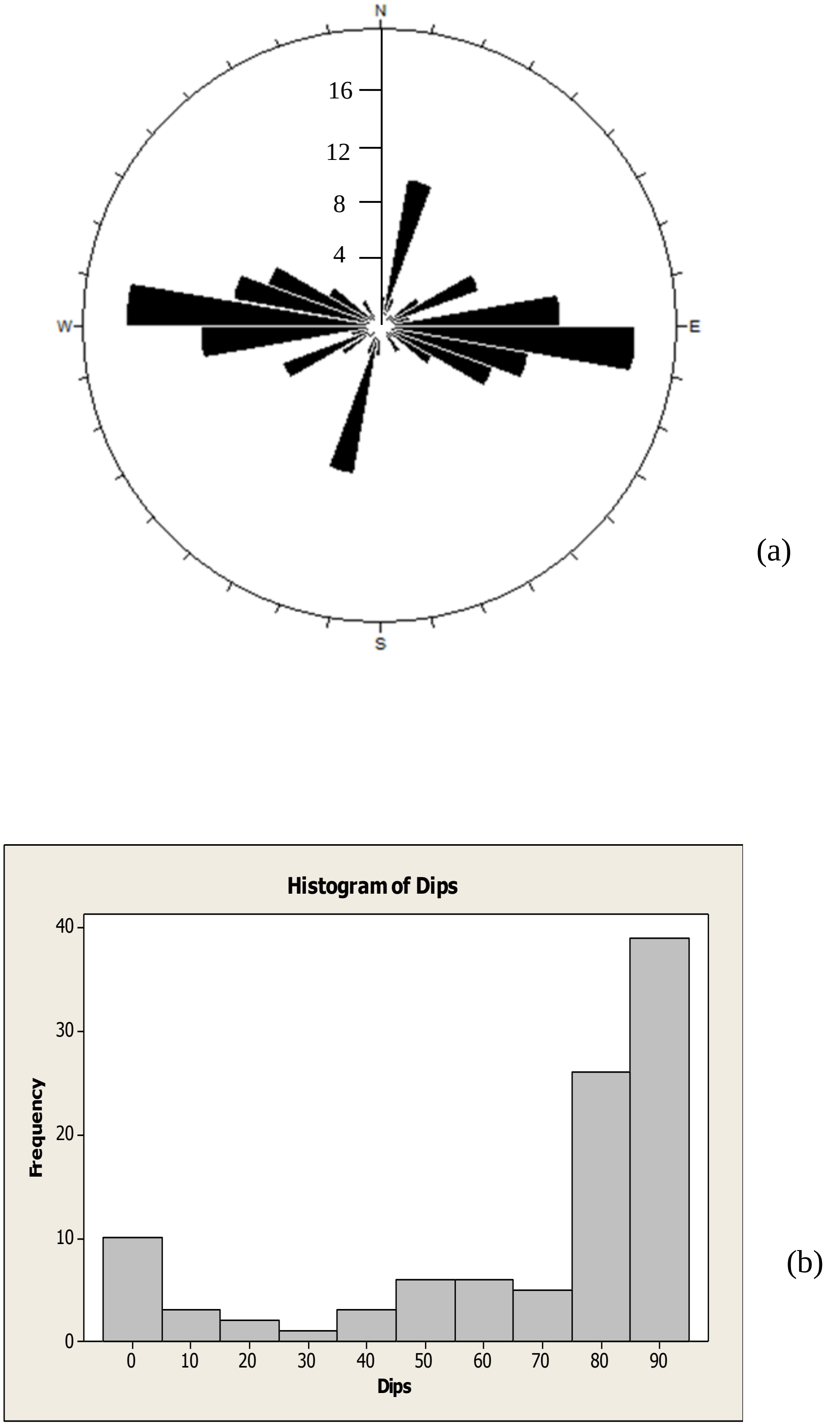

Figure 2.5. Representation of orientation data, (a) rose diagram of 101 dip directions from a rock cut in southern Missouri. The marked scale represents the frequency, (b) histogram of the corresponding dips of the data sets in (a).

Stereographic or hemispherical projections enable the representation of orientation data on a stereonet. In stereographic or hemispherical projection, the orientation of a line in 3-D space is represented by the position of a point within a circular projection. There are two hemispherical projection methods used by engineers. These methods are the lower hemisphere equal angle projection, and the lower hemisphere equal area projection. In both methods, the perimeter of the circular area represents the range of the trend directions. Additionally, the radial distance of the point from the projection is a function of the plunge. However, the relationships between the radial distance, the circular radius, and the plunge, vary for the two methods.

Considering a point with a radial distance “r” within a circular projection area of radius “R”, the plunge “β” is obtained as follows:

In a lower hemisphere equal angle projection,

$$\beta = 90^0 - \tan^{-1}\left(\frac{2r}{R}\right) \tag{2.2}$$

In a lower hemisphere equal area projection,

$$\beta = \mathrm{Cos}^{-1}\frac{2r}{R\sqrt{2}} - 90^0 \tag{2.3}$$

Contouring can be applied to a stereographic projection in order to increase its visual impact. It is very important to accommodate the weighting factor of the points when contouring. Figure 2.6 presents a stereographic projection, and a contoured stereographic projection of 101 discontinuity orientations collected from one of our research sites in southeastern Missouri.

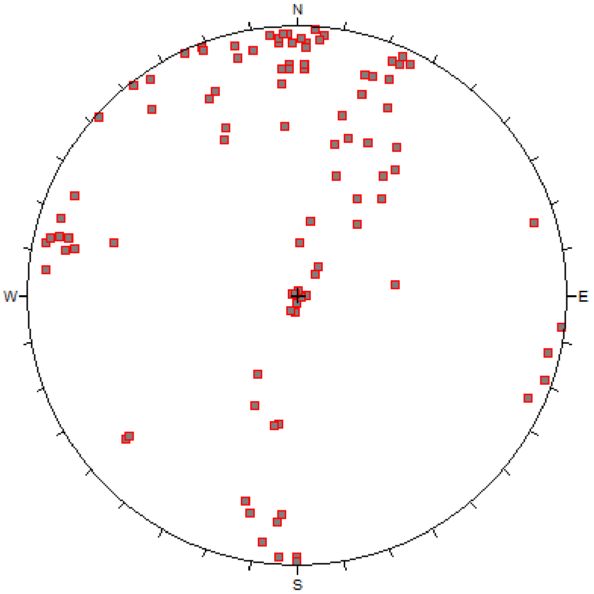

(a)

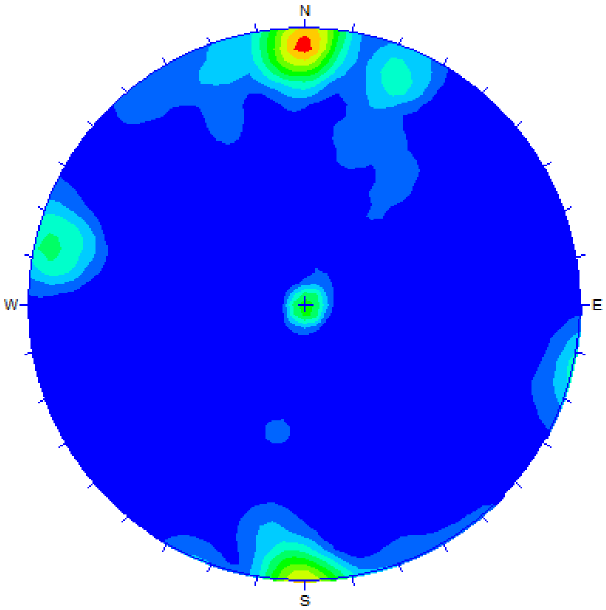

(b)

Figure 2.6. Representation of Orientation data, (a) lower hemisphere equal angle stereographic projection of 101 discontinuity orientations from a rock cut in southeastern Missouri, (b) corresponding contoured stereographic projection of the dataset in (a), the contours increases the visual impact of the different discontinuity sets.

2.4.2 Clustering of Discontinuity Orientations. Cluster analysis primarily divides data into useful groups based on a common characteristic or characteristics found in the data. Thus, cluster analysis can be used to summarize, compress, and to find the nearest neighbors of a data point. Cluster analysis has been used successfully in several fields. More room, however, still exists for research on the use of cluster analysis in the characterization of geological discontinuities.

The two main types of clustering techniques are the hierarchical and partitioning clustering. Hierarchical clustering is commonly known as nested clustering, and it involves the division of objects in a data set into overlapping subsets. The clusters are primarily organized as a tree. Partitioning clustering, however, involves the division of objects in a data into non-overlapping subsets, such that each data point is in only one subset. Terms such as exclusive, non-exclusive, and fuzzy, are also used to describe clusters. In an exclusive cluster, each object in the data is assigned to a single cluster. In a non-exclusive cluster, objects in the data are placed in more than a single cluster. Clusters in a fuzzy cluster are treated as fuzzy sets. Thus, an object in the data belongs to any set with a weight between 0 and 1.

Nearest neighbor, k-means, fuzzy c-means, and vector quantization, are the main concepts involved in the clustering analysis of discontinuity data. The nearest neighbor concept employs the similarities between discontinuities based on distance measurements. The Euclidean distance between two discontinuities is given by the relationship below:

$$D_{ij} = \left\{\sum_{k=1}^{p} \left|X_{ik} - X_{jk}\right|^{2}\right\}^{\frac{1}{2}} \tag{2.4}$$

where p is the number of parameters of each discontinuity, D_{ij} is the Euclidean distance between two discontinuities *i* and *j* in a p-dimensional space, X_{ik} is the measurement collected on the *i* th object or individual on the *k* th parameter (Dillon and Goldstein, 1984).

The k-mean concept assumes that the number of clusters in a data is known and specified in advance before clustering. Thus, given a discontinuity data, the basic steps for k-means clustering include; the formation of initial clusters, allocation of the discontinuities to the formed clusters, and the reallocation of inaccurate discontinuity clusters.

The fuzzy c-mean concept allows a data to belong to two or more clusters. The concept is frequently used in pattern recognition. The concept was initially developed by Dunn (1973), and improved by Bezdek (1981). The fuzzy c-mean concept is based on the minimization of the following objective function (Bezdek, 1981):

$$J_m = \sum_{j=1}^{n} \sum_{i=1}^{c} \left(u_{ij}^{m}\right) d_{xj,vi}^{2} \tag{2.5}$$

where u_{ij} is the fuzzy membership, v_i is the cluster centroid, c is the number of clusters, n is the number of discontinuities, $d^2_{xj,vi}$ is inner product metric, and *m* is the degree of fuzzification, (a real number greater than 1).

The fuzziness of the membership of a data is controlled by the degree of fuzzification. A degree of fuzzification value of 2 is used by most researchers (Hammah and Curran, 1998). The vector quantization concept clusters discontinuities based on distance functions within a Euclidean space. The vector quantization concept was originally used in data compression. The vector quantization concept allows points or data sets to be clustered into groups having the same number of points closet to them. Each group is represented by its centroid. Presented in Figure 2.7 is a stereographic projection and its corresponding cluster of 101 discontinuities orientations collected from one of our research sites in southeastern Missouri.

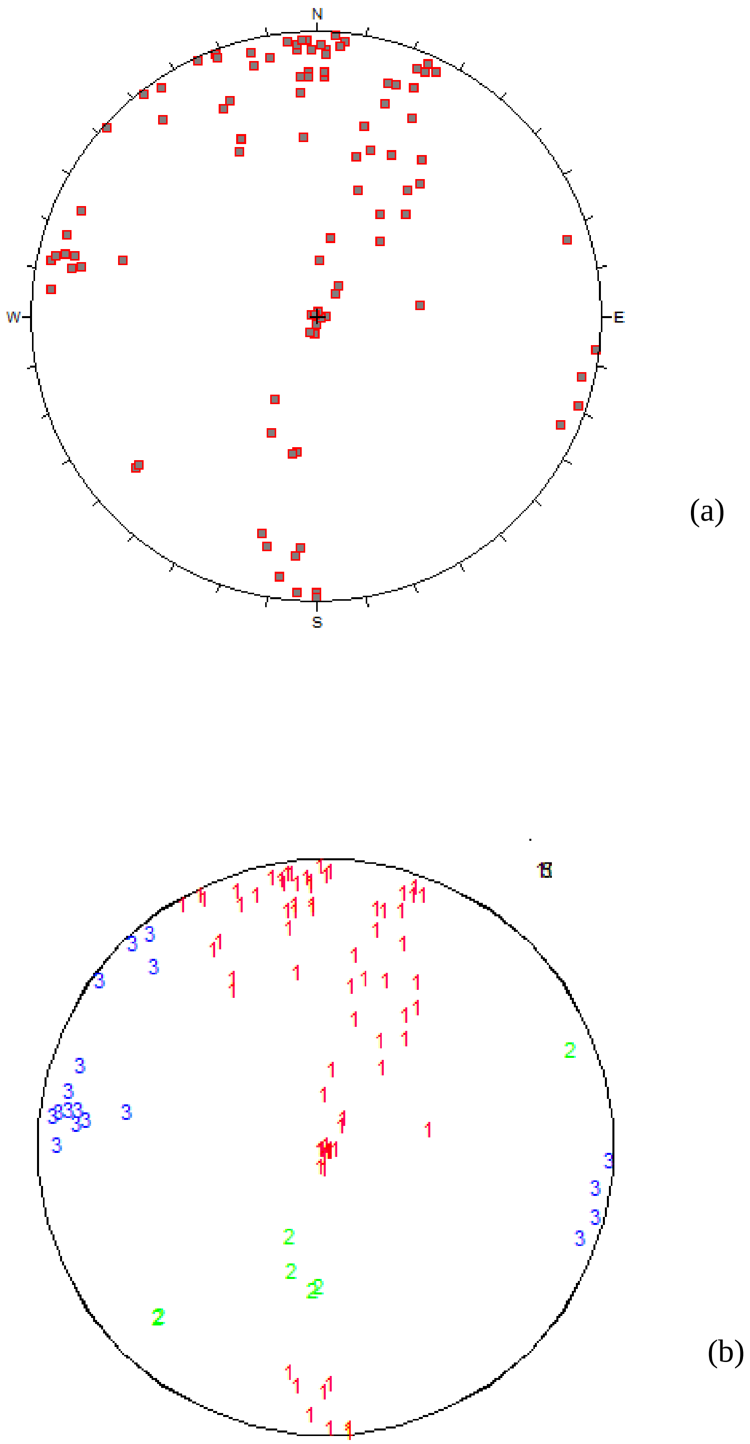

Figure 2.7. Clustering of discontinuity orientation, (a) stereographic projection of the 101 discontinuities from a research site in southeastern Missouri, (b) corresponding cluster of the 101 discontinuity orientations into sets. The different numbers of different colors represent different clusters.

3. MATERIALS AND METHODS

This chapter presents the materials and methods used for the accomplishment of the objectives of this research.

3.1 EQUIPMENT AND MATERIALS

Equipment and materials used for this research included the following:

- Brunton compass
- LiDAR ScanStation unit
- Global Positioning System (GPS)
- Handheld digital camera
- Surveyor’s tape measure
- Safety cones

3.1.1 Brunton Compass. The Brunton compass is an instrument primarily used by geologist and engineers to take accurate degree and measurements in the field. This compass can be used to locate the north of an area, measure bearings, measure dip and strike of planes, measure trend and plunge of lines, and to measure vertical angles. In this research, the compass was used primarily to measure the dip and the strike of facets, as well as the trend and plunge of traces. Figure 3.1 presents the labeled Brunton compass used for this research. The strike is obtained by leveling the compass along the plane to be measured. The dip is obtained by first laying the side of the compass perpendicular to the strike measurement and then rotating the horizontal level until the bubble is stable at the center. The trend is measured by pointing the sighting arm of the compass parallel to the direction the feature plunges. The plunge is measured by placing the side of the compass parallel to the feature**.**

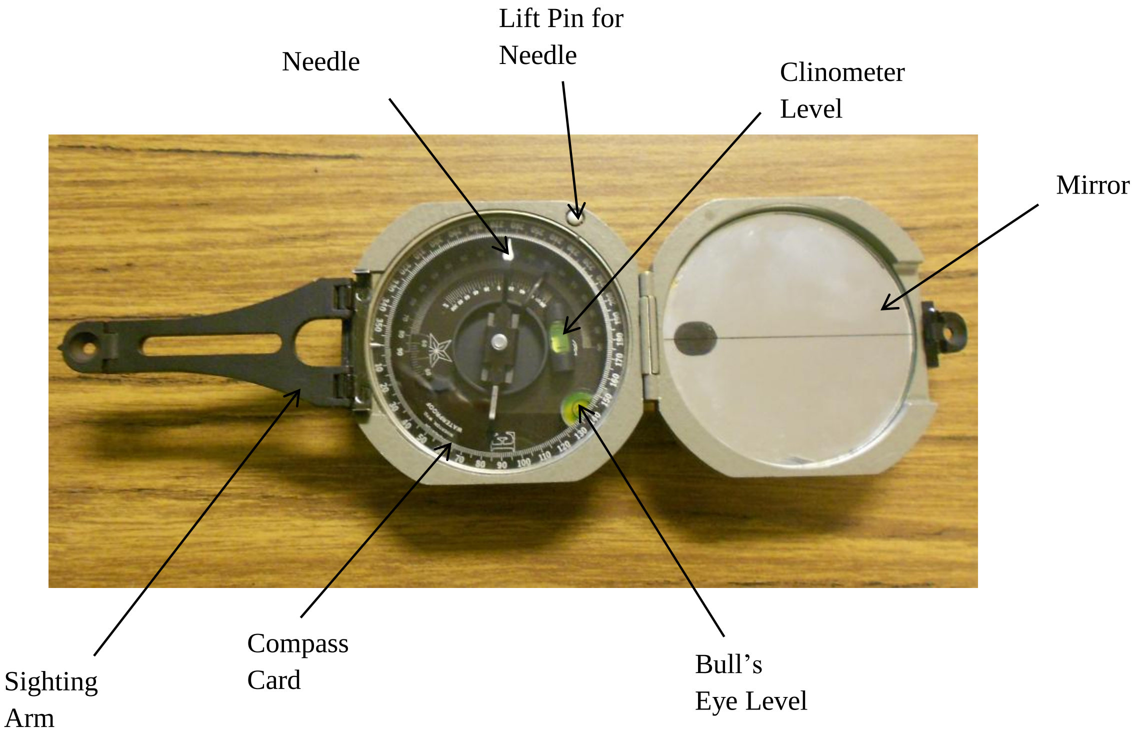

Figure 3.1. Brunton compass used for this research

3.1.2 LiDAR ScanStation Unit. Missouri University of Science and Technology's (Missouri S&T) LiDAR ScanStation 2 unit was used for this research. The unit consists of a Leica ScanStation 2 scanner, tripod stand, a laptop, and a generator (Figure 3.2). The Leica ScanStation 2 scanner (Figure 3.3) was used for all the 3-D scans. This scanner has 50,000 points per second maximum instantaneous scan speed, and the ability to conduct full-dome scans using its oscillating mirror with front and top-window design. Features and specifications of the Leica ScanStation 2 scanner are summarized in Table 3.1. The scanner uses a time of flight sensor to generate 3-D images of surfaces. The scanner is mounted on a tripod stand and connected to a laptop which controls it. The generator supplies power to both the laptop and the scanner. The scanning procedure is documented under the methodology section of this chapter.

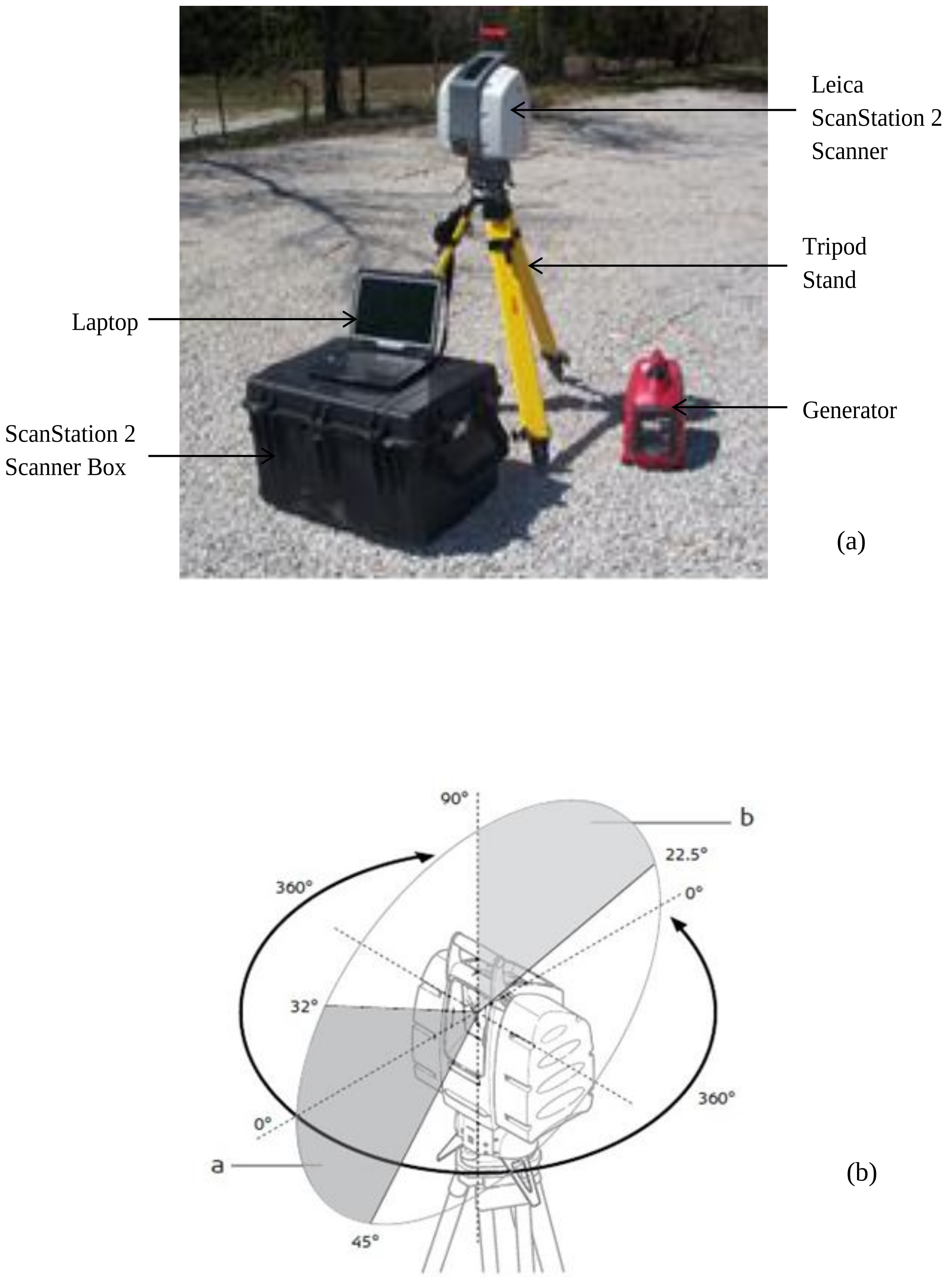

Figure 3.2. (a) Missouri S&T’s LiDAR unit (Leica ScanStation II, tripod stand, a laptop, and a generator set), (b) Image showing the rotation ability of the ScanStation II scanner (Leica Geosystems, 2012).

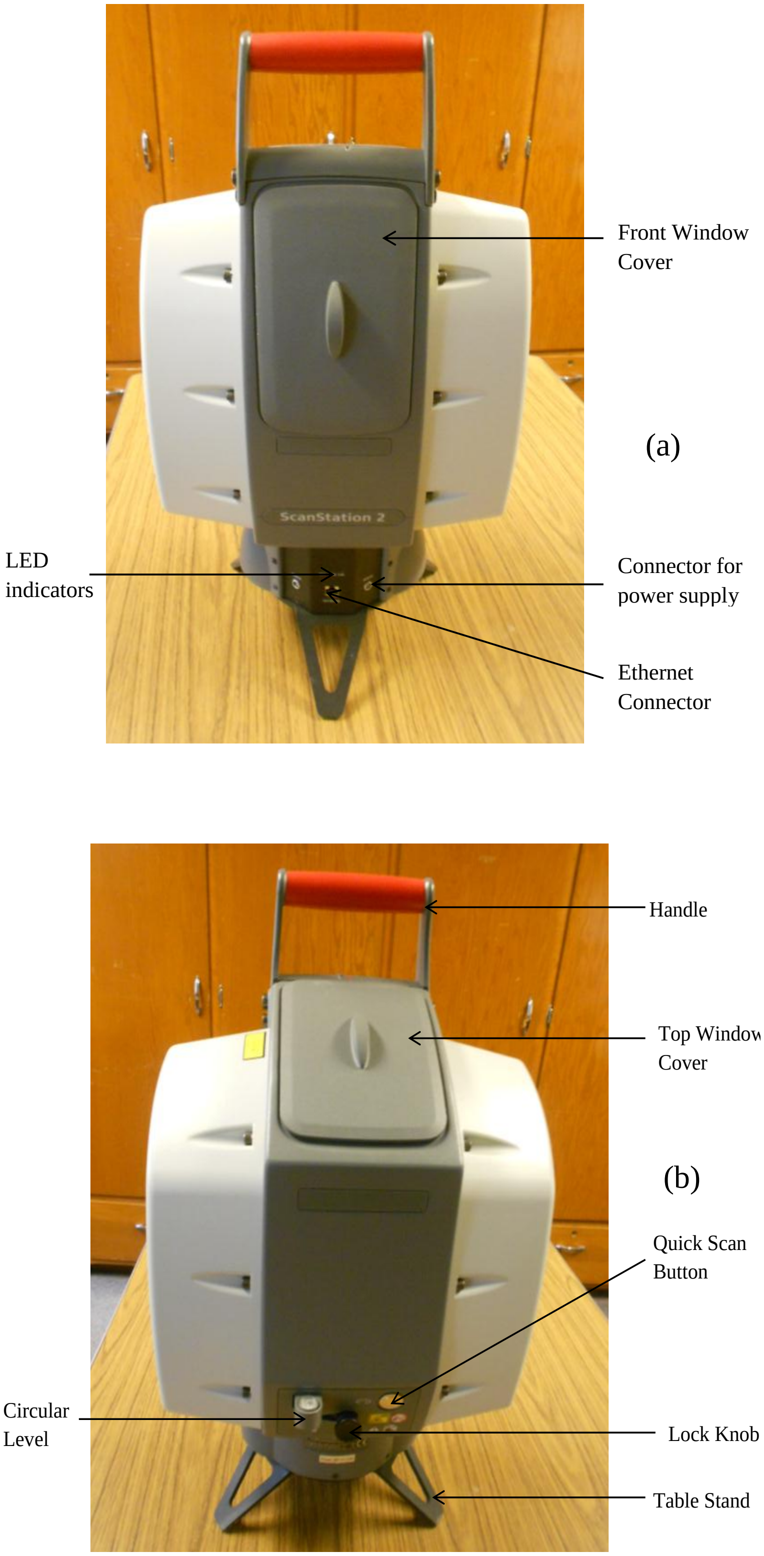

Figure 3.3. Labelled Leica ScanStation 2 scanner, (a) Front view, (b) Back view.

Table 3.1. Features and specifications of the ScanStation 2 unit (modified from Leica, 2012)

Feature	Specification
Laser scanning type	Pulsed; proprietary microchip
Color	Green
Laser class	3R (IEC 60825-1)
Range	300m at 90% ; 134 at 18% albedo
Scan rate	Up to 50,000 points/seconds maximum instantaneous rate
Scan resolution	
Spot size	From 0 - 50 m : 4 mm (FWHH-based) 6 mm (Gausian - based)
Selectability	Independently, fully selectable vertical and horizontal point-to-point measurement spacing
Point spacing	Fully selectable horizontal and vertical; < 1 mm minimum spacing , through full range; single point dwell capacity
Maximum sample density	< 1 mm
Field of view	
Horizontal	Maximum of 360 degrees
Vertical	Maximum of 270 degrees
Aim/Sighting	Optical sighting using QuickScan button
Scanning optics	Single mirror, panoramic, front and upper window design
Digital imaging	Low, Medium, High automatically spatially rectified
Camera	Integrated high-resolution digital camera
Scanner Dimensions	265 mm x 370 mm x 510 mm without handle and table stand
Weight	18.5 kg
Data storage	On laptop through ethernet cable
Power supply	36V; AC or DC
Power consumption	Averagely less than 80W
Typical duration	Greater than 6hrs of continuous use

3.1.3 Global Positioning System. GARMIN GPS 12 CX system was used in the site selection and identification process of this research (Figure 3.4). The GARMIN GPS 12 CX system is easy to use and allows the user to zoom in and zoom out in order to manipulate the map page. "The system has an enhanced graphic interface that organizes 1000 waypoints into an easily accessible tab-file system. It also comes with a full complement of advanced software features such as a point data base of cities" (Garmin, 2012).

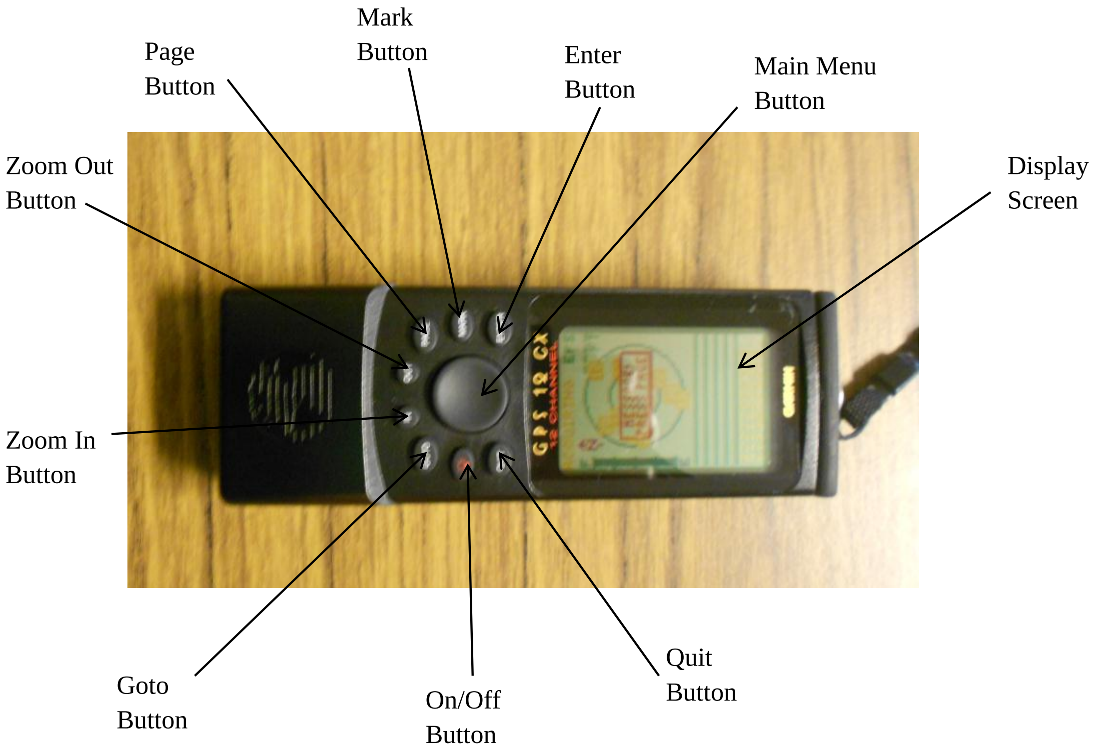

Figure 3.4. The GARMIN GPS used for the research.

3.1.4 Handheld Digital Camera. Most of the pictures used for this research were taken using KODAK Z1275 digital camera. KODAK Z1275 is a small user friendly high zoom digital camera offering a 12-megapixel imaging sensor combined with a 5X optical zoom. The camera is equipped with features like digital image stabilization, and KODAK perfect touch technologies which helps to take better shots (KODAK. 2012). Figure 3.5 is a picture of the handheld camera used for this research.

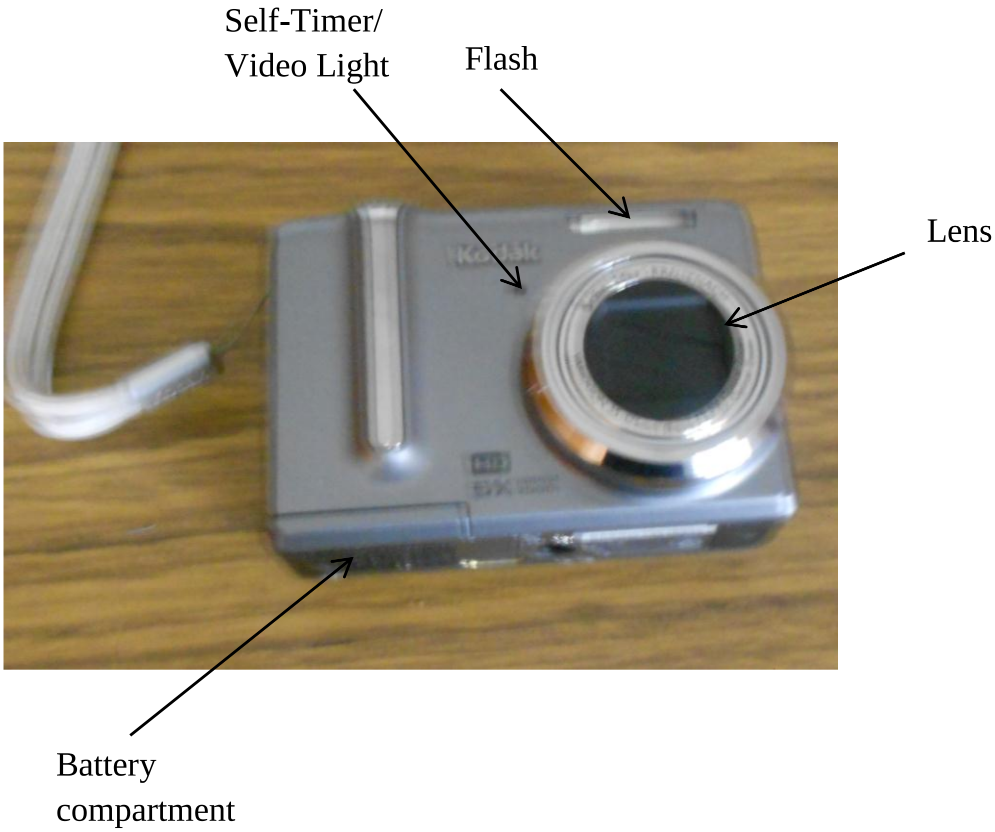

Figure 3.5. The handheld digital camera used for the research.

3.1.5 Surveying Tape Measure. A surveying tape measure with an open housing was used for all length related measurements in the field (Figure 3.6). This type of housing allows for easy cleaning of debris that may be caught on the measuring tape. The tape has a handle for a strong grip. This tape has a locker which can hold a measurement and the measuring tape in place when not in use.

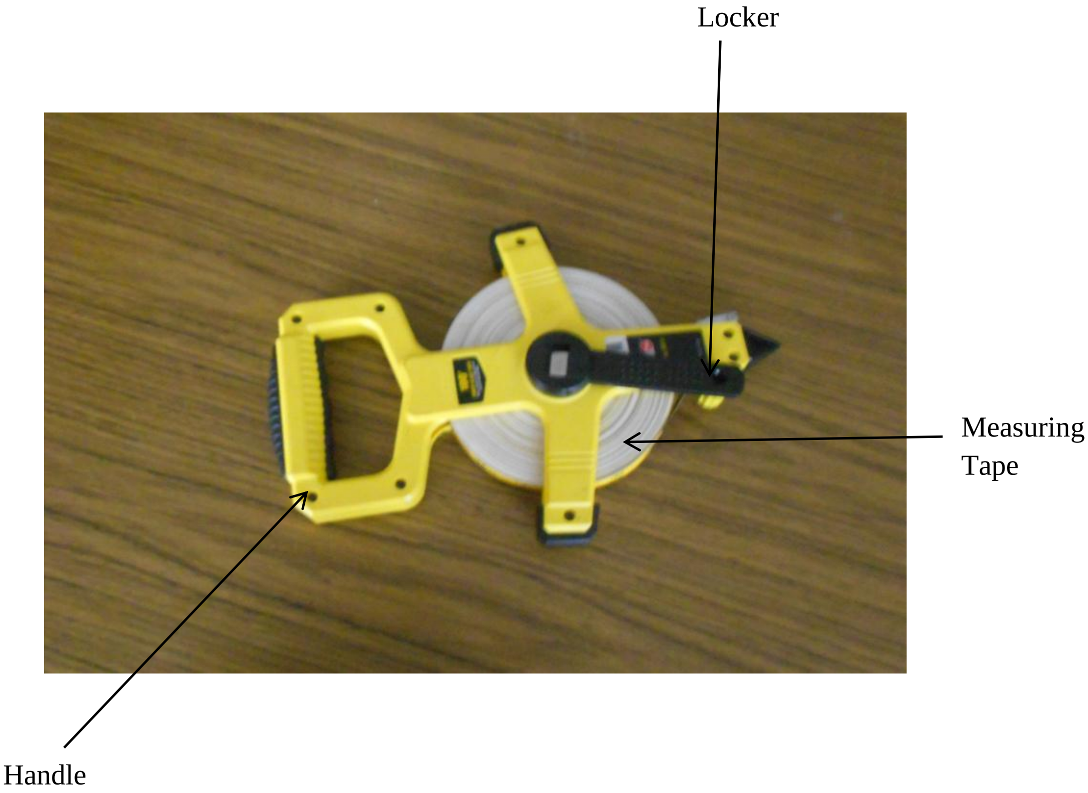

Figure 3.6. The surveying tape measure used for the research.

3.1.6 Safety Cones. Reflective, and stable safety cones of approximately 0.3 meters (12 inches) in height were used to define the boundaries of the research sites in the field.

3.2 METHODOLOGY

The methodology for the research involved the following six major steps:

- Selection of the research sites
- Acquisition of 3-D LiDAR, digital images, and data treatment
- Conducting of field manual measurement
- Preparation of manual facets and traces map
- Development of algorithms
- Validation of results

3.2.1 Selection of Research Sites. The site selection process involved driving around areas noted to have discontinuous rock cuts (outcrops). Several areas were visited and ranked. Rock cuts with both well-defined facets and traces were preferred over others. The stability of the rock face, accessibility to the rock face, and safety of the working team were all considered in the site selection process. Six sites were selected in Missouri. Two in Rolla, and four in the Ironton area. Thirteen sites were selected in Colorado. Seven of these thirteen were located in the Golden Gate Canyon road area, two were in the Parmales Gulch area, two in the Idaho Spring area, and the remaining two were in the Boulder area. Lists of the selected sites are given in Table 3.2 and Figure 3.7. Individual site location maps are presented in appendix B.

Table 3.2. List of selected research sites

State	Area	GPS Coordinates	Number of Sites Selected in Area
Missouri	Rolla	N 037° 56.93'	2
		W 091° 45.78'	
	Ironton	N 037° 33.96'	4
		W 090° 21.74'	
Colorado	Golden Gate Canyon Road	N 039° 49.85'	7
		W 105° 24.63'	
	Parmales Gulch	N 039° 36.92'	2
		W 105° 14.04'	
	Idaho Springs	N 039° 45.64'	2
		W 105° 39.61'	
	Boulder	N 040° 00.92'	2
		W 105° 19.54'	

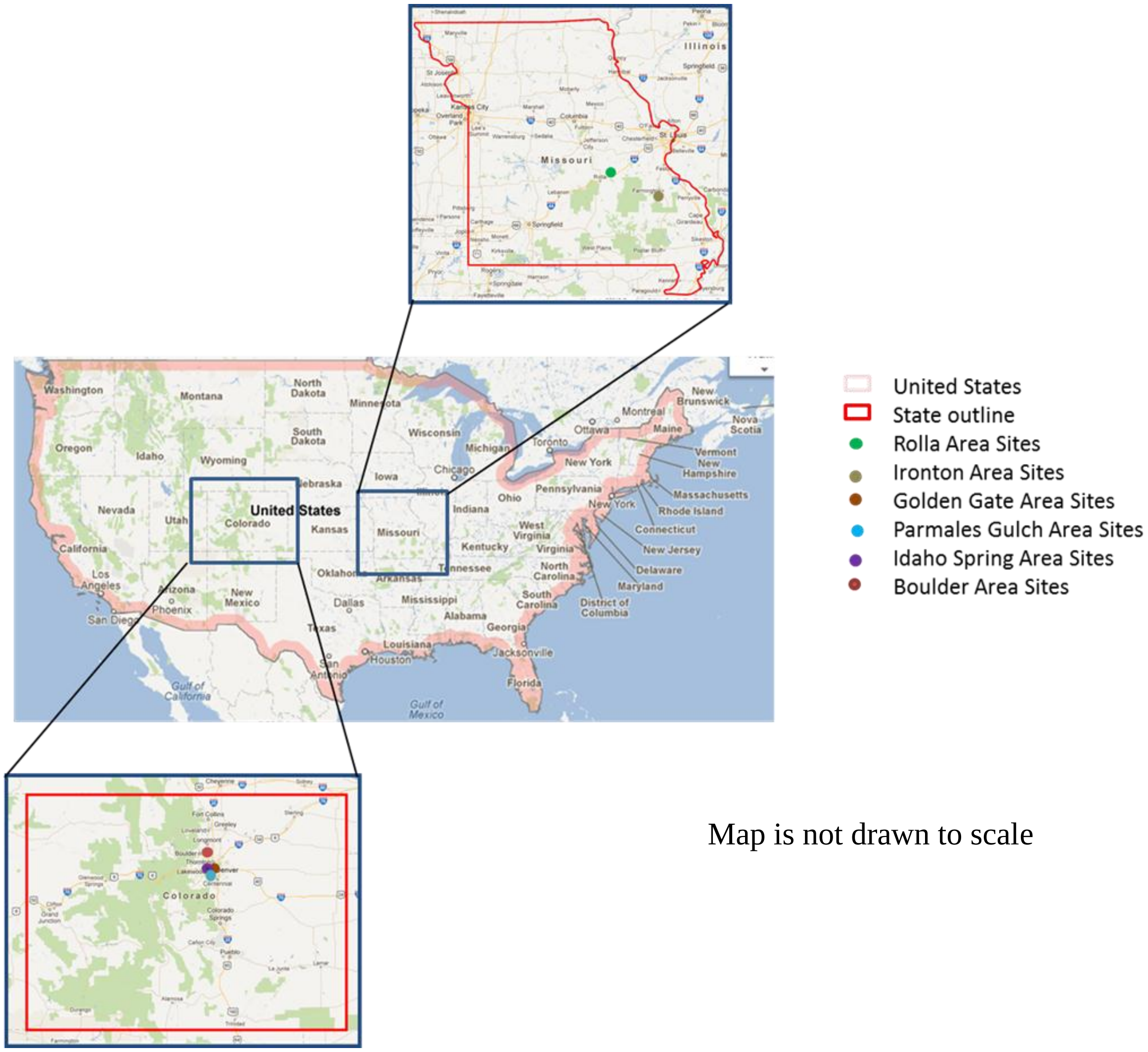

Map is not drawn to scale

Figure 3.7. Sites location map.

3.2.2 Acquisition of 3-D LiDAR Data, Digital Images, and Data Treatment.

3-D LiDAR data was collected using the LiDAR unit. The first step in the image acquisition process was to determine where to set the LiDAR unit. In this research, the LIDAR unit was first set at 90° to the rock face. Back-up scans were then made at 45° to the east and the west of the rock face respectively (Figure 3.8). The ScanStation 2 scanner is able to scan from several meters away. A position as close as possible to the rock face was chosen, however, to generate better results. On the contrary, a distance too close to the rock is not recommended, as the electronics of the scanner can have problems measuring extremely short reflection times. In this research, the scanner was positioned at a distance of not more than 10 meters from the rock face.

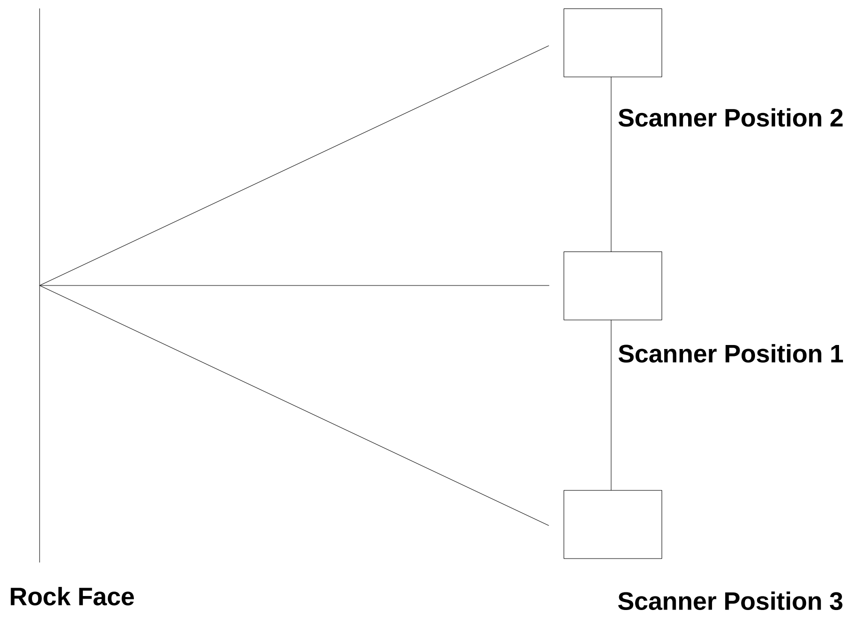

Figure 3.8. Map view or rock face and LiDAR scanner positions.

An overview of the scanning procedure is presented below:

1. The tripod is first positioned, and then the tribrach (Figure 3.5) is mounted on its head, the tribrach should be leveled with its optical plummet pointing towards the rock face of interest (Figure 3.9).
2. The ScanStation 2 is then mounted on the tribrach and the tripod, it is leveled, and locked in place. Leveling both the tribrach and the ScanStation 2 will help avoid the collection of angled data.
3. The mirror covers of the ScanStation 2 are then removed and the scanner is unlocked to allow it to rotate (Figure 3.9). The laptop can then be connected to the scanner through the ethernet cable. At this point, both the laptop and the scanner can be connected to the generator for power supply. The scanner takes about 5 minutes to warm up before scans can be made after power is supplied. The scanner should be unlocked at this point to allow it to rotate during its warm up process.
4. Connect the laptop to the scanner. The connection this time is done on the laptop, thus, different from the first connection between the scanner and the laptop. This connection is done by opening the manufacturer's program on the laptop. In this research, in order to connect the scanner to the laptop, the Cyclone program was opened, ScanStation 2 was selected from scanners, a project was selected, and then the "connect to scanner" option was selected. The boundaries of the area to be scanned, known as the field of view (FOV), and the LiDAR point spacing known as resolution should be defined.

5. An image of the rock face is then acquired using the inbuilt optical camera of the ScanStation 2 scanner. This image is probed in order to determine the distance between the scanner and the field of view. This image can also be used to modify the field of view, and to also add natural colors of the rock face to the LiDAR data. The exposure of the image and resolution can be adjusted at any time to suit one's need.
6. Scanning can now be conducted. Figure 3.10 shows screen shots of some of the important stages.

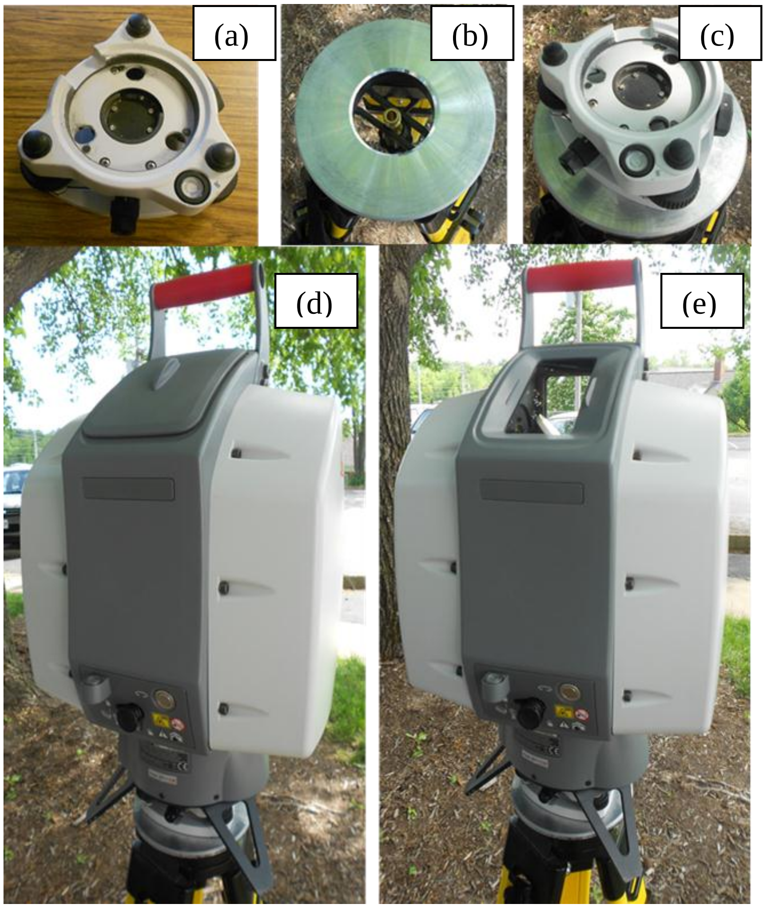

Figure 3.9. (a) Tribrach, with its optical plummet pointing to the front, (b) Head of tripod, with the screw for mounting the tribrach, (c) Tribrach mounted on tripod, (d) Scanner mounted on tribrach and tripod, leveled and locked in place with windows closed (e) Scanner mounted on tribrach and tripod, leveled and locked in place with windows opened.

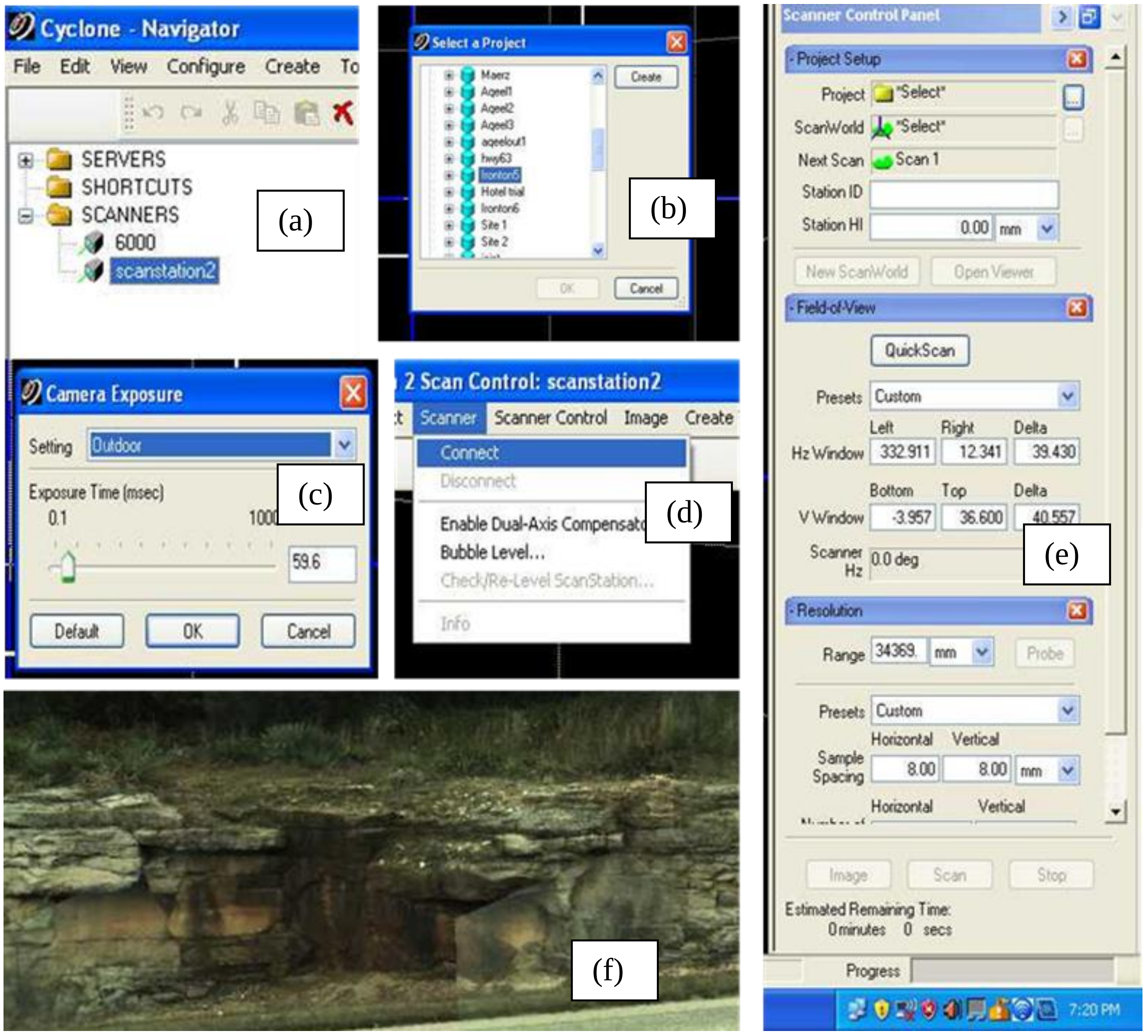

Setting: Outdoor
Exposure Time (msec): 0.1 – 1000; 59.6

Project: "Select"
ScanWorld: "Select"
Next Scan: Scan 1
Station ID:
Station HI: 0.00 mm
Presets: Custom
Hz Window: Left 332.911, Right 12.341, Delta 39.430
V Window: Bottom -3.957, Top 36.600, Delta 40.557
Scanner Hz: 0.0 deg
Range: 34369 mm
Presets: Custom
Sample Spacing: Horizontal 8.00, Vertical 8.00 mm
Estimated Remaining Time: 0 minutes 0 secs

Figure 3.10. Screen shots of some of the important scanning stages. (a) Scanstation selection, (b) Project selection, (c) Exposure setting, (d) Scanner connection, (e) FOV, resolution, and probe setting, (f) Point cloud image with natural rock colors.

The scanning process involved emitting light pulse from the liDAR. This pulse was reflected by the rock face and returned back to the LiDAR. The LiDAR received and measured the returned pulse. Both the travel time and the intensity of the returned pulse were measured by a high precision counter. Additionally, the pulse source measured the angle at which the light pulse was emitted and received. These enabled the spatial location of a point on the rock face to be calculated. The result was millions of points reflected from the rock face.

Despite efforts to remove all weed and unwanted materials from the rock face before scanning, some weed and unwanted areas remained on the scan (Figure 3.11). These areas needed to be removed from the data. The removal of unwanted material from the collected data is termed “data cleaning”. In this research, all files, including the cleaned data were exported to .PTS format before processing.

Digital images of the rock face were also acquired using the handheld digital camera. The camera was held upright to the rock face in order to get an image as vertical as possible. In situations where a vertical image cannot be guaranteed, a pendulum was set in front of the rock face to help check verticality and to set the image vertical using the digimizer software.

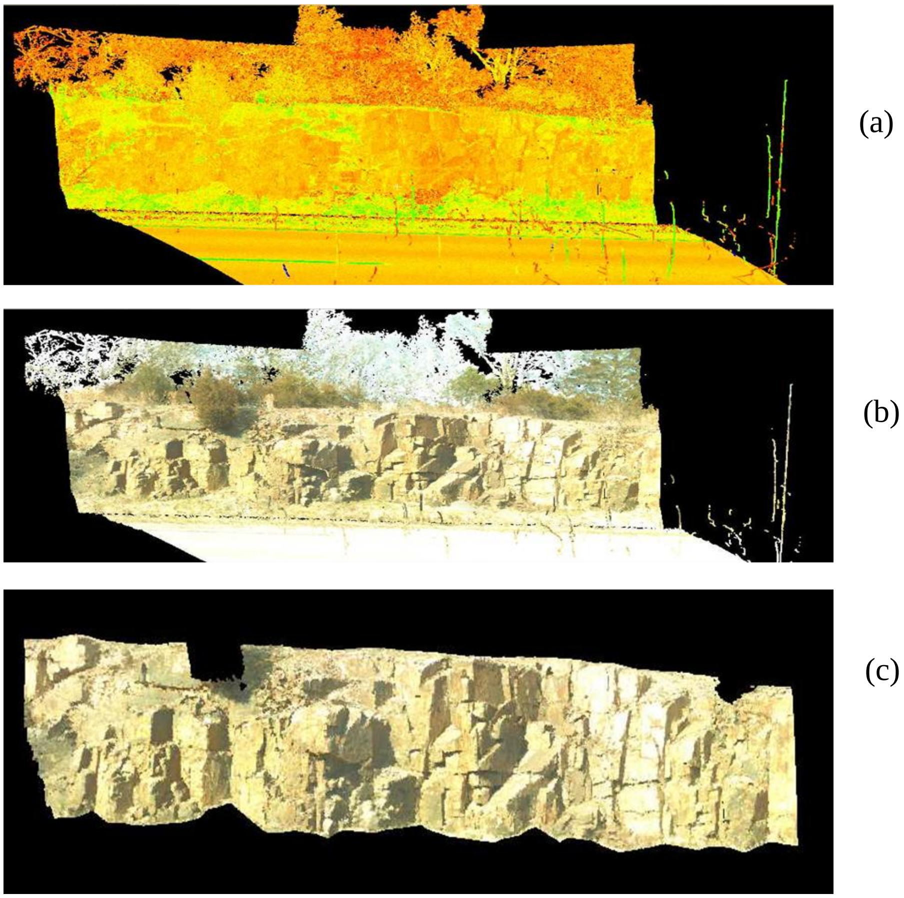

Figure 3.11. Point cloud data of a rock face in southeastern Missouri, (a) Raw point cloud data, (b) Raw point cloud data being viewed with natural colors from scanner, (c) Cleaned point cloud data, ready to be processed.

3.2.3 Conducting Field Manual Measurements. Field measurements of dips, dip directions, plunge, and trends were obtained using the Brunton compass. Dips and dip directions were measured on the facets, whiles plunges and trends were measured on the traces (Figure 3.12). Measurements were made using the right hand rule.

In order to measure low dip angles, an edge of the Brunton was placed over or under the surface to be measured. The clinometer was rotated until it was leveled or the bubble was centered. The Brunton was then removed and the dip angle was recorded from the scale of the Brunton compass. In order to measure high dip angles, the Brunton was held with an edge against the surface to be measured. The edge of the Brunton was sight with the surface of interest. The clinometer was then rotated until it was leveled or the bubble was centered. The dip angle was then read and recorded from the scale in the compass. In order to measure the strike, the Brunton was placed on the surface to be measured, or on a non-magnetic clip board held parallel to the surface. It was ensured that the dip is to the right when looking towards the front of the Brunton, it is also ensured that the back edge of the Brunton is flush with the surface to be measured. The Brunton was tilted until the bubble in the bull's eye was centered or leveled, while still keeping its back edge flush to the surface to be measured. The azimuth at the tip of the marked needle was then read and recorded. The dip direction was obtained by adding 90^o to the value of the strike. The plunge was measured just as the dip was measured. In order to measure the trend, the sighting arm of the Brunton was pointed parallel to the direction the feature plunges. The Brunton was then leveled, and its marked end was read and recorded.

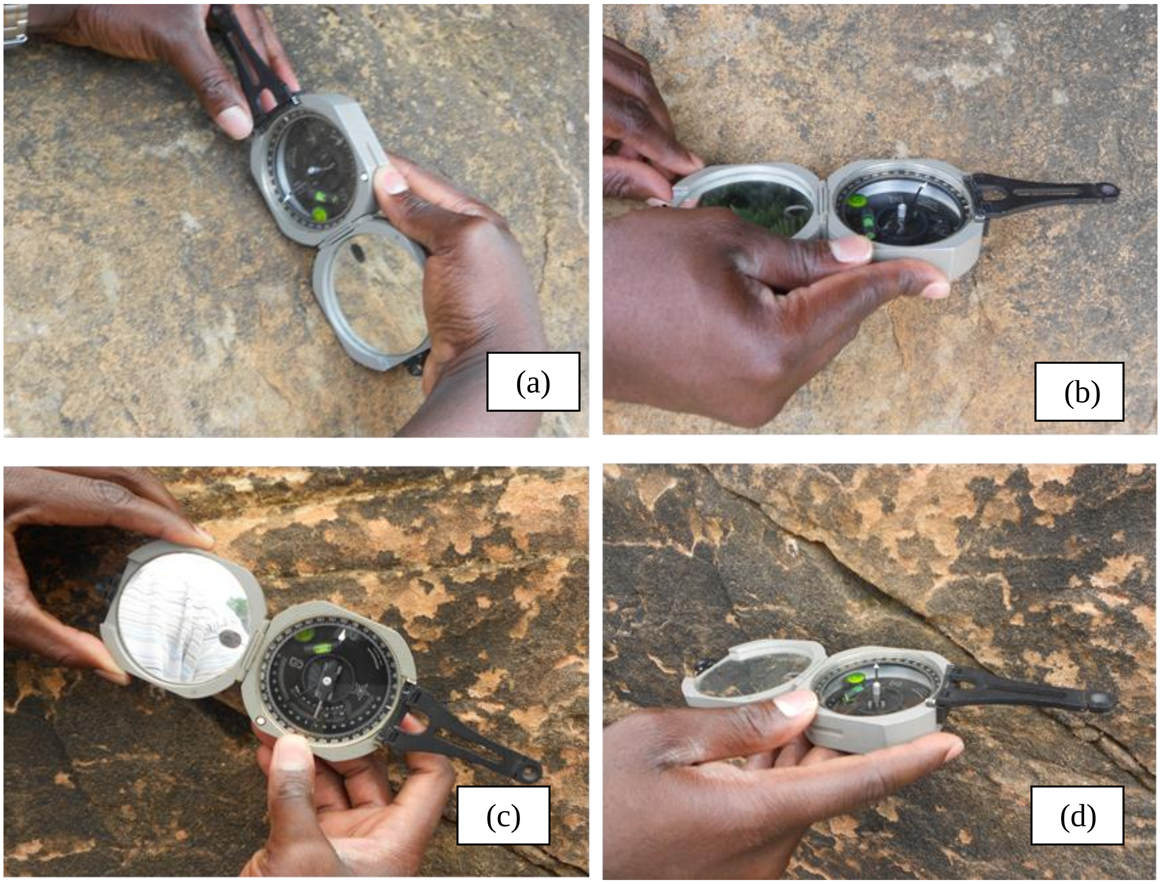

Figure 3.12. Manual measurement of orientation in the field. (a) Measuring dip of a facet, (b) Measuring strike of a facet, (c) Measuring plunge of a trace, (d) Measuring trend of a trace.

3.2.4 Preparation of Manual Facets and Traces Map. Manual maps of facets and traces were prepared from the digital image taken with the handheld camera. The image was first made faint using image processing techniques. Facets on the image were represented with polygons, and traces were represented with lines. The traces and facets were then marked with numbers for easy identification. An example of a manually prepared facets and traces map is given in Figure 3.13.

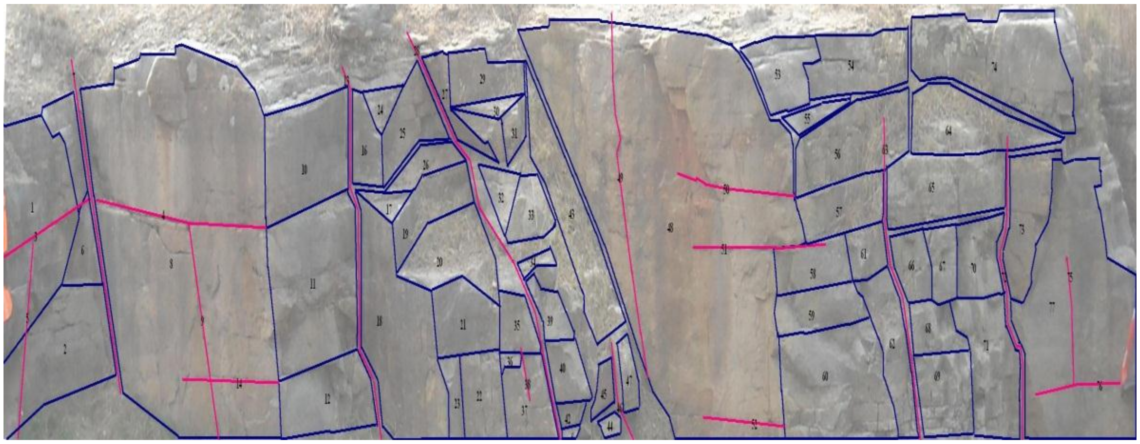

Figure 3.13. Manually prepared facet and trace map of a rock face in Rolla, Missouri. Red lines represent linear traces and blue polygons represent planar facets.

3.2.5 Development of Algorithms. Algorithms were developed from the LiDAR point cloud data using C++. This step involved both the continuous design and analysis of algorithms based on feedback from field comparisons. Details of the algorithms are presented in chapter 5 of this dissertation. Figure 3.14 represents a simplified flowchart of the algorithm.

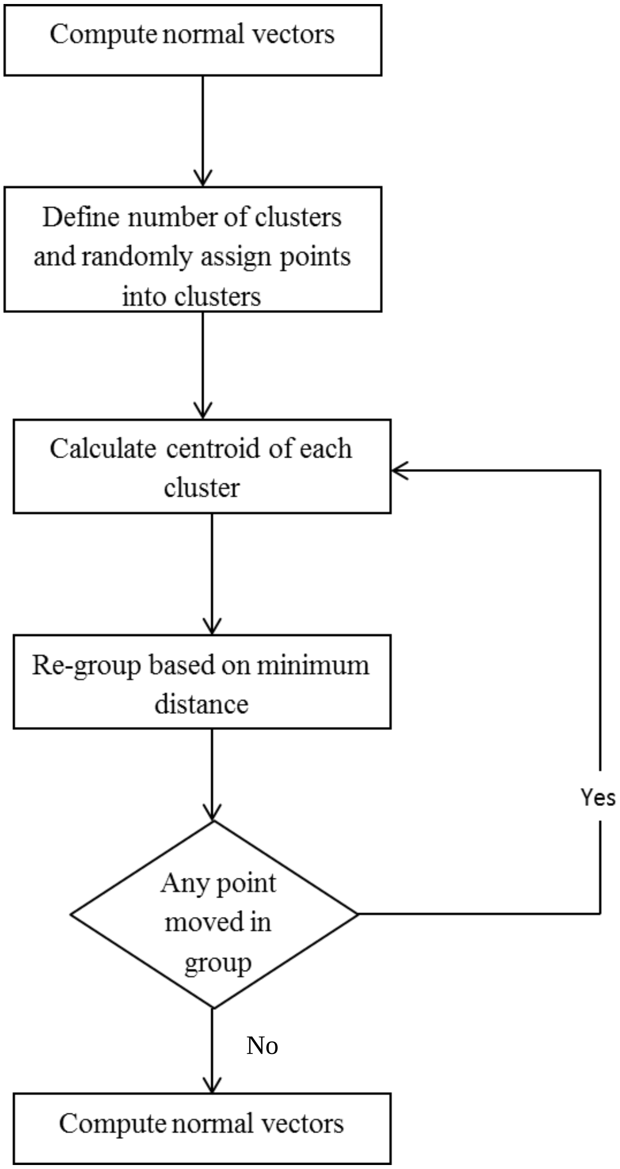

Figure 3.14. Simplified flow chart of algorithm

3.2.6 Validation of Results. This is the final step of our methodology. This step involved comparing results from the algorithm to results obtained from the field. The algorithm was revisited and modified each time an unacceptable difference appeared in the results.

4. DIFFRERENCES BETWEEN TRACES, NATURAL FACETS, AND INDUCED FACETS

This chapter is an observational study that outlines the primary differences between a trace, natural facet, and an induced (blasted) facet.

4.1 OVERVIEW

Analyzing data on discontinuities in rocks is very necessary for both the design and the characterization of rock structures. Discontinuities exist either as “traces” or as “facets”. These traces and facets could be caused by natural or human activities. Traces are linear features that intersect with both the discontinuity and the rock cut, whilst facets are the actual discontinuity surfaces that are exposed in the rock cut. In most cases, identifying a discontinuity as either natural or induced (blasted) is very difficult, especially in situations where the rock face is highly weathered. Analytical results can be very misleading if natural discontinuities are treated as induced (blasted), and vice versa.

The activities, or processes, that caused the occurrence of the discontinuity, morphology, surface color, weathering level, and a discontinuity’s trend on a stereonet are very important when differentiating natural facets from induced facets. An image of a rock cut in Rolla, Missouri, showing a natural facet (yellow polygon), a trace (red line) and a blasted facet (blue polygon) is given in Figure 4.1.

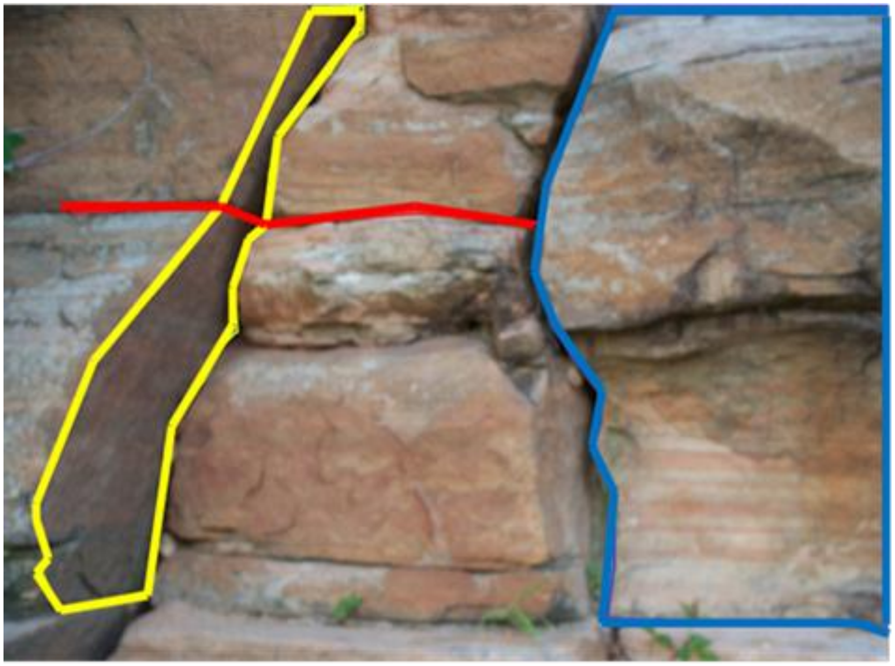

Figure 4.1. Image of a rock cut showing a natural facet (yellow polygon), a trace (red line) and a blasted facet (blue polygon).

4.1.1 Occurrence of Discontinuities. Discontinuities are formed through failure in tension, in shear, or through a combination of both (Bell, 1992). “In horizontal beds which have suffered little tectonic compression two sets of tension joints may be developed, whereas in those rocks which have been subjected to considerable tectonic compression but have remained unfolded, two sets of shear joints may be formed. If uplift follows compression then two sets of tension joints may be developed subsequent to the shear joints” (Bell, 1992). Traces, natural facets, and induced facets are all believed to be formed through failure in tension, in shear, or through a combination of both. Traces are primarily caused by either natural geological processes or human activities, natural facets are caused by natural geological processes or activities, and induced facets result from human activities. The origination of discontinuities in a triaxial stress state can be categorized into one of two groups (Scheidegger, 1978). The first group predicts jointing to occur at some intermediate angle (30-45°) to the maximum pressure direction. The second group predicts jointing to occur either parallel or normal to a principal stress direction.

4.2 RESEARCH METHODOLOGY

The research was primarily field based, with analysis conducted in the office. Field investigations included:

- Physical observation of rock faces
- Collection of images of rock faces with a LiDAR unit and an handheld camera

Office investigations included:

- Observation of LiDAR and optical images of rock cuts
- Analysis of facets and traces on a stereonet

4.2.1 Physical Observation of Rock Faces. Physical observations that were made on the rock faces included the following:

- Morphology of the discontinuity
- Color of the discontinuity
- Freshness and weathering levels

Morphology of the discontinuity essentially refers to the characteristics of the discontinuity, such as both the shape and the appearance of the surface. Color of the discontinuity refers to its look in color. A discontinuity can be stained, giving it a dark brown color, or non-stained, leaving it mostly with the original color of the rock. Discontinuity faces that have not undergone weathering can be referred to as fresh discontinuities. Depending on the level of weathering, a discontinuity can be referred to as either highly or moderately weathered.

4.2.2 Collection of Images of Rock Faces with a LiDAR Unit. Images of rock faces that show well defined traces, natural facets, and induced facets were collected by setting a LiDAR unit at right angles to rock faces. The images were collected at three different resolutions of 4mm x 4mm, 6mm x 6mm and 8mm x 8mm. Auxiliary images were also collected with the handheld digital camera.

4.2.3 Analysis of Discontinuity Facets. Collected orientation data were analyzed on stereonets using the dips software. Discontinuities with same or similar orientations were clustered as sets during the analysis. Both LiDAR scans and handheld images of the rock faces were also analyzed.

4.3 RESULTS AND DISCUSSION

Traces can easily be differentiated from both natural and induced facets because they always exist as linear features. It is not uncommon for a discontinuity to exist as a trace from one angle and then as either a natural or an induced facet from another angle (Figure 4.2). In cases like this, the engineer or geologist can acceptably treat the discontinuity as both a trace and as a facet. Thus, the discontinuity should first be counted as a trace, and then be counted as a facet.

One distinct indication of induced facets is the presence of blast hole marks, commonly known as “half barrels” or “half-casts”. These blast hole marks are common in both mining and quarrying environments, and can also be found on some road cuts (Figure 4.3). However, the presence of blast hole marks on a blasted rock face primarily depends on the lithology of the rock. A high possibility of not seeing blast hole marks on a blasted rock face exists, especially in situations where the rock is highly weathered.

Natural facets have relatively smooth surfaces compared to induced facets (Figure 4.4). This smoothness could be due to geological processes and activities that have acted on the natural facets for ages. Natural facets in most rocks existed long before the development of the induced facets. The surfaces of natural facets are more likely to be stained with mineral coatings when compared to induced facets (Figure 4.3c, Figure 4.5).

Induced facets appear to be more irregular, whilst natural facets mostly appear to be regular. On the same rock face, induced facets appear to be more secondary than primary. Primary in the context of this research refers to those discontinuities are believed to be formed first, all other discontinuities are referred to as secondary. Induced facets were found to deviate from normal trends when their orientations were plotted on a stereonet (Figure 4.6). Additionally, induced facets are more likely to be parallel to the rock face when dealing with rock cuts. In terms of weathering, the surface of induced facets appear to be more weathered when compared to that of natural facets. This difference is somewhat difficult to observe when dealing with highly weathered sedimentary rocks. A summary of the observable differences are presented in Table 4.1.

Figure 4.2. A rock cut showing a discontinuity occurring as a trace (red line) from one direction and a facet (blue polygon) from another direction.

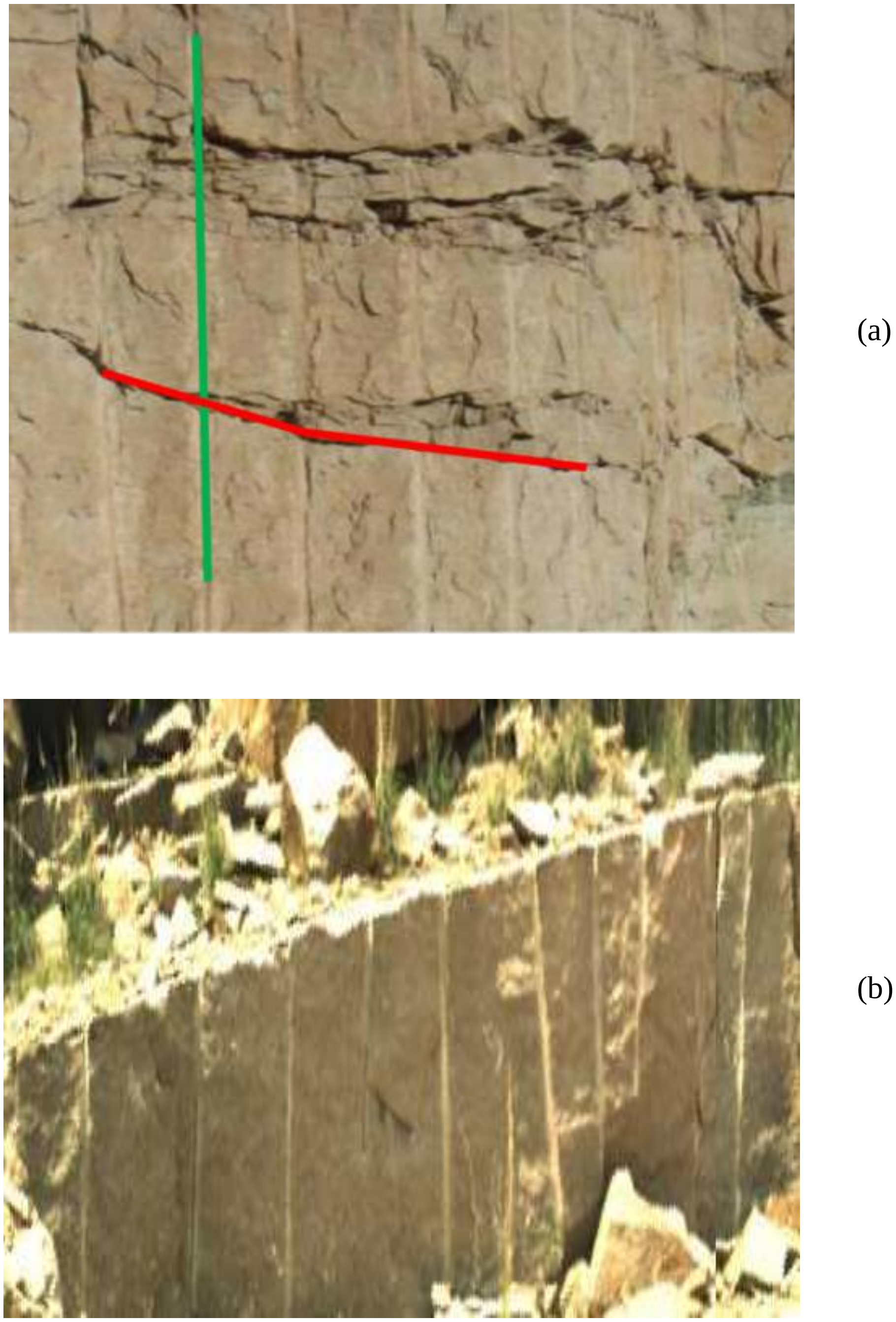

Figure 4.3. Rock face showing blast hole marks (green) and traces (red) from a controlled blasting (modified from Hoek and Bray, 1981), (b) LiDAR optical image of a rock face in Missouri also showing drill hole marks.

Figure 4.4. Rock face showing both a relatively smooth, stained, natural facet (yellow polygon) and an induced facet (blue polygon).

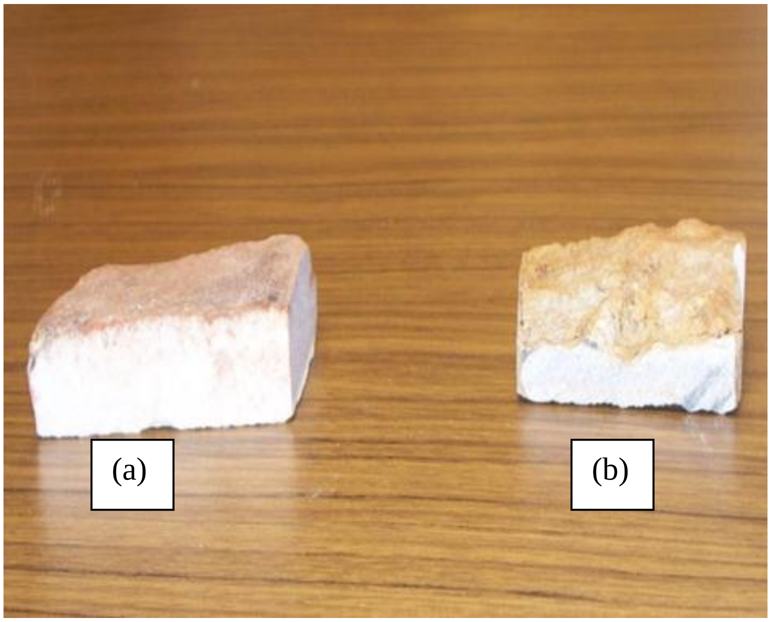

Figure 4.5. Two rock pieces from the same rock mass (a) showing a rock piece of a natural facet, (b) showing a rock piece of an induced facet. The natural facet is relatively smooth and stained when compared to the blasted face.

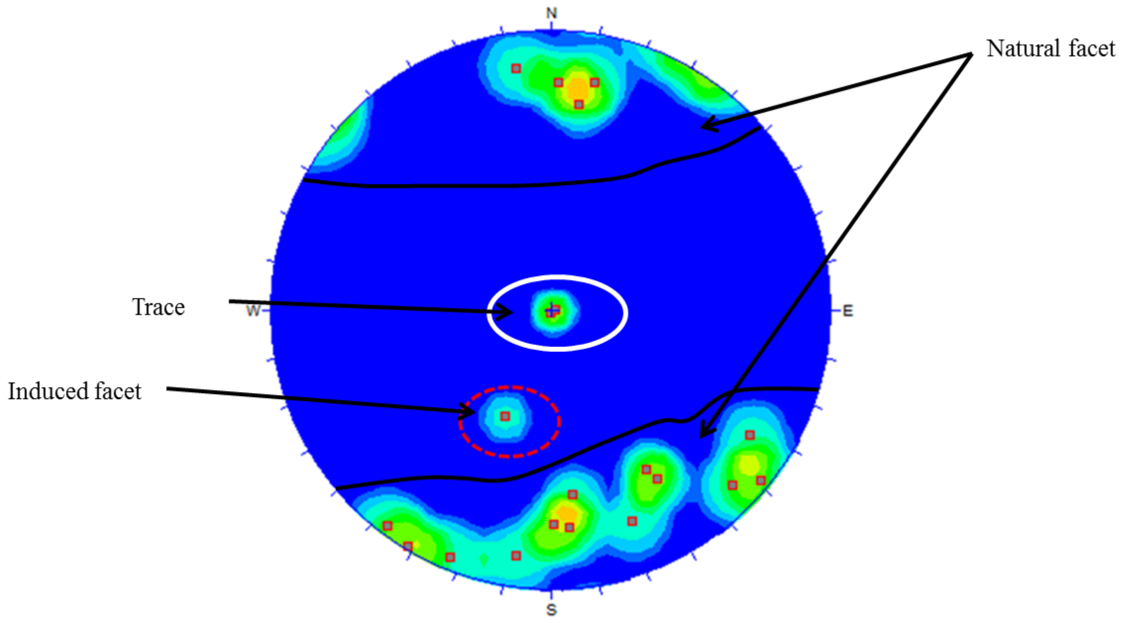

Figure 4.6. Stereonet plot showing orientations of traces (white oval), natural facet (black section), and induced facets (in red oval).

Table 4.1. Summary of observable differences between traces, natural, and induced facets

Discontinuity	**Caused by**	**Morphology**				**Surface Color**	**Weathering Level**	**Orientation on Stereonet**	**LiDAR Data**
		Features	**Surface**	**Shape**	**Class**				
Trace	Natural and human activities	N/A	N/A	Linear	Both primary and secondary	N/A	N/A	Mostly follows observable trend	N/A
Natural facets	Natural geological processes	N/A	Mostly smooth	Mostly regular	Mostly primary	Stained	Mostly low	Mostly follows observable trend	Low intensity values
Induced facets	Human activities (blasting)	Blast hole marks	Mostly rough and	Mostly irregular	Mostly secondary	Unstained	Mostly moderate	Mostly deviate from observable trends	High intensity values

4.4 SUMMARY AND CONCLUSION

As previously mentioned, discontinuities are present in every rock mass. Their presence influences all the engineering properties and behavior of rocks. Thus, their presence affects engineering designs and projects. One must understand the discontinuity type to accurately analyze a discontinuity data.

Determining the discontinuity type can be very difficult, especially when dealing with both natural and induced facets. Experience can be very helpful, both in the field and in the office. Situations still exists, however, in which it is still very difficult to differentiate between natural facets and induced facets, even with tremendous experience.

The activities or processes that caused the occurrence of the discontinuity, morphology, surface color, weathering level, and the discontinuity’s trend on a stereonet are very important when differentiating natural facets from induced facets. Traces are caused by natural geological processes or human activities. Traces are linear in shape, exist as both primary and secondary discontinuities, and their orientations mostly follow observable trends when plotted on a stereonet. Natural facets are caused by natural geological processes. They mostly have relatively smooth surfaces and stained when compared to induced facets. Natural facets appear regular in shape, primary in class, mostly follow observable orientation trends when plotted on stereonets, and mostly have low levels or degree of weathering compared to induced facets. Induced facets are caused by human activities such as blasting, they mostly exhibit drill hole marks, their surfaces mostly appear rough and unstained compared to natural facets. They are mostly irregular, mostly secondary, mostly deviate from observable trends when plotted on stereonets, and moderately weathered compared to natural facets.

5. 3-D DISCONTINUITY ORIENTATIONS FROM COMBINED OPTICAL IMAGING AND LIDAR DATA

This chapter elaborates on how 3-D discontinuity orientations can be determined from combined optical and LiDAR imaging. Orientations of facets and traces were estimated from the LiDAR point clouds and optical images respectively.

5.1 ESTIMATION OF FACET ORIENTATION FROM LIDAR DATA.

Estimating orientation of facets from LiDAR data can be very tedious. General known methods of estimating facet orientations involve processes which include the registering of a point cloud data to a known coordinate system, creating of polygonal surface models or mesh using triangulations, and the grouping of neighboring element into patches based on their normal vectors (Donovan et al. 2005; Slob et al. 2005). These processes can be very useful; however, training, significant expertise, and experience are needed to complete most of them.

In this research, the orientations of facets were estimated using the simple 3 point problem method described in one of our papers (Maerz et al. 2012). This method involves the selection of three non-collinear points (x,y,z triplets) on the facets from the point cloud data. The point cloud data was reoriented using the orientation of a known sub-vertical joint, negating the need to register the point cloud to a global coordinate system. Orientations of the facets were then computed using the equation of a plane.

5.1.1 The Three Point Program. The program allows the selection of individual discontinuities from a point cloud by browsing through the point cloud in a LiDAR viewer. The program requires only the orientation of one sub-vertical facet to calibrate or reorient the LiDAR data. The method involves the selection of 3 non-collinear points on a facet from a LiDAR data. These points should be spread out as far as possible on the same facet. Many significant digits as possible should be retained for each point, as the dip direction is really sensitive to the number of significant digits especially in the case of low angle sub-vertical joints. The xyz coordinates of the points are noted and entered into the program on a simple spreadsheet.

5.1.1.1 Calculation of the equation of a plan (local coordinate system). The unit vector of the facet can be obtained from the equation of a plane. Assuming, (x_1,y_1,z_1), (x_2,y_2,z_2), (x_3,y_3,z_3) are the points on a facet in a local (arbitrary) coordinate space defined by the LIDAR unit :

The equation of a plane, is defined as:

$$Ax + By + Cz + D = 0 \tag{5.1}$$

where (A,B,C) is a vector normal to the plane. The values of A, B, C, and D are determined as follows:

$$A = y1z2 + z1y3 + y2z3 - z2y3 - z3y1 - z1y2 \tag{5.2}$$

$$B = z2x3 + z3x1 + z1x2 - x1z2 - z1x3 - x2z3 \tag{5.3}$$

$$C = x1y2 + y1x3 + x2y3 - y2x3 - y3x1 - y1x2 \tag{5.4}$$

$$D = z1y2x3 + z2y3x1 + z3y1x2 - x1y2z3 - y1z2x3 - z1x2y3 \tag{5.5}$$

(A,B,C) is then converted in to a unit normal vector:

$$(x, y, z) = \frac{(A,B,C)}{\sqrt{(A^2+B^2+C^2)}} \tag{5.6}$$

5.1.1.2 Conversion from Cartesian to spherical coordinates (local coordinate system).

The cartesian coordinates (x,y,z) are then converted to spherical coordinates (r,θ,φ). The value of r will always be equal to 1, since we are concerned with unit normal's on the unit hemisphere.

The values of dip of the facet (θ) and the dip direction (φ) in radians are calculated: as follows:

$$\mathrm{Cos}\,\theta = \frac{z}{r} \tag{5.7}$$

$$Tan\ \varphi = \frac{y}{x} \tag{5.8}$$

5.1.1.3 Rectification of φ value (local coordinate system).

The value of φ when determined in equation (5.8) will always result in a value between 0 and π/2 (0 and 90˚) or between 0 and -π/2 (0 and -90˚), whereas the geographical coordinate system requires a value between (0 and 2π (0 and 360˚) in a clockwise direction.

The transformation is as follows:

1. If in quadrant 1 ($x > 0$, $y < 0$) $\varphi \rightarrow 90-\varphi$
2. If in quadrant 2 ($x < 0$, $y < 0$) $\varphi \rightarrow 180-\varphi$
3. If in quadrant 3 ($x < 0$, $y > 0$) $\varphi \rightarrow 180-\varphi$
4. If in quadrant 4 ($x > 0$, $y > 0$) $\varphi \rightarrow 360-\varphi$

5.1.1.4 Rotation of φ value (local coordinate system to global). The φ angle is then aligned (rotated) from the local coordinate system to a global coordinate system (with North as the reference for the y axis) (Figure 8). This is simply done empirically, by manually measuring a single discontinuity in the field using a compass and comparing the φ value measured in the field with the φ value measured on the LIDAR image.

Figure 5.1. presents an example of selected points on a facet of LiDAR data of a rock cut in Colorado. The xyz coordinates of the selected points are presented in Table 5.1.

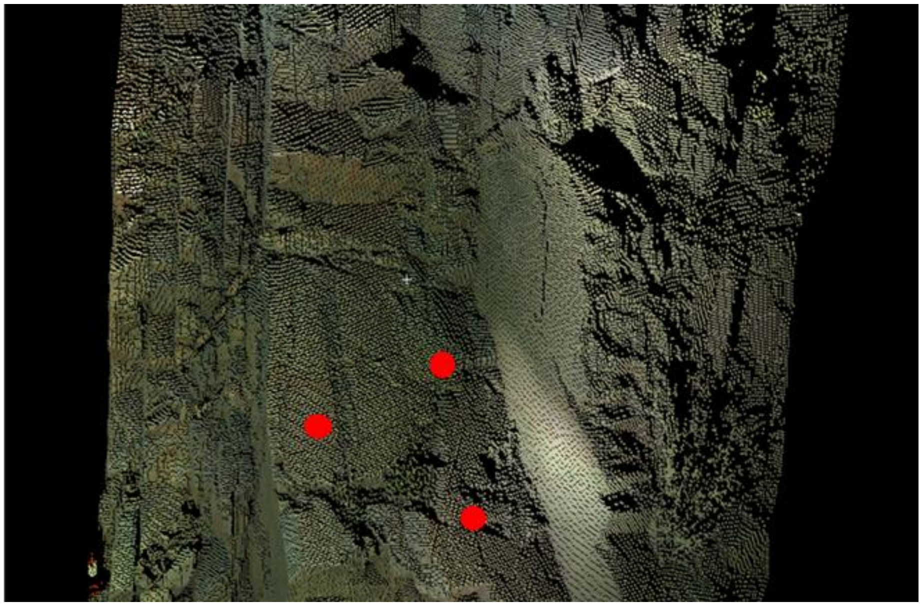

Figure 5.1 Three non-collinear points (red circles) selected on a facet of LiDAR data of a rock cut in Colorado.

Table 5.1. xyz coordinates of the selected points in Figure 5.1

Points	x	y	z
1	1663.93	8823.15	3020.68
2	1124.73	7326.5	1641.05
3	2123.63	7931.35	1792.57

Presented in Figure 5.2 are randomly selected facets of a point cloud data of a rock cut in Colorado. Estimation of the orientations of the selected facets using the 3-point program is presented in Table 5.2.

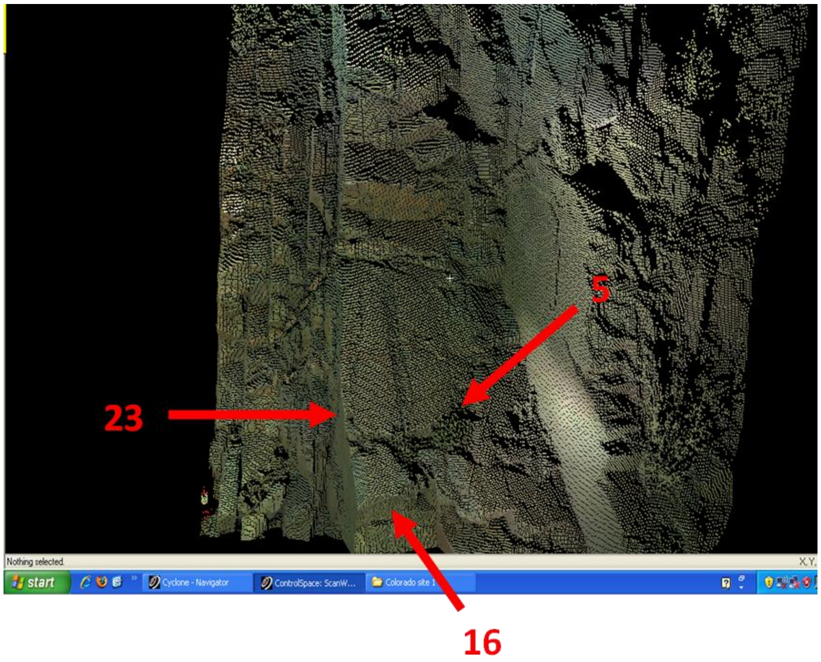

Figure 5.2. Randomly selected facets (5, 16, 23) of a point cloud data of a rock cut in Colorado.

Table 5.2. Orientations estimations using the 3-point program on facets in Figure 5.2

Facet	x	y	z	Unit Normals			Field Dir/Dip	3-point Dir/Dip	Difference
5	1663.93	8823.15	3020.68	0.32879	-0.7014	0.6324	245/50	245/51	000/01
	1124.73	7326.5	1641.05						
	2123.63	7931.35	1792.57						
16	1345.67	6623.48	670.24	0.33807	-0.7108	-0.6168	065/56	065/52	000/04
	958.17	6675.31	398.11						
	1398.96	6888.24	394.32						
23	585.71	7106.15	993.79	-0.9235	-0.3831	-0.0194	161/88	157/89	004/01
	531.23	7263.65	477.01						
	725.01	6807.58	258.66						

Figure 5.3 and Table 5.3 presents the results of orientations obtained from point cloud data and those obtained manually (from field) from one of our research sites in Rolla, Missouri.

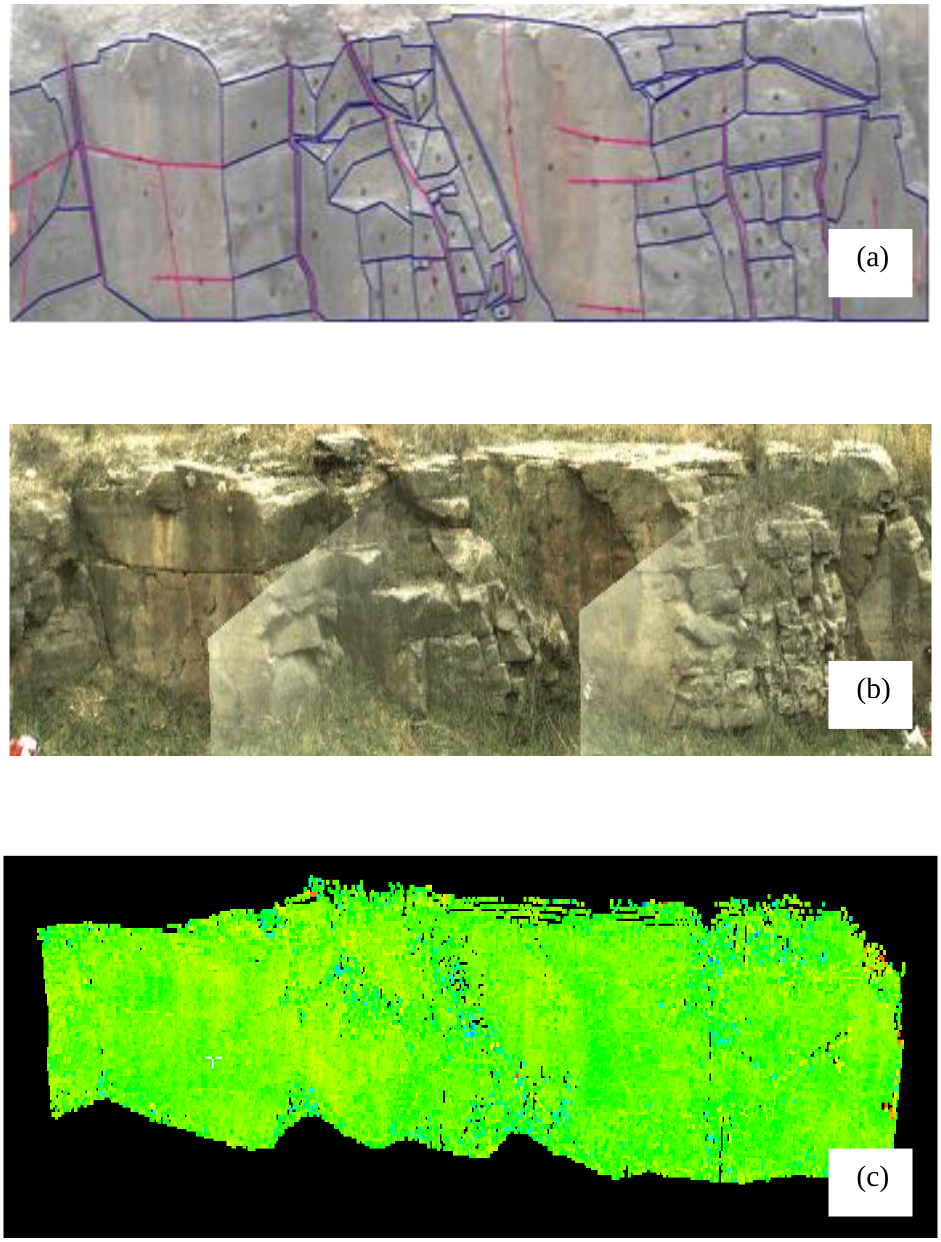

Figure 5.3. (a) Optical image from hand held camera, (b) optical image from LiDAR unit, (c) LiDAR intensity data, (d) LiDAR intensity data mapped with natural colors of the rock, (e) Lower hemispherical equal angle projection of poles of orientation measurements obtained from field (blue triangles) and from LiDAR (red squares).

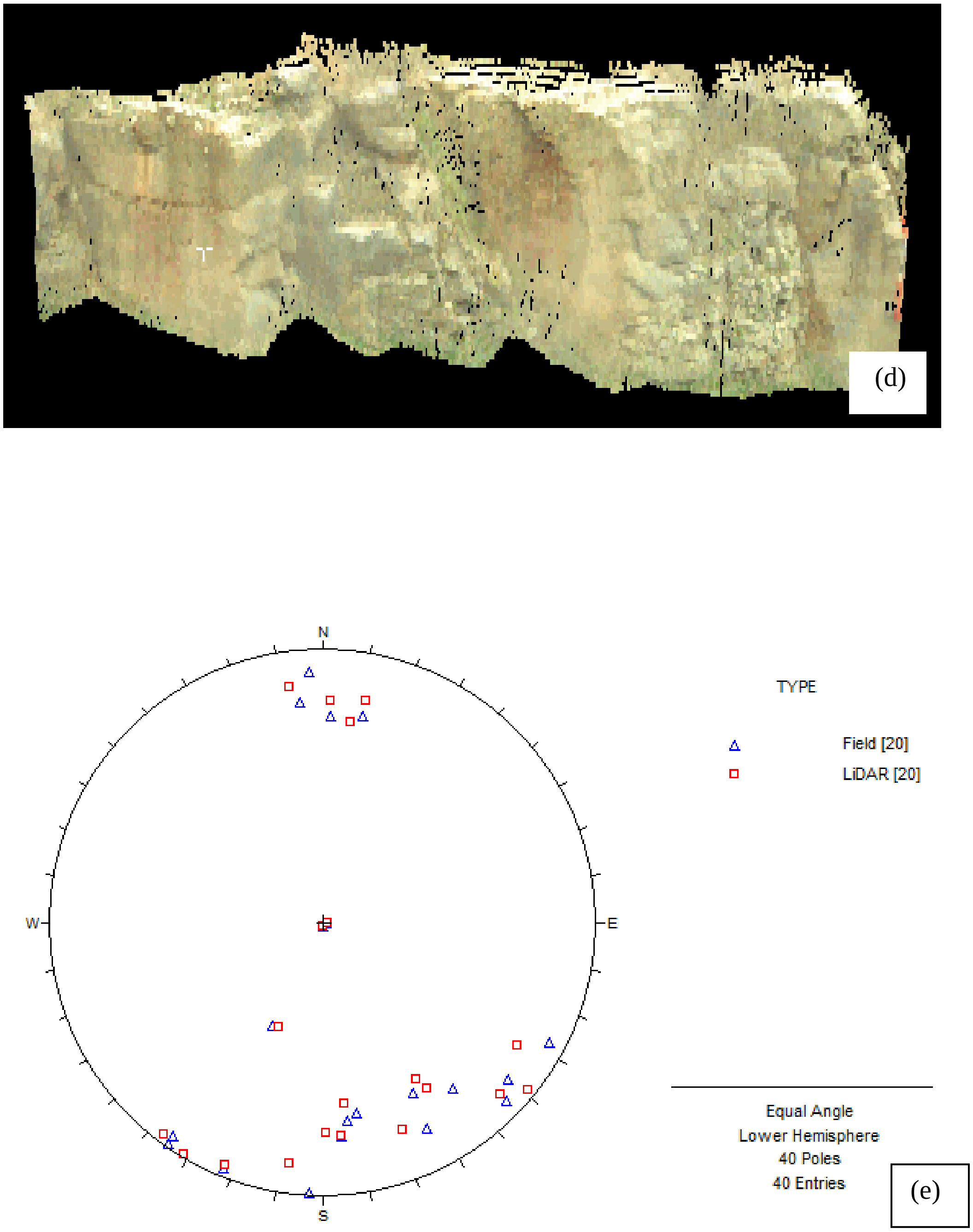

Figure 5.3. (a) Optical image from hand held camera, (b) optical image from LiDAR unit, (c) LiDAR intensity data, (d) LiDAR intensity data mapped with natural colors of the rock, (e) Lower hemispherical equal angle projection of poles of orientation measurements obtained from field (blue triangles) and from LiDAR (red squares). (cont.)

Table 5.3. Dip directions and dip angles of facets from manual (field) and LiDAR data using the 3-point program on the site in Figure 5.3

Facet	Field	3-point	Difference
	Dir/Dip (Deg)	Dir/Dip (Deg)	(Deg)
1	314/86	309/88	005/02
2	332/70	329/67	003/03
8	022/88	022/87	000/01
10	310/83	314/84	004/01
11	333/80	339/78	006/02
12	322/75	328/71	006/04
18	035/87	031/89	004/02
19	298/86	302/80	004/06
20	355/1	358/1	003/00
21	177/85	172/82	005/03
22	174/78	182/78	004/00
30	274/1	274/2	000/01
32	026/45	023/45	003/00
35	182/74	188/73	006/01
37	191/75	191/79	000/04
56	355/76	355/76	000/00
58	353/72	359/75	006/03
60	350/70	353/67	003/03
73	035/89	037/88	002/01
77	003/89	008/83	005/06

The method was tested on over fifty sites. Results indicated that over ninety eight percent (98%) of the differences between measurements obtained from the field and those from LiDAR using the 3-pont program were below dip direction and dip values of 005/05 degrees.

5.1.2 Estimation of the azimuth of a rock face from a point cloud data. The azimuth of the strike of a rock face can be estimated using the 3-point program. The first step is to select a portion of the rock face whose azimuth best represents the azimuth of the entire rock face. Three non-collinear points are then selected on this portion. The dip and the dip directions of the rock face are then estimated using the 3-point program. The azimuth of the strike of the rock face is then estimated from the dip direction. An example is presented in Appendix A of this dissertation.

5.2 ESTIMATION OF TRACE ORIENTATION FROM OPTICAL IMAGES

Two methods were used to estimate the orientation of traces from an optical image. One for vertical rock faces, and the other was for non- vertical rock faces. The first method is for vertical rock faces. This method requires the azimuth of the strike of the rock face to be known. The second method was proposed by Kemeny and Post (2003). This method was used for non-vertical rock faces. The method requires that both the azimuth of the strike of the rock face, and the plane on which the trace belong is known. This azimuth of the strike of the rock face or plane can easily be estimated from a LiDAR data using the three point program described above. The steps involved in estimating the azimuth of a rock face or joint plane are presented in Appendix A.

5.2.1 Estimation of Trace Orientation for Vertical Rock Faces. It is very important to keep the image of the rock face vertical. In this research, a vertical pendulum was placed in front of the rock face as a reference to help set the image as vertical as possible (Figure 5.4). The trend and plunge of the traces in the plane of the face can be easily estimated from the optical image after the azimuth of the rock face has been estimated (Appendix A). The fact is that, for vertical rock faces the measurements of the trend and plunge will always be in the plane of the rock cut. The traces on a vertical rock face either trend to the left or to the right of the rock face. Thus, the traces will have only two possible values of trend.

The two strikes of the rock face in Figure 5.5, are 113^o and 293^o. Thus, the azimuth of the rock face has values of 113^o and 293^o. 293^o is to the left, and 113^o is to the right. This azimuth is represented with a double head arrow on top of the optical image of the rock face (Figure 5.5). Three sets of traces that can be identified on the image are represented with different color. These are the blue set, the yellow set, and the green set (Figure 5.5). The blue set of traces are all trending to the left hence their estimated trend is 293° based on the azimuth of the rock face. The green and yellow traces are trending to the right hence their estimated trend is 113°.

The angle between the trace and a line drawn horizontal to the rock face is known as the rake. For vertical rock faces, such as the image in Figure 5.3, the rake is equivalent to the plunge. The following steps were followed in order to estimate the dip angle of a trace from an optical image of a vertical rock face.

1. The trace was identified
2. A horizontal line that intersects the trace was drawn
3. The acute angle between the trace and the horizontal was measured
4. This angle is the plunge of the trace

These can be done manually by the use of a protractor or the Digimizer^R software. Efforts must be made to set the image upright in both cases. Plunge and trend values estimated from the optical image in Figure 5.5 are presented in Table 5.4.

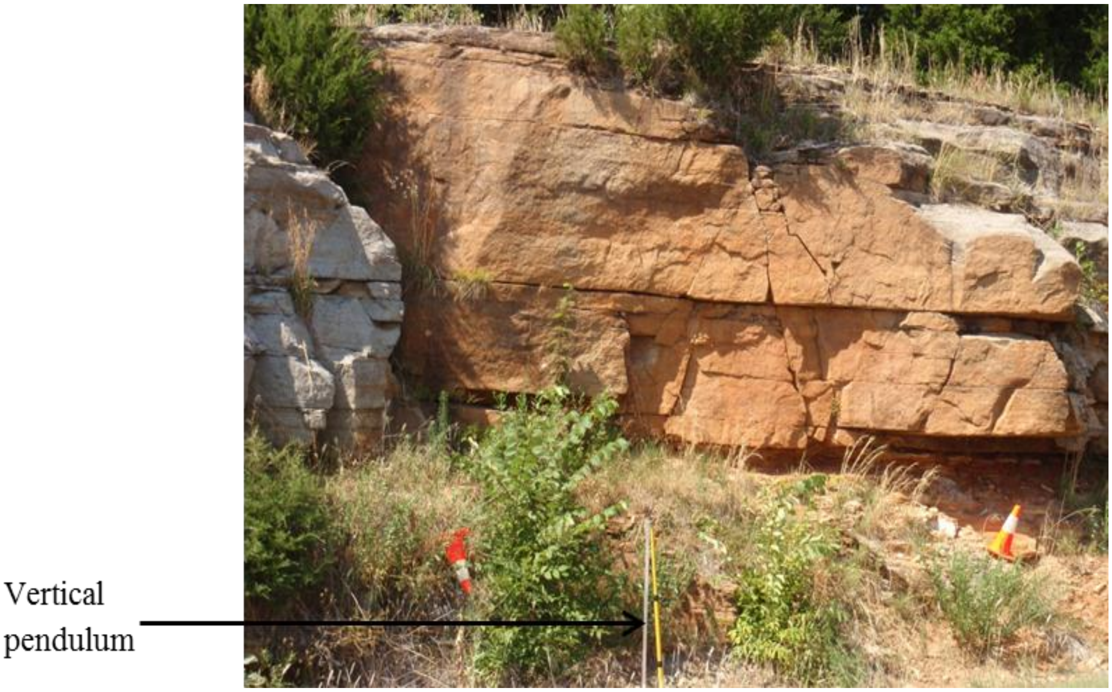

Figure 5.4. An optical image of a rock face showing the vertical pendulum.

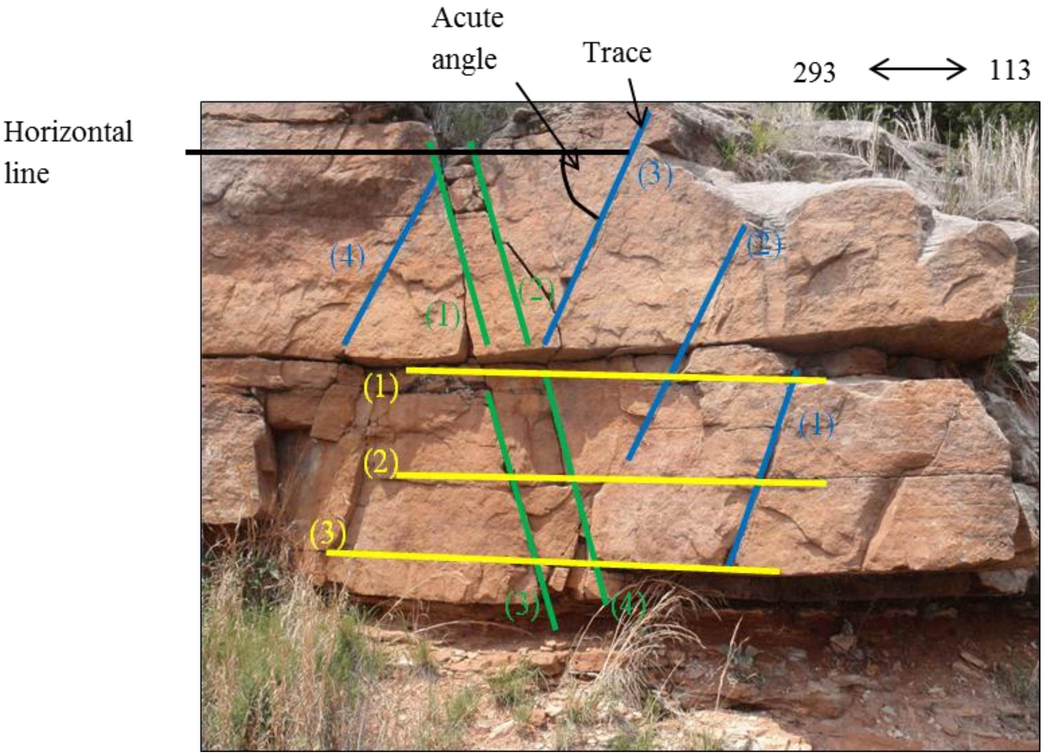

Figure 5.5. An optical image of a rock face showing blue, green, and yellow trace sets.

Table 5.4. Plunge and trend values of the traces in Figure 5.5

Set 1			
Trace No.	Trace Color	Plunge (Acute Angle)	Trend (Inclination)
1	Blue	70	293
2	Blue	66	293
3	Blue	60	293
4	Blue	60	293
Set 2			
Trace No.	Trace Color	Plunge (Acute Angle)	Trend (Inclination)
1	Green	77	113
2	Green	78	113
3	Green	77	113
4	Green	76	113
Set 3			
Trace No.	Trace Color	Plunge (Acute Angle)	Trend (Inclination)
1	Yellow	2	113
2	Yellow	3	113
3	Yellow	3	113

5.2.2 Estimation of Trace Orientation for Non-Vertical Rock Faces. For non-vertical rock faces, the trace vector can be estimated from an optical image when the orientation of the joint plane and the orientation of the effective rock face are known. The orientation of the joint plane and that of the rock face can be estimated from the 3-point program (Appendix A).

The trace vector is the cross product of the unit normal perpendicular to the joint plane and the unit normal perpendicular to the rock face (Kemeny and Post, 2003). Knowing the trace vector, the trend and plunge of the trace can easily be estimated (Appendix A).

5.3 MERGING TRACES AND FACETS ORIENTATIONS

Cluster sets of measured azimuth and plunge of traces from the optical image will have a set of facets that it belongs to. In Figure 5.6, it is obvious that the set of traces of the same color belong to the set of facets with the same color. Thus, the blue set of traces belong to the blue set of facets, yellow set of traces belong to yellow set of facets, and green set of traces belong to green set of facets. Tables 5.5 and 5.6 respectively presents the mean plunge and trend of trace sets obtained from the optical image, and the mean dip and dip direction of facet sets obtained from LiDAR point clouds. On a stereonet, the trace vector will fall on the facet great circle if it belongs to the facet (Figure 5.7). Using the equation of the angle between two lines, the dot product of the trace vector and facet unit normal vector will be zero if the trace belongs to the facet, thus, the angle should be 90° or close to 90° when the trace is contained within the plane of the facet (Table 5.7).

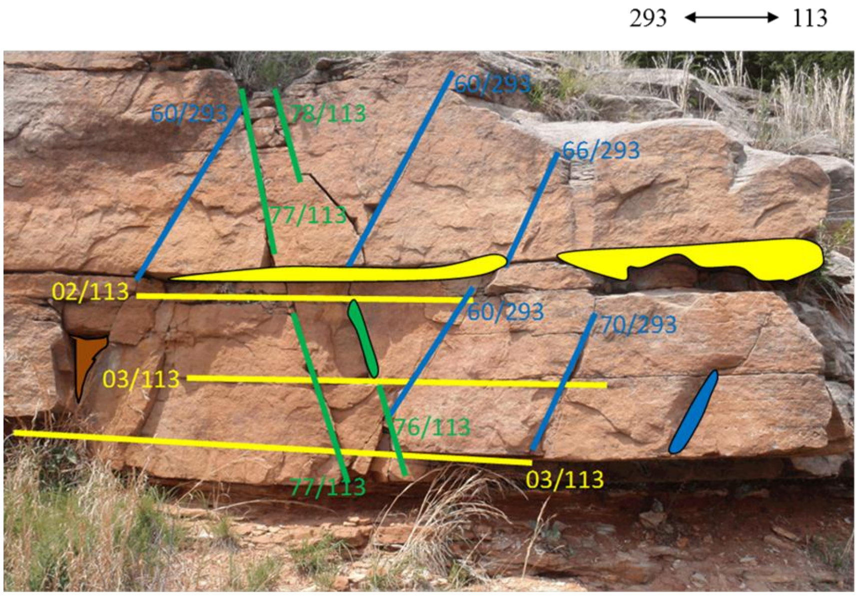

Figure 5.6. Image of a rock cut showing traces and facets. Same colors traces and facets form sets. Thus, set of traces of the same color belongs to the set of facets of the same color.

Table 5.5. Mean plunge and trend of trace sets obtained from optical image

Set	Plunge	Trend	Color
Set 1	64	293	Blue
Set 2	77	113	Green
Set 3	2.6	113	Yellow

Table 5.6. Mean dip and dip direction of facet sets obtained from LiDAR data

Set	Dip	Dip Direction	Color
Set 1	70	315	Blue
Set 2	81	71	Green
Set 3	2.9	157.6	Yellow
Set 4	70	222	Brown

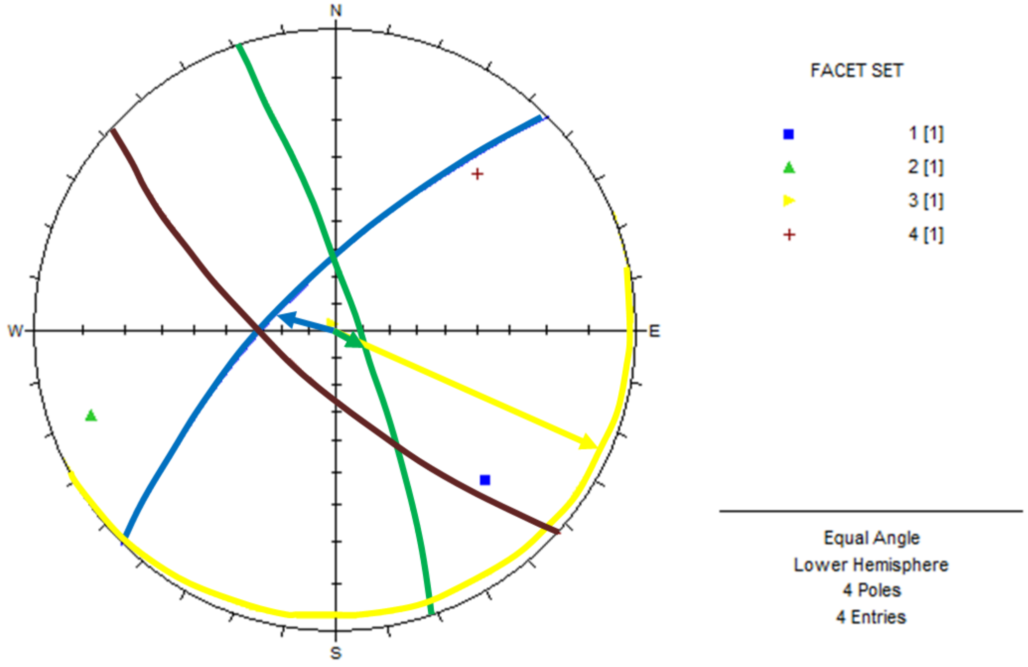

Figure 5.7. Trace vectors (arrows) and great circles (arcs) of facet on a stereonet. Blue, green, and yellow vectors (traces) falls on the blue, green, and yellow great circle (facets) respectively. The brown great circle (facet) has no trace that belongs to its set, hence no vector falls on it.

Table 5.7. Summary of Angles (from dot products) of the trace vectors and facet unit normals. Angles that are very close to 90 degrees indicate facets and traces of the same set.

	Traces		
Facets	Set 1 (Blue)	Set 2 (Green)	Set 3 (Yellow)
Set 1 (Blue)	94	58	27
Set 2 (Green)	62	91	136
Set 3 (Yellow)	26	14	87
Set 4 (Brown)	80	66	71

More examples on the merging of traces and facets are presented in Appendix A of this dissertation.

6. SUMMARY, CONCLUSION, AND RECOMMENDATIONS

6.1 SUMMARY

A discontinuity is a significant mechanical break or fracture of negligible tensile strength in a rock, low shear strength, and high fluid conductivity when compared to the rock itself (Priest, 1993). Discontinuities are present in every rock, and their presence affects both the engineering properties and the behavior of a rock. Geological processes typically generate one or more clusters of usually parallel or sub-parallel discontinuities in a given rock mass (Priest, 1993).

Orientation is arguably the most important discontinuity property. Orientations influence the potential of a rock mass to move, the direction of movement, and the volume of material moved (Donovan et al, 2005). Measurement of discontinuity orientations is critical for analysis of discontinuous rock masses. These orientation measurements are typically conducted using the Brunton compass. The time honored method of manual measurements with Brunton compasses is both time consuming and often inconvenient, given issues such as restricted access to measurement areas.

Progress has been made towards automated measurements using both LiDAR scanning and optical imaging methods. LiDAR scanners use either a time of flight or phase shift sensors to generate a 3-D image of a surface. An optical image is 2-D image, primarily produced by a camera.

Discontinuities manifest themselves in rock cuts either as facets or as fracture traces. The orientation of facets can be measured by LIDAR techniques. The orientation of fracture traces can be measured, at least in 2-D, by optical imaging methods. Facets are defined as the actual discontinuity surfaces that are exposed in the rock cut (most commonly observed in rough irregular rock cuts). The facets in a rock can be either natural or induced. Analytical results can be very misleading if natural discontinuities are treated as induced, and vice versa. Fracture traces are the linear features that intersect both the discontinuity and the rock cut (most commonly observed in smooth planar rock cuts). Unfortunately LIDAR scanning cannot measure traces nor can optical imaging measure facets. This is complicated by the fact that both facets and traces are often present in the same rock cut. Thus, the needs for the development of methods and tools that can help combine both optical images and LiDAR data, in order to effectively analyze discontinuity data.

6.2 CONCLUSION

Traces are caused by natural geological processes or human activities. Natural facets are caused by natural geological processes. Induced facets are caused by human activities such as blasting. The set of traces in a rock mass usually belong to a set of facets of the same rock mass. These sets of traces and facets can be combined either by the use of stereonets or by the equation of the angle between two lines. On a stereonet, the trace vector will fall on the facet great circle if the trace belongs to the facet. Using the equation of the angle between two lines, the dot product of the trace vector and facet unit normal vector will be zero if the trace belongs to the facet.

Orientations of facets were estimated from LiDAR data using a novel algorithm (3 point program). Using the 3-point program together with both manual and the Digimizer software, the orientation of traces were estimated from optical images.
3-D laser scanning and digital imaging technologies can provide information on discontinuities without having to make physical contact with the rock surface to measure

discontinuity properties such as orientation. The technologies provide higher safety and can be used to obtain data on inaccessible rock faces. Also, a bigger statistical sample is possible and not restricted to only those parts of the rock face that is accessible. The technologies also reduce bias due to humans which is very common when the traditional manual methods are used. Finally, the technologies provide a fast way for data collection and the analysis of discontinuous rock.

This research has extended knowledge on 3-D LiDAR and optical imaging applications in discontinuity data analysis.

The research led to the following developments:

- A simple method by which the orientations of facets can be estimated from a point cloud data. This method has been shown to work on extensive field data on over 50 sites in the United Staes, Canada, and Saudi Arabia. Over ninety five percent (95%) of the time, the differences between results obtained from this method when compared to field measurements were less than five degrees (5^o).
- A simple method by which the orientation of traces could be estimated from 2-D images.
- A reasonable way by which professionals could differentiate between trace, natural and induced (blasted) facets.
- A methodology by which optical images can be combined to point cloud data for better analysis of discontinuity orientation data.

Results obtained from all the developments mentioned above have been shown to be very good.

6.3 RECOMMENDATIONS

Generally, the LiDAR should be set at a distance that is equal to the height of the rock face of interest. This helps to eliminate a sharp angle between the scanner's field of view and the dip of the rock face. In general it is best if the scanner's horizontal field of view is set to less than 50^o. The LiDAR unit should always be leveled before scanning, to avoid the collection of angled data. For discontinuity property estimations such as orientation, it is recommended that the LiDAR is set perpendicular to the rock face. If extra scans are needed at different angles, the angle that the scanner is positioned should be noted with reference to the rock face. Efforts should be made to avoid shadow zones. Shadow zones can obscure discontinuity sets. The appropriate scanner field of view should always be used to reduce the size of the point cloud. Resolutions should greater than 2x2 mm but less than 5cm for optimum scanning. Optical image of the rock face should be collected. This image can be used to both modify the field of view, and to add natural colors of the rock face to the LiDAR data.

6.3.1 Future Work and Research. The following future work and research are recommended.

- More geologically inclined LiDAR data processing software needs to be developed.
- The possibilities of estimating other discontinuity properties, such as discontinuity roughness and spacing, with the LiDAR equipment should be investigated.

- More research on the intensity of LiDAR data and its use beyond visualization should be conducted.
- Research on how to incorporate LiDAR data into other geological software should be conducted.
- Research on the determination of lithology and mineral composition of rocks from point cloud data should be conducted.
- Research on the estimation of the degree of weathering of rock surfaces from point cloud data should be conducted.

APPENDIX A
(CONCEPTS AND AUXILIARY CALCULATIONS)

Estimating the azimuth of a rock face from a LiDAR Image, using the 3-point program

1) Select a portion of the rock face whose azimuth best represents the azimuth of the entire rock face

2) Select 3 non-collinear points on that portion (Figure A.1, Table, A.1).

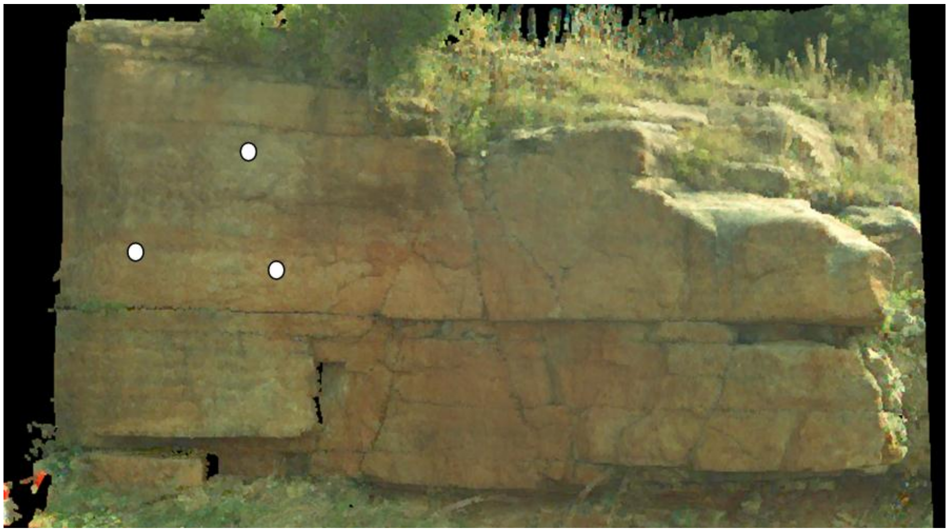

Figure A.1. 3 selected points on a rock face. The azimuth of the portion of the rock face with the 3 points represents the azimuth of the rock face.

Table A.1. Coordinates of the selected points in Figure A.1

Point	x	y	z
1	391.34	16224.08	2883.71
2	23.43	16197.51	2043.48
3	696.69	16274.94	2032.99

3) Enter the coordinates of the 3 selected points into the 3-point program (Figure A.2).

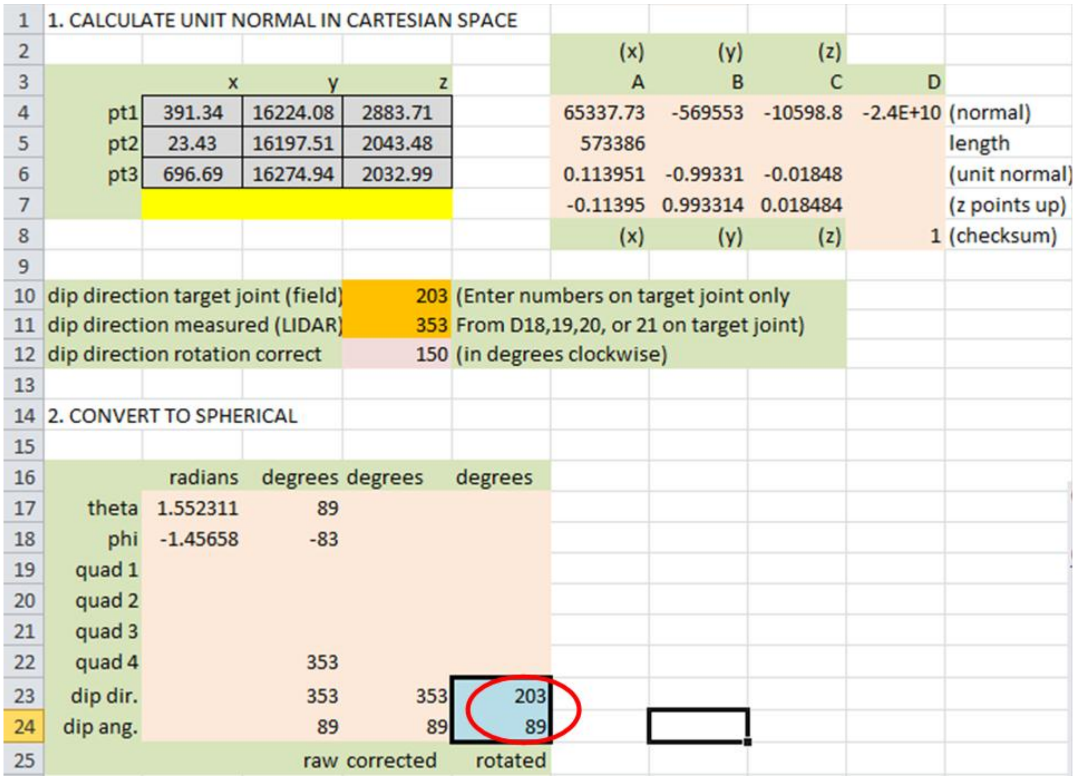

1	1. CALCULATE UNIT NORMAL IN CARTESIAN SPACE									
2						(x)	(y)	(z)		
3		x	y	z		A	B	C	D	
4	pt1	391.34	16224.08	2883.71		65337.73	-569553	-10598.8	-2.4E+10	(normal)
5	pt2	23.43	16197.51	2043.48		573386				length
6	pt3	696.69	16274.94	2032.99		0.113951	-0.99331	-0.01848		(unit normal)
7						-0.11395	0.993314	0.018484		(z points up)
8						(x)	(y)	(z)	1	(checksum)
9										
10	dip direction target joint (field)			203	(Enter numbers on target joint only					
11	dip direction measured (LIDAR)			353	From D18,19,20, or 21 on target joint)					
12	dip direction rotation correct			150	(in degrees clockwise)					
13										
14	2. CONVERT TO SPHERICAL									
15										
16		radians	degrees	degrees	degrees					
17	theta	1.552311	89							
18	phi	-1.45658	-83							
19	quad 1									
20	quad 2									
21	quad 3									
22	quad 4		353							
23	dip dir.		353	353	203					
24	dip ang.		89	89	89					
25			raw	corrected	rotated					

Figure A.2. Screen shot of the coordinates (green oval) in Table A.2 entered in the 3 point program.

4) A dip direction of 30^{o} and a dip angle of 89^{o} are obtained from the 3-point program (red oval of screen shot in Figure A.2).

$$Strike = DD - 90$$

$$Strike = 203 - 90$$

$$Strike = 113$$

Now, the fact is that every rock face has 2 strike values, separated by an angle of 180^{o}. Hence the 2 strike values of the face are 293^{o} and 113^{o}. The question is whether 293^{o} is to the left hand or to the right hand side of the face. To answer this question, we randomly select a facet with a defined orientation from the face. Thus, the facet should be dipping to the left hand or to the right hand of the entire face.

In the example in Figure A.3, the white polygon near the base of the rock cut is a facet dipping towards the right hand side of the image.

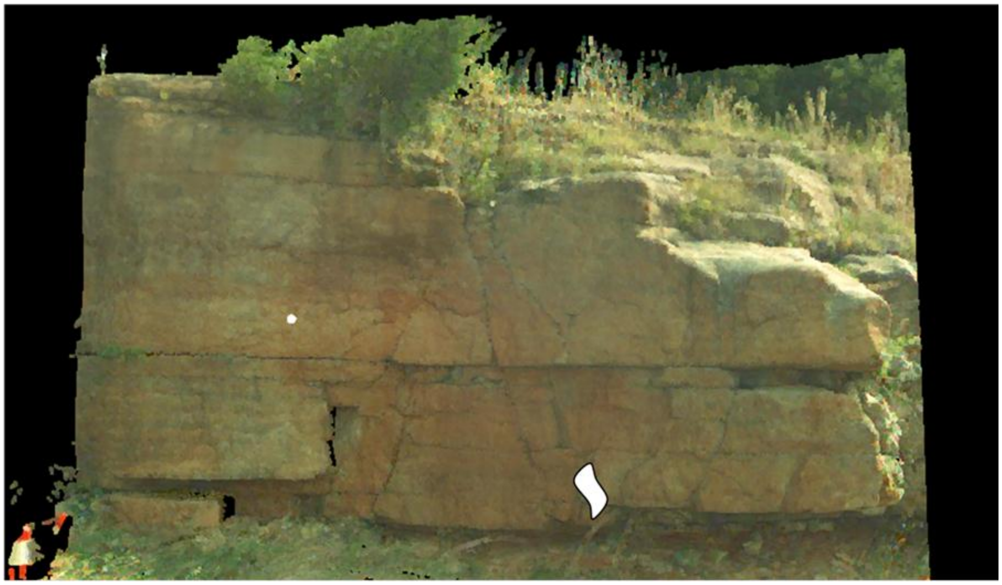

Figure A.3. Rock cut showing a facet (white polygon) dipping to the right hand side of the rock face.

5) Select 3 points from this facet (white polygon) into the 3-point program to determine the dip and the dip direction of the facet. The coordinates of the 3 selected points are presented in Table A.3

Table A.3. Coordinates of the 3 points selected from the white facet in Figure A.5

Point	x	y	z
1	644.09	16478.05	1034.66
2	594.72	16533.89	881.35
3	676.96	16457.31	915

Putting these points into the 3 point program gives us a dip of 87 and a dip direction of 79 (Figure A.4)

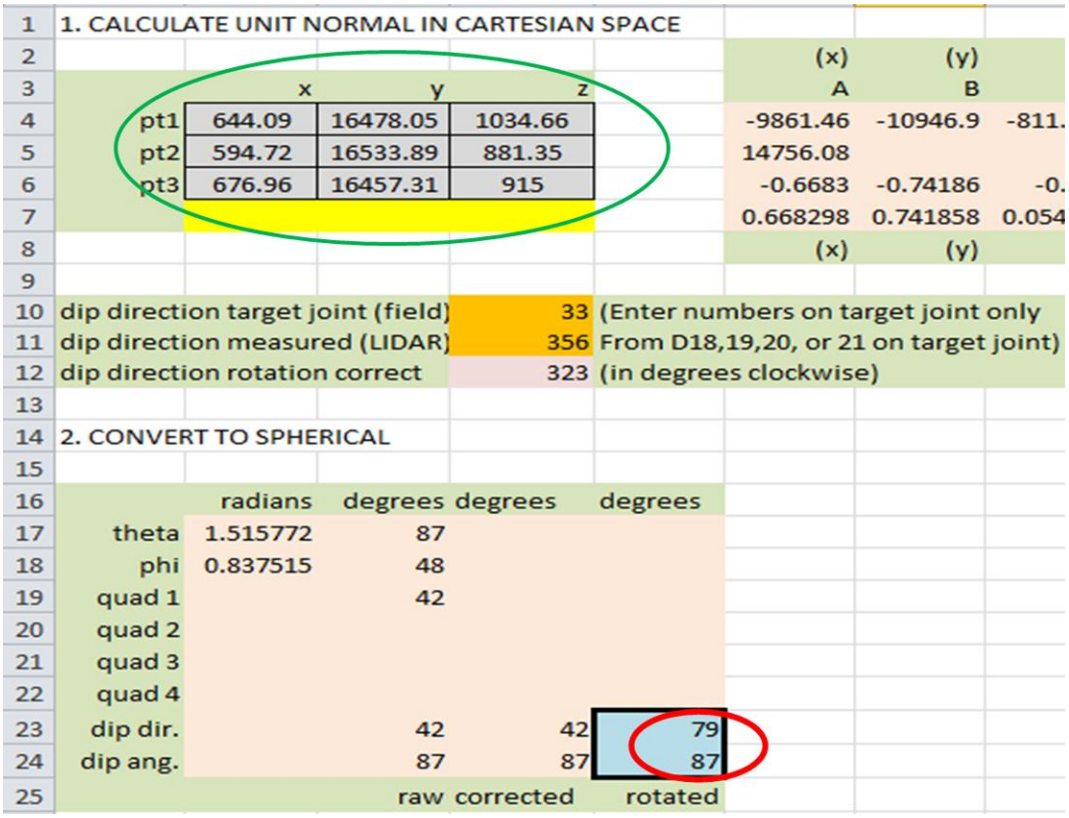

1	1. CALCULATE UNIT NORMAL IN CARTESIAN SPACE							
2						(x)	(y)	
3		x	y	z		A	B	
4	pt1	644.09	16478.05	1034.66		-9861.46	-10946.9	-811.
5	pt2	594.72	16533.89	881.35		14756.08		
6	pt3	676.96	16457.31	915		-0.6683	-0.74186	-0.
7						0.668298	0.741858	0.054
8						(x)	(y)	
9								
10	dip direction target joint (field)			33	(Enter numbers on target joint only			
11	dip direction measured (LIDAR)			356	From D18,19,20, or 21 on target joint)			
12	dip direction rotation correct			323	(in degrees clockwise)			
13								
14	2. CONVERT TO SPHERICAL							
15								
16		radians	degrees	degrees	degrees			
17	theta	1.515772	87					
18	phi	0.837515	48					
19	quad 1		42					
20	quad 2							
21	quad 3							
22	quad 4							
23	dip dir.		42	42	79			
24	dip ang.		87	87	87			
25			raw	corrected	rotated			

Figure A.4. Screen shot of the coordinates (green oval) in Table A.4 entered in the 3 point program.

The dip direction of 79^o is just enough to infer that the azimuth value of 113^o is to the right hand side of the rock face, hence the azimuth value of 293^o is to the opposite side (direction) of the rock face. Hence the azimuth value of the rock face can be concluded as 293° and 113°. This value is the same as the azimuth value of 293° and 113° obtained from the field.

Another facet could be chosen if the user is not convinced with his or her azimuth values.

Vector Calculus

Considering the two vectors,

$$A = (a_1, a_2, a_3) \text{ and } B = (b_1, b_2, b_3)$$

Dot Product

The Dot product of A and B is defined as

$$A.B = |A||B| \cos\theta$$

where, $|A|$ and $|B|$ are the magnitude of the vectors A and B, θ is the angle between A and B.

For Unit vectors, $|A| = 1$ and $|B| = 1$

Thus, $A.B = \cos\theta$

$A.B = (a_1b_1 + a_2b_2 + a_3b_3)$

Cross Product

The cross product of A and B is defined as:

$$A\ x\ B = |A||B|\ \sin\theta . N$$

where $|A|$ and $|B|$ are the magnitude of the vectors A and B, θ is the angle between A and B and N is the unit vector perpendicular to the plane containing A and B in a given direction.

$$A\ x\ B = (a_2b_3 - a_3b_2,\ a_3b_1 - a_1b_3,\ a_1b_2 - a_2b_1)$$

Estimating Trend and Plunge from a Unit Vector

Using the right hand rule, the trend (α) and plunge (β) of a unit vector with direction cosines of U_x, U_y, and U_z can be estimated from the following relationships (Priest, 1993).

$$\alpha = \arctan\left(\frac{Uy}{Ux}\right) + Q$$

$$\beta = \arctan\left(\frac{Uz}{\sqrt{Ux^2 + Uy^2}}\right)$$

Q, known as the quadrant parameter ensures that the trend lies in the correct quadrant, and can be obtained from the Table A.4.

Table A.4. The quadrant parameter Q (Priest, 1993)

U_x	U_y	Q (Degree)
$\geqslant 0$	$\geqslant 0$	0
< 0	$\geqslant 0$	180
< 0	< 0	180
$\geqslant 0$	< 0	360

Combining Facets and Traces (More Examples)

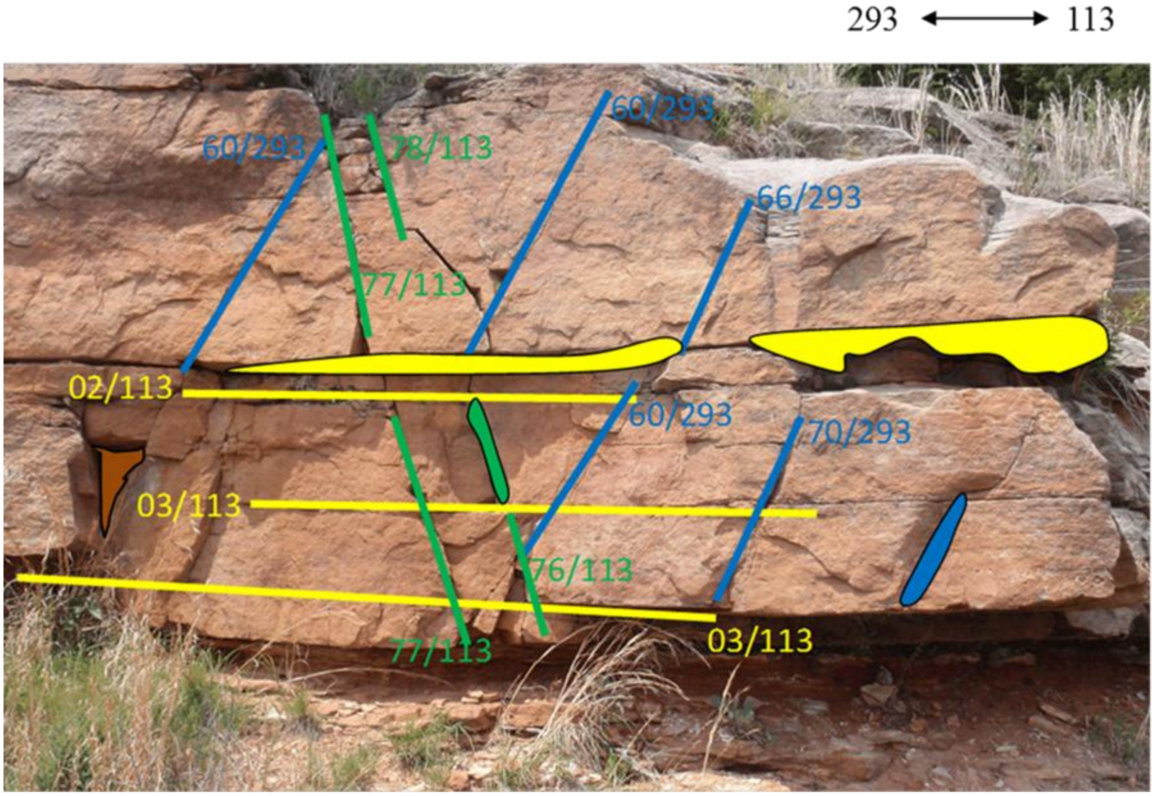

Figure A.5. Optical image of a rock cut showing sets of traces and sets of facets.

Table A.5. Plunge and Trend of traces from optical image

Plunge	Trend
70	293
66	293
60	293
60	293
60	293
60	293
77	113
78	113
77	113
76	113
2	113
3	113
3	113

Table A.6. Mean plunge and trend of trace sets

Set	Plunge	Trend	Color
Set 1	64	293	Blue
Set 2	77	113	Green
Set 3	2.6	113	Yellow

Table A.7. Mean dip and dip direction of facet sets

Set	Dip	Dip Direction	Color
Set 1	70	315	Blue
Set 2	81	71	Green
Set 3	2.9	157.6	Yellow
Set 4	70	222	Brown

SET 1 (BLUE TRACE AND BLUE FACET)

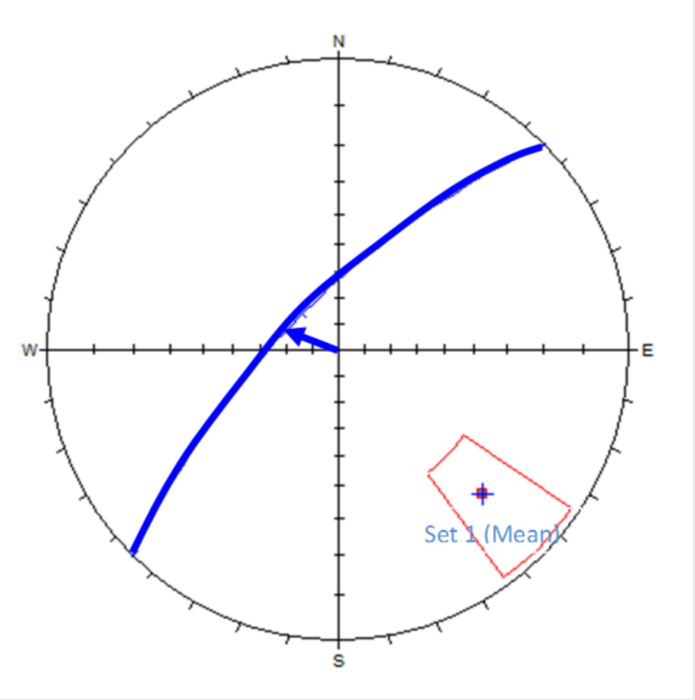

Figure A.6. Blue trace vector (arrows) intersects great circle of facet on a stereonet.

OR

USING DOT PRODUCT of FACET UNIT NORMAL VECTOR AND TRACE VECTOR

Facet unit normal

Trend (α) = 315 + 180 = 135

Plunge (β) = 90 – 70 = 20

Ux = Cos 135 x Cos 20 = - 0.664

Uy = Sin 135 x Cos 20 = 0.664

Uz = Sin 20 = 0.342

Trace vector

Ux = Cos 293 x Cos 64 = 0.169

Uy = Sin 293 x Cos 64 = - 0.403

Uz = Sin 64 = 0.899

DOT PRODUCT

$$\theta = \cos^{-1}(T.F)$$

$$\theta = 94^{o}$$

94^{0} (Angle is close to 90^{0}, which is ok though it is about 4^{0} too high)

SET 2 (GREEN TRACE AND GREEN FACET)

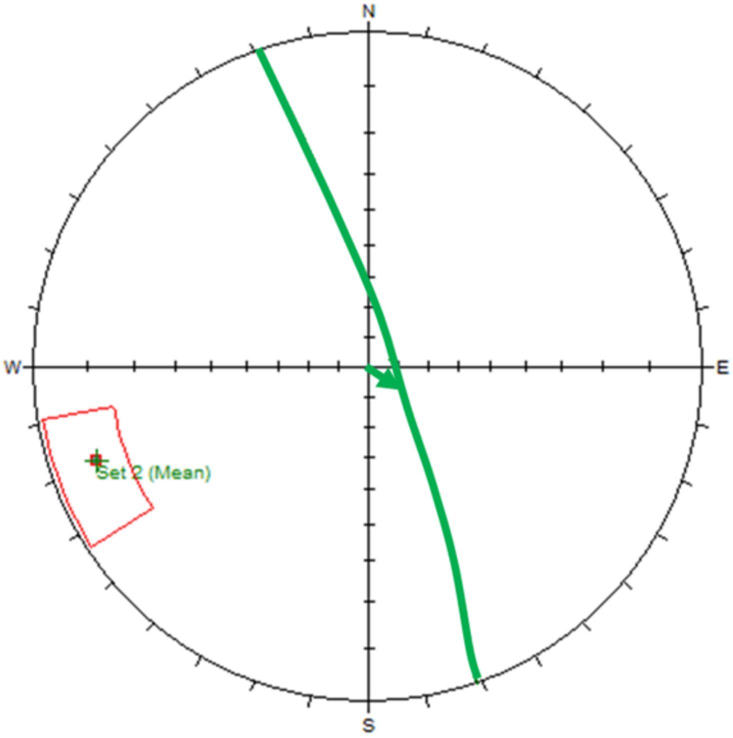

Figure A.7. Green trace vector (arrows) intersects great circle of facet on a stereonet.

Facet unit normal

Trend (α) = 071 + 180 = 251

Plunge (β) = 90 – 81= 9

Ux = Cos 251 x Cos 9 = - 0.320

Uy = Sin 251 x Cos 9 = - 0.932

Uz = Sin 9 = 0.156

Trace vector

Ux = Cos 113 x Cos 77 = - 0.087

Uy = Sin 113 x Cos 77 = 0.206

Uz = Sin 77 = 0.974

DOT PRODUCT

$$\theta = \cos^{-1}(T.F)$$

$$\theta = 91^{o}$$

91^{0} (Angle is almost exactly 90^{0}, which is very good)

SET 3 (YELLOW TRACE AND YELLOW FACET)

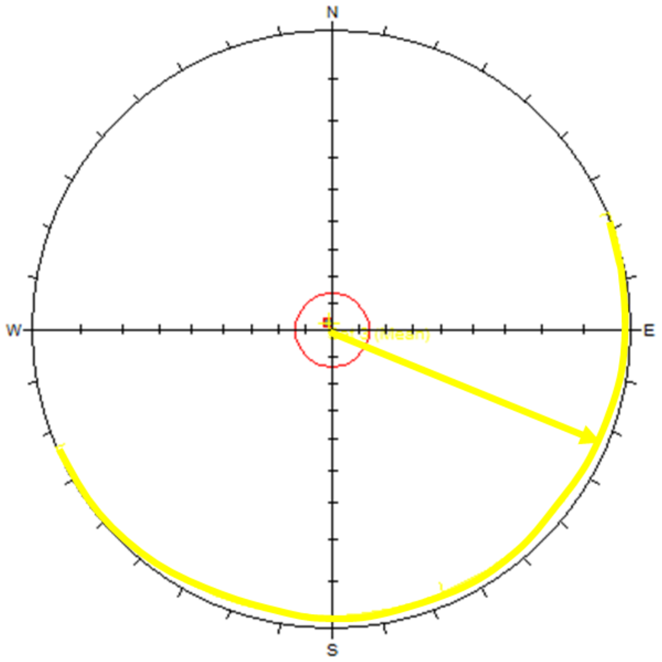

Figure A.8. Yellow trace vector (arrows) intersects great circle of facet on a stereonet.

Facet unit normal

Trend (α) = 157.6 + 180 = 336.6

Plunge (β) = 90 – 2.9 = 87.1

Ux = Cos 336.6 x Cos 87.1 = 0.046

Uy = Sin 336.6 x Cos 87.1 = 0.020

Uz = Sin 87.1 = 0.998

Trace vector

Ux = Cos 113 x Cos 2.6 = - 0.390

Uy = Sin 113 x Cos 2.6 = 0.919

Uz = Sin 2.6 = 0.045

DOT PRODUCT

$$\theta = \cos^{-1}(T.F)$$

$$\theta = 87$$

87 (angle is close to 90^0, which is ok)

SET 4 (BROWN FACET (no brown set found in this example)

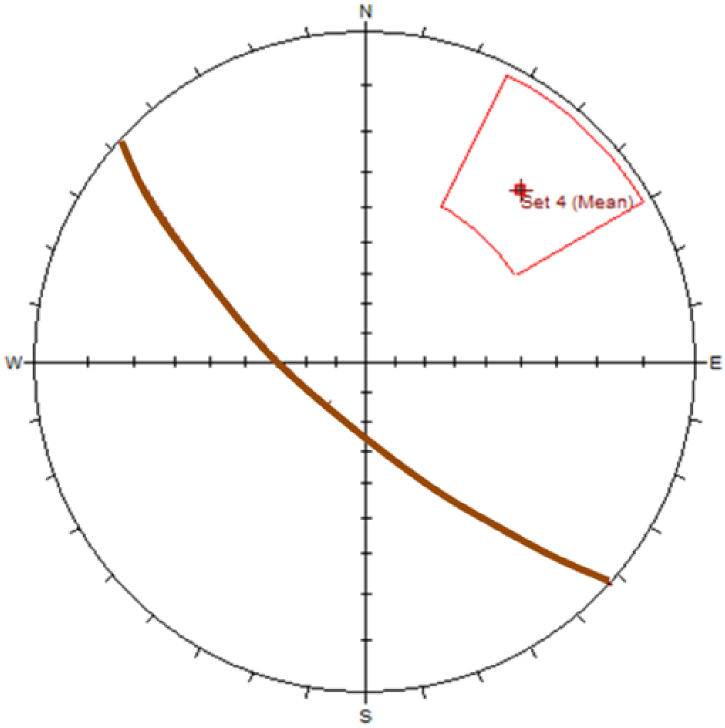

Figure A.9. Brown great circle of facet on a stereonet. There are no traces that fall in the same set with brown facets.

SET 1 (BLUE TRACE) vs Set 2 (GREEN FACET)

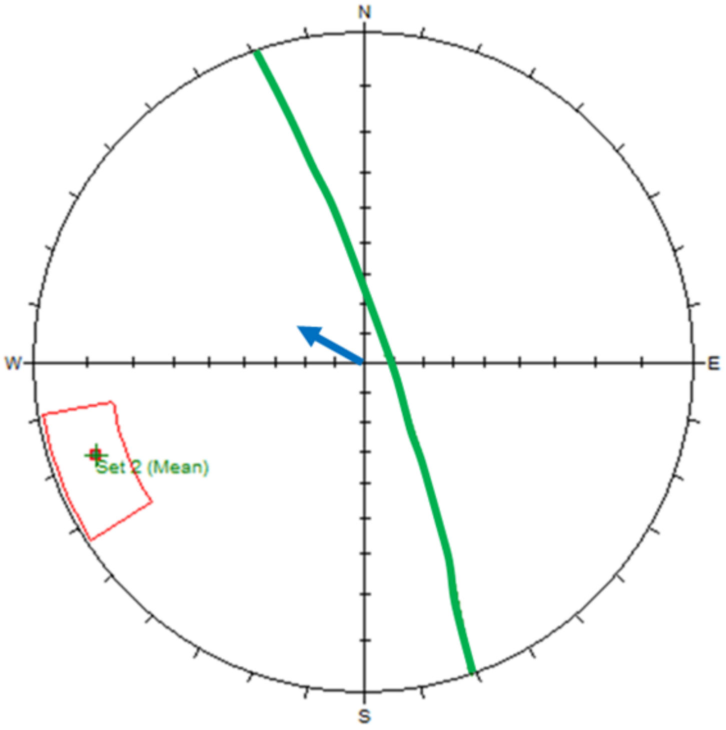

Figure A.10. Green great circle of facet on a stereonet. There are no traces that fall in the same set with brown facets.

Facet unit normal

Trend (α) = 071 + 180 = 251

Plunge (β) = 90 – 81= 9

Ux = Cos 251 x Cos 9 = - 0.320

Uy = Sin 251 x Cos 9 = - 0.932

Uz   = Sin 9 = 0.156

Trace vector

Ux = Cos 293 x Cos 64 = 0.169

Uy = Sin 293 x Cos 64 = - 0.403

Uz = Sin 64 = 0.899

DOT PRODUCT

$$\theta = \cos^{-1}(T.F)$$

$$\theta = 62^{o}$$

62 (is not close to 90)

Table A.8. Summary of Angles (from dot products) of the trace vectors and facet unit normals

	Traces		
Facets	Set 1	Set 2	Set 3
Set 1	94	58	27
Set 2	62	91	136
Set 3	26	14	87
Set 4	80	66	71

Table A.9. Spreadsheet showing the dot products of the facets and traces in Figure A.7

	Set 1 Blue						Set 1 Blue Facet vs Set 2 Green Trace						Set 1 Blue Facet vrs Set 3 Yellow Trace			
	Facet unit	Trace vector	Dot product	Angle			Facet unit	Trace vect	Dot produ	Angle			Facet unit	Trace vector	Dot product	Angle
x	-0.664	0.169	-0.112216			x	-0.664	-0.087	0.057768			x	-0.664	-0.39	0.25896	
y	0.664	-0.403	-0.267592			y	0.664	0.206	0.136784			y	0.664	0.919	0.610216	
z	0.342	0.899	0.307458			z	0.342	0.974	0.333108			z	0.342	0.045	0.01539	
			-0.07235	94.14905					0.52766	58.15256					0.884566	27.80186
	Set 2 Green						Set 2 Green Facet vs Set 3 YellowTrace						Set 2 Green Facet vrs set 1 Blue Trace			
	Facet unit	Trace vector	Dot product	Angle			Facet unit	Trace vect	Dot produ	Angle			Facet unit	Trace vector	Dot product	Angle
x	-0.32	-0.087	0.02784			x	-0.32	-0.3939	0.126048			x	-0.32	0.169	-0.05408	
y	-0.932	0.206	-0.191992			y	-0.932	0.919	-0.85651			y	-0.932	-0.403	0.375596	
z	0.156	0.974	0.151944			z	0.156	0.045	0.00702			z	0.156	0.899	0.140244	
			-0.012208	90.69956					-0.72344	136.3393					0.46176	62.49932
	Set 3 Yellow						Set 3 Yellow Facet vs Set 1 Blue Trace						Set 3 Yellow Facet vrs Set 2 Green Trace			
	Facet unit	Trace vector	Dot product	Angle			Facet unit	Trace vect	Dot produ	Angle			Facet unit	Trace vector	Dot product	Angle
x	0.046	-0.39	-0.01794			x	0.046	0.169	0.007774			x	0.046	-0.087	-0.004002	
y	0.02	0.919	0.01838			y	0.02	-0.403	-0.00806			y	0.02	0.206	0.00412	
z	0.998	0.045	0.04491			z	0.998	0.899	0.897202			z	0.998	0.974	0.972052	
			0.04535	87.40082					0.896916	26.24442					0.97217	13.57782
	Set 4 Brown vs Set 3 Yellow Trace						Set 4 Brown Facet vs Set 1 Blue Trace						Set 4 Brown Facet vs Set 2 Green trace			
	Facet unit	Trace vect	Dot produ	Angle			Facet unit	Trace vect	Dot produ	Angle			Facet unit	Trace vect	Dot produ	Angle
x	0.697	-0.39	-0.27183				0.697	0.169	0.117793			x	0.697	-0.087	-0.060639	
y	0.628	0.919	0.577132				0.628	-0.403	-0.25308			y	0.628	0.206	0.129368	
z	0.342	0.045	0.01539				0.342	0.899	0.307458			z	0.342	0.974	0.333108	
			0.320692	71.29528					0.172167	80.08623					0.401837	66.30699

Colorado Site 5

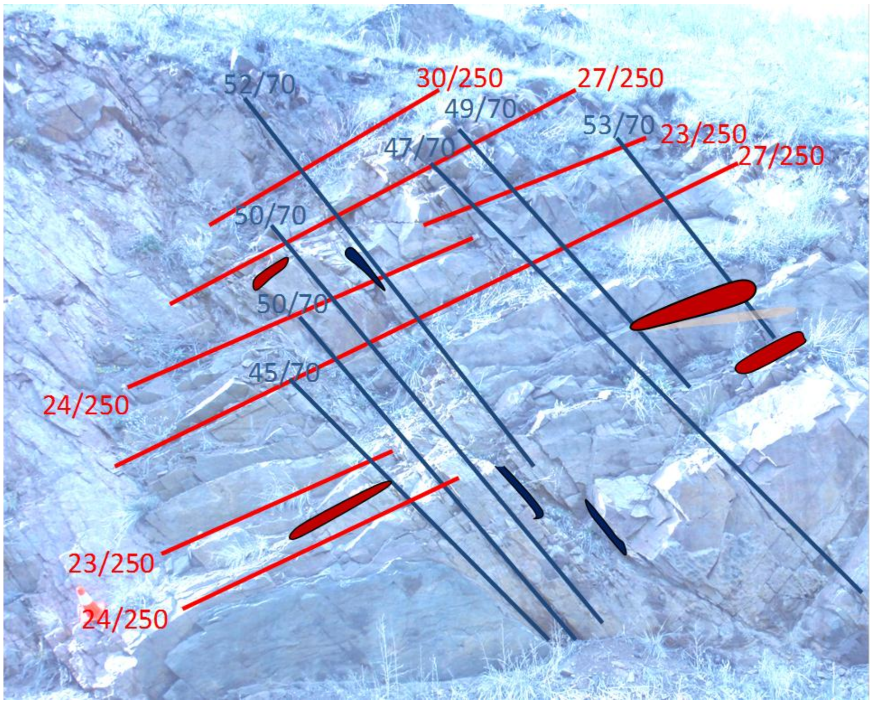

Figure A.11. Image of a rock cut in Colorado.

Table A.10. Plunge and Trend of defined traces from optical image

Plunge	Trend
24	250
23	250
27	250
24	250
23	250
27	250
30	250
45	70
50	70
50	70
52	70
47	70
49	70
53	70

Table A.11. Maen plunge and trend

Set	Plunge	Trend
Set 1	25	250
set 2	49	70

Table A. 12. Dip and Dip Direction of defined traces from field using the Brunton compass

Dip	Direction
43	67
56	76
51	65
48	70
52	71
52	70
54	73
25	256
24	252
26	251
25	252
24	252
26	251
29	252

Table A.13. Dip and dip directions of facets using the 3-point program

Facet	X	Y	Z	Dip	Direction
1	-4844.2	13339.4	-401.47	86	346
	-6174	13048.8	-1054.5		
	-4399.5	13495.3	-1001.5		
3	-980.94	14338.9	1243.94	80	346
	-1186.8	14363.5	820.18		
	-893.4	14450.1	737		
4	489.65	14726.6	1620.95	88	344
	-82.12	14629	1065.05		
	731.25	14876.2	1003.98		
5	1928.1	14627.2	448.54	82	345
	1417.06	14577.4	-112.46		
	1893.53	14672.6	93.12		
6	-2392.7	15437.1	4138.61	71	340
	-2889.8	15475.1	3524.97		
	-1309	15853.6	4081.37		
7	1173.82	15862.8	4421.55	76	345
	427.42	15815.8	3841.71		
	1409.01	16011.2	4097.89		
8	-1908.4	17381	6606.68	67	342
	-2496.8	17365.4	6204.02		
	-1713.8	17549.6	6365.01		
9	-826.09	15874.7	4146.17	25	208
	-1125.1	15441.4	3906.1		
	33	15781.6	4294.93		
10	-7609.3	13958.3	1270.47	27	222
	-7802.5	13781.7	1138.79		
	-7381.8	13892.6	1322.05		
11	-5362.6	13702.6	1063.5	39	209
	-5500.5	13610.6	942.26		
	-5265.5	13668.9	1077.81		
12	-7510.7	14010.9	1327.65	27	226
	-7614.7	13835.1	1226.25		
	-7320.3	13910.2	1362.37		
13	-3385.4	13792.3	489.85	46	85
	-3143.2	13834.9	240.3		
	-3301	13969.7	388.29		

Table A.14. Mean dip and dip directions of facets using the 3-point program

Set	Dip	Direction
Set 1	46	85
Set 2	29	215
Set 3	79	344

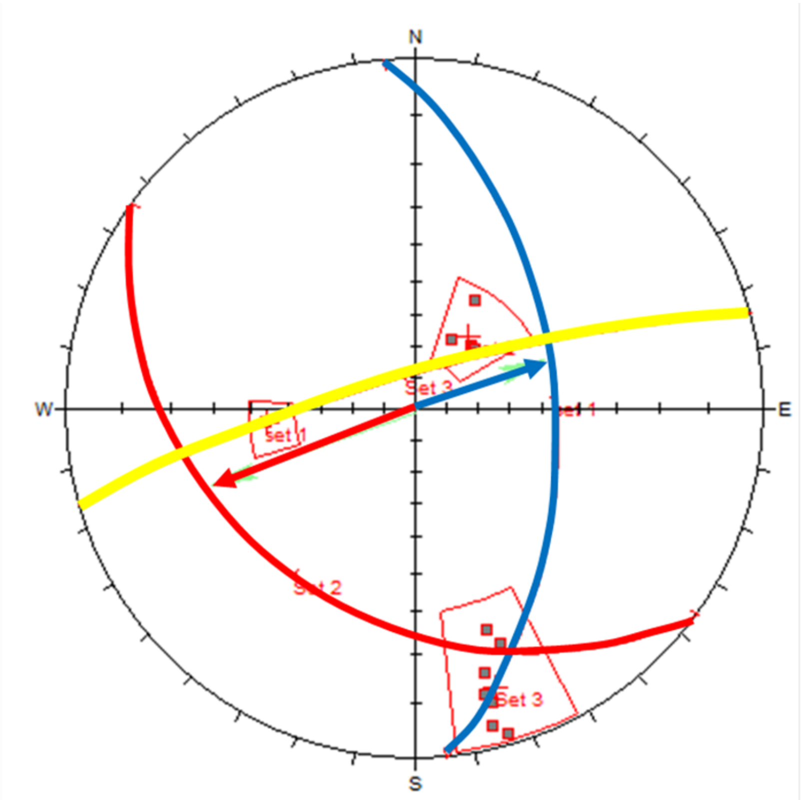

Figure A.12. Trace vectors (arrows) and great circles of Figure A.11.

USING COS PRODUCT of FACET UNIT NORMAL VECTOR AND TRACE VECTOR

Set 1 (blue)

Facet unit normal

Trend (α) = 85 + 180

= 265

Plunge (β) = 90 – 46

= 44

Ux = Cos 265 x Cos 44

= -0.063

Uy = Sin 265 x Cos 44

= -0.716

Uz = Sin 44

= 0.694

Trace vector

Ux = Cos 70 x Cos 49

= 0.224

Uy = Sin 70 x Cos 49

= 0.616

Uz = Sin 49

= 0.755

COS PRODUCT

$$\theta = \cos^{-1}(T.F)$$

$$\theta = 86^{o}$$

86^{o} is close to 90.

Set 2 (Green)

Facet unit normal

Trend (α) = 215 + 180

= 35

Plunge (β) = 90 – 29

= 61

Ux = Cos 35 x Cos 61

= 0.396

Uy = Sin 35 x Cos 61

= 0.277

Uz = Sin 61

= 0.874

Trace vector

Ux = Cos 250 x Cos 25

= -0.309

Uy = Sin 250 x Cos 25

= -0.850

Uz = Sin 25

= 0.423

COS PRODUCT

$$\theta = \cos^{-1}(T.F)$$

$$\theta = 89^{o}$$

Table A.15. Summary of Angles (from dot products) of the trace vectors and facet unit normals

	Traces	
Facets	Set 1	Set 2
	(Blue)	(Green)
Set 1 (Blue)	86	23
Set 2 (Green)	23	89
Set 3 (Yellow)	103	53

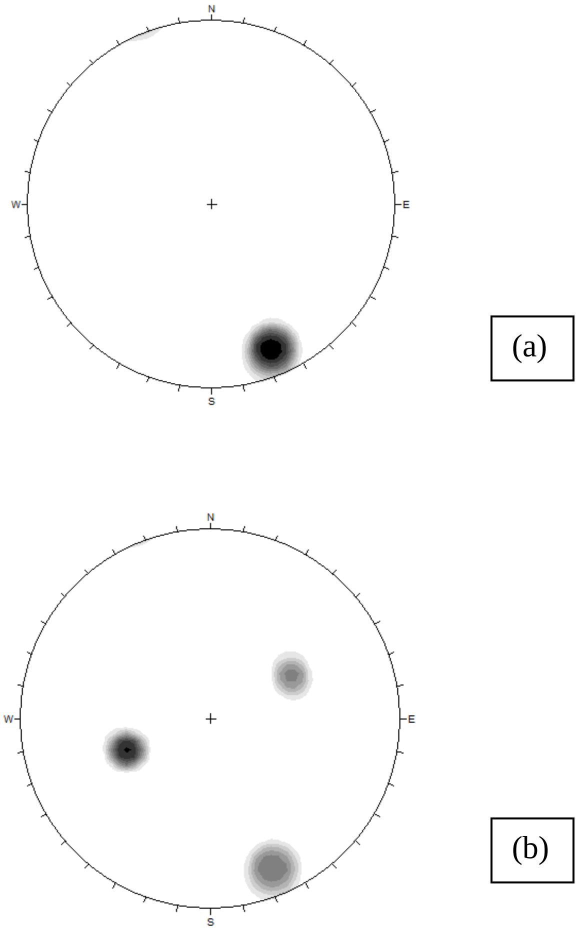

Figure A.13. (a) Contour plot of facets, (b) Contour plot of facets and traces.

Table A.16. Spreadsheet showing the dot products of the facets and traces in Figure A.13

	Set 1 Blue						Set 1 Blue Facet vs Set 2 Green Trace			
	Facet unit	Trace vector	Dot product	Angle			Facet unit	Trace vect	Dot produ	Angle
x	-0.063	0.224	-0.014112			x	-0.063	-0.309	0.019467	
y	-0.716	0.616	-0.441056			y	-0.716	-0.85	0.6086	
z	0.694	0.755	0.52397			z	0.694	0.423	0.293562	
			0.068802	86.05489					0.921629	22.83461
	Set 2 Green						Set 2 Green Facet vs Set 1 Blue Trace			
	Facet unit	Trace vector	Dot product	Angle			Facet unit	Trace vect	Dot produ	Angle
x	0.396	-0.309	-0.122364			x	0.396	0.224	0.088704	
y	0.277	-0.85	-0.23545			y	0.277	0.616	0.170632	
z	0.874	0.423	0.369702			z	0.874	0.755	0.65987	
			0.011888	89.31893					0.919206	23.18974
	Set 3 Yellow vrs Blue trace						Set 3 Yellow Facet vs Set 1 Green Trace			
	Facet unit	Trace vector	Dot product	Angle			Facet unit	Trace vect	Dot produ	Angle
x	-0.942	0.224	-0.211008			x	-0.942	-0.309	0.291078	
y	-0.269	0.616	-0.165704			y	-0.269	-0.85	0.22865	
z	0.19	0.755	0.14345			z	0.19	0.423	0.08037	
			-0.233262	103.4893					0.600098	53.12313

Colorado Site 6

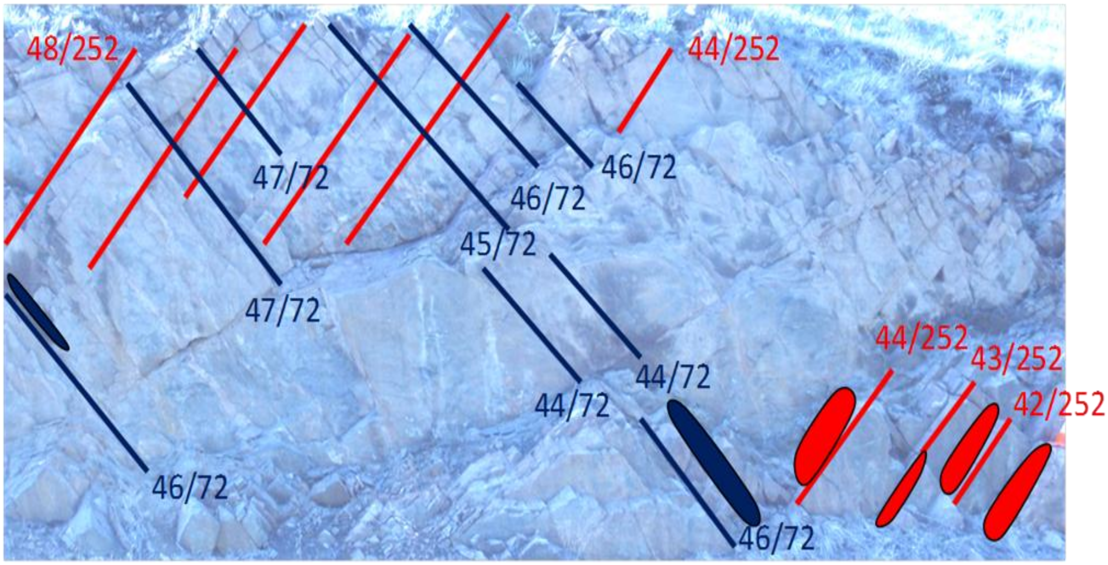

Figure A.14. Image of a rock cut in Colorado.

Table A.15. Plunge and Trend of traces from optical image

Plunge	Trend
42	252
43	252
44	252
44	252
46	252
45	252
46	252
47	252
48	252
46	72
47	72
47	72
45	72
46	72
46	72
44	72
44	72
46	72

Table A.16. Mean Plunge and Trend of traces from optical image

Set	Plunge	Trend
Set 1	45	252
Set 2	46	72

Table A.17. Dip and Dip Directions of facets using the 3-point program

Facets	X	Y	Z	Dip	Direction
4	-5460.6	14261.7	-566.59	71	343
	-5280	14330.2	-720.68		
	-5628	14296.1	-704.86		
8	-6150.9	14567.1	47.28	68	340
	-6503.8	14631.4	-238.45		
	-6031.2	14744.6	-357.01		
5	-4007.8	14506.3	-511.91	69	342
	-4230.3	14550.2	-686.5		
	-3922.7	14575.4	-664.71		
21	-5369.3	14427	-449.1	84	259
	-5381.9	14283.7	-536.93		
	-5256.5	14416.2	-589.92		
22	5498.94	16015.9	552.72	53	233
	5011.84	16204.4	77.02		
	5222.85	15761.9	86.01		
23	7695.07	15924	147.01	55	232
	7257.57	16020.8	-348.01		
	7481.33	15833.3	-182.06		
24	8325.32	15805.3	-114.98	59	227
	7990.72	15912.1	-506.94		
	8158.44	15744.5	-410.01		
25	6552.83	16062.6	-146	52	230
	6091.73	15963.5	-725.78		
	6388.89	15844.7	-463.16		
26	-5417.7	14433	-376.53	55	111
	-5357.3	14305	-546.26		
	-5260	14426.1	-569.89		
27	648.27	15078.1	205.33	15	90
	2094.63	15045	-172.49		
	2117.06	15131.5	-173.53		
28	1054.73	15245.6	545.64	61	5
	2293.92	15136.6	73.35		
	583.41	15480.3	387.08		
29	3550.5	15689.1	224.72	87	201
	3654.16	15616.3	137.98		
	3511.36	15712.6	192.84		
30	-3890.1	15234.5	3406.85	53	86
	-3613.9	15247.5	3046.3		
	-3736.1	15444.7	3243.93		
31	-3403.6	15554.2	2819.12	55	83
	-3182.8	15477.7	2493.63		
	-3226.2	15690.3	2583.95		

Table A.18. Mean Plunge and Trend of facets from 3-point program

Set	Dip	Direction
Set 1	54	84
Set 2	53	231
Set 3	69	341

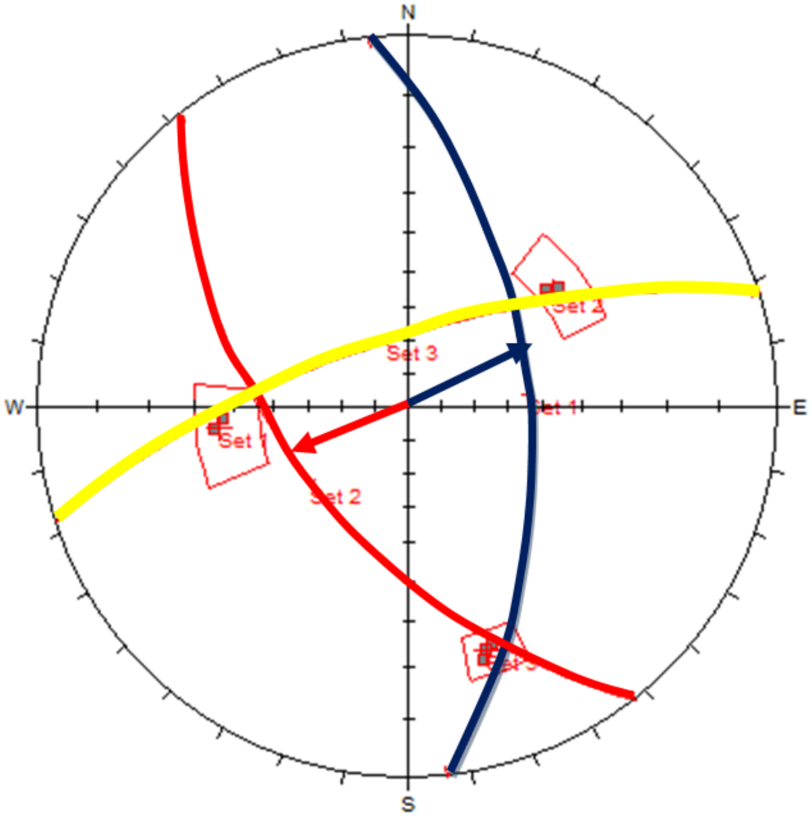

Figure A.15. Trace vectors (arrows) and great circles of Figure A.13.

USING COS PRODUCT of FACET UNIT NORMAL VECTOR AND TRACE VECTOR

Set 1 (blue)

Facet unit normal

Trend (α) = 84 + 180

= 264

Plunge (β) = 90 – 54

= 36

Ux = Cos 264 x Cos 36

= -0.085

Uy = Sin 264 x Cos 36

= -0.804

Uz = Sin 36

= 0.588

Trace vector

Ux = Cos 72 x Cos 46

= 0.215

Uy = Sin 72 x Cos 46

= 0.661

Uz = Sin 46

= 0.719

COS PRODUCT

$$\theta = \cos^{-1}(T.F)$$

$$\theta = 97$$

Set 2 (Green)

Facet unit normal

Trend (α) = 231 + 180

= 51

Plunge (β) = 90 – 53

= 37

Ux = Cos 51 x Cos 37

= 0.502

Uy = Sin 51 x Cos 37

= 0.621

Uz = Sin 37

= 0.602

Trace vector

Ux = Cos 252 x Cos 45

= -0.218

Uy = Sin 252 x Cos 45

= -0.672

Uz = Sin 45

= 0.707

COS PRODUCT

$$\theta = \cos^{-1}(T.F)$$

$$\theta = 96^{o}$$

Table A.19. Summary of Angles (from dot products) of the trace vectors and facet unit normals

	Traces	
Facets	Set 1	Set 2
	(Blue)	(Green)
Set 1 (Blue)	97	13
Set 2 (Green)	18	96
Set 3 (Yellow)	74	80

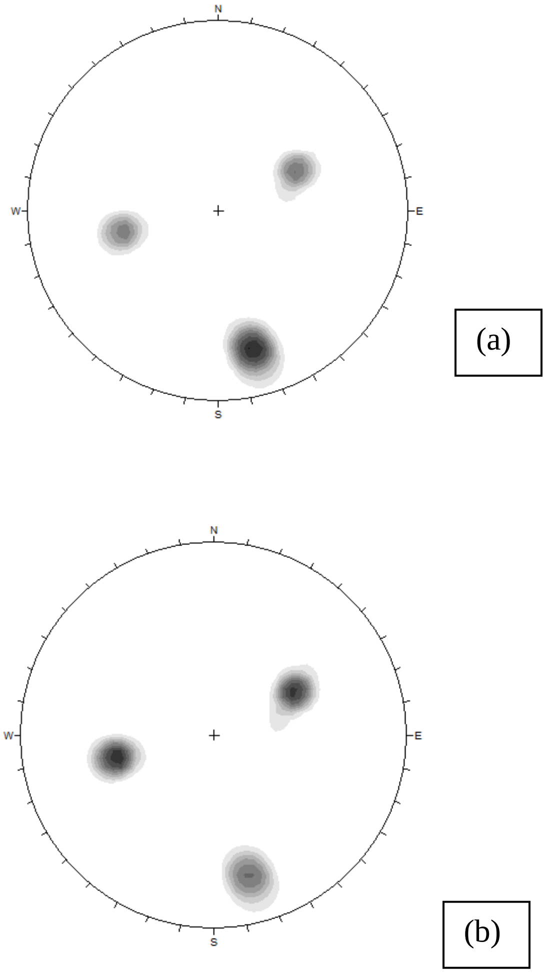

Figure A.16. (a) Contour plot of facets, (b) Contour plot of facets and traces.

Table A.20. Spreadsheet showing the dot products of the facets and traces in Figure A.15

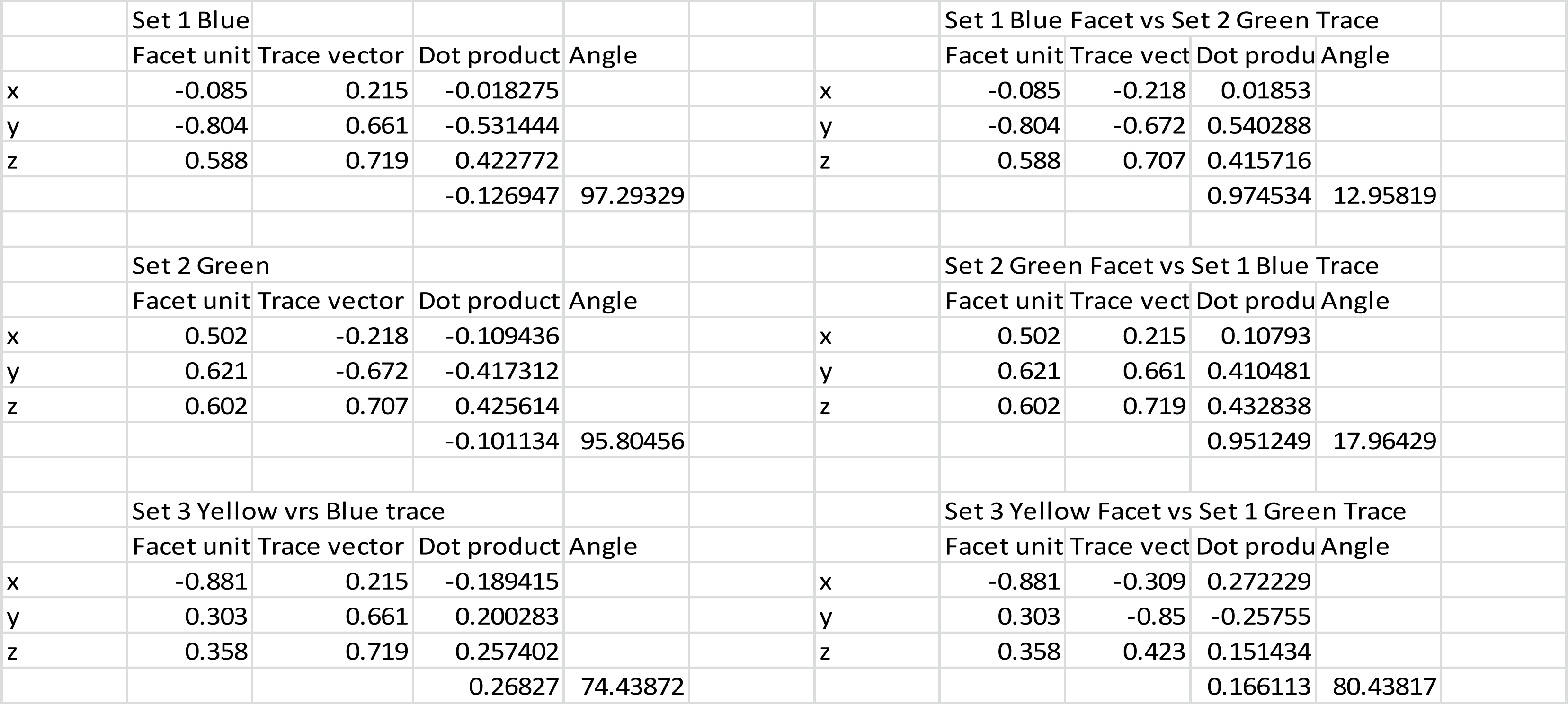

	Set 1 Blue						Set 1 Blue Facet vs Set 2 Green Trace				
	Facet unit	Trace vector	Dot product	Angle			Facet unit	Trace vect	Dot produ	Angle	
x	-0.085	0.215	-0.018275			x	-0.085	-0.218	0.01853		
y	-0.804	0.661	-0.531444			y	-0.804	-0.672	0.540288		
z	0.588	0.719	0.422772			z	0.588	0.707	0.415716		
			-0.126947	97.29329					0.974534	12.95819	
	Set 2 Green						Set 2 Green Facet vs Set 1 Blue Trace				
	Facet unit	Trace vector	Dot product	Angle			Facet unit	Trace vect	Dot produ	Angle	
x	0.502	-0.218	-0.109436			x	0.502	0.215	0.10793		
y	0.621	-0.672	-0.417312			y	0.621	0.661	0.410481		
z	0.602	0.707	0.425614			z	0.602	0.719	0.432838		
			-0.101134	95.80456					0.951249	17.96429	
	Set 3 Yellow vrs Blue trace						Set 3 Yellow Facet vs Set 1 Green Trace				
	Facet unit	Trace vector	Dot product	Angle			Facet unit	Trace vect	Dot produ	Angle	
x	-0.881	0.215	-0.189415			x	-0.881	-0.309	0.272229		
y	0.303	0.661	0.200283			y	0.303	-0.85	-0.25755		
z	0.358	0.719	0.257402			z	0.358	0.423	0.151434		
			0.26827	74.43872					0.166113	80.43817	

Non-Vertical face

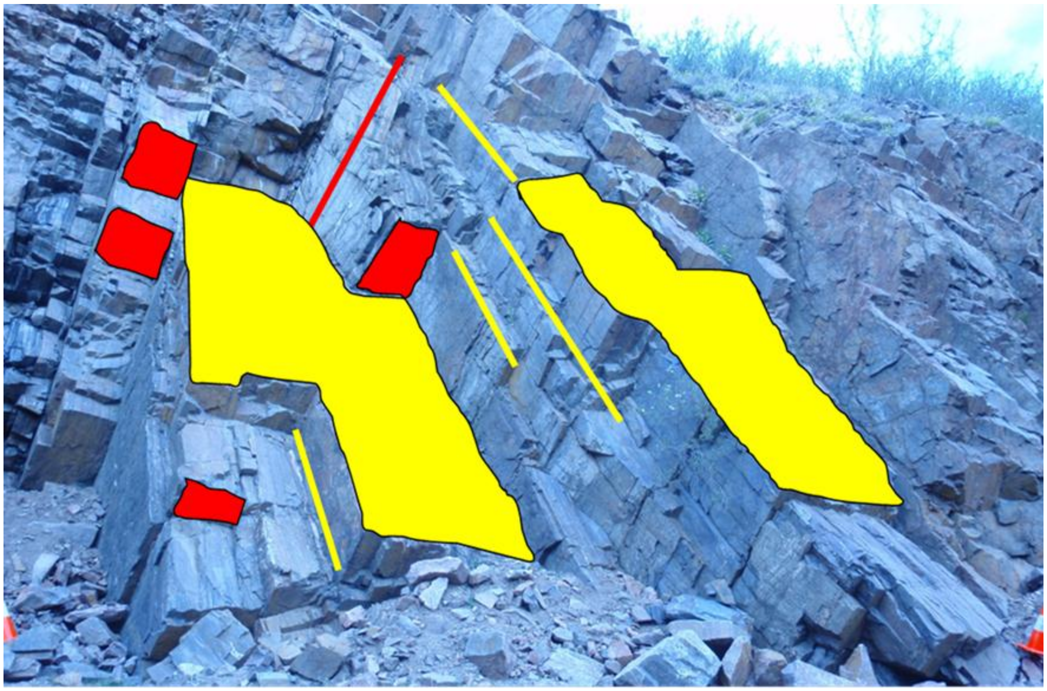

Figure A.17. Non-vertical rock face showing a trace (red line) and facets (red rectangles) belonging to the same set.

The unit normal perpendicular to the joint plane of the red trace is given by;

Ux = Sin 34 x Sin 248 = -0.518

Uy = Sin 34 x Cos 248 = -0.209

Uz = Cos 34 = 0.829

The unit normal perpendicular to the rock face is given by:

Ux = Sin 38 x Sin 246 = -0.561

Uy = Sin 38 x Cos 246 = -0.153

Uz = Cos 38 = 0.788

The red trace vector can be obtained from the cross product of the unit normal perpendicular to the joint plane and the unit normal perpendicular to the rock face.

Thus, Trace vector = (-0.126 + 0.164), (-0.408 + 0.465), (0.117-0.031)

= (0.038, 0.057, 0.086)

Thus,

$U_x = 0.038$

$U_y = 0.057$

$U_z = 0.086$

Calculating the trend and plunge from the trace vector;

Trend (α) = arctan (0.057/0.038) = 56°

Plunge (β) = arctan (0.086/0.067) = 52°

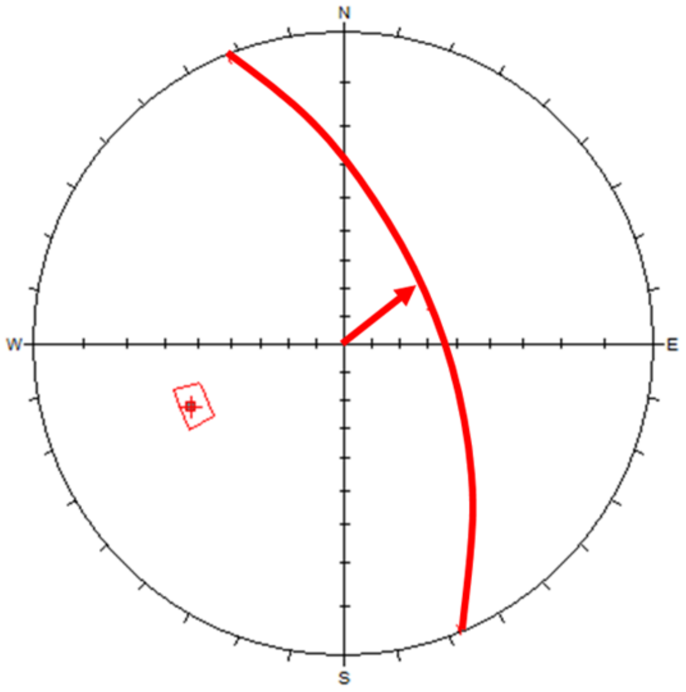

Figure A.18. Red trace vector (arrows) intersects great circle of facet on a stereonet.

Facet Unit normal

Ux = Cos 248 x Cos 34 = -0.310

Uy = Sin 248 x Cos 34 = -0.768

Uz = Sin 34 = 0.559

COS PRODUCT

$$\theta = \cos^{-1}(T.F)$$

$$\theta = 90.42^{\circ} \text{ (good)}$$

The unit normal perpendicular to the joint plane of the yellow trace is given by;

Ux = Sin 39 x Sin 242 = - 0.554

Uy = Sin 39 x Cos 242 = - 0.295

Uz = Cos 34 = 0.777

The unit normal perpendicular to the rock face is given by:

Ux = Sin 38 x Sin 246 = - 0.561

Uy = Sin 38 x Cos 246 = - 0.153

Uz = Cos 38 = 0.788

The red trace vector can be obtained from the cross product of the unit normal perpendicular to the joint plane and the unit normal perpendicular to the rock face.

Thus, Trace vector = (- 0.118 + 0.232), (- 0.344 + 0.244), (0.165 - 0.084)

= (0.114, - 0.1, 0.081)

Thus,

Ux = 0.114

Uy = - 0.1

Uz = 0.081

Calculating the trend and plunge from the trace vector;

Trend (α) = arctan (- 0.1/0.114) + 360^0 = 56°

Plunge (β) = arctan (0.081/0.151) = 28°

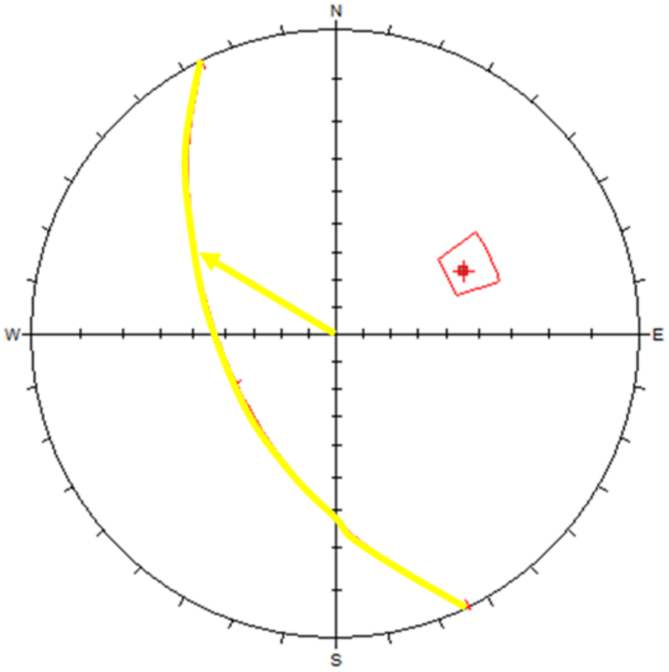

Figure A.19. Yellow trace vector (arrows) intersects great circle of facet on a stereonet.

Facet Unit normal

Ux = Cos 64 x Cos 40 = 0.335

Uy = Sin 64 x Cos 40 = 0.687

Uz = Sin 40 = 0.642

COS PRODUCT

$$\theta = \cos^{-1}(T.F)$$

$\theta = 89^{\circ}$ (good)

Table A.19. Summary of Angles (from dot products) of the trace vectors and facet unit normals

	Traces	
Facet	Set 1	Set 2
Set 1	90	35
Set 2	52	89

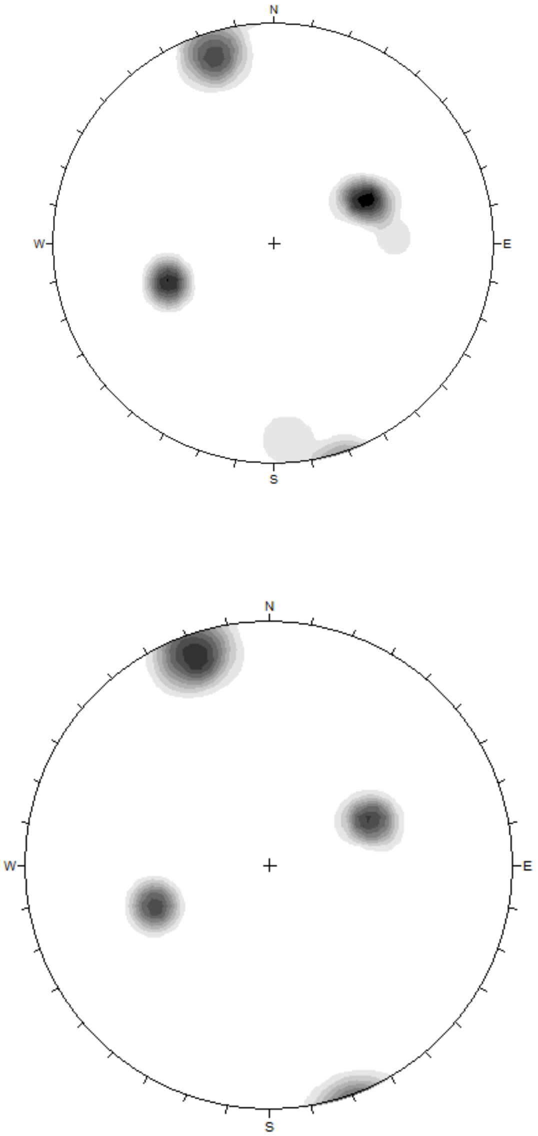

Figure A.18. (a) Contour plot of facets, (b) Contour plot of facets and traces.

APPENDIX B
(MAPS, OPTICAL AND LIDAR IMAGES, CONTOURS, AND FIELD DATA)

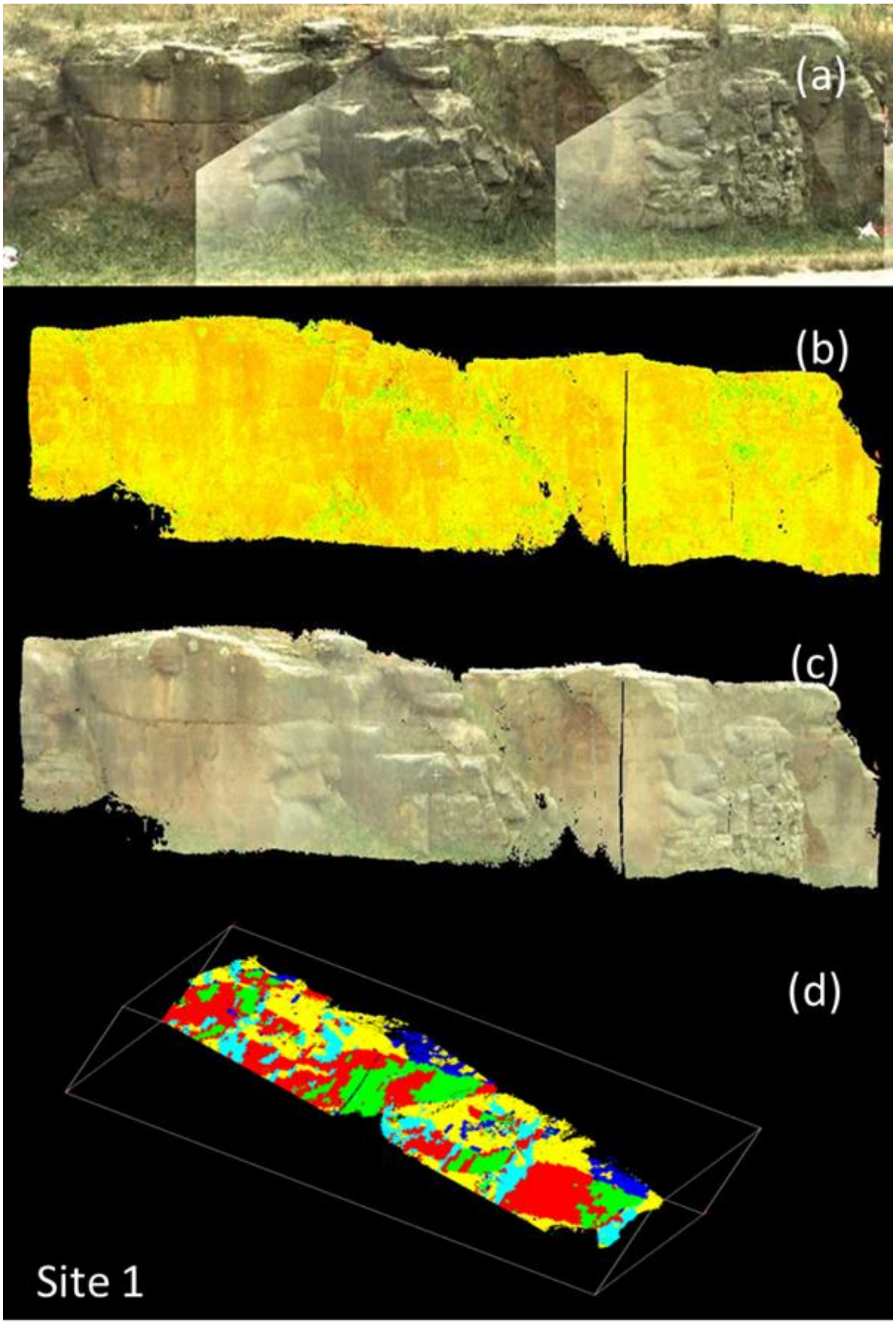

Figure B.1. Discontinuity orientation measurement for a site in Rolla, MO. (a) Optical image from LiDAR scanner, (b) point cloud data, (c) point cloud data viewed with natural colors from scanner (d) discontinuity orientation map, different colors represent different orientations.

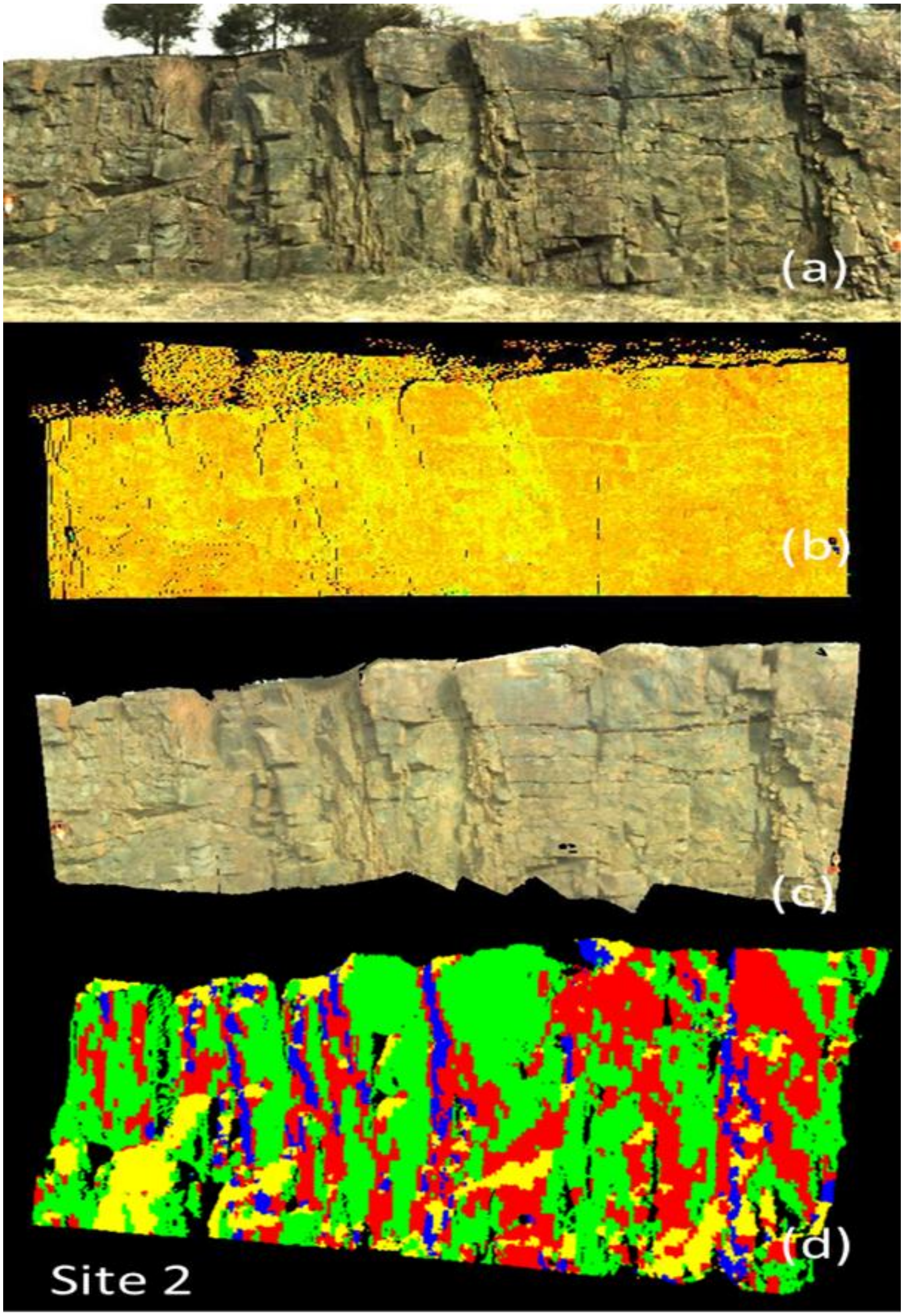

Figure B.2. Discontinuity orientation measurement for a site in Ironton, MO. (a) Optical image from LiDAR scanner, (b) point cloud data, (c) point cloud data viewed with natural colors from scanner (d) discontinuity orientation map, different colors represent different orientations.

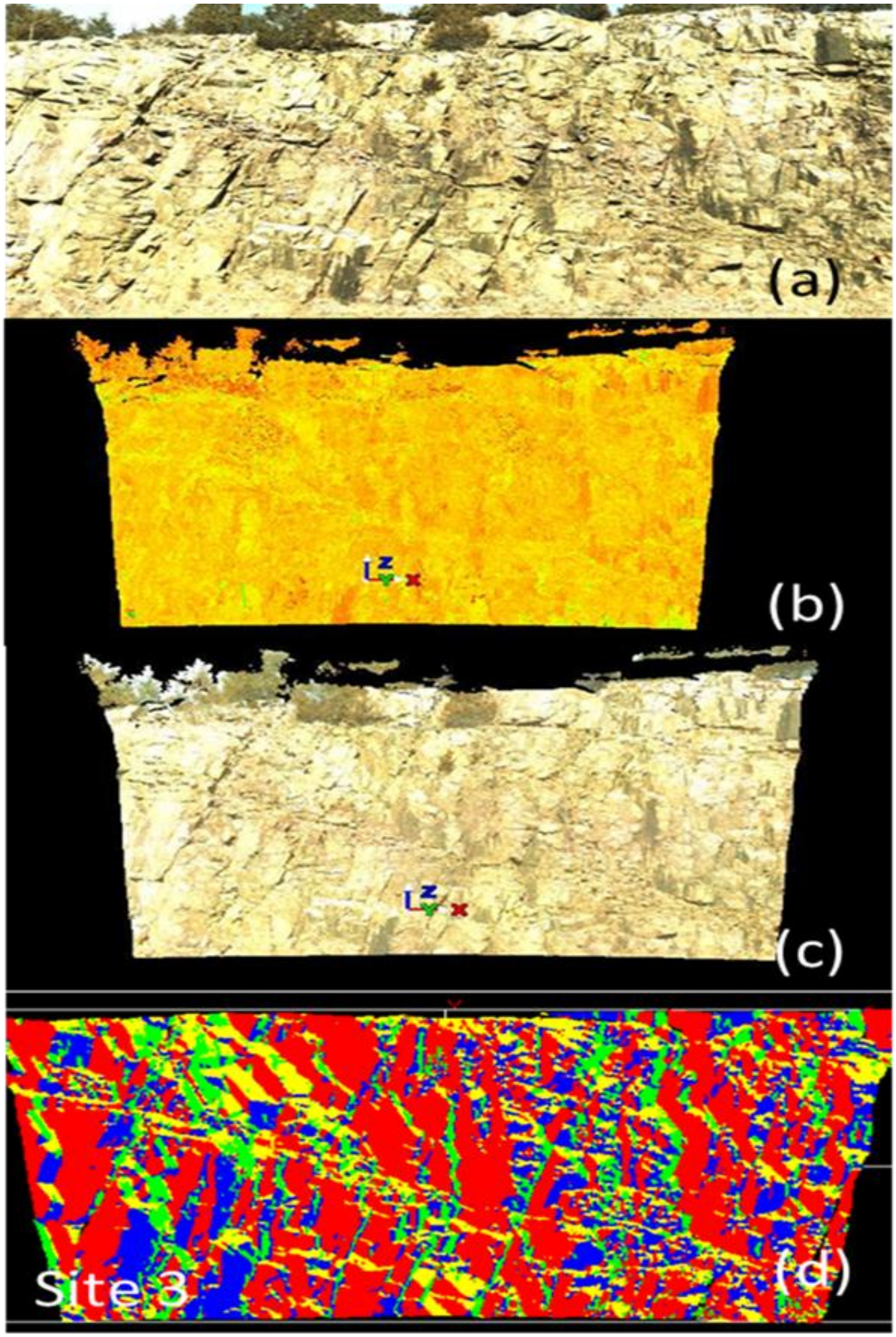

Figure B.3. Discontinuity orientation measurement for a site in Ironton, MO. (a) Optical image from LiDAR scanner, (b) point cloud data, (c) point cloud data viewed with natural colors from scanner (d) discontinuity orientation map, different colors represent different orientations.

Figure B.4. Point cloud data of a site in Rolla. This data consists of over 2 million points.

Table A.1. First 10 lines of the PTS file of the point cloud data of Figure B.4. Each line represents a point. Thus, the PTS file has over 2 million lines

-3684.677124	-24224.960327	-3588.760376	-916	138	116	75
-3560.348511	-24059.921265	-3562.667847	-402	91	91	63
-3659.744263	-24061.447144	-3616.256714	-649	194	154	103
-3591.751099	-24271.530151	-3542.251587	-925	40	40	32
-3692.825317	-24278.518677	-3547.164917	-912	96	92	65
-3606.582642	-24371.475220	-3505.630493	-1040	43	38	16
-3671.340942	-24137.649536	-3679.763794	-990	244	164	117
-3705.123901	-24696.945190	-3291.915894	-998	83	81	56
-3765.762329	-24756.759644	-3251.174927	-758	105	100	68
-3689.712524	-24594.284058	-3328.933716	-964	79	73	59

Missouri Sites

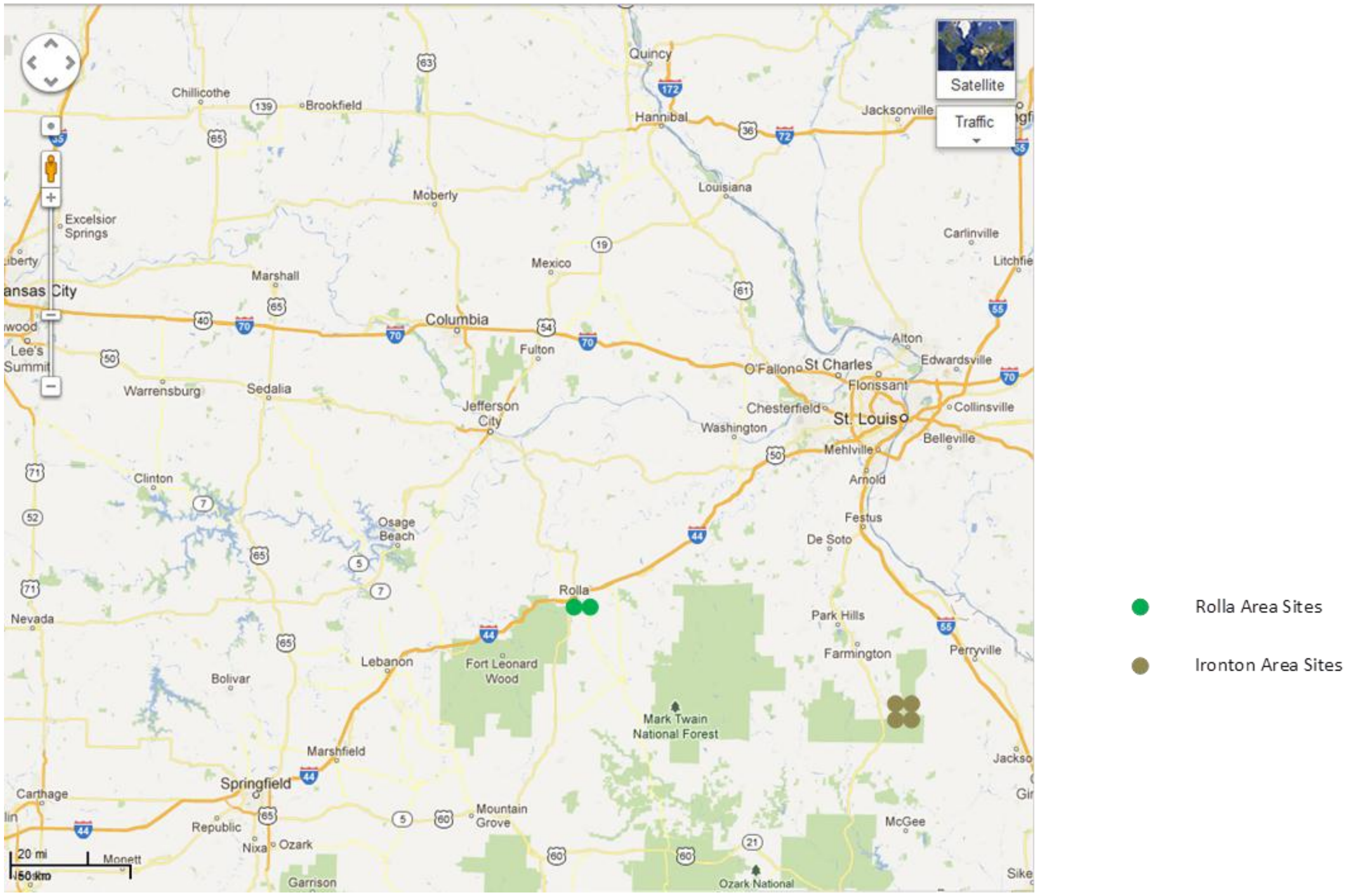

Figure B.5. Location map of Missouri sites with reference to St. Louis (Google maps, 2012).

Rolla Sites

Site 1

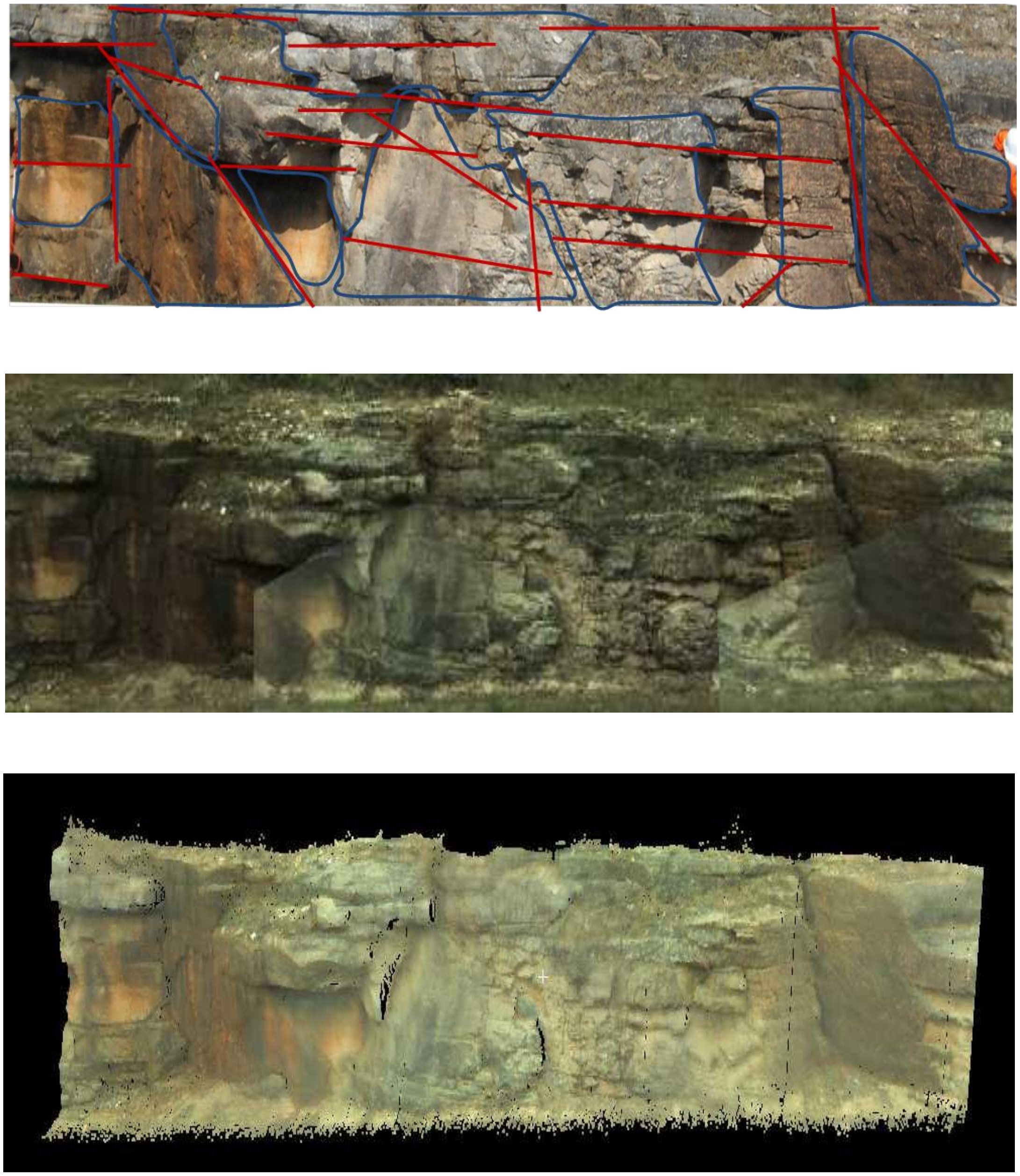

Figure B.6. (a) Manually prepared facets and traces map, red lines represent traces whereas blue polygons represents facets, (b) LiDAR optical image, and (b) LiDAR point cloud of Rolla Site 1.

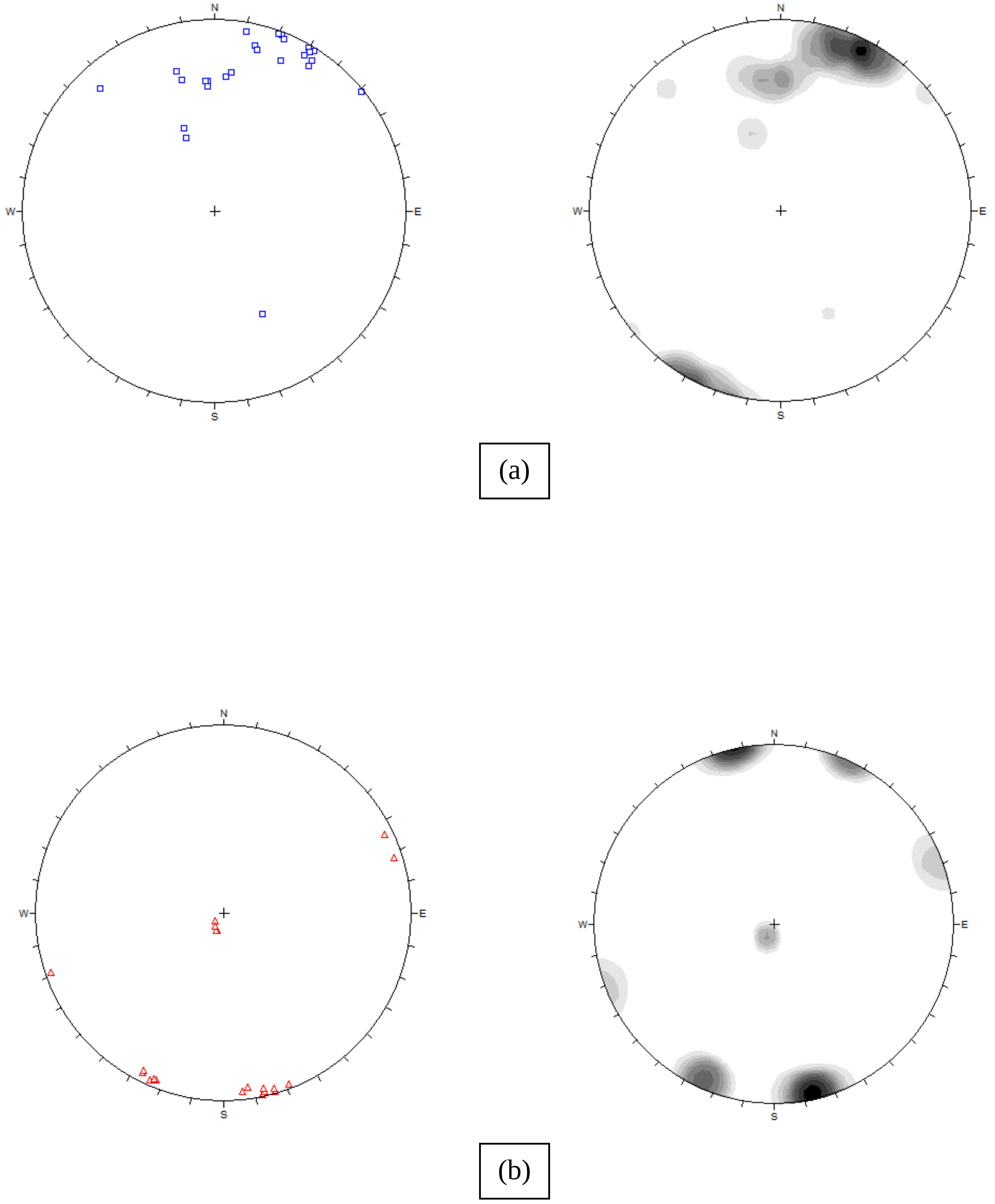

Figure B.7. (a) Poles and corresponding contour of manually measured facets, (b) Poles and corresponding contour of manually measured traces, of Rolla Site 1.

Site 2

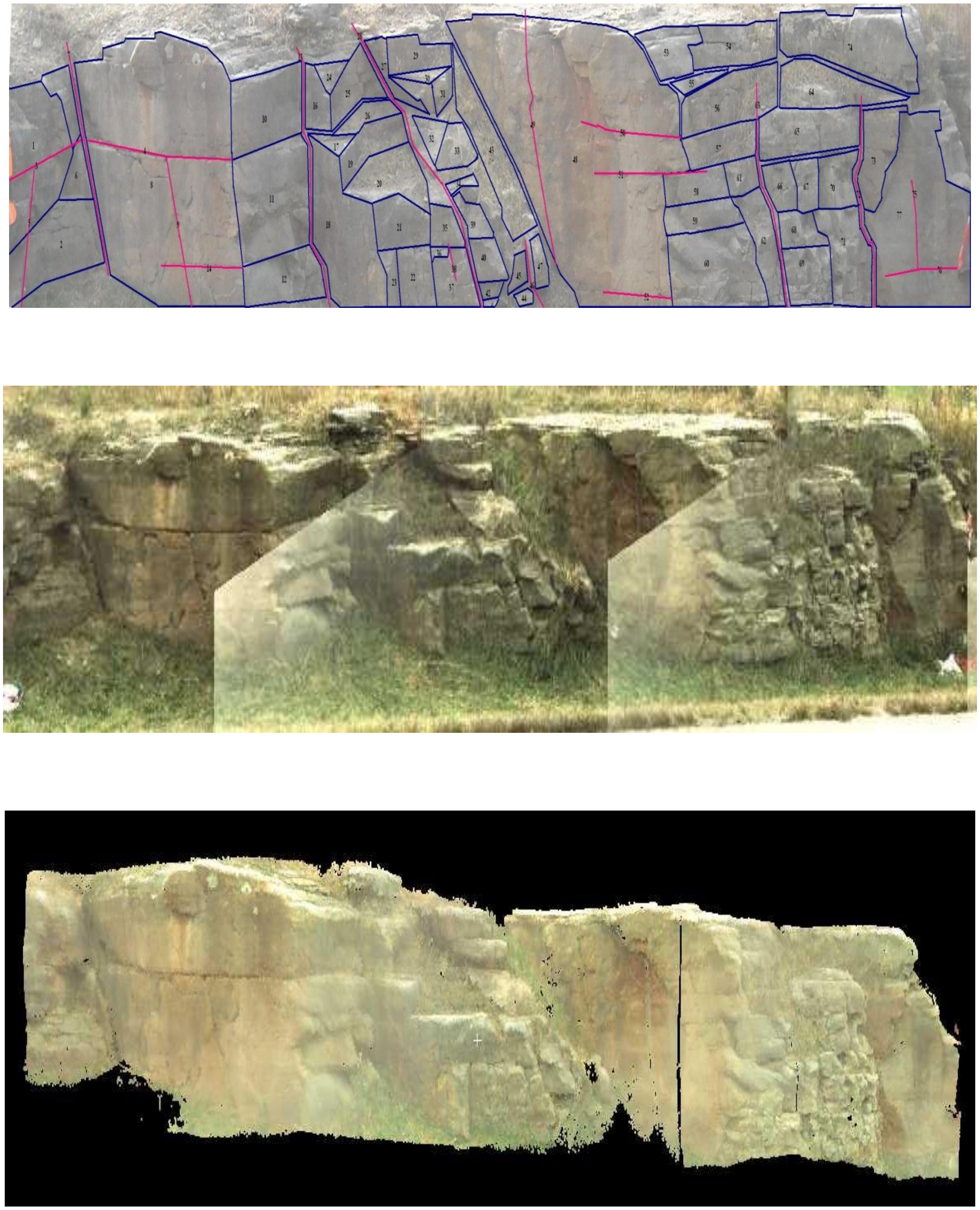

Figure B.8. (a) Manually prepared facets and traces map, red lines represent traces whereas blue polygons represents facets, (b) LiDAR optical image, and (b) LiDAR point cloud of Rolla Site 2.

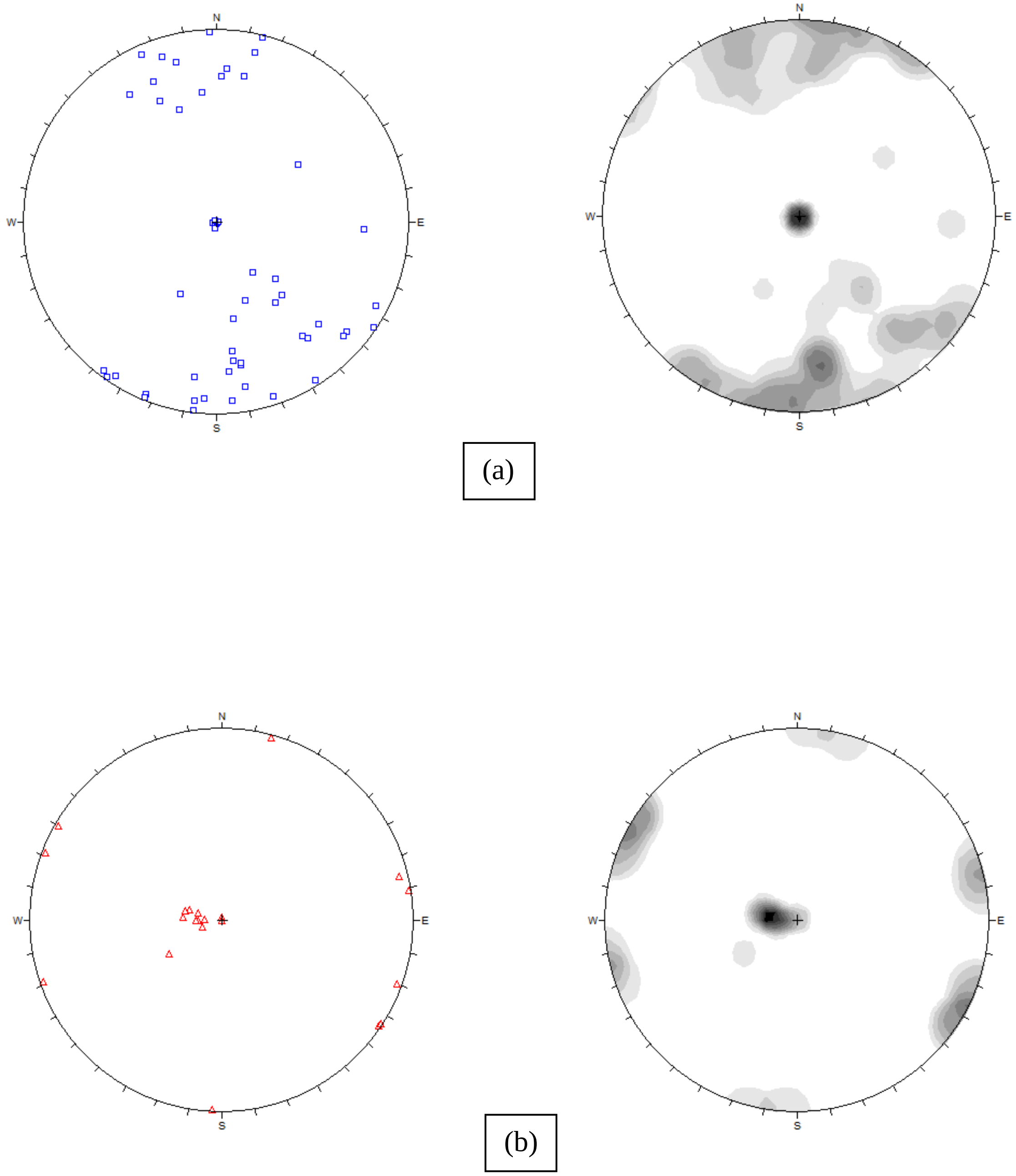

Figure B.9. (a) Poles and corresponding contour of manually measured facets, (b) Poles and corresponding contour of manually measured traces, of Rolla Site 2.

Southeast Missouri Sites

Site 1

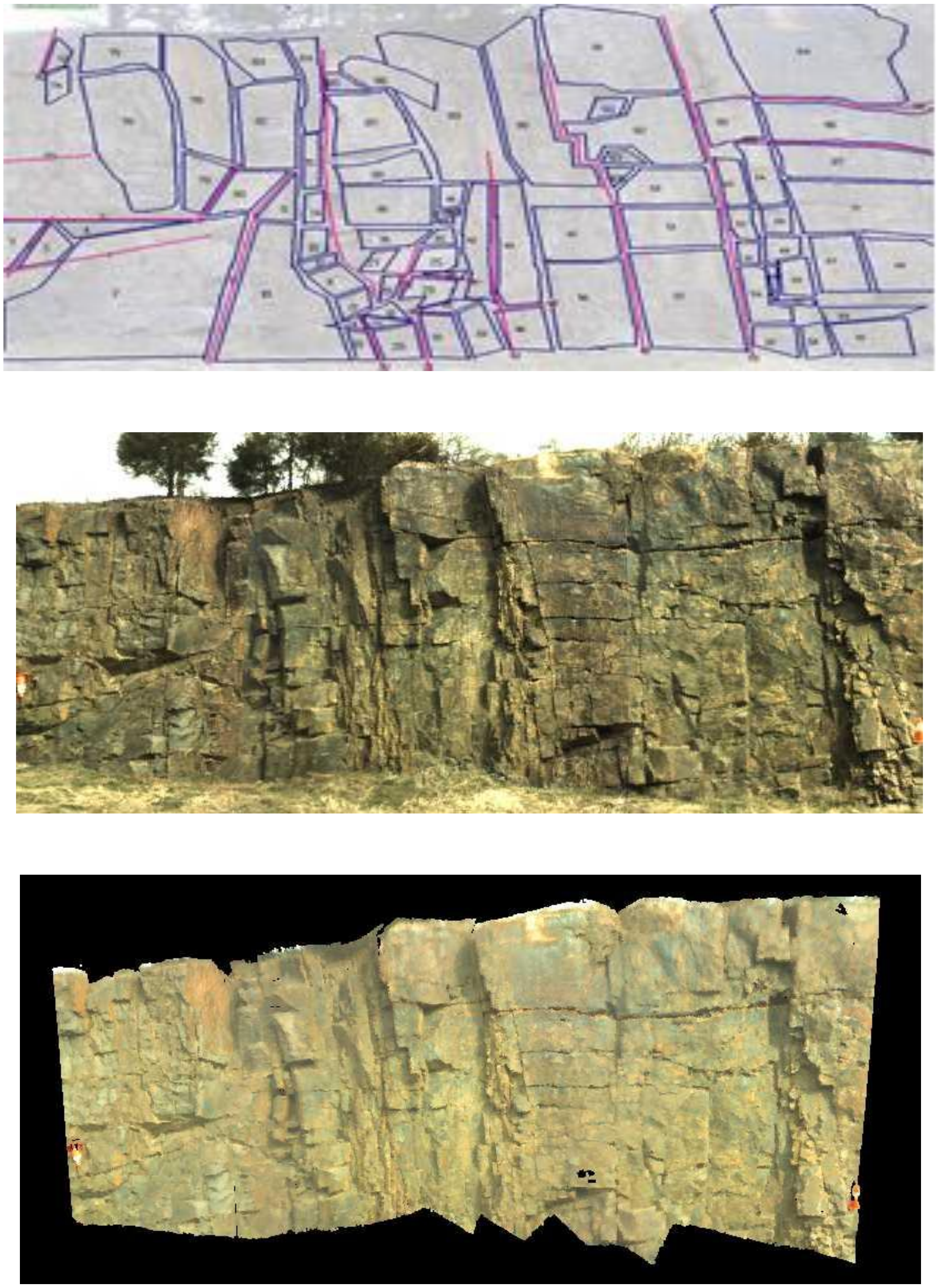

Figure B.10. (a) Manually prepared facets and traces map, red lines represent traces whereas blue polygons represents facets, (b) LiDAR optical image, and (b) LiDAR point cloud of Southeast Missouri Site 1.

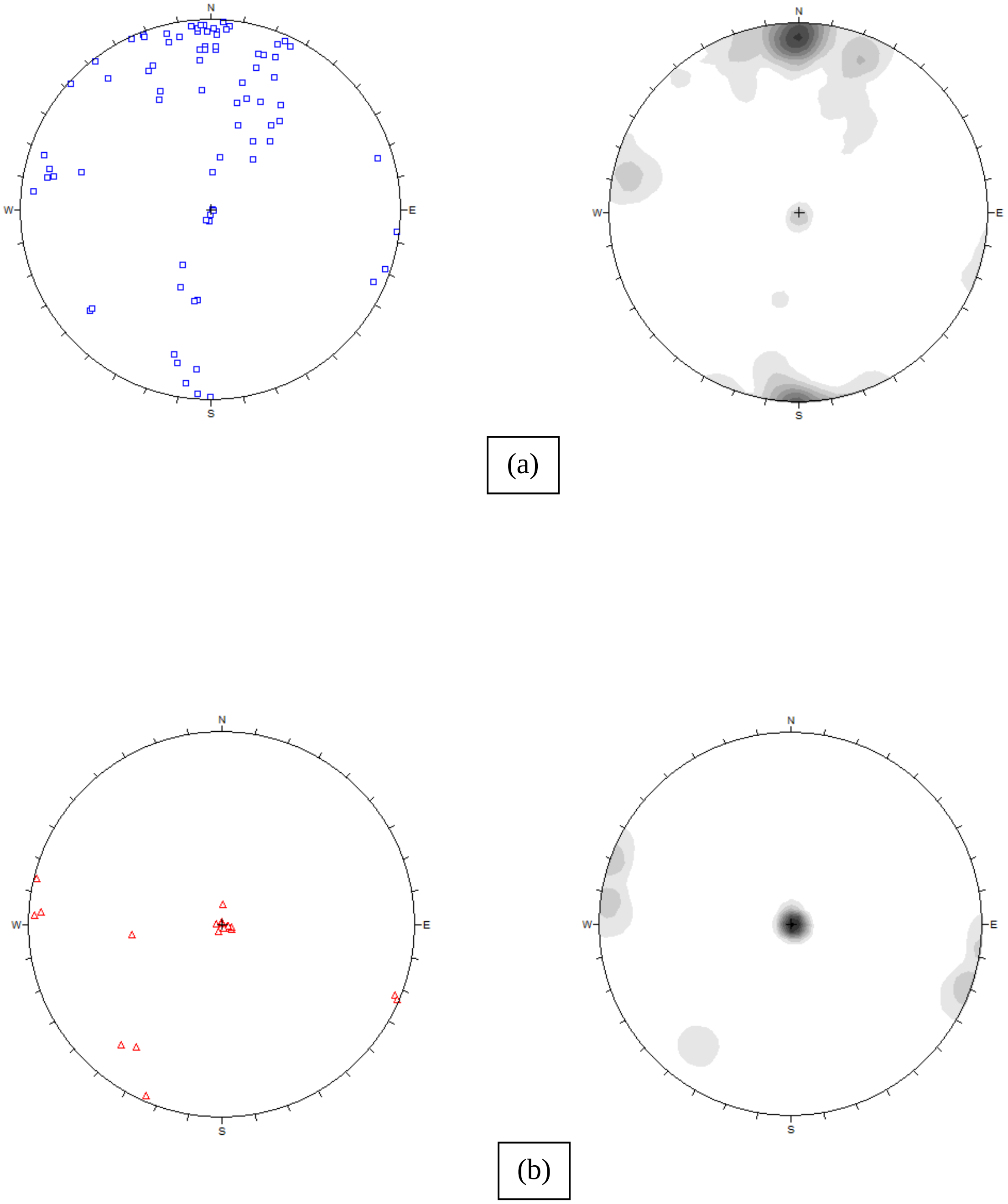

Figure B.11. (a) Poles and corresponding contour of manually measured facets, (b) Poles and corresponding contour of manually measured traces, of Southeast Missouri Site 1.

Site 2

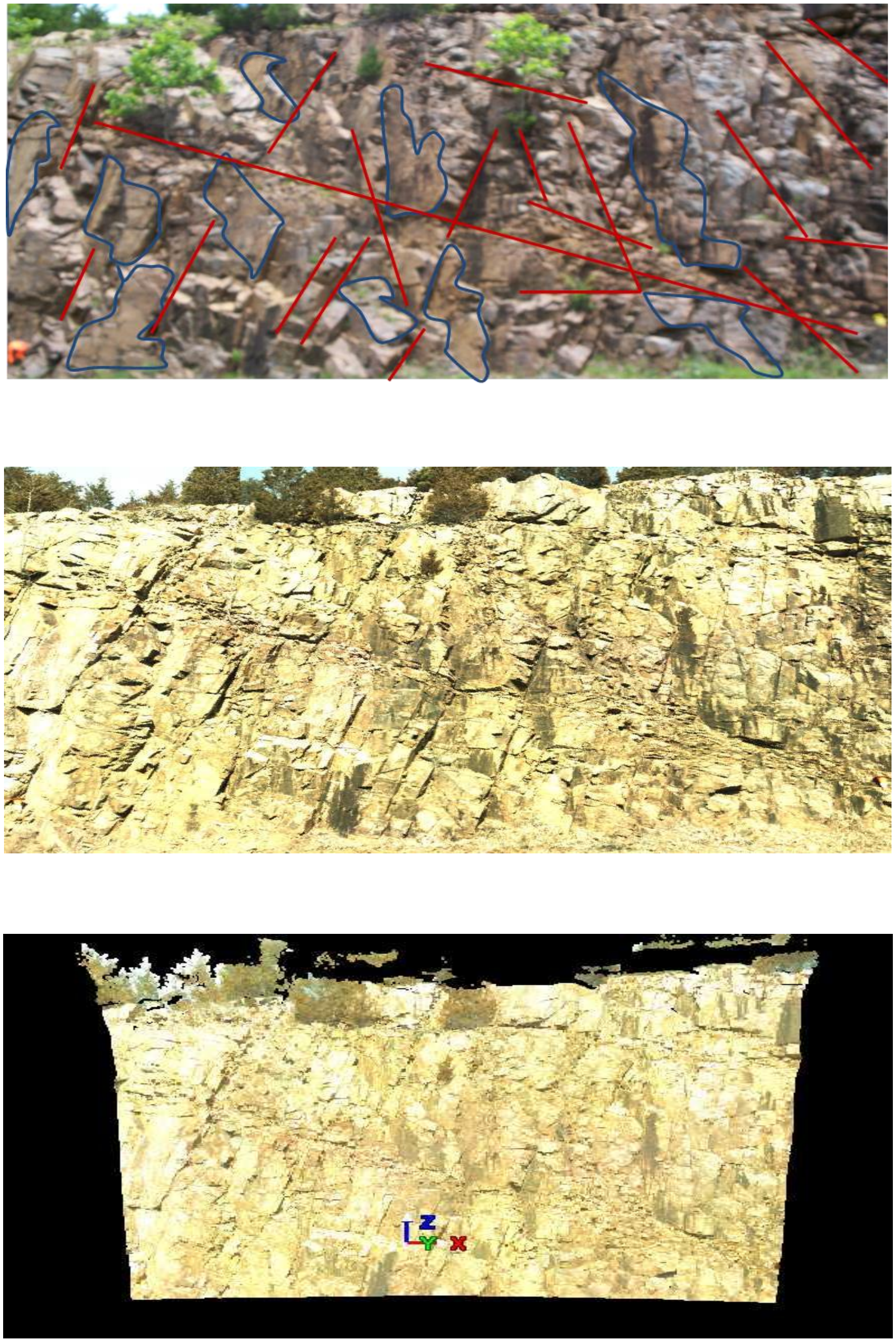

Figure B.12. (a) Manually prepared facets and traces map, red lines represent traces whereas blue polygons represents facets, (b) LiDAR optical image, and (b) LiDAR point cloud of Southeast Missouri Site 2.

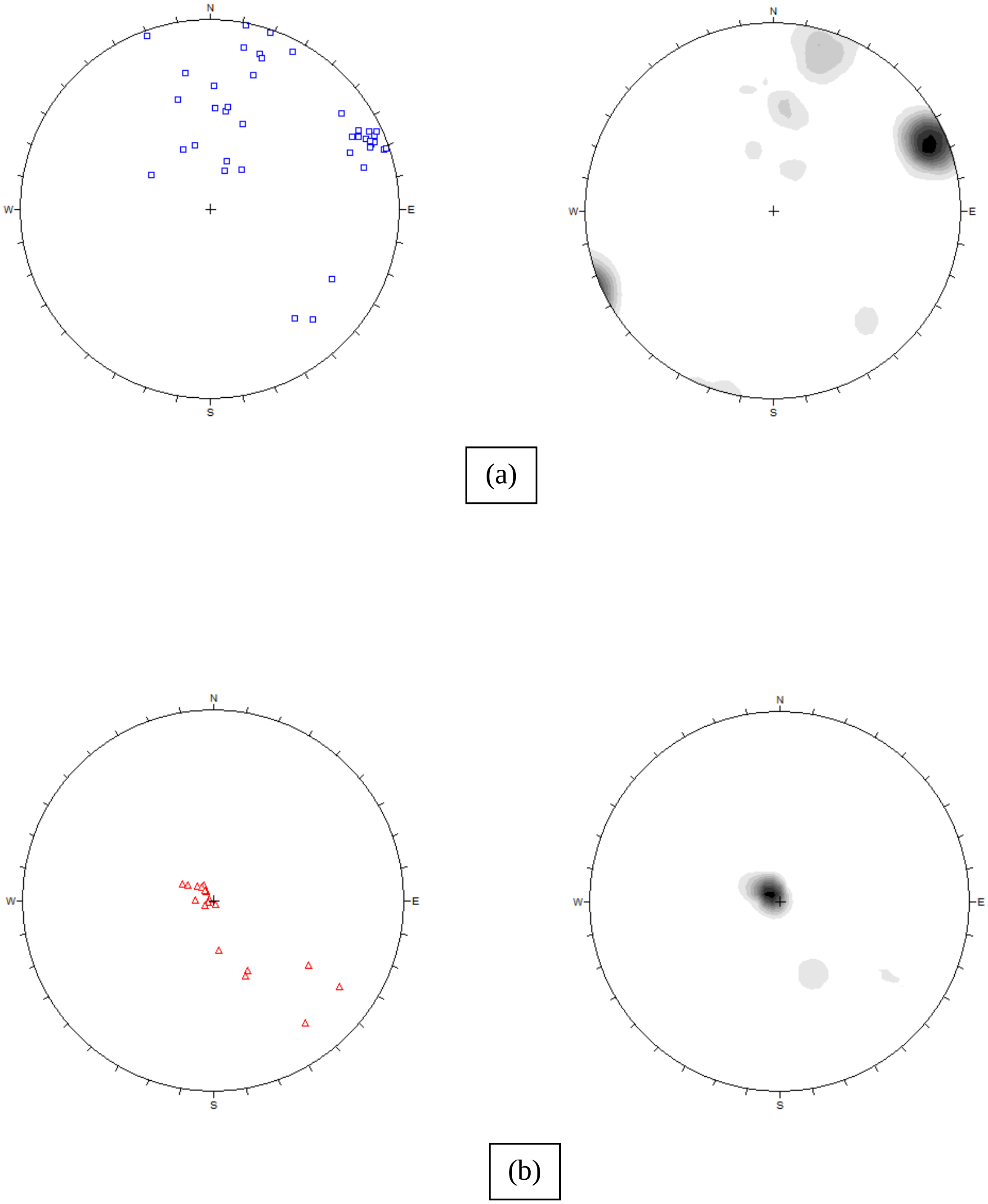

Figure B.13. (a) Poles and corresponding contour of manually measured facets, (b) Poles and corresponding contour of manually measured traces, of Southeast Missouri Site 2.

Site 3

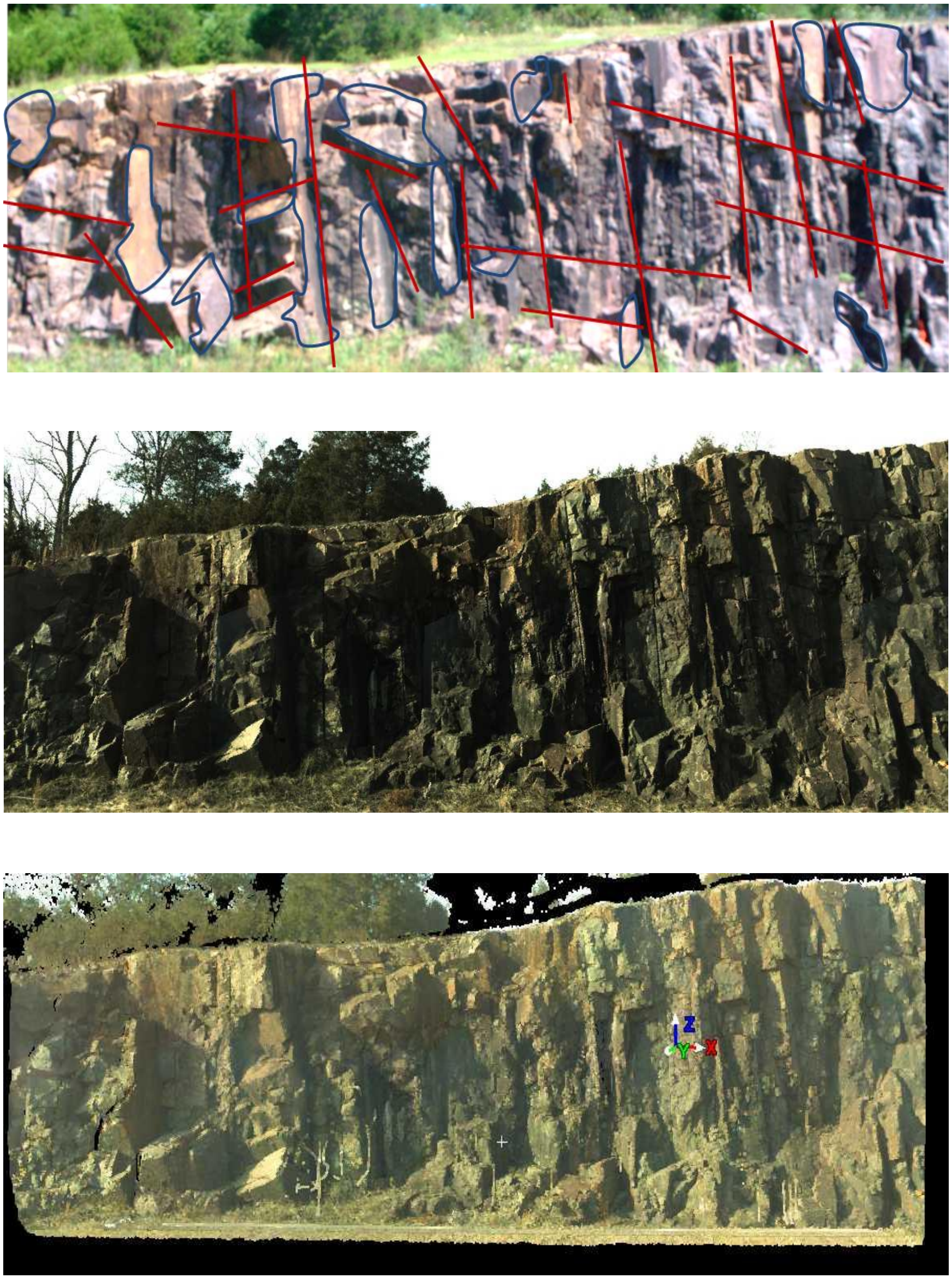

Figure B.14. (a) Manually prepared facets and traces map, red lines represent traces whereas blue polygons represents facets, (b) LiDAR optical image, and (b) LiDAR point cloud of Southeast Missouri Site 3.

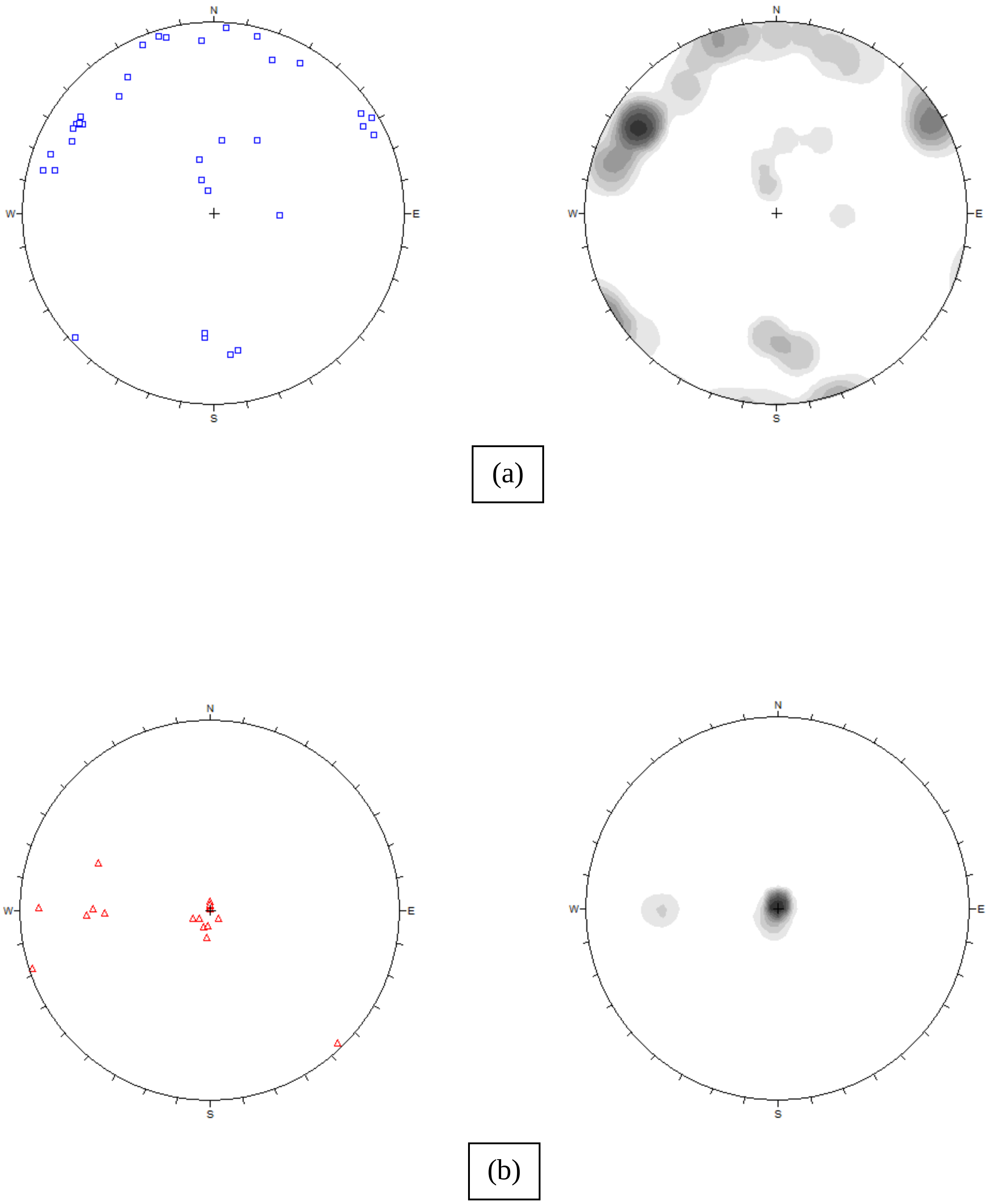

Figure B.15. (a) Poles and corresponding contour of manually measured facets, (b) Poles and corresponding contour of manually measured traces, of Southeast Missouri Site 3.

Site 4

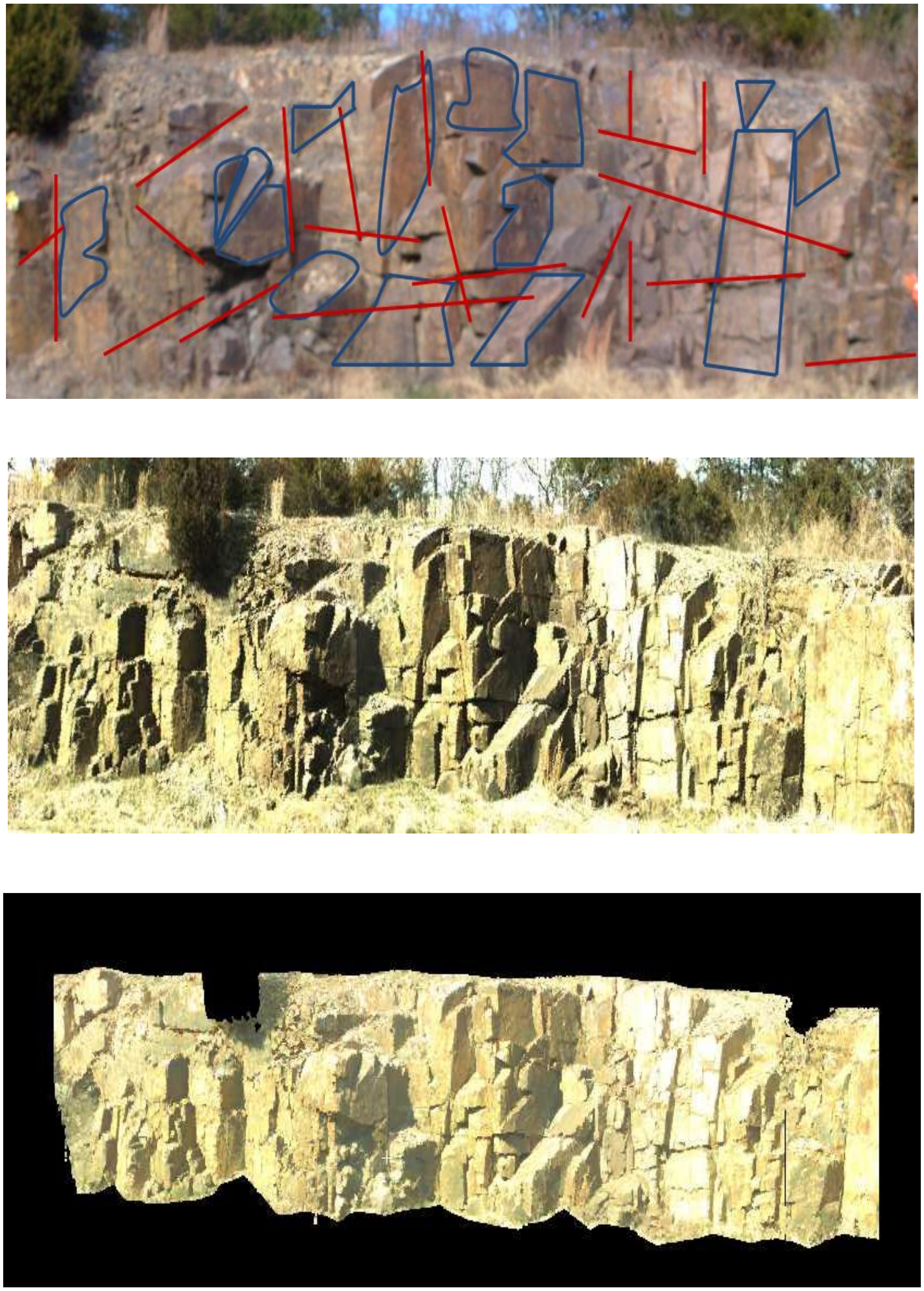

Figure B.16. (a) Manually prepared facets and traces map, red lines represent traces whereas blue polygons represents facets, (b) LiDAR optical image, and (b) LiDAR point cloud of Southeast Missouri Site 4.

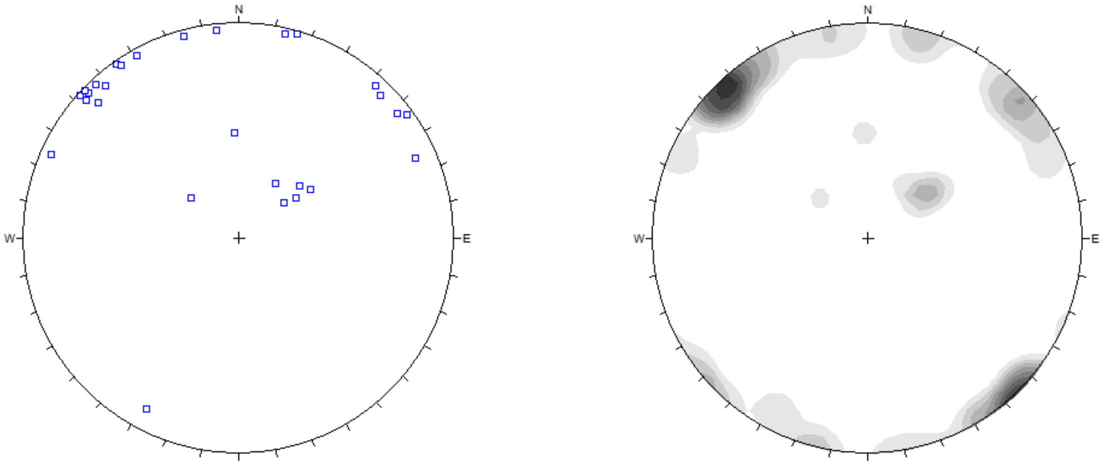

(a)

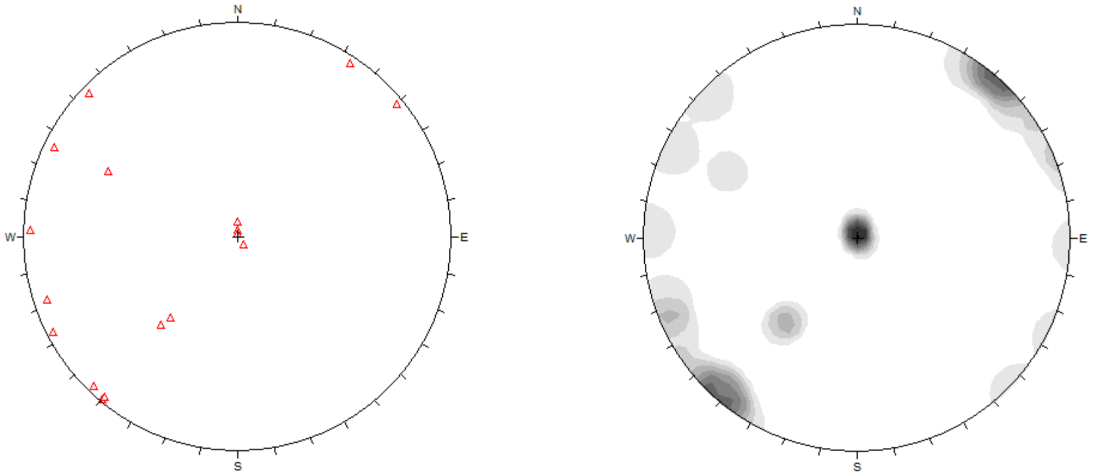

(b)

Figure B.17. (a) Poles and corresponding contour of manually measured facets, (b) Poles and corresponding contour of manually measured traces, of Southeast Missouri Site 4.

Colorado Sites

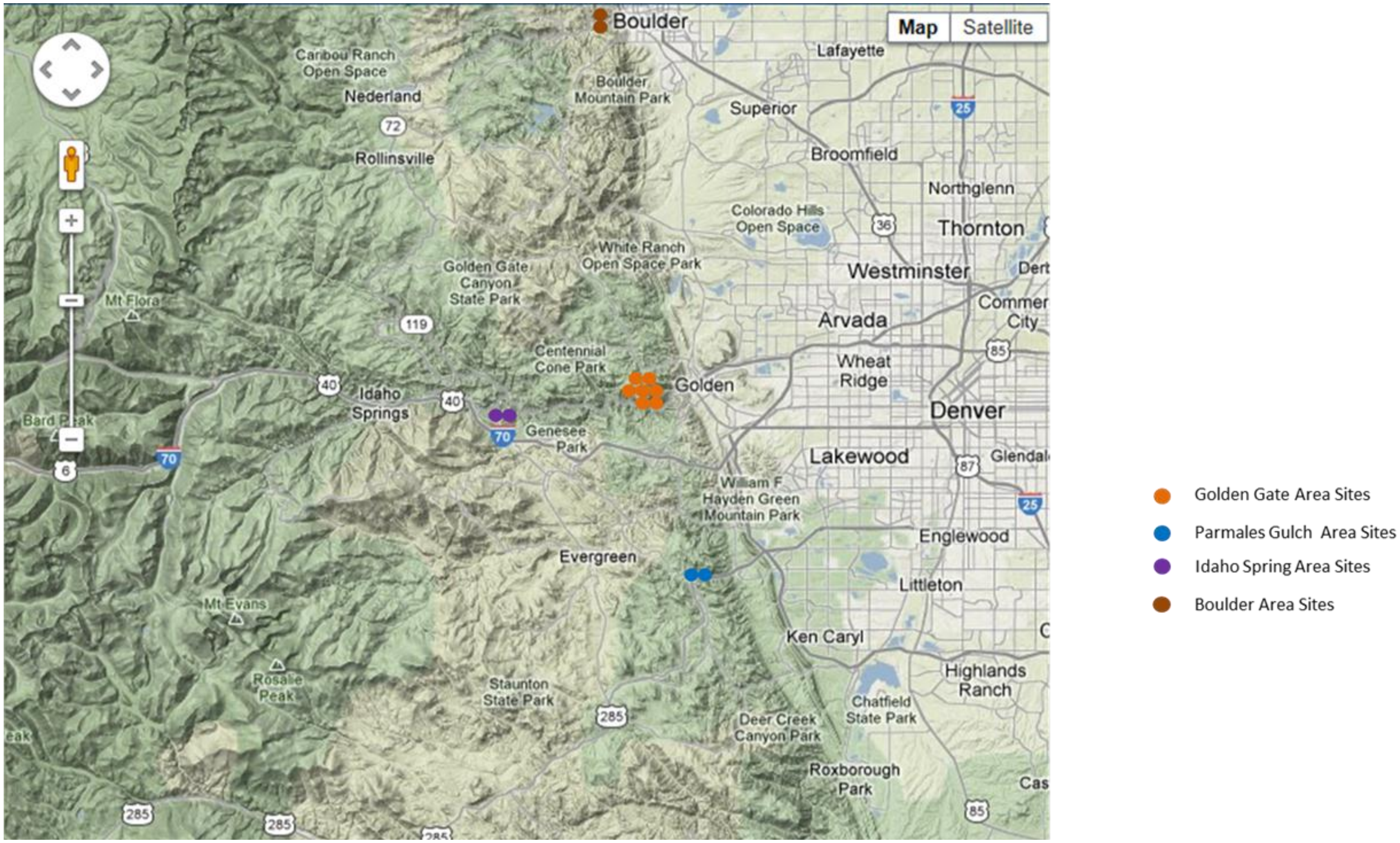

Figure B.18. Location map of Colorado sites with reference to Denver (Google maps, 2012).

Site 1

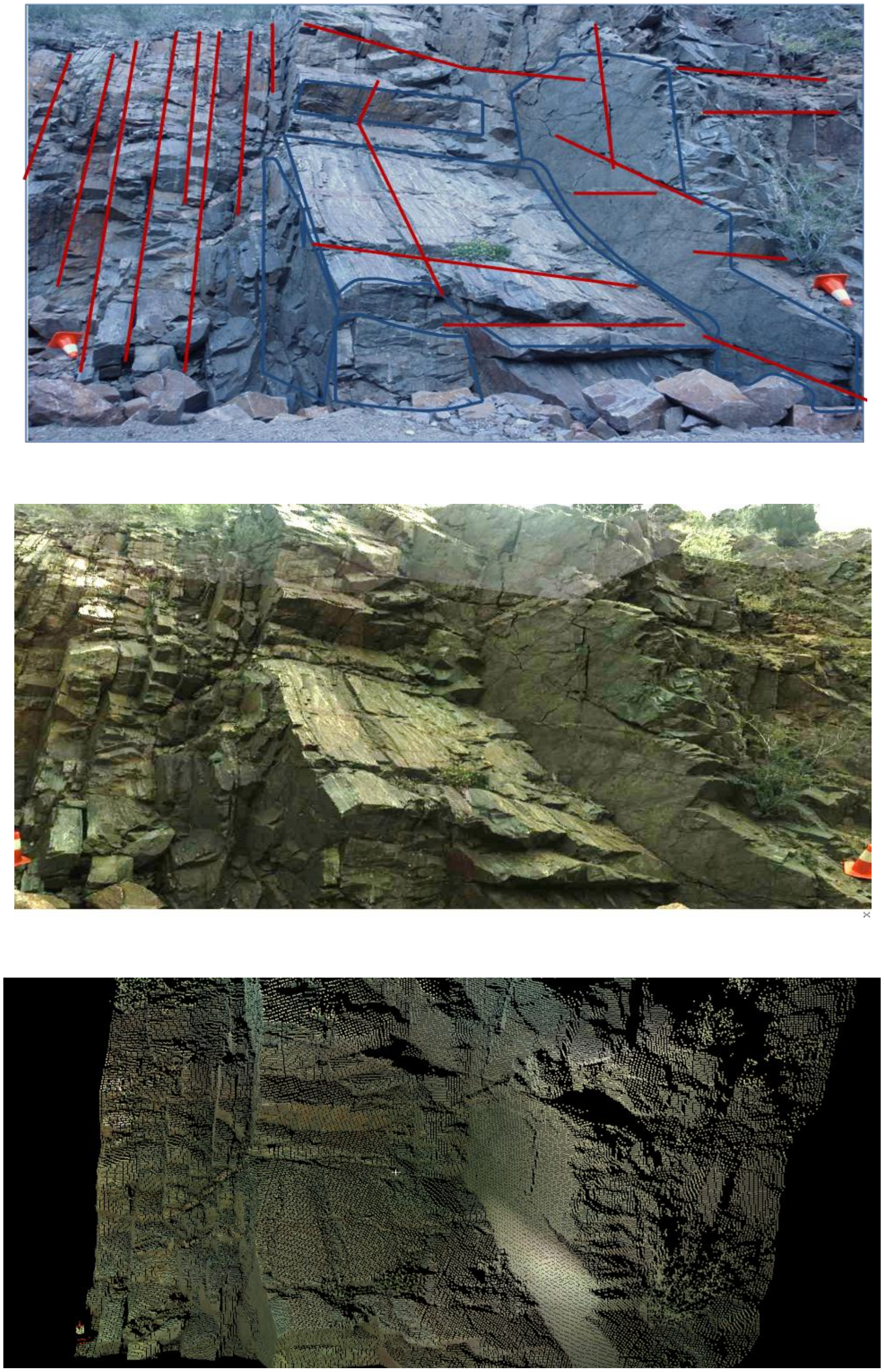

Figure B.19. (a) Manually prepared facets and traces map, red lines represent traces whereas blue polygons represents facets, (b) LiDAR optical image, and (b) LiDAR point cloud of Colorado Site 1.

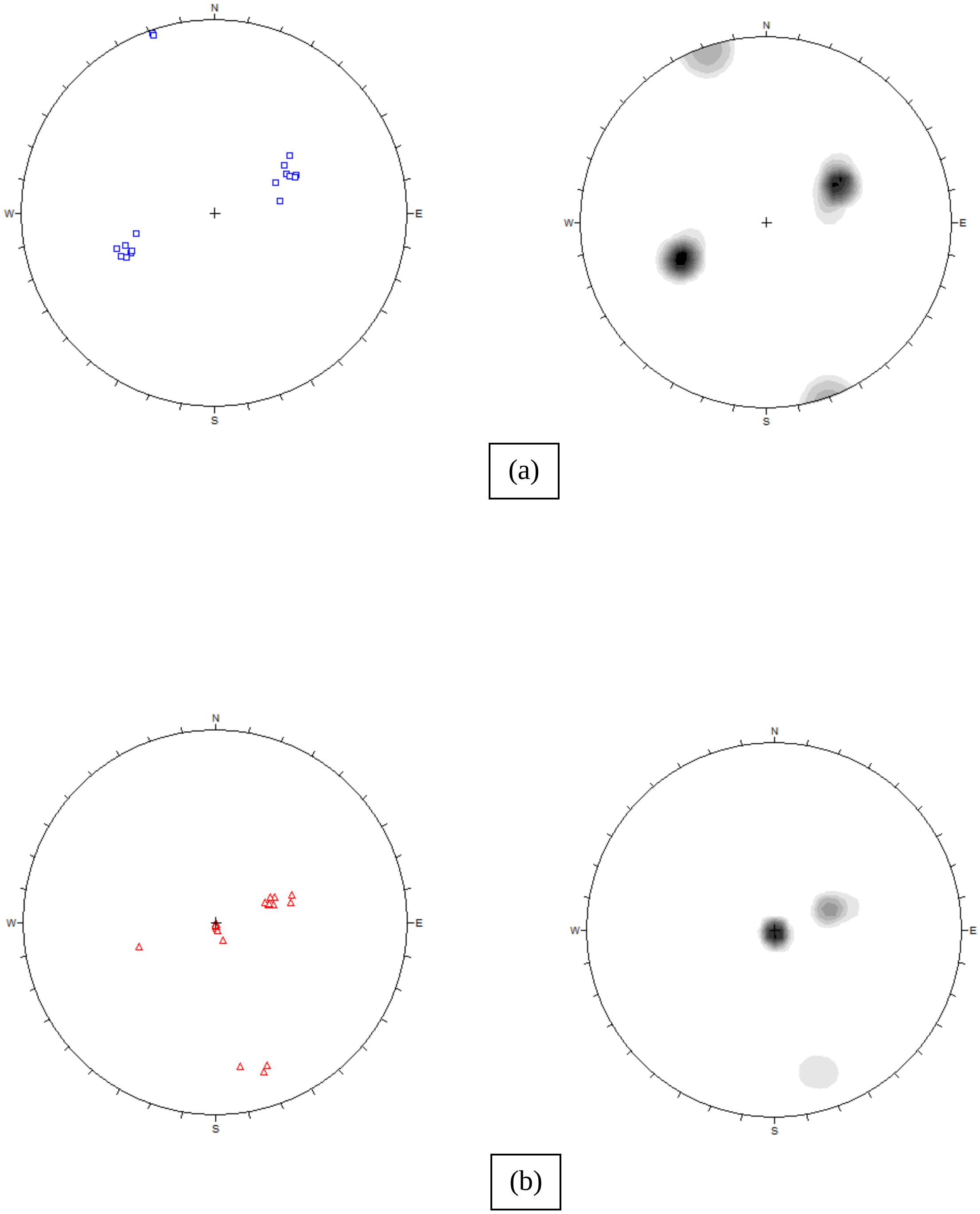

Figure B.20. (a) Poles and corresponding contour of manually measured facets, (b) Poles and corresponding contour of manually measured traces, of Colorado Site 1.

Site 2

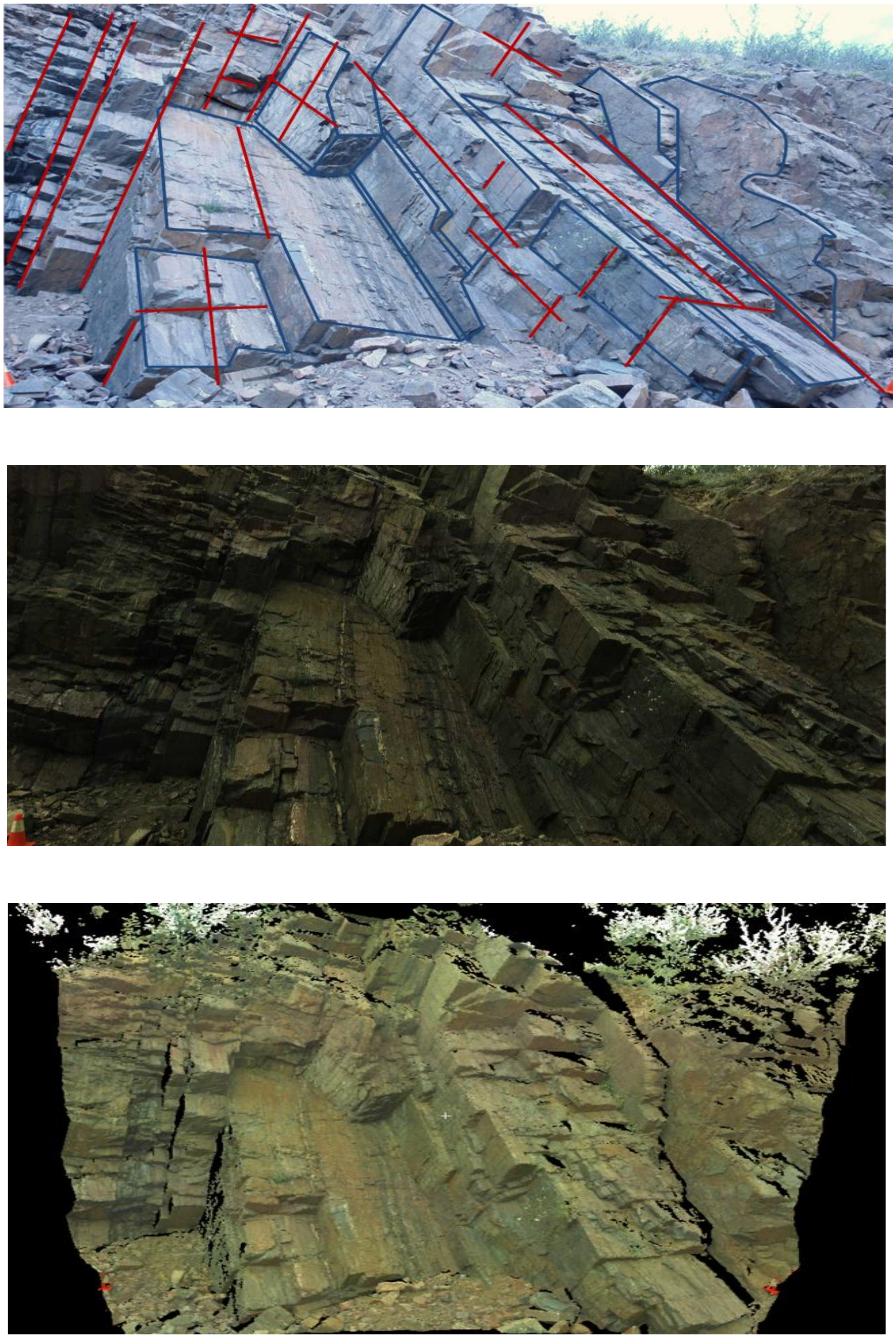

Figure B.21. (a) Manually prepared facets and traces map, red lines represent traces whereas blue polygons represents facets, (b) LiDAR optical image, and (b) LiDAR point cloud of Colorado Site 2.

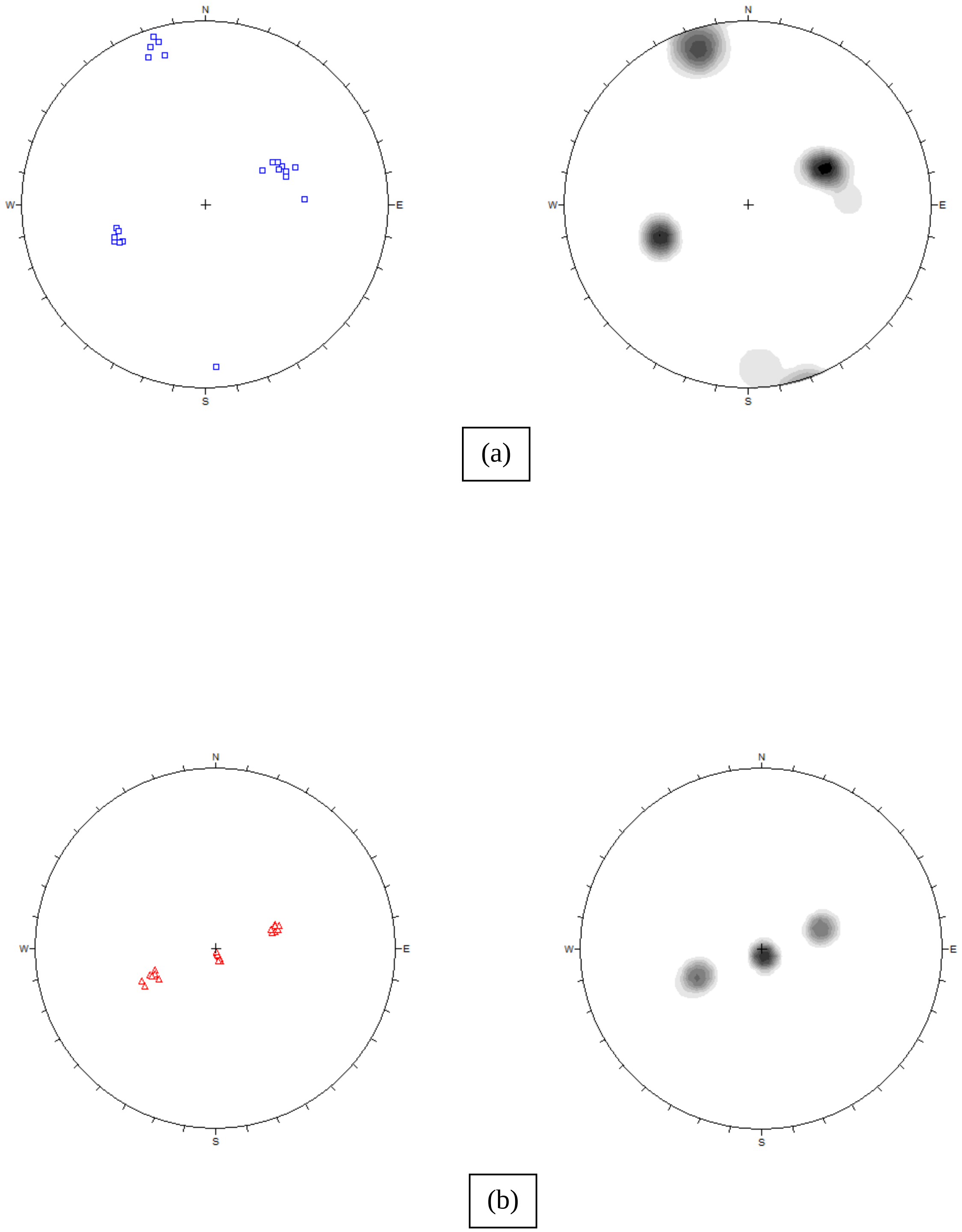

Figure B.22. (a) Poles and corresponding contour of manually measured facets, (b) Poles and corresponding contour of manually measured traces, of Colorado Site 2.

Site 3

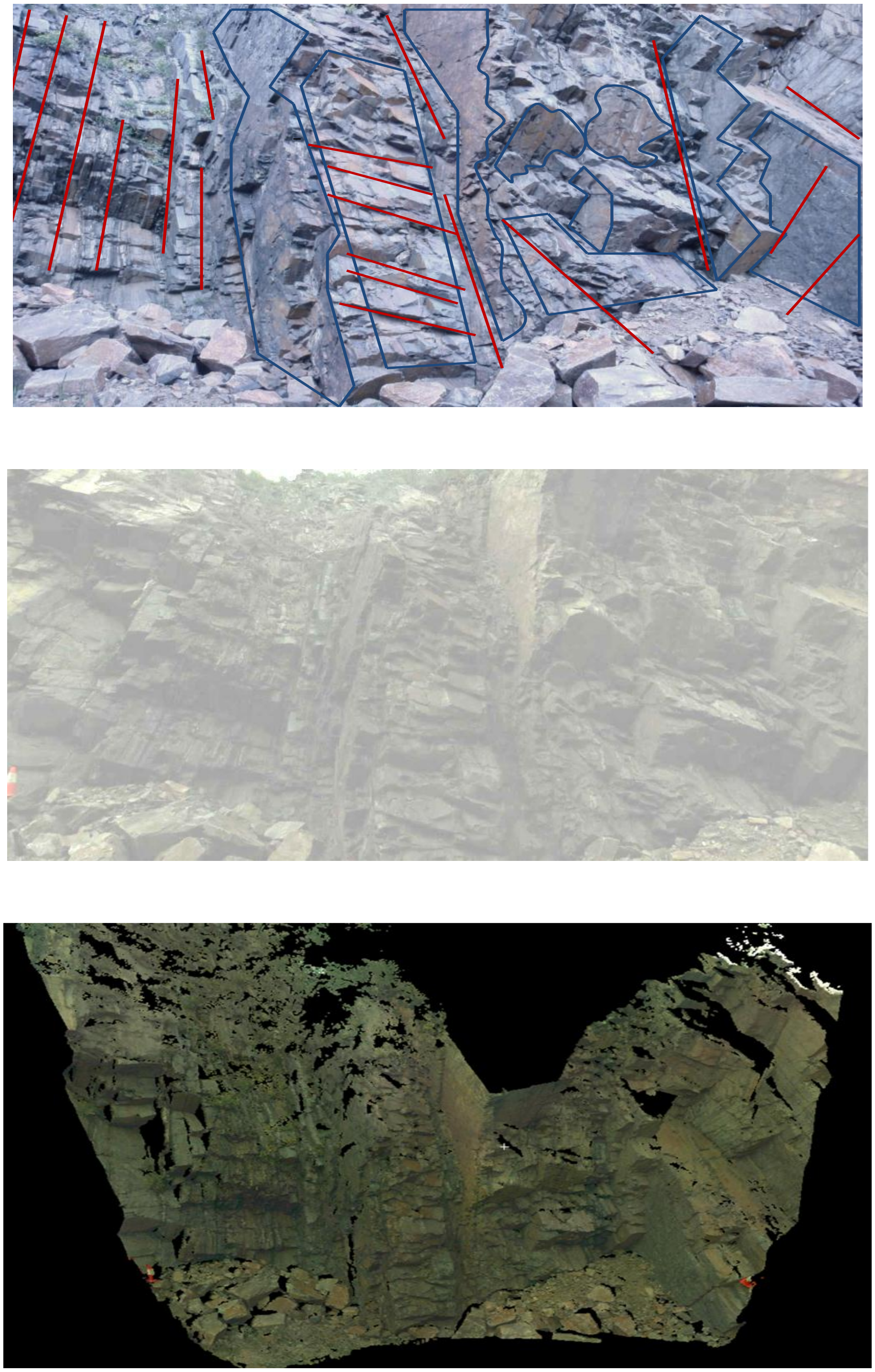

Figure B.23. (a) Manually prepared facets and traces map, red lines represent traces whereas blue polygons represents facets, (b) LiDAR optical image, and (b) LiDAR point cloud of Colorado Site 3.

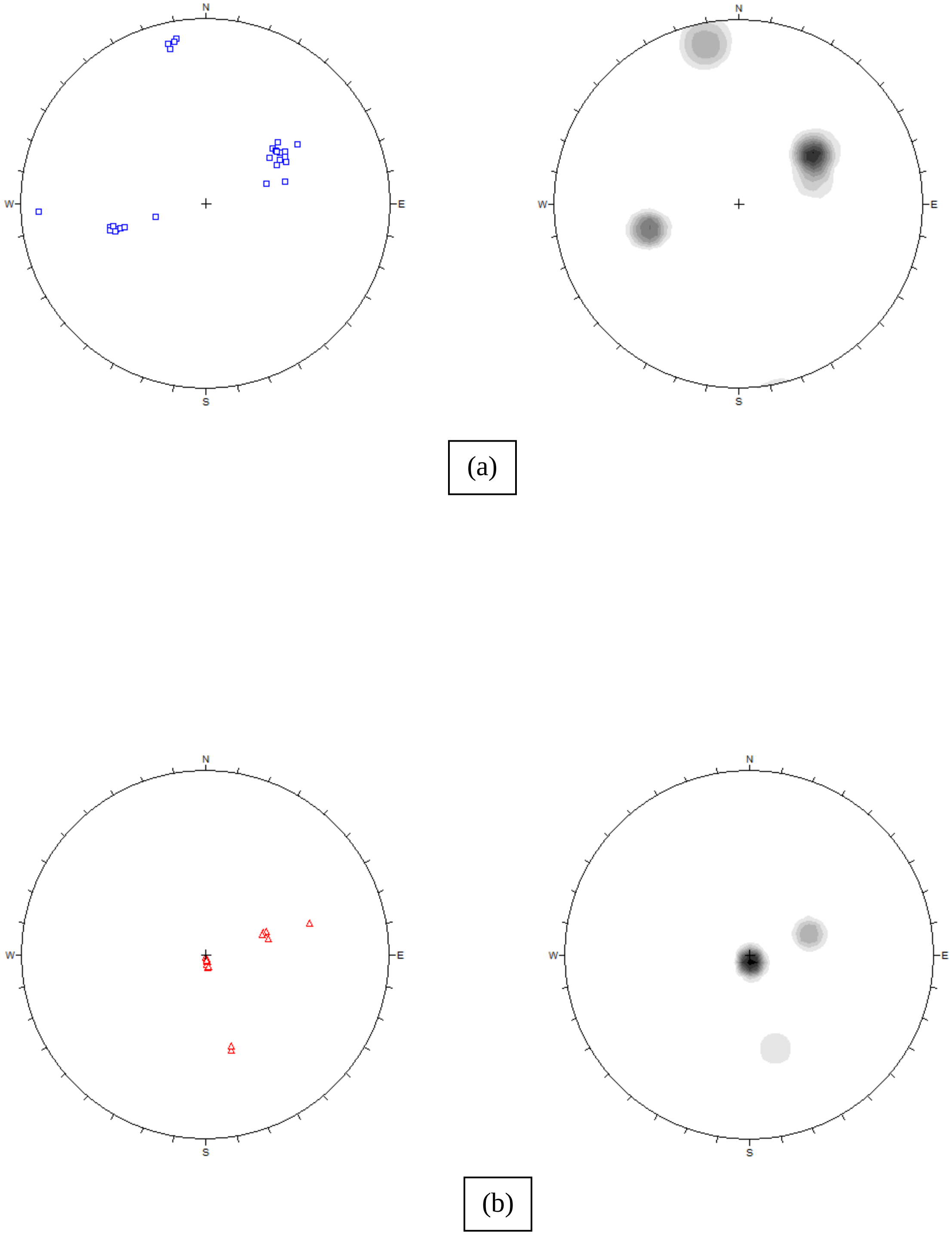

Figure B.24. (a) Poles and corresponding contour of manually measured facets, (b) Poles and corresponding contour of manually measured traces, of Colorado Site 3.

Site 4

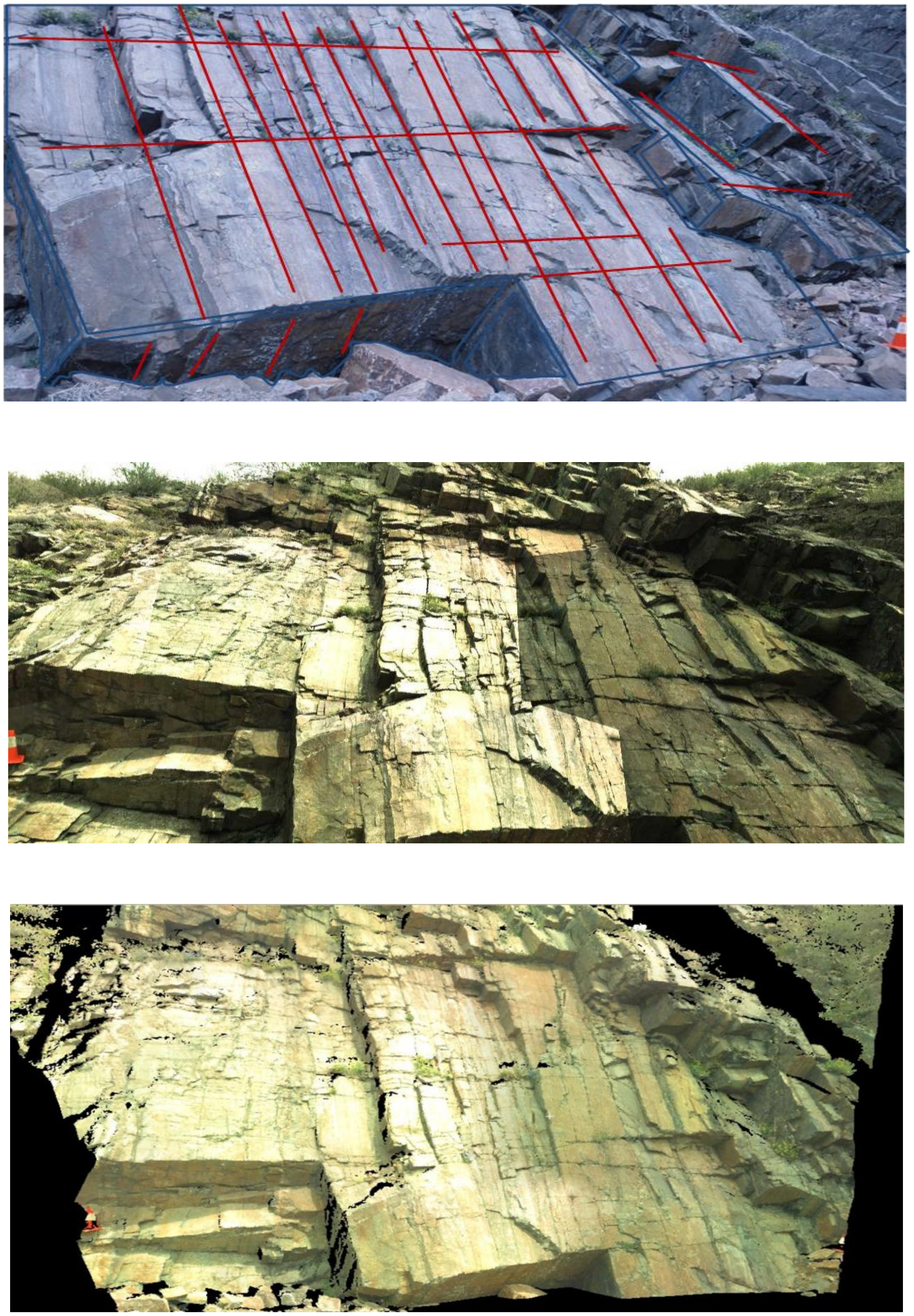

Figure B.25. (a) Manually prepared facets and traces map, red lines represent traces whereas blue polygons represents facets, (b) LiDAR optical image, and (b) LiDAR point cloud of Colorado Site 4.

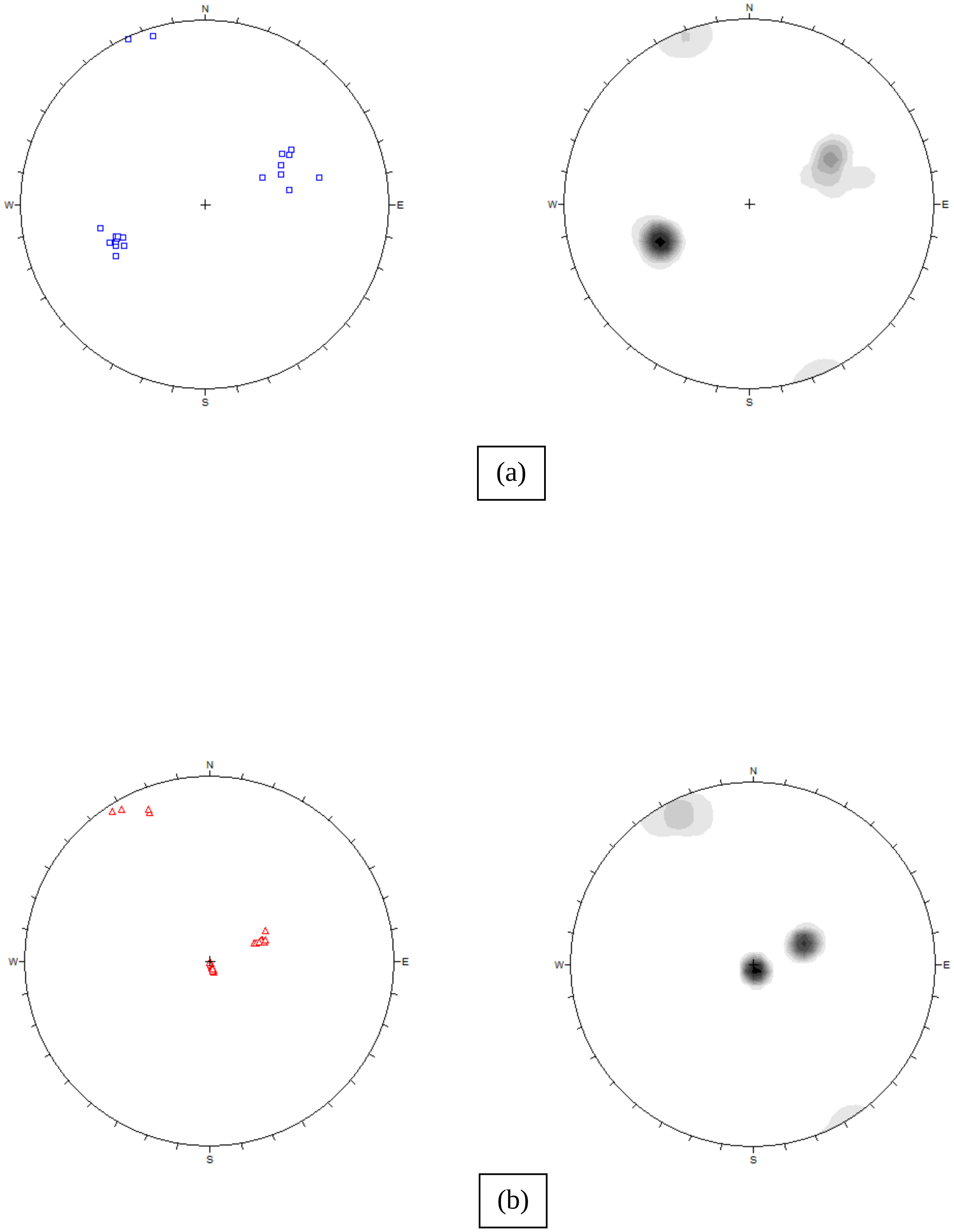

Figure B.26. (a) Poles and corresponding contour of manually measured facets, (b) Poles and corresponding contour of manually measured traces, of Colorado Site 4.

Site 5

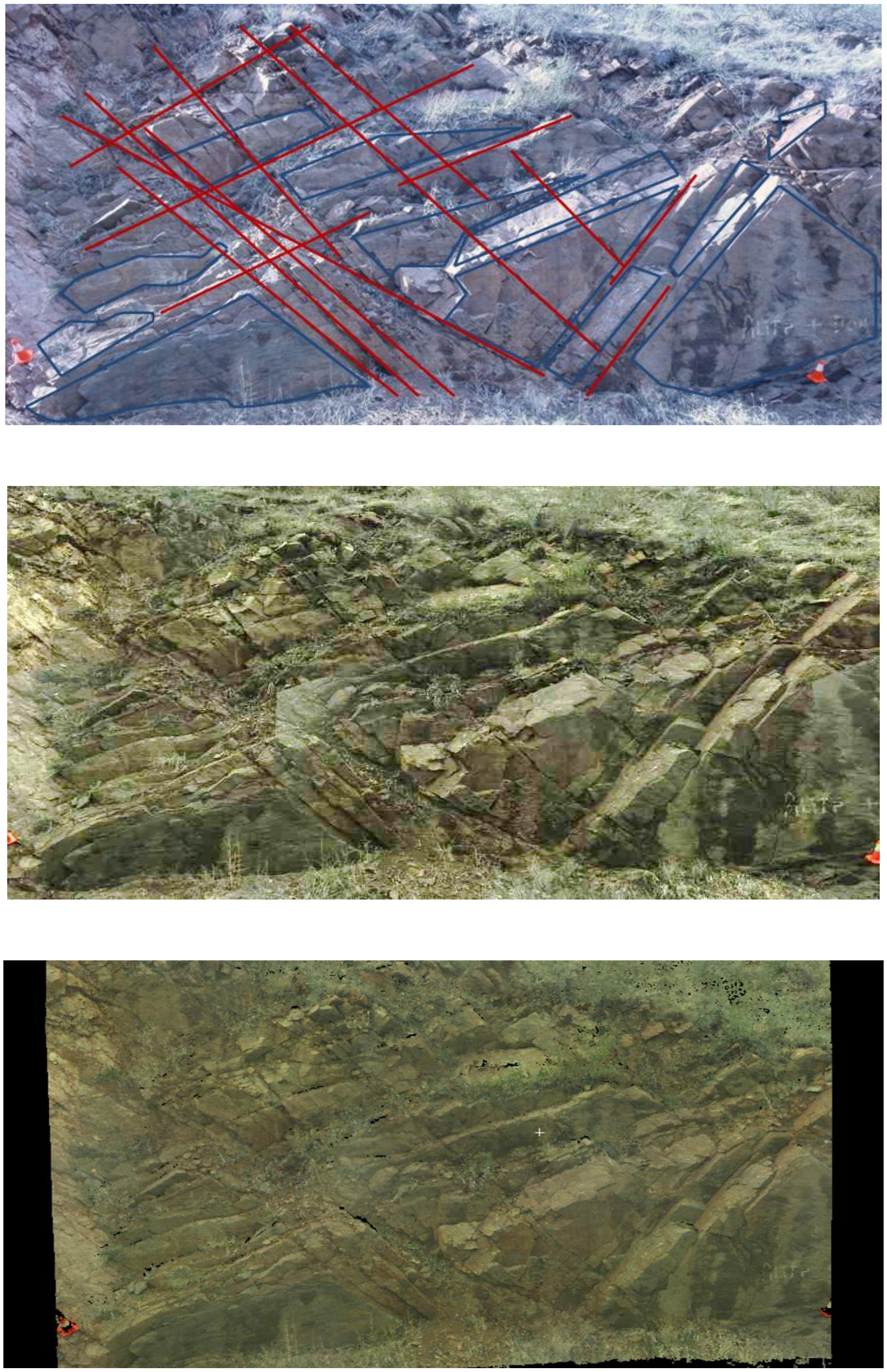

Figure B.27. (a) Manually prepared facets and traces map, red lines represent traces whereas blue polygons represents facets, (b) LiDAR optical image, and (b) LiDAR point cloud of Colorado Site 5.

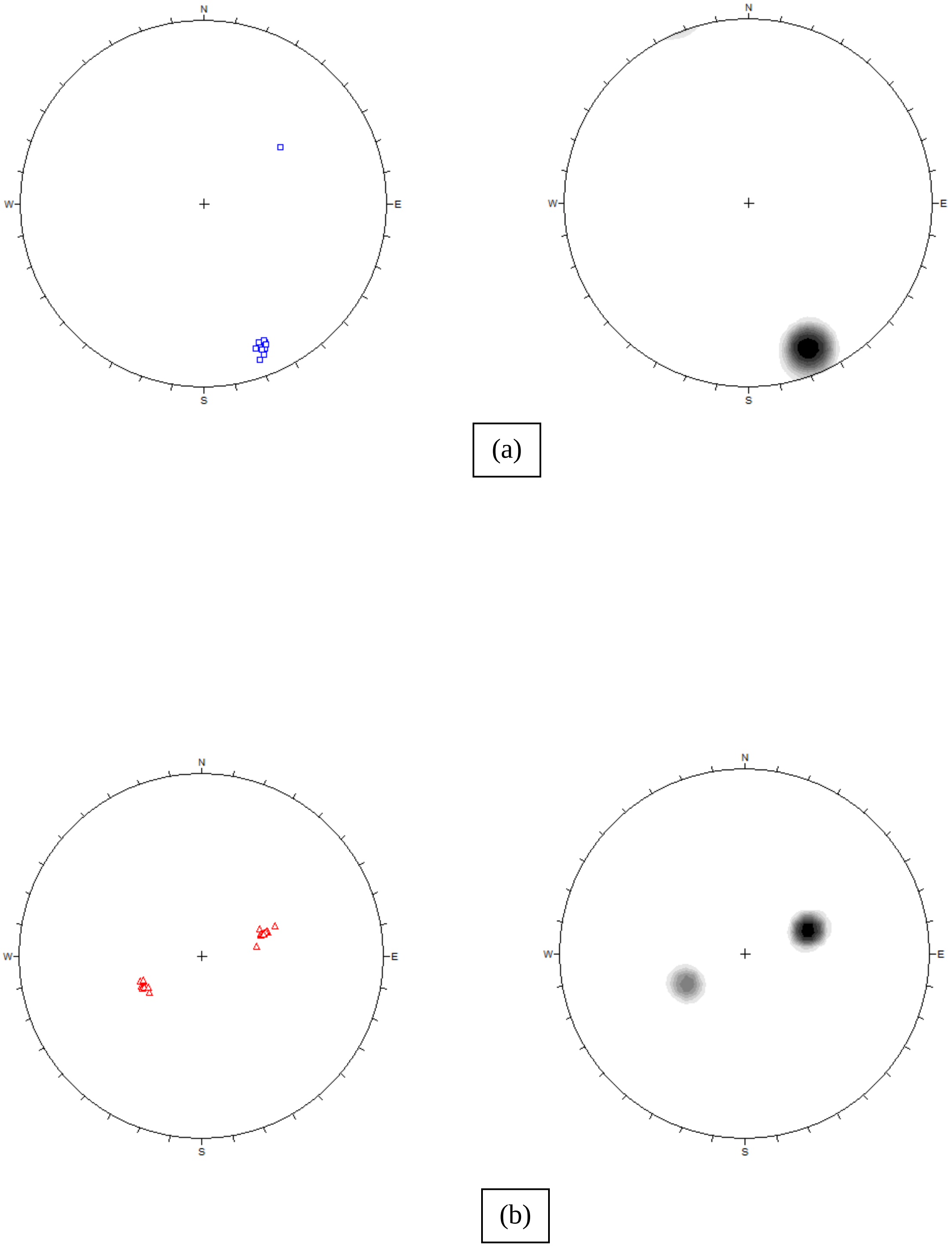

Figure B.28. (a) Poles and corresponding contour of manually measured facets, (b) Poles and corresponding contour of manually measured traces, of Colorado Site 5.

Site 6

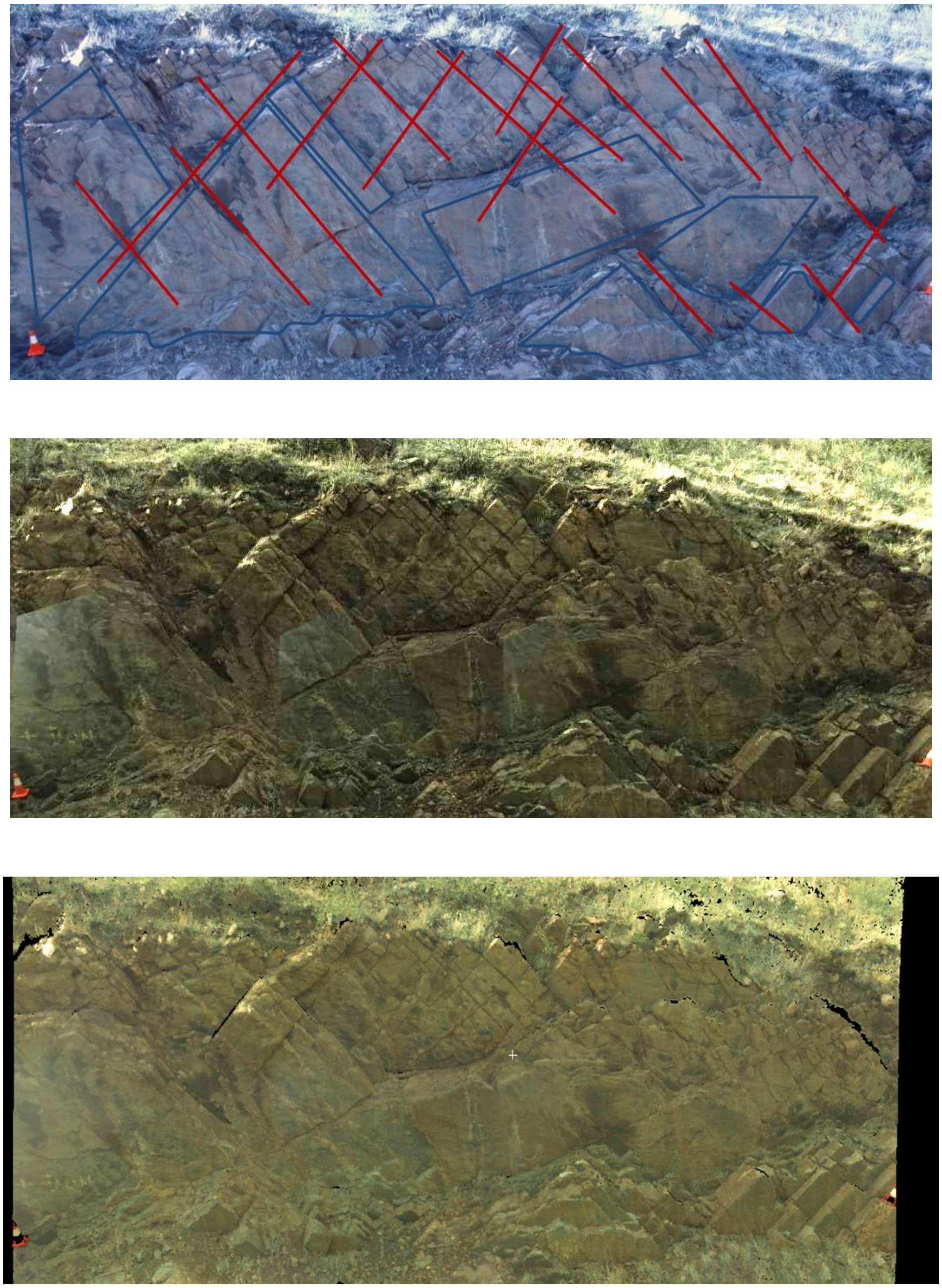

Figure B.29. (a) Manually prepared facets and traces map, red lines represent traces whereas blue polygons represents facets, (b) LiDAR optical image, and (b) LiDAR point cloud of Colorado Site 6.

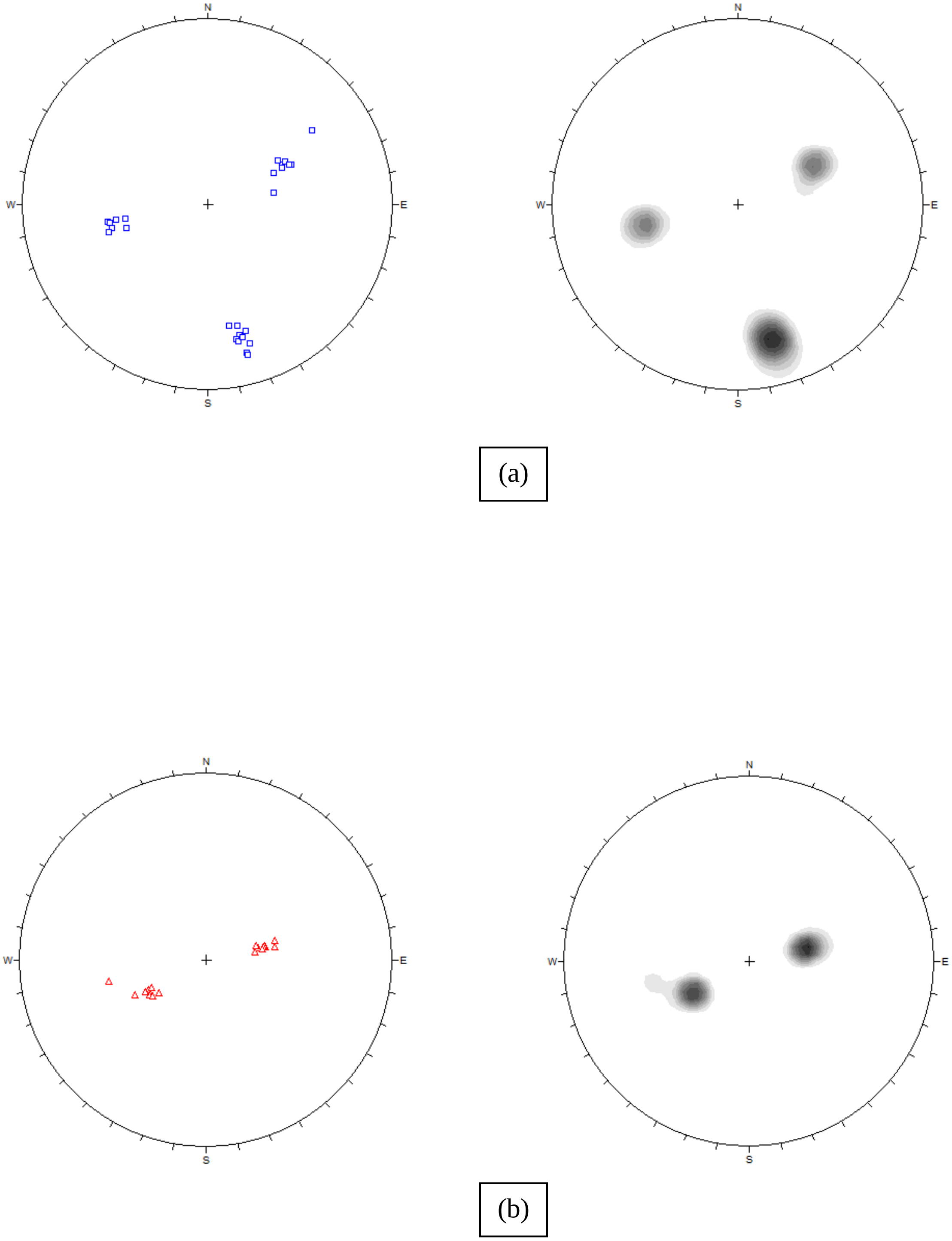

Figure B.30. (a) Poles and corresponding contour of manually measured facets, (b) Poles and corresponding contour of manually measured traces, of Colorado Site 6.

Site 7

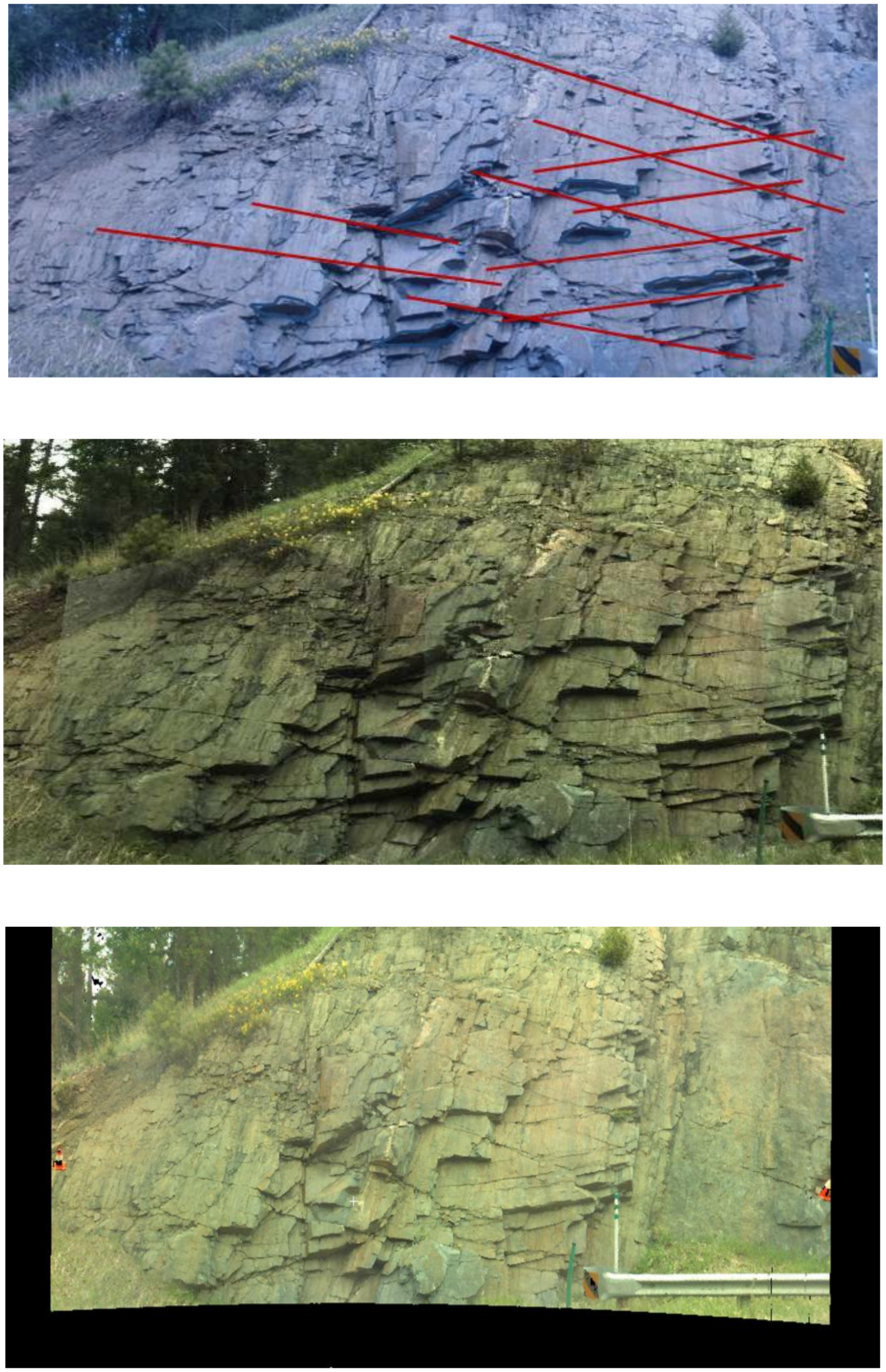

Figure B.31. (a) Manually prepared facets and traces map, red lines represent traces whereas blue polygons represents facets, (b) LiDAR optical image, and (b) LiDAR point cloud of Colorado Site 7.

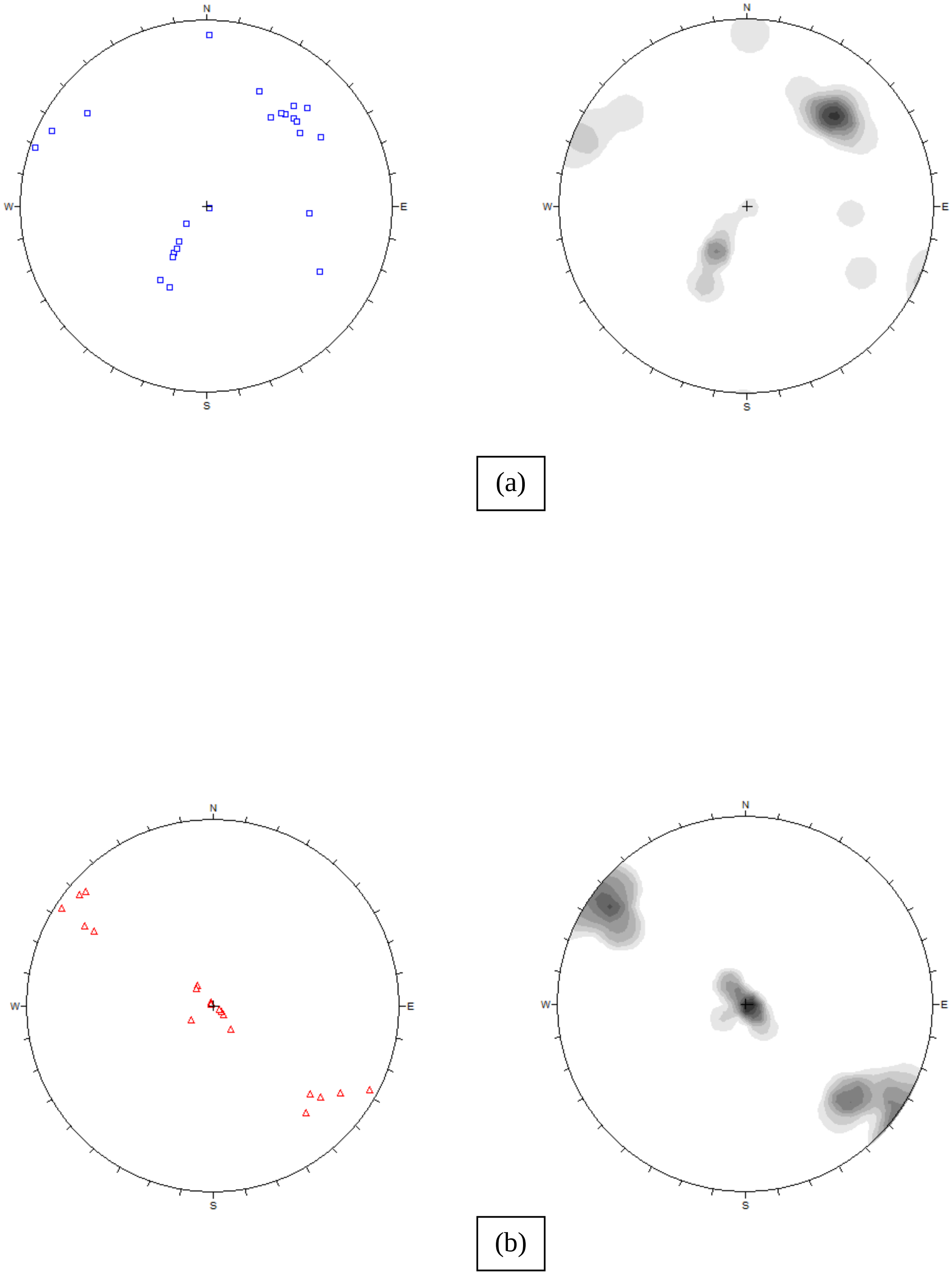

Figure B.32. (a) Poles and corresponding contour of manually measured facets, (b) Poles and corresponding contour of manually measured traces, of Colorado Site 7.

Site 8

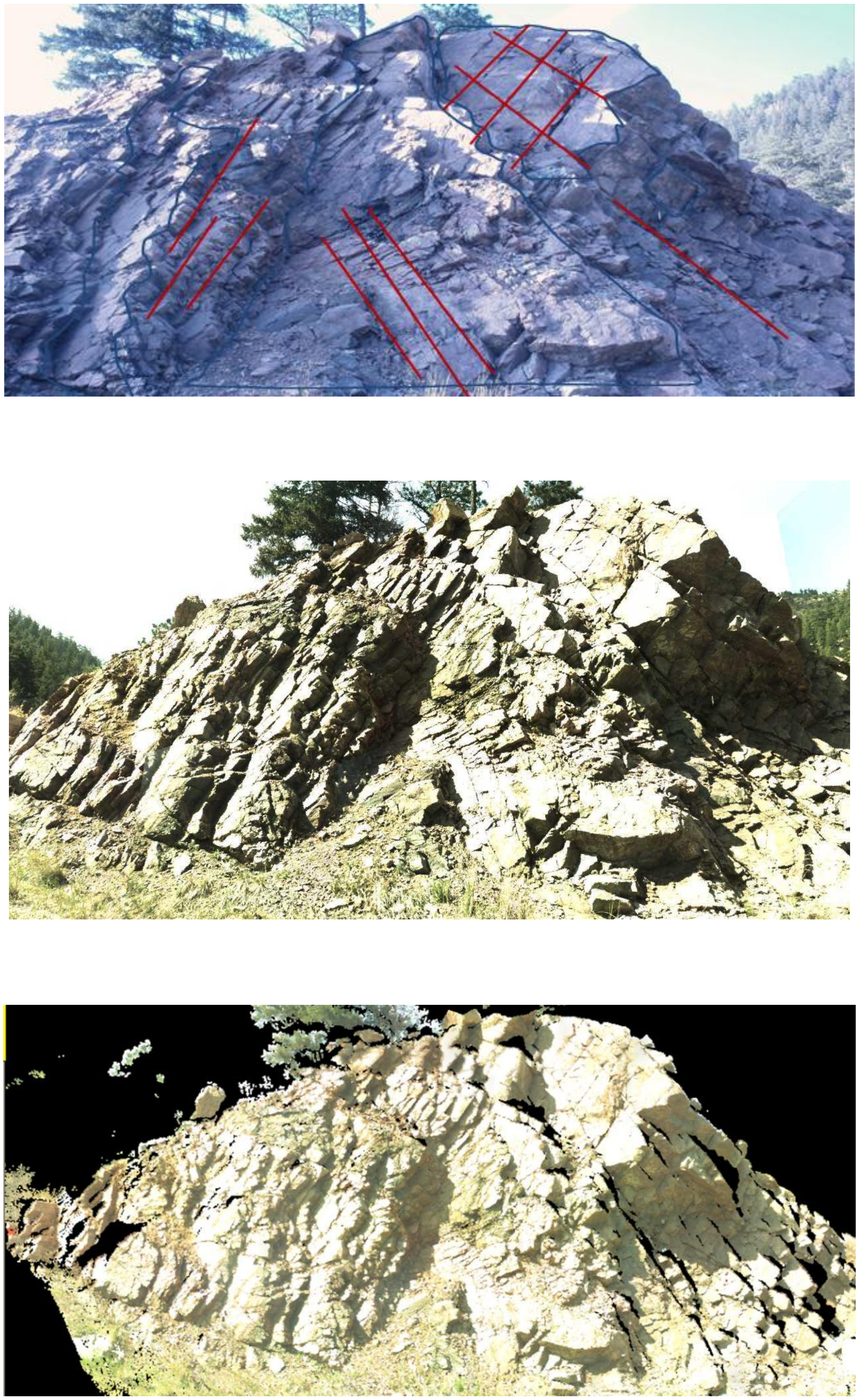

Figure B.33. (a) Manually prepared facets and traces map, red lines represent traces whereas blue polygons represents facets, (b) LiDAR optical image, and (b) LiDAR point cloud of Colorado Site 8.

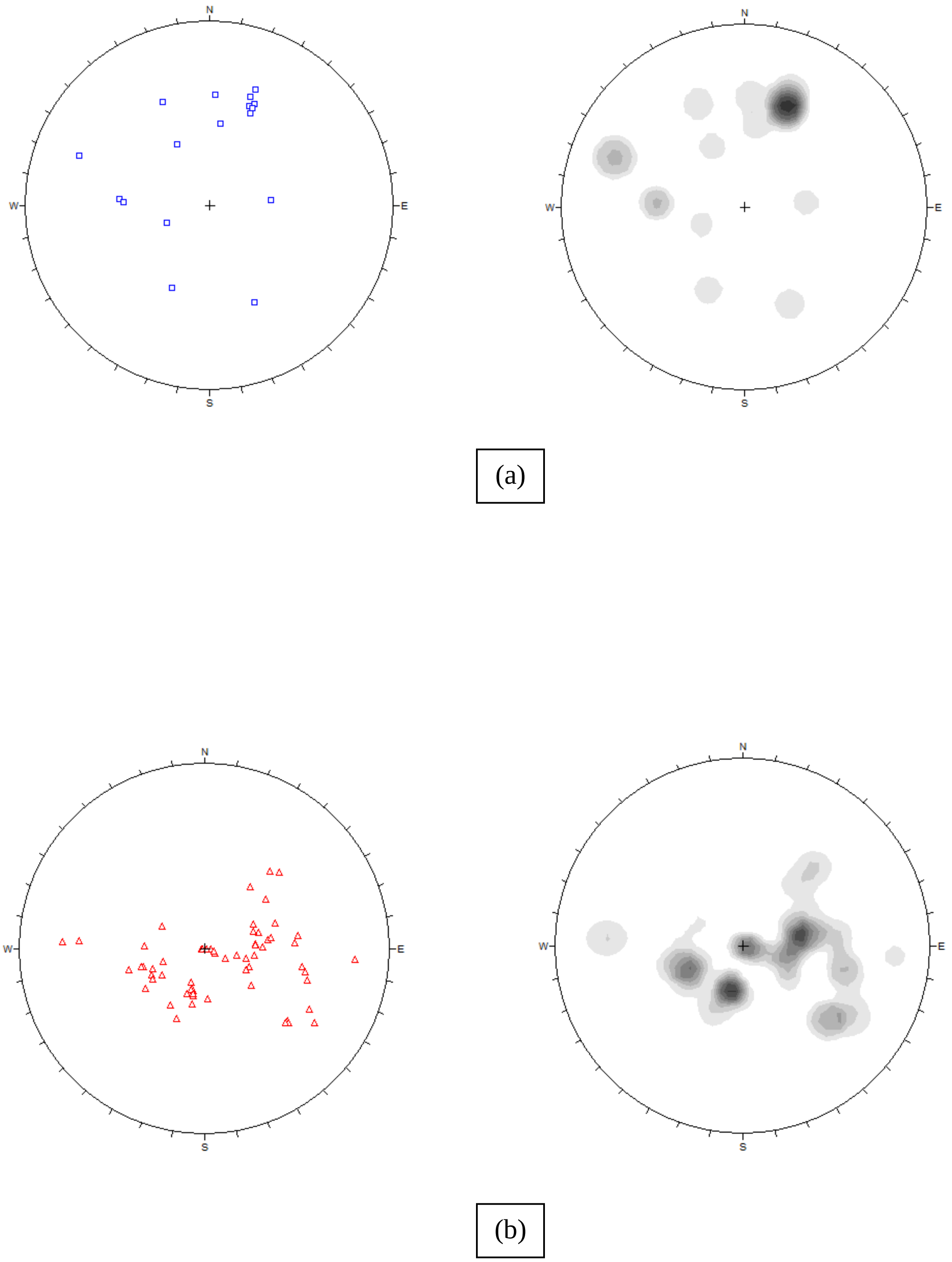

Figure B.34. (a) Poles and corresponding contour of manually measured facets, (b) Poles and corresponding contour of manually measured traces, of Colorado Site 8.

Site 9

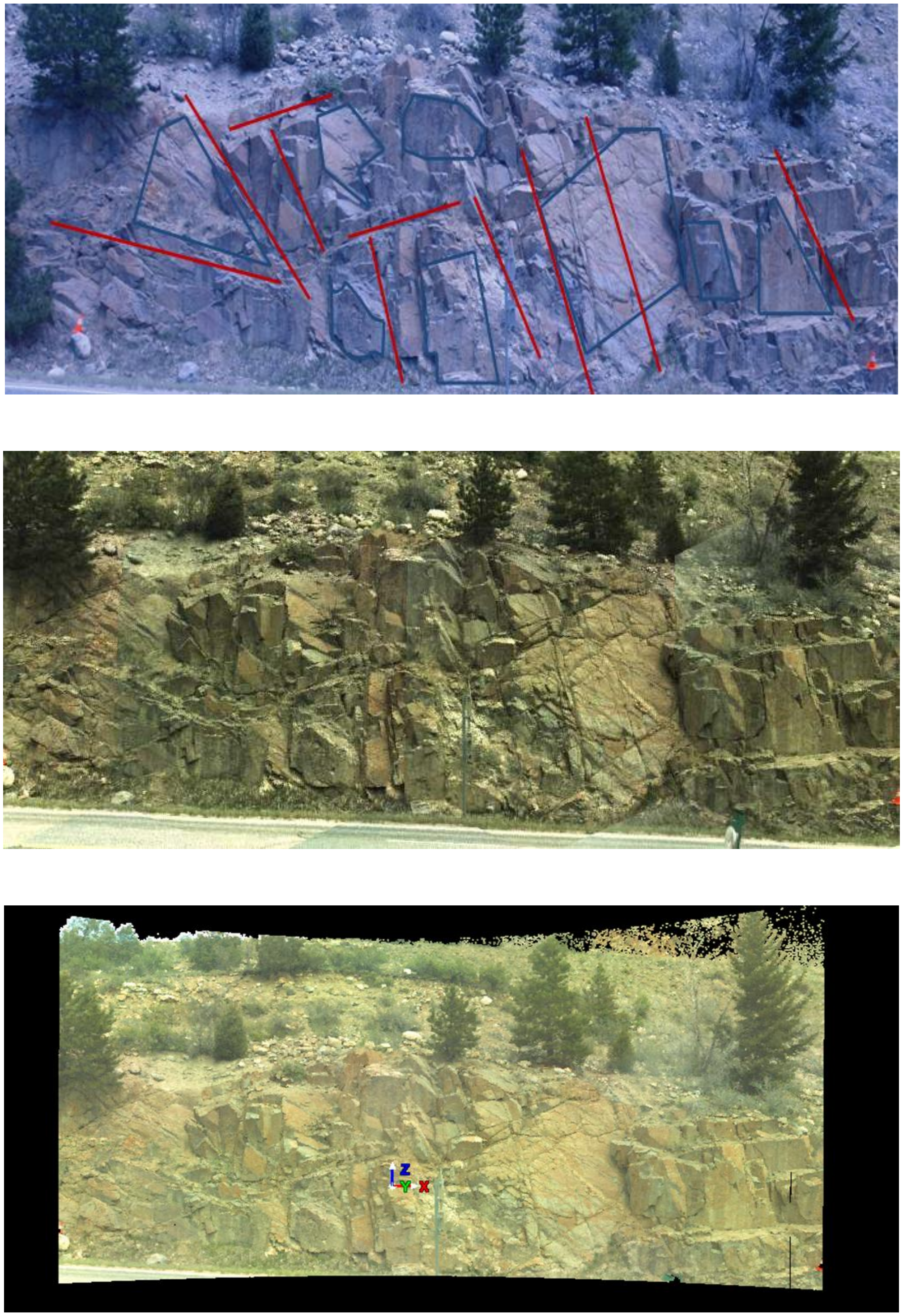

Figure B.35. (a) Manually prepared facets and traces map, red lines represent traces whereas blue polygons represents facets, (b) LiDAR optical image, and (b) LiDAR point cloud of Colorado Site 9.

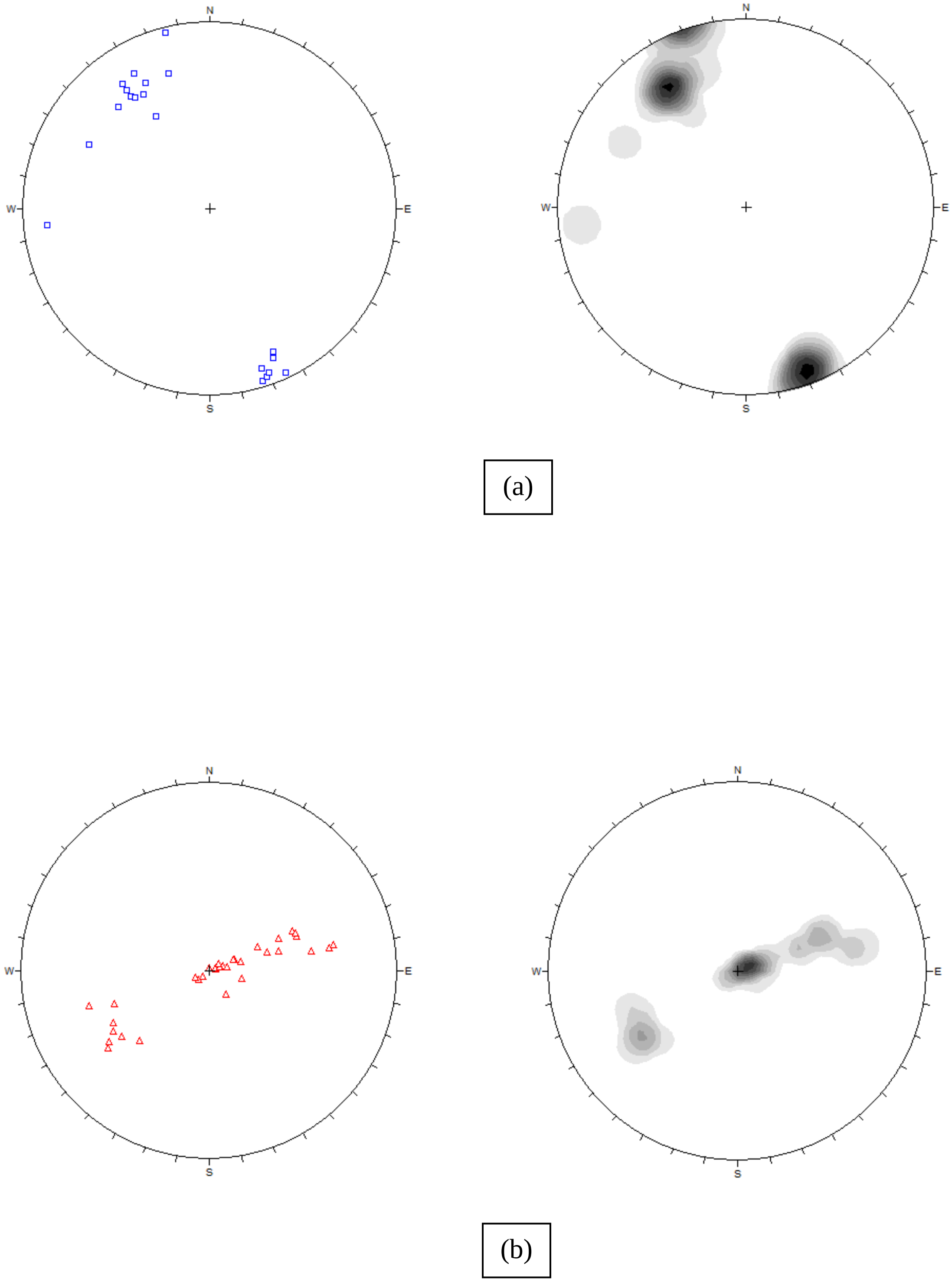

Figure B.36. (a) Poles and corresponding contour of manually measured facets, (b) Poles and corresponding contour of manually measured traces, of Colorado Site 9.

Site 10

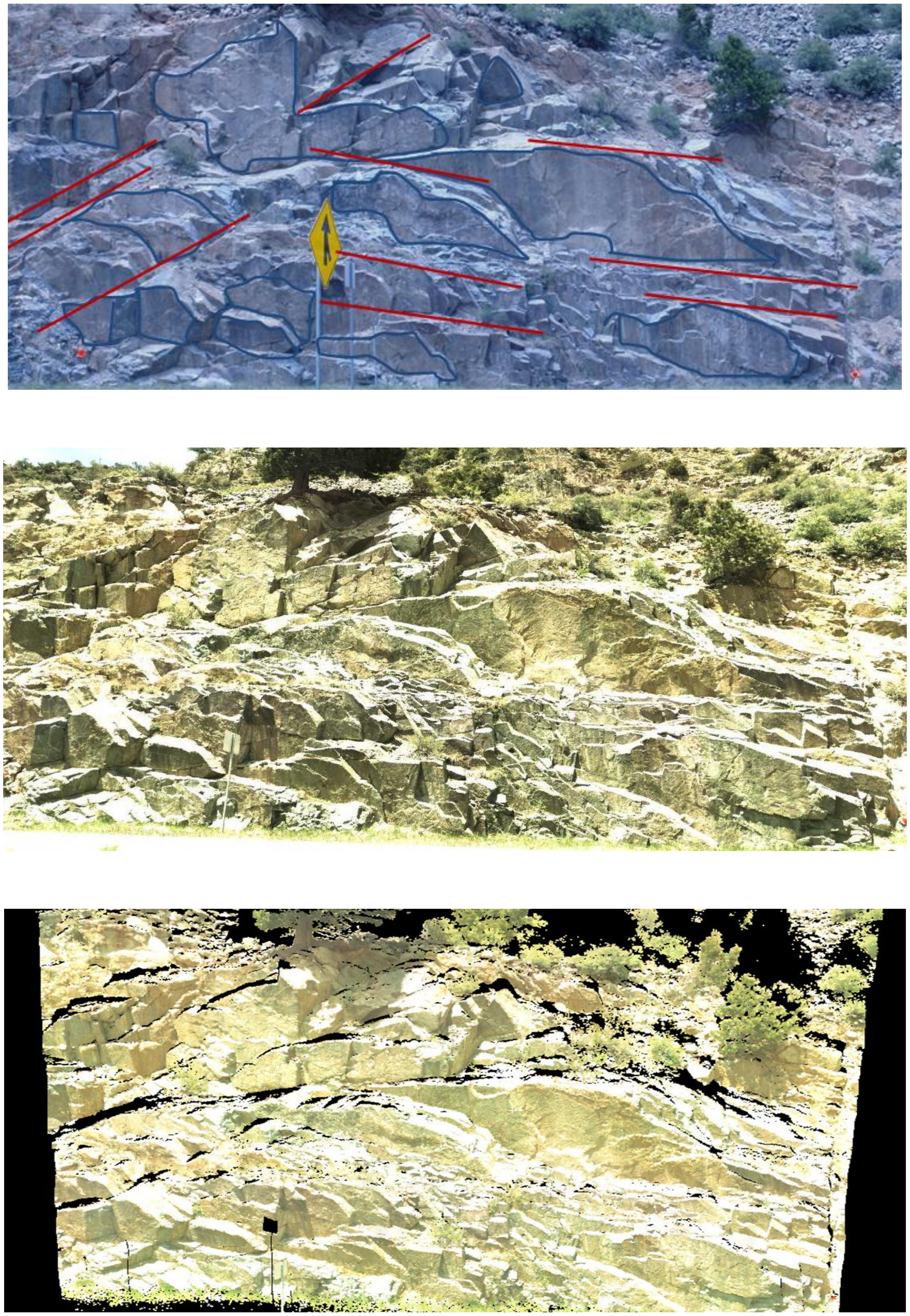

Figure B.37. (a) Manually prepared facets and traces map, red lines represent traces whereas blue polygons represents facets, (b) LiDAR optical image, and (b) LiDAR point cloud of Colorado Site 10.

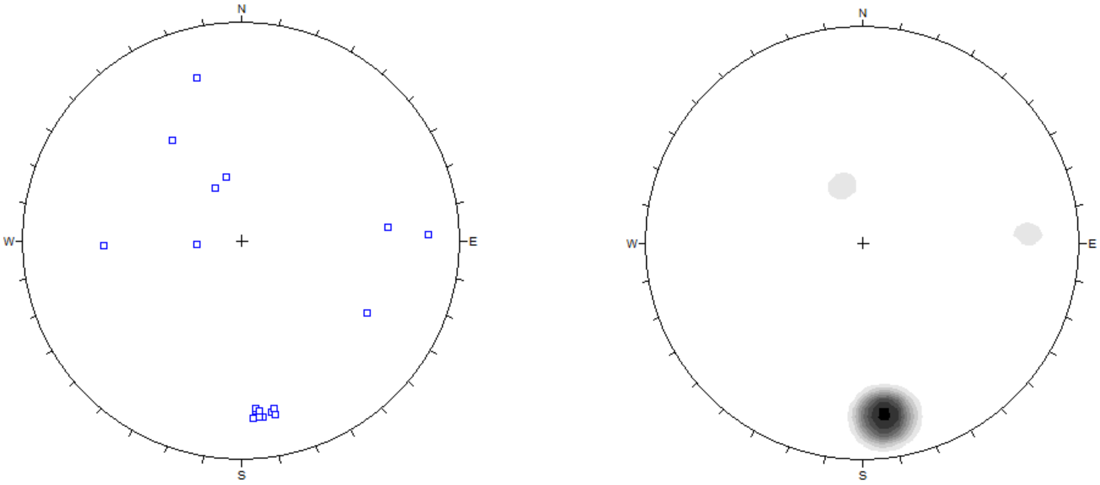

(a)

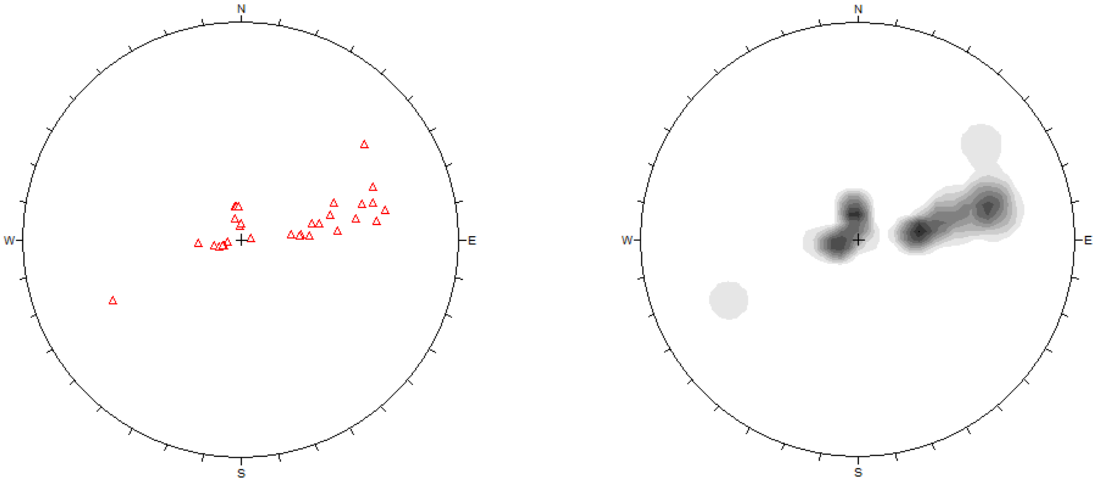

(b)

Figure B.38. (a) Poles and corresponding contour of manually measured facets, (b) Poles and corresponding contour of manually measured traces, of Colorado Site 10.

Site 11

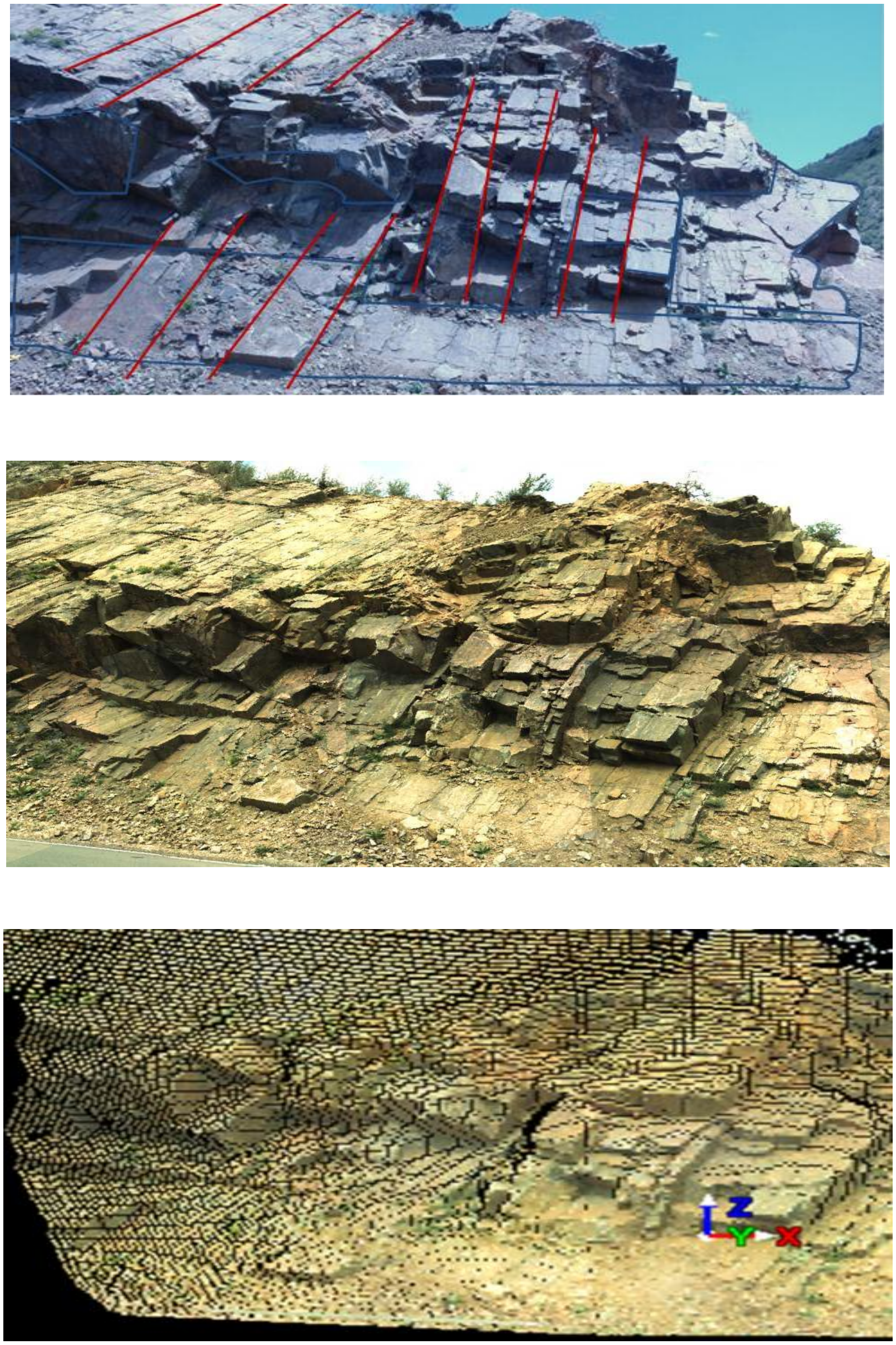

Figure B.39. (a) Manually prepared facets and traces map, red lines represent traces whereas blue polygons represents facets, (b) LiDAR optical image, and (b) LiDAR point cloud of Colorado Site 11.

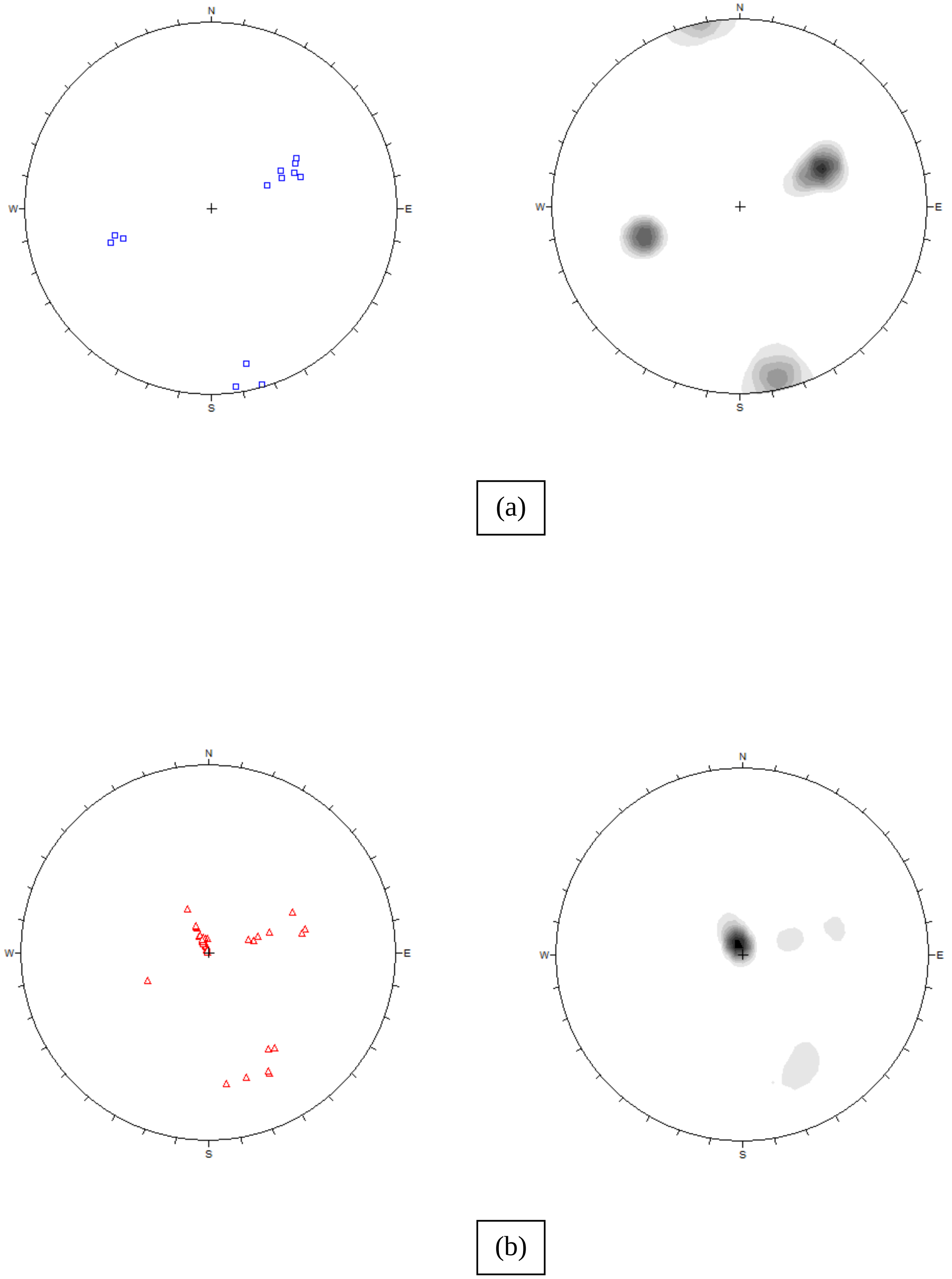

Figure B.40. (a) Poles and corresponding contour of manually measured facets, (b) Poles and corresponding contour of manually measured traces, of Colorado Site 11.

Site 12

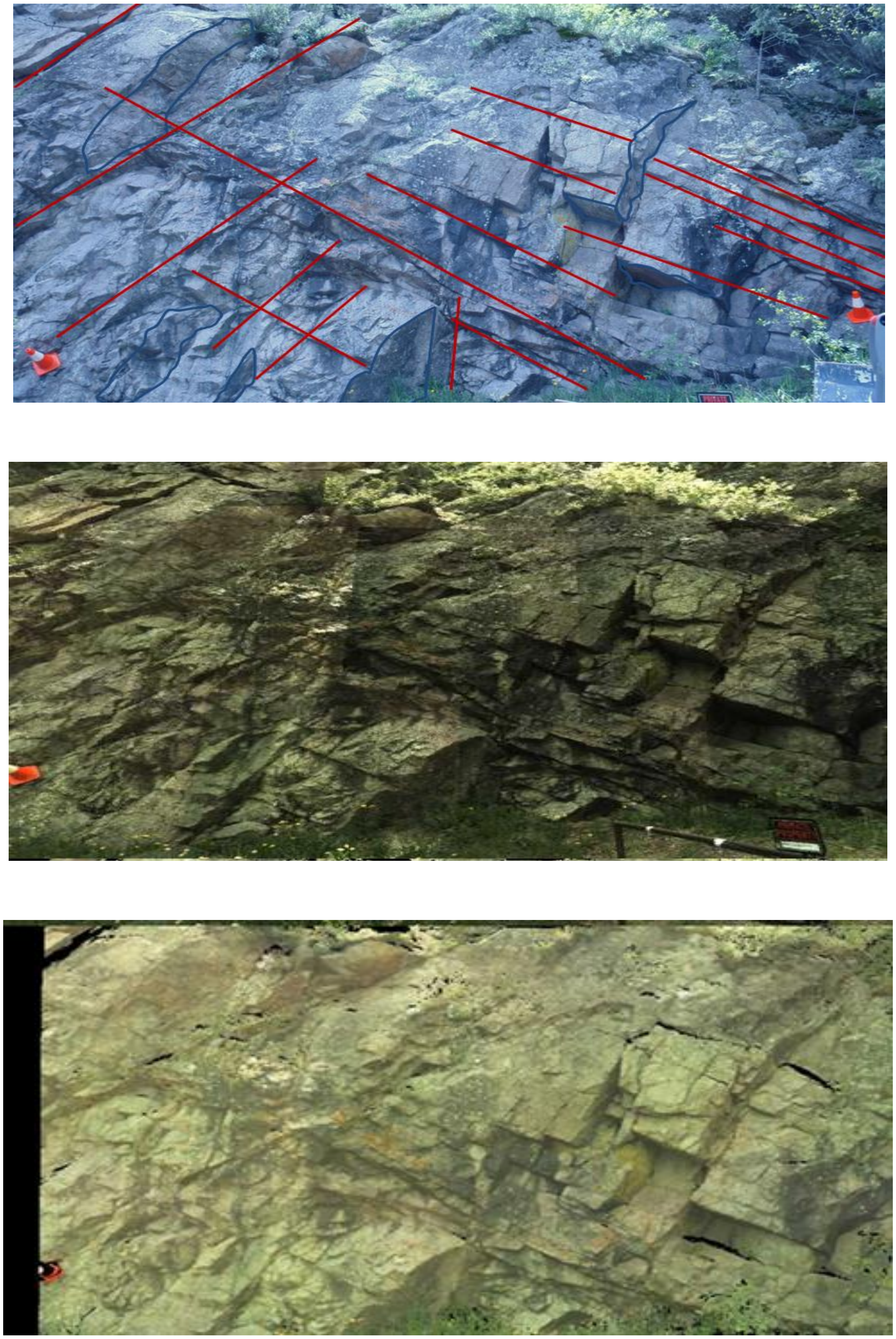

Figure B.41. (a) Manually prepared facets and traces map, red lines represent traces whereas blue polygons represents facets, (b) LiDAR optical image, and (b) LiDAR point cloud of Colorado Site 12.

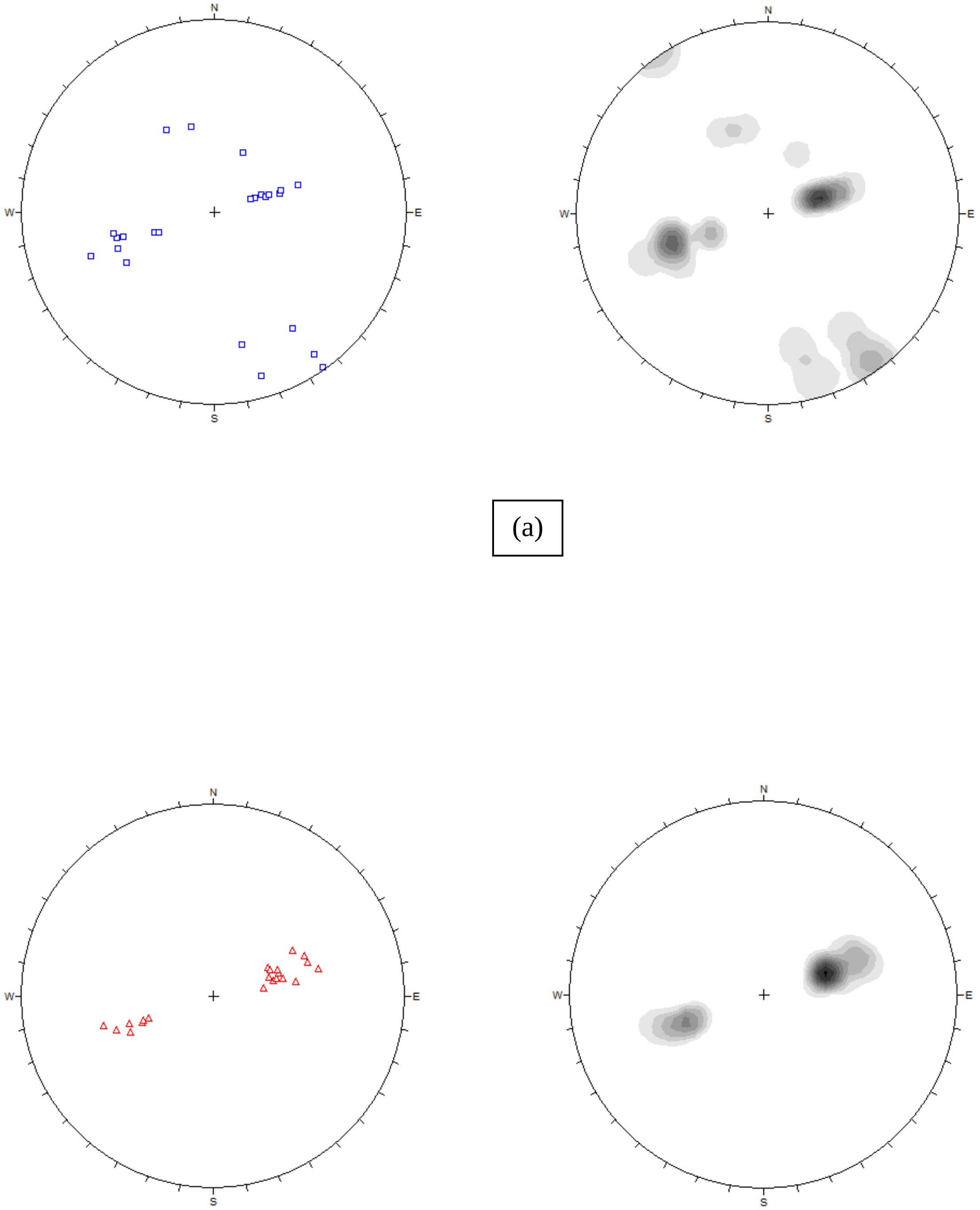

(a)

(b)

Figure B.42. (a) Poles and corresponding contour of manually measured facets, (b) Poles and corresponding contour of manually measured traces, of Colorado Site 12.

Site 13

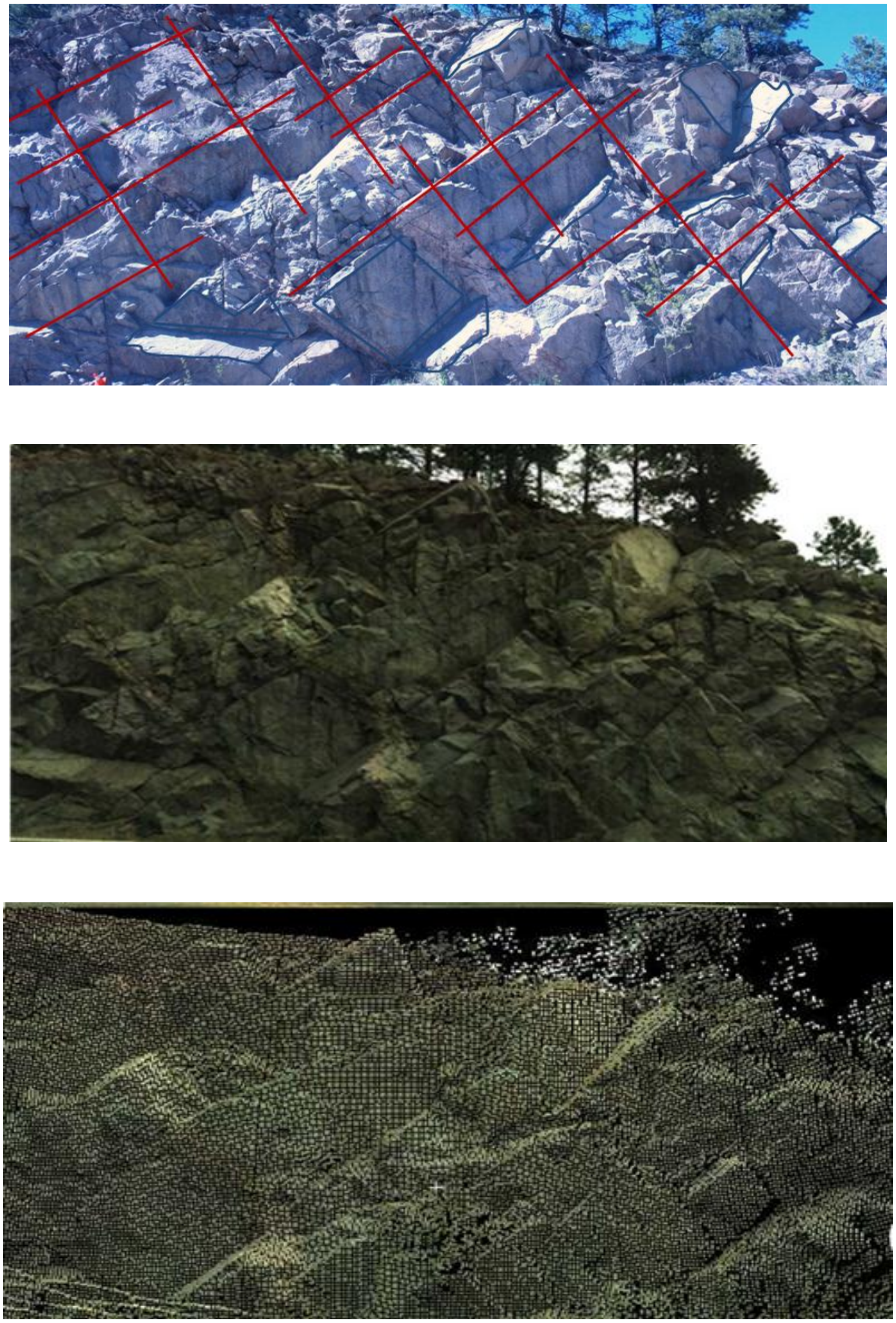

Figure B.43. (a) Manually prepared facets and traces map, red lines represent traces whereas blue polygons represents facets, (b) LiDAR optical image, and (b) LiDAR point cloud of Colorado Site 13.

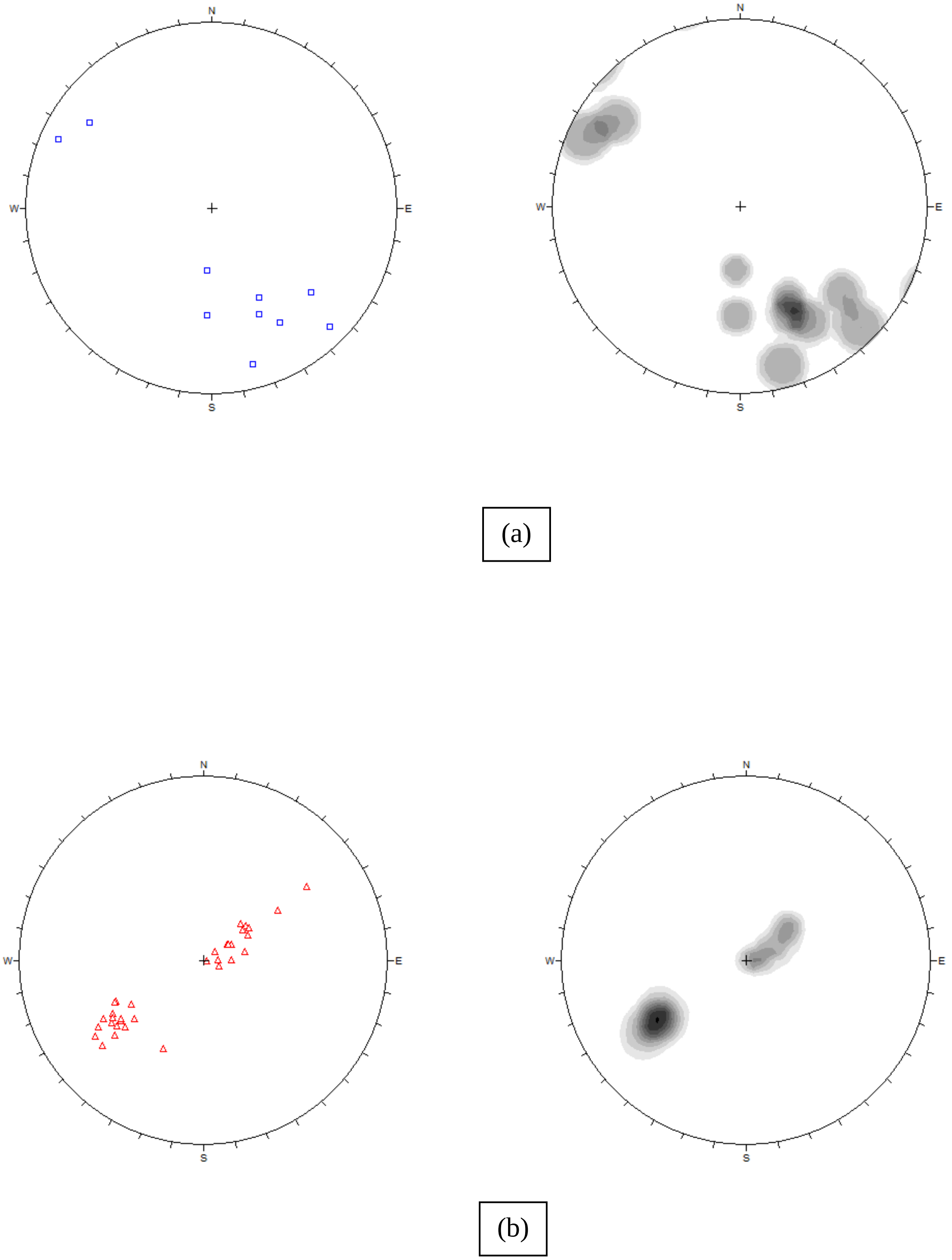

Figure B.44. (a) Poles and corresponding contour of manually measured facets, (b) Poles and corresponding contour of manually measured traces, of Colorado Site 13.

Manual Data

Project: NSF			
Area: Rolla			
Site :1			
No.	Dip (degrees)	Dip Direction (degrees)	Feature Type
1	61	335	Facet
2	70	166	Facet
3	89	201	Facet
4	74	165	Facet
5	87	190	Facet
6	44	159	Facet
7	81	204	Facet
8	89	231	Facet
9	68	177	Facet
10	70	185	Facet
11	89	210	Facet
12	82	195	Facet
13	89	212	Facet
14	82	137	Facet
15	89	200	Facet
16	88	202	Facet
17	49	160	Facet
18	83	194	Facet
19	82	195	Facet
20	66	177	Facet
21	72	187	Facet
22	88	211	Facet
23	86	210	Facet
24	84	213	Facet
25	81	204	Facet
26	86	213	Facet
27	68	176	Facet

Project: NSF			
Area: Rolla			
Site :1			
No.	Trend (degrees)	Plunge (degrees)	Feature Type
1	204	2	Trace
2	207	3	Trace
3	203	3	Trace
4	207	4	Trace
5	202	3	Trace
6	164	1	Trace
7	159	2	Trace
8	167	2	Trace
9	64	3	Trace
10	72	3	Trace
11	230	83	Trace
12	202	79	Trace
13	203	79	Trace
14	213	81	Trace
15	167	2	Trace
16	168	1	Trace
17	174	3	Trace
18	167	2	Trace
19	203	3	Trace
20	251	2	Trace
21	164	2	Trace
22	167	3	Trace
23	172	4	Trace

Project: NSF			
Area: Rolla			
Site: 2			
No.	Dip (degrees)	Dip Direction (degrees)	Feature type
1	77	146	Facet
2	69	155	Facet
3	88	22	Facet
4	82.5	310	Facet
5	83	312	Facet
6	75	322	Facet
7	75	273	Facet
8	89	22	Facet
9	2	63	Facet
10	87	33	Facet
11	86	298	Facet
12	1	355	Facet
13	85	4	Facet
14	78	8	Facet
15	89	304	Facet
16	2	17	Facet
17	74	315	Facet
18	4	5	Facet
19	55	235	Facet
20	87	342	Facet
21	1	274	Facet
22	86	355	Facet
23	45	26	Facet
24	54	350	Facet
25	1	335	Facet
26	74	182	Facet
27	1	271	Facet
28	75	191	Facet
29	73	323	Facet
30	54.5	324	Facet
31	89	178	Facet
32	46	314	Facet
33	36	324	Facet
34	76.5	156	Facet
35	54	318	Facet
36	89	7	Facet
37	47	340	Facet
38	84	162	Facet
39	76	355	Facet
40	82	350	Facet
41	72	353	Facet
42	77	184	Facet
43	74	350	Facet
44	68	174	Facet
45	88	328	Facet
46	1	127	Facet
47	73	350	Facet
48	68	353	Facet
49	86	7	Facet
50	84	193	Facet
51	87	156	Facet
52	63	162	Facet
53	81	166	Facet
54	89	35	Facet
55	88	37	Facet
56	89	194	Facet

Project: NSF
Area: Rolla
Site: 2

No.	Trend (degrees)	Plunge (degrees)	Feature type
1	300	1	Trace
2	110	2	Trace
3	273	80	Trace
4	251	1	Trace
5	253	78	Trace
6	288	75	Trace
7	0	88	Trace
8	15	1	Trace
9	238	54	Trace
10	271	76	Trace
11	81	1	Trace
12	271	75	Trace
13	289	70	Trace
14	291	1	Trace
15	124	1	Trace
16	123	1	Trace
17	183	1	Trace
18	274	67	Trace
19	0	90	Trace
20	285	68	Trace
21	76	3	Trace

Project: NSF
Area: Southeast Missouri
Site: Ironton 1

Number	Dip (degrees)	Dip Direction (degrees)	Feature Type
1	50	198	Facet
2	51	8	Facet
3	89	0	Facet
4	60	194	Facet
5	82	104	Facet
6	85	108	Facet
7	51	221	Facet
8	38	220	Facet
9	76	14	Facet
10	67	214	Facet
11	70	106	Facet
12	86	294	Facet
13	52	10	Facet
14	7	6	Facet
15	82	142	Facet
16	79	12	Facet
17	31	190	Facet
18	7	20	Facet
19	64	205	Facet
20	63	198	Facet
21	88	289	Facet
22	82	203	Facet
23	1	283	Facet
24	81	199	Facet
25	87	166	Facet
26	22	184	Facet
27	89	159	Facet
28	80	5	Facet
29	89	155	Facet
30	79	50	Facet
31	2	293	Facet
32	78	50	Facet
33	86	96	Facet
34	86	176	Facet
35	76	176	Facet
36	88	159	Facet
37	85	170	Facet
38	80	182	Facet
39	86	179	Facet
40	76	198	Facet
41	75	206	Facet
42	85	253	Facet
43	65	155	Facet
44	3	6	Facet
45	89	184	Facet
46	89	132	Facet
47	88	4	Facet
48	64	176	Facet
49	81	178	Facet
50	77	156	Facet
51	78	158	Facet
52	68	157	Facet
53	81	197	Facet
54	84	166	Facet
55	2	282	Facet
56	69	194	Facet
57	86	182	Facet
58	82	101	Facet
59	80	102	Facet
60	85	8	Facet
61	88	174	Facet
62	89	142	Facet
63	46	212	Facet
64	85	182	Facet
65	80	178	Facet
66	87	181	Facet
67	47	21	Facet
68	86	202	Facet
69	88	204	Facet
70	87	206	Facet
71	81	182	Facet
72	89	277	Facet
73	88	186	Facet
74	87	185	Facet
75	61	218	Facet
76	88	178	Facet
77	80	176	Facet
78	87	176	Facet
79	88	177	Facet
80	57	216	Facet
81	36	27	Facet

Project: NSF			
Area: Southeast Missouri			
Site: Ironton 1			
Number	Trend (degrees)	Plunge (degrees)	Feature Type
1	220	12	Trace
2	215	15	Trace
3	0	88	Trace
4	114	84	Trace
5	0	88	Trace
6	0	89	Trace
7	283	87	Trace
8	284	1	Trace
9	273	2	Trace
10	102	87	Trace
11	274	4	Trace
12	104	84	Trace
13	103	86	Trace
14	264	40	Trace
15	4	78	Trace
16	204	2	Trace
17	146	88	Trace
18	204	86	Trace
19	112	2	Trace
20	113	1	Trace

Project: NSF			
Area: Southeast Missouri			
Site: Ironton 2			
Number	Dip (degrees)	Dip Direction (degrees)	Feature Type
1	82	244	Facet
2	89	199	Facet
3	62	164	Facet
4	84	246	Facet
5	66	182	Facet
6	72	170	Facet
7	85	248	Facet
8	82	192	Facet
9	89	191	Facet
10	73	300	Facet
11	88	160	Facet
12	30	200	Facet
13	80	255	Facet
14	84	249	Facet
15	30	219	Facet
16	38	167	Facet
17	82	244	Facet
18	77	248	Facet
19	81	198	Facet
20	51	201	Facet
21	56	183	Facet
22	86	244	Facet
23	77	317	Facet
24	55	189	Facet
25	72	322	Facet
26	83	242	Facet
27	88	251	Facet
28	86	208	Facet
29	81	234	Facet
30	24	201	Facet
31	80	199	Facet
32	86	248	Facet
33	73	198	Facet
34	85	247	Facet
35	87	246	Facet
36	80	243	Facet
37	89	251	Facet
38	88	245	Facet
39	39	120	Facet
40	38	156	Facet
41	57	190	Facet

Project: NSF
Area: Southeast Missouri
Site: Ironton 2

Number	Trend (degrees)	Plunge (degrees)	Feature Type
1	274	79	Trace
2	174	61	Trace
3	298	69	Trace
4	302	72	Trace
5	302	87	Trace
6	258	87	Trace
7	154	46	Trace
8	151	88	Trace
9	143	13	Trace
10	323	83	Trace
11	321	82	Trace
12	326	82	Trace
13	330	79	Trace
14	157	44	Trace
15	313	77	Trace
16	124	13	Trace
17	321	79	Trace
18	323	82	Trace
19	124	28	Trace
20	244	84	Trace

Project: NSF
Area: Southeast Missouri
Site: Ironton 3

Number	Dip (degrees)	Dip Direction (degrees)	Feature Type
1	73	353	Facet
2	81	105	Facet
3	14	167	Facet
4	72	350	Facet
5	85	104	Facet
6	84	176	Facet
7	76	141	Facet
8	81	123	Facet
9	87	194	Facet
10	42	187	Facet
11	38	272	Facet
12	84	110	Facet
13	81	121	Facet
14	66	4	Facet
15	81	126	Facet
16	88	48	Facet
17	81	201	Facet
18	79	117	Facet
19	87	165	Facet
20	21	160	Facet
21	80	148	Facet
22	79	124	Facet
23	88	239	Facet
24	88	163	Facet
25	87	157	Facet
26	88	184	Facet
27	32	165	Facet
28	86	236	Facet
29	80	124	Facet
30	86	244	Facet
31	84	240	Facet
32	84	210	Facet
33	48	211	Facet
34	64	4	Facet

Project: NSF
Area: Southeast Missouri
Site: Ironton 3

Number	Trend (degrees)	Plunge (degrees)	Feature Type
1	246	79	Trace
2	187	74	Trace
3	4	87	Trace
4	268	24	Trace
5	269	32	Trace
6	4	86	Trace
7	271	27	Trace
8	3	88	Trace
9	131	83	Trace
10	252	1	Trace
11	271	6	Trace
12	201	80	Trace
13	2	87	Trace
14	293	25	Trace
15	3	88	Trace
16	136	2	Trace
17	3	84	Trace
18	187	81	Trace
19	2	87	Trace
20	234	82	Trace
21	2	86	Trace
22	3	89	Trace
23	2	87	Trace
24	0	86	Trace

Project: NSF
Area: Southeast Missouri
Site: Ironton 4

Number	Dip (degrees)	Dip Direction (degrees)	Feature Type
1	87	114	Facet
2	86	225	Facet
3	84	28	Facet
4	88	151	Facet
5	32	130	Facet
6	87	132	Facet
7	88	165	Facet
8	88	193	Facet
9	89	145	Facet
10	34	214	Facet
11	36	236	Facet
12	88	174	Facet
13	89	196	Facet
14	84	246	Facet
15	88	146	Facet
16	41	230	Facet
17	88	137	Facet
18	44	236	Facet
19	87	222	Facet
20	86	232	Facet
21	84	134	Facet
22	88	234	Facet
23	89	132	Facet
24	30	233	Facet
25	88	134	Facet
26	89	134	Facet
27	52	178	Facet
28	86	139	Facet

Project: NSF
Area: Southeast Missouri
Site: Ironton 4

Number	Trend (degrees)	Plunge (degrees)	Feature Type
1	220	1	Trace
2	1	88	Trace
3	297	22	Trace
4	296	3	Trace
5	50	2	Trace
6	2	82	Trace
7	252	4	Trace
8	224	2	Trace
9	220	2	Trace
10	272	2	Trace
11	33	2	Trace
12	0	86	Trace
13	220	38	Trace
14	221	33	Trace
15	243	2	Trace
16	2	88	Trace
17	314	2	Trace
18	2	88	Trace
19	144	85	Trace

Project: LiDAR
Area: Golden Gate Canyon Road
Site: 1

Number	Dip (degree)	Dip direction (degree)	Feature Type
1	89	161	Facet
2	39	244	Facet
3	50	245	Facet
4	52	233	Facet
5	46	242	Facet
6	38	260	Facet
7	56	65	Facet
8	49	246	Facet
9	51	64	Facet
10	88	161	Facet
11	50	65	Facet
12	52	70	Facet
13	54	63	Facet
14	45	75	Facet
15	47	244	Facet
16	47	236	Facet
17	56	70	Facet

Project: LiDAR			
Area: Golden Gate Canyon Road			
Site: 1			
Number	Trend (degree)	Plunge (degree)	Feature Type
1	160	89	Trace
2	174	88	Trace
3	75	46	Trace
4	156	79	Trace
5	164	89	Trace
6	69	56	Trace
7	161	89	Trace
8	66	53	Trace
9	65	55	Trace
10	253	45	Trace
11	170	87	Trace
12	163	85	Trace
13	160	89	Trace
14	164	89	Trace
15	163	89	Trace
16	168	88	Trace
17	165	89	Trace
18	160	88	Trace
19	70	44	Trace
20	72	55	Trace
21	170	88	Trace
22	166	89	Trace
23	160	14	Trace
24	162	12	Trace
25	170	16	Trace
26	71	58	Trace
27	68	59	Trace
28	70	57	Trace

Project: LiDAR

Area: Golden Gate Canyon Road

Site: 2

Number	Dip (degree)	Dip Direction (degree)	Feature Type
1	85	164	Facet
2	47	238	Facet
3	84	161	Facet
4	57	267	Facet
5	83	356	Facet
6	87	163	Facet
7	50	244	Facet
8	56	68	Facet
9	80	165	Facet
10	48	245	Facet
11	52	66	Facet
12	54	66	Facet
13	53	75	Facet
14	55	70	Facet
15	56	248	Facet
16	40	240	Facet
17	81	159	Facet
18	51	248	Facet
19	50	251	Facet
20	49	240	Facet
21	52	73	Facet

Project: LiDAR			
Area: Golden Gate Canyon Road			
Site: 2			
Number	Trend (degree)	Plunge (degree)	Feature Type
1	154	85	Trace
2	248	49	Trace
3	162	88	Trace
4	68	51	Trace
5	74	52	Trace
6	74	54	Trace
7	71	54	Trace
8	71	54	Trace
9	73	50	Trace
10	70	49	Trace
11	69	51	Trace
12	246	50	Trace
13	246	42	Trace
14	158	84	Trace
15	161	86	Trace
16	164	87	Trace
17	157	82	Trace
18	160	86	Trace
19	158	84	Trace
20	157	83	Trace
21	161	86	Trace
22	166	82	Trace
23	158	88	Trace
24	248	47	Trace
25	251	51	Trace
26	247	50	Trace
27	242	42	Trace
28	247	48	Trace
29	242	51	Trace

Project: LiDAR			
Area: Golden Gate Canyon Road			
Site: 3			
Number	Dip (degree)	Dip direction (degree)	Feature Type
1	84	170	Facet
2	83	169	Facet
3	56	76	Facet
4	47	242	Facet
5	53	74	Facet
6	81	167	Facet
7	56	74	Facet
8	83	167	Facet
9	38	252	Facet
10	48	255	Facet
11	54	76	Facet
12	52	243	Facet
13	54	73	Facet
14	51	74	Facet
15	48	255	Facet
16	46	235	Facet
17	50	231	Facet
18	49	74	Facet
19	50	240	Facet
20	61	237	Facet
21	84	87	Facet
22	53	240	Facet
23	31	75	Facet
24	54	230	Facet
25	51	233	Facet
26	52	236	Facet
27	54	237	Facet
28	51	234	Facet

Project: LiDAR			
Area: Golden Gate Canyon Road			
Site: 3			
Number	Trend (degree)	Plunge (degree)	Feature Type
1	172	86	Trace
2	170	82	Trace
3	166	89	Trace
4	73	29	Trace
5	75	51	Trace
6	165	34	Trace
7	164	36	Trace
8	69	51	Trace
9	68	53	Trace
10	70	54	Trace
11	171	84	Trace
12	168	86	Trace
13	167	88	Trace
14	164	86	Trace
15	162	86	Trace
16	168	87	Trace
17	166	83	Trace

Project: LiDAR
Area: Golden Gate Canyon Road
Site: 4

Number	Dip (degree)	Dip direction (degree)	Feature Type
1	60	77	Facet
2	50	260	Facet
3	48	249	Facet
4	58	238	Facet
5	56	240	Facet
6	51	68	Facet
7	65	257	Facet
8	53	237	Facet
9	38	245	Facet
10	56	65	Facet
11	58	60	Facet
12	87	163	Facet
13	89	155	Facet
14	55	67	Facet
15	52	63	Facet
16	50	243	Facet
17	54	69	Facet
18	58	68	Facet
19	54	70	Facet
20	53	70	Facet

Project: LiDAR

Area: Golden Gate Canyon Road

Site: 4

Number	Trend (degree)	Plunge (degree)	Feature Type
1	338	8	Trace
2	338	7	Trace
3	330	3	Trace
4	327	2	Trace
5	160	83	Trace
6	156	87	Trace
7	153	84	Trace
8	154	87	Trace
9	160	89	Trace
10	161	88	Trace
11	164	89	Trace
12	163	86	Trace
13	159	84	Trace
14	155	86	Trace
15	156	85	Trace
16	70	55	Trace
17	68	56	Trace
18	68	60	Trace
19	67	61	Trace
20	68	60	Trace
21	67	56	Trace
22	61	52	Trace
23	69	54	Trace
24	68	58	Trace
25	69	54	Trace

Project: LiDAR
Area: Golden Gate Canyon Road
Site: 5

Number	Dip (degree)	Dip direction (degree)	Feature Type
1	80	340	Facet
2	81	337	Facet
3	80	336	Facet
4	81	338	Facet
5	83	338	Facet
6	84	340	Facet
7	55	234	Facet
8	79	336	Facet
9	78	336	Facet
10	78	338	Facet
11	80	336	Facet
12	81	338	Facet

Project: LiDAR

Area: Golden Gate Canyon Road

Site: 5

Number	Trend (degree)	Plunge (degree)	Feature Type
1	242	52	Trace
2	67	43	Trace
3	79	56	Trace
4	65	51	Trace
5	70	48	Trace
6	69	50	Trace
7	69	51	Trace
8	70	50	Trace
9	70	51	Trace
10	69	49	Trace
11	70	52	Trace
12	70	50	Trace
13	69	48	Trace
14	69	50	Trace
15	244	50	Trace
16	242	50	Trace
17	244	51	Trace
18	242	50	Trace
19	248	50	Trace
20	235	52	Trace
21	242	51	Trace
22	240	53	Trace
23	248	52	Trace
24	69	52	Trace
25	69	51	Trace
26	70	51	Trace
27	69	49	Trace
28	70	50	Trace

Project: LiDAR			
Area: Golden Gate Canyon Road			
Site: 6			
Number	Dip (degree)	Dip Direction (degree)	Feature Type
1	79	345	Facet
2	80	345	Facet
3	72	346	Facet
4	76	343	Facet
5	74	347	Facet
6	67	350	Facet
7	73	348	Facet
8	74	347	Facet
9	71	343	Facet
10	73	345	Facet
11	49	242	Facet
12	68	346	Facet
13	43	245	Facet
14	69	235	Facet
15	40	260	Facet
16	51	241	Facet
17	48	80	Facet
18	56	76	Facet
19	53	80	Facet
20	58	74	Facet
21	49	74	Facet
22	53	245	Facet
23	48	238	Facet
24	52	244	Facet
25	48	244	Facet
26	57	80	Facet
27	56	79	Facet

Project: LiDAR

Area: Golden Gate Canyon Road

Site: 6

Number	Trend (degree)	Plunge (degree)	Feature Type
1	244	44	Trace
2	77	54	Trace
3	76	58	Trace
4	76	54	Trace
5	243	52	Trace
6	79	49	Trace
7	77	55	Trace
8	81	60	Trace
9	241	52	Trace
10	235	56	Trace
11	74	59	Trace
12	74	48	Trace
13	243	54	Trace
14	258	34	Trace
15	239	51	Trace
16	236	52	Trace
17	243	50	Trace
18	78	56	Trace

Project: LiDAR
Area: Parmales Gluch
Site: 7

Number	Dip (degree)	Dip Direction (degree)	Feature Type
1	61	216	Facet
2	66	221	Facet
3	71	221	Facet
4	85	116	Facet
5	34	34	Facet
6	2	303	Facet
7	58	274	Facet
8	67	225	Facet
9	65	232	Facet
10	74	226	Facet
11	67	227	Facet
12	70	300	Facet
13	36	33	Facet
14	27	37	Facet
15	50	32	Facet
16	31	34	Facet
17	51	24	Facet
18	88	109	Facet
19	71	239	Facet
20	85	181	Facet
21	16	48	Facet
22	78	128	Facet
23	68	205	Facet
24	65	219	Facet

Project: LiDAR
Area: Parmales Gluch
Site: 7

Number	Trend (degree)	Plunge (degree)	Feature Type
1	124	11	Trace
2	130	16	Trace
3	132	20	Trace
4	333	87	Trace
5	310	4	Trace
6	312	5	Trace
7	118	3	Trace
8	130	82	Trace
9	142	72	Trace
10	302	12	Trace
11	302	16	Trace
12	322	88	Trace
13	124	84	Trace
14	324	74	Trace
15	303	2	Trace
16	139	16	Trace
17	238	74	Trace
18	114	86	Trace
19	317	75	Trace

Project: NSF

Area: Parmales Gulch (Rock Road)

Site: 8

Number	Dip (degree)	Dip Direction (degree)	Feature Type
1	68	202	Facet
2	52	94	Facet
3	57	204	Facet
4	63	156	Facet
5	64	201	Facet
6	28	68	Facet
7	60	202	Facet
8	62	204	Facet
9	60	204	Facet
10	62	183	Facet
11	52	24	Facet
12	41	152	Facet
13	60	335	Facet
14	74	111	Facet
15	50	92	Facet
16	48	188	Facet
17	37	265	Facet
18	74	111	Facet

Project: NSF
Area: Parmales Gulch (Rock Road)
Site: 8

Number	Trend (degree)	Plunge (degree)	Feature Type
1	100	34	Trace
2	124	19	Trace
3	131	29	Trace
4	111	61	Trace
5	120	24	Trace
6	131	28	Trace
7	86	38	Trace
8	268	88	Trace
9	272	89	Trace
10	132	29	Trace
11	111	83	Trace
12	103	32	Trace
13	93	86	Trace
14	176	60	Trace
15	104	84	Trace
16	202	68	Trace
17	273	15	Trace
18	274	22	Trace
19	101	89	Trace
20	82	36	Trace
21	94	12	Trace
22	114	76	Trace
23	84	59	Trace
24	128	55	Trace
25	73	56	Trace
26	117	62	Trace
27	82	52	Trace
28	202	46	Trace
29	249	57	Trace
30	244	55	Trace
31	240	54	Trace
32	85	59	Trace
33	273	54	Trace
34	254	52	Trace
35	236	48	Trace
36	253	64	Trace
37	254	51	Trace
38	238	60	Trace
39	298	61	Trace
40	107	30	Trace
41	88	55	Trace
42	101	70	Trace
43	255	44	Trace
44	97	60	Trace
45	102	64	Trace
46	196	64	Trace
47	194	61	Trace
48	197	65	Trace
49	202	61	Trace
50	198	64	Trace
51	194	62	Trace
52	211	51	Trace
53	193	56	Trace
54	63	57	Trace
55	70	59	Trace
56	51	44	Trace
57	44	30	Trace
58	40	33	Trace
59	80	50	Trace
60	80	50	Trace
61	70	46	Trace
62	36	45	Trace

Project: NSF

Area: Idaho Spring

Site: 9

Number	Dip (degree)	Dip Direction (degree)	Feature Type
1	88	343	Facet
2	72	138	Facet
3	80	336	Facet
4	72	145	Facet
5	70	150	Facet
6	88	166	Facet
7	75	145	Facet
8	84	342	Facet
9	82	337	Facet
10	87	341	Facet
11	88	335	Facet
12	82	84	Facet
13	74	163	Facet
14	86	340	Facet
15	74	153	Facet
16	71	146	Facet
17	72	118	Facet
18	78	145	Facet
19	79	151	Facet
20	59	150	Facet

Project: NSF			
Area: Idaho Spring			
Site: 9			
Number	Trend (degree)	Plunge (degree)	Feature Type
1	79	24	Trace
2	225	35	Trace
3	78	22	Trace
4	74	48	Trace
5	66	86	Trace
6	231	82	Trace
7	0	88	Trace
8	72	82	Trace
9	71	81	Trace
10	74	86	Trace
11	64	58	Trace
12	72	54	Trace
13	64	86	Trace
14	233	22	Trace
15	67	83	Trace
16	65	73	Trace
17	65	74	Trace
18	73	70	Trace
19	243	81	Trace
20	254	23	Trace
21	68	37	Trace
22	64	38	Trace
23	66	37	Trace
24	79	32	Trace
25	231	85	Trace
26	144	73	Trace
27	102	70	Trace
28	75	79	Trace
29	52	83	Trace
30	65	46	Trace
31	235	24	Trace
32	238	28	Trace
33	242	30	Trace
34	251	34	Trace
35	233	30	Trace

Project: NSF			
Area: Idaho Spring			
Site: 10			
Number	Dip (degree)	Dip Direction (degree)	Feature Type
1	78	356	Facet
2	33	167	Facet
3	78	353	Facet
4	30	154	Facet
5	64	88	Facet
6	77	350	Facet
7	78	353	Facet
8	78	349	Facet
9	76	355	Facet
10	78	354	Facet
11	76	349	Facet
12	75	355	Facet
13	67	300	Facet
14	76	354	Facet
15	23	85	Facet
16	81	268	Facet
17	58	146	Facet
18	75	165	Facet
19	68	265	Facet

Project: NSF
Area: Idaho Spring
Site: 10

Number	Trend (degree)	Plunge (degree)	Feature Type
1	52	19	Trace
2	68	41	Trace
3	78	22	Trace
4	76	85	Trace
5	260	76	Trace
6	82	26	Trace
7	73	30	Trace
8	84	42	Trace
9	74	44	Trace
10	68	24	Trace
11	76	53	Trace
12	346	78	Trace
13	265	83	Trace
14	355	82	Trace
15	350	72	Trace
16	352	72	Trace
17	358	81	Trace
18	356	72	Trace
19	255	81	Trace
20	84	59	Trace
21	83	64	Trace
22	267	68	Trace
23	256	78	Trace
24	245	24	Trace
25	85	60	Trace
26	255	80	Trace
27	86	55	Trace
28	78	50	Trace
29	79	34	Trace
30	74	26	Trace
31	83	64	Trace

Project: NSF			
Area: Golden Gate Canyon Road			
Site: 11			
Number	Dip (degree)	Dip Direction (degree)	Feature Type
1	36	248	Facet
2	59	71	Facet
3	54	251	Facet
4	56	74	Facet
5	89	344	Facet
6	88	352	Facet
7	56	240	Facet
8	53	71	Facet
9	54	242	Facet
10	45	247	Facet
11	46	242	Facet
12	81	347	Facet
13	52	247	Facet
14	56	74	Facet

Project: NSF			
Area: Golden Gate Canyon Road			
Site: 11			
Number	Trend (degree)	Plunge (degree)	Feature Type
1	325	89	Trace
2	327	89	Trace
3	324	88	Trace
4	330	78	Trace
5	336	73	Trace
6	334	72	Trace
7	336	72	Trace
8	76	34	Trace
9	78	36	Trace
10	341	80	Trace
11	71	52	Trace
12	64	37	Trace
13	345	86	Trace
14	340	84	Trace
15	75	62	Trace
16	71	65	Trace
17	355	81	Trace
18	335	61	Trace
19	335	85	Trace
20	342	85	Trace
21	340	83	Trace
22	334	78	Trace
23	346	81	Trace
24	342	80	Trace
25	338	88	Trace
26	330	82	Trace
27	246	51	Trace
28	330	83	Trace
29	334	82	Trace
30	337	81	Trace
31	172	20	Trace
32	163	21	Trace
33	153	19	Trace
34	153	20	Trace
35	145	27	Trace
36	148	28	Trace
37	71	59	Trace

Project: NSF
Area: Boulder
Site: 12

Number	Dip (degrees)	Dip Direction (degrees)	Feature Type
1	49	165	Facet
2	70	348	Facet
3	89	325	Facet
4	84	325	Facet
5	72	326	Facet
6	83	344	Facet
7	25	251	Facet
8	38	206	Facet
9	52	150	Facet
10	29	250	Facet
11	23	251	Facet
12	39	254	Facet
13	40	252	Facet
14	49	252	Facet
15	55	75	Facet
16	52	75	Facet
17	55	60	Facet
18	56	69	Facet
19	56	78	Facet
20	68	70	Facet
21	36	71	Facet
22	34	70	Facet
23	31	254	Facet
24	33	253	Facet

Project: NSF
Area: Boulder
Site: 12

Number	Trend (degrees)	Plunge (degrees)	Feature Type
1	252	41	Trace
2	252	51	Trace
3	75	54	Trace
4	74	52	Trace
5	62	54	Trace
6	60	39	Trace
7	65	54	Trace
8	70	50	Trace
9	80	60	Trace
10	71	56	Trace
11	75	49	Trace
12	75	31	Trace
13	250	47	Trace
14	251	48	Trace
15	247	40	Trace
16	70	35	Trace
17	66	35	Trace
18	255	29	Trace
19	251	34	Trace
20	80	43	Trace
21	67	50	Trace

Project: NSF
Area: Boulder
Site: 13

Number	Dip (degrees)	Dip Direction (degrees)	Feature Type
1	84	114	Facet
2	71	329	Facet
3	57	332	Facet
4	82	345	Facet
5	77	125	Facet
6	64	336	Facet
7	60	362	Facet
8	37	364	Facet
9	84	315	Facet
10	70	310	Facet

Project: NSF			
Area: Boulder			
Site: 13			
Number	Trend (degrees)	Plunge (degrees)	Feature Type
1	78	64	Trace
2	45	58	Trace
3	110	80	Trace
4	85	81	Trace
5	88	73	Trace
6	88	88	Trace
7	88	88	Trace
8	87	88	Trace
9	230	26	Trace
10	236	28	Trace
11	239	41	Trace
12	230	19	Trace
13	205	35	Trace
14	245	35	Trace
15	245	34	Trace
16	230	38	Trace
17	238	22	Trace
18	240	31	Trace
19	240	26	Trace
20	238	30	Trace
21	233	29	Trace
22	230	32	Trace
23	234	32	Trace
24	50	57	Trace
25	60	59	Trace
26	54	56	Trace
27	60	70	Trace
28	55	72	Trace
29	51	81	Trace
30	56	72	Trace
31	235	33	Trace
32	54	21	Trace
33	56	38	Trace
34	52	60	Trace
35	235	19	Trace

REFERENCES

Abellan, A., Vilpalana, J., and Martinez, J. 2006. Application of a long range terrestrial laser scanner to detailed rock fall study at Val de Nuria (Eastern Pyrences, Spain). Journal of Engineering Geology: 88, p: 136-148.

Allam, M.M. 1978. The estimation of fractures and slope stability of rock faces using analytical photogrammetry. Photogrammetria 34, 89-99.

Attewell, P.B., and Farmer, I.W. 1976. Principles of Engineering Geology, Chapman and Hall, London.

Baecher, G.B. 1983. Statistical analysis of rock mass fracturing. Journal of Mathematical Geology, Vol. 15, 2, pp. 329-347.

Becker, G.F. 1893. Finite homogeneous strain, flow, and rapture of rocks. Geological Society of America bulletin. Vol. 4, pp. 13-90.

Bezdek, J.C. 1981. Pattern Recognition with Fuzzy Objective Function Algorithms. Plenum Press, New York.

Bieniawski, Z.T. 1989. Engineering Rock Mass Classification. Wiley, New York, USA, 251 pp.

Brady, B.H.G., and Brown, E.T. 2004. Rock Mechanics for Underground Mining, 3rd Edition. Kluwer Academic Publishers, London. U.K.

Bridges, M.C. 1975. Presentation of fracture data for rock mechanics. Proc. of the 2nd Australia-New Zealand Conf. on Geomechanics, Brisbane. Institution of Engineers, Australia.

Bridges, M.C. 1990. Identification and characterisation of sets of fractures and faults in rock. Proc. of the Int. symp. On Rock Joints, Leon, Norway, N. Barton and O. Stephansson (eds), Balkema, Rotterdam, 19-26.

Buckley, S.J., Howell, J.A., Enge, H.D., and Kurz, T.H. 2008. Terrestrial laser scanning in geology: data acquisition, processing, and accuracy considerations. Journal of Geological society, London., 165: 625-638.

Cambridge in Color homepage, 2012. http://www.cambridgeincolour.com/tutorials.htm

Cawsey, D.C. 1977. The measurement of fracture patterns in the Chalk of Southern England. Engineering Geology, 11, 210 – 215.

Chandler, J.H., Fryer, J.G. and Jack, A. 2005. Metric capabilities of low-cost digital cameras for close range surface measurement, The Photogrammetric Record, 20(109): 12-26.

Cheeney, R.F. 1983. Statistical Methods in Geology, George Allen and Unwin, London.

Coli, N., Berry, P., Boldine, D., and Bruno, R. 2012. The contribution of geostatistics to the characterization of some bimrock properties. Journal of Engineering Geology. Vol. 137-138. June 2012. Pp 53-63

Crosta, G. 1997. Evaluating rock mass geometry from photographic images. Rock Mech Rock Eng 30(1):35-58.

Deb, D., Hariharan, S., Rao, U.M., and Chang-Ha, R. 2008. Automatic detection and analysis of discontinuity geometry of rock mass from digital images. Computers and Geosciences. 34:115-126.

Donovan, J., Kemeny, J., and Handy, J. 2005. The Application of Three-Dimensional Imaging to Rock Discontinuity Characterization, Alaska Rocks 2005.

Duan, Y., Xiaoling, L., Maerz, N., Otoo, J., 2011. Automatic 3D facet orientations from LiDAR imaging. NSF, CMMI, Atlanta, GA, January 4-7, 2011. 5pp

Duda, R.O., Hart, P.E., and Stork, D.G. 2000. Pattern Classification, Wiley-Interscience; 2 edition October 2000.

Dunn, J.C. 1973. A Fuzzy Relative of the ISODATA Process and its Use in Detecting Compact Well-Separated Clusters. Journal of Cybernetics 3: 25-57.

Enge, H.D., buckley, S.J., Rotevatn, A. and Howell, J.A. 2007. From outcrop to reservoir simulation model: workflow and procedures. Geosphere, 3, 469-490.

Einstein, H. 1993. Modern Development in Discontinuity Analysis – the persistence-connectivity problem, in comprehensive rock engineering principles, practice and projects. Volume 3: rock testing and site characterization, pp. 193-213, Oxford Pergamon Press.

Feng, Q. 2001. Novel Methods for 3D Semi-Automatic Mapping of Fracture Geometry at Exposed Rock Faces. PhD Thesis. Royal Institute of Technology, Stockholm, Sweden.

Fernandez, J.C., Singhania, A., Caceres, J., Slatton, K.C., Starek, M., Kumar, R. 2007. An overview of Lidar software Point Cloud processing software. GEM Center Report No. Rep_2007-12-001. Pp 27.

Forsyth, A.D., and Ponce, J. 2003. Computer Vision, A modern Approach. Prentice Hall Inc. New Jersey, USA.

Franklin, J.A., Maerz, N.H., Bennett, C.P. 1988. Rock mass characterization using photoanalysis. Int Journal of Mining and Geological Engineering, 1988;6;97-112.

Gaich, A., Potsch M., Schubert W. 2006. Basics, principles and applications of 3D imaging systems with conventional and high-resolutions cameras. In: Tonon F, Kottenstette J (eds) Laser and photogrammetric methods for rock face characterization. ARMA Golden, Colorado.

Gaich, A., Schubert, W., and Potsch, M., 2004. Reproducible rock mass description in 3D using the JointMetriX3D system. In: Schubert W (ed) Proceedings of EUROCK 2004 and 53rd geomechanics colloquium. Salzburg, Austria, pp 61-64.

Garmin home page. 2012. https://buy.garmin.com/shop/shop.do?pID=118&ra=true

Gigli, G., and Casagli, N. 2011. Semi-automatic extraction of rock mass structural data from high resolution LiDAR point clouds. International Journal of rock Mechanics and Mining Sciences 48, p:187-198.

Gonzalez-Jorge, H., Riverio, B., Armesto, J., and Arias, P. 2011. Standard artifact of a geometric verification of terrestrial laser scanning systems. Optics and Laser Technology, 43, p:1249-1256.

Gonzalez, R.C., and Wintz, P. 1987. Digital image processing, 2 edn. Addison –Wesley, Boston.

Hadjigeorgiou, J., Lessard, J.F., Villaescusa, E., Germain, P. 1995. An appraisal of structural mapping techniques. In: Proc., 2nd Intl. Conf. Jointed and Faulted Rocks. Vienna, 191-197.

Hadjigeorgiou, J., Lemy, F., Cote, P., and Maldague, X. 2003. An Evaluation of Image Analysis Algorithms for Constructing Discontinuity Trace Maps. Rock Mech. and Rock Eng. Journal. 36:163-179.

Hagan, T.O. 1980. A case for terrestrial photogrammetry in deep-mine rock structure studies. Int J of Rock Mech and Mining Sciences. 17:4, Pp 191-198

Handy, J., Kemeny, J., Donovan, J., Thiam, S., 2004. Automatic discontinuity characterization ot rock faces using 3D laser scanners and digital imaging. In Proc. Gulf Rocks 2004, June 5-10, Houston TX, 11 pp.

Harrison, J.P. 1993. Improved analysis of rock mass geometry using mathematical and photogrammetric methods. Ph.D. thesis, Imperial College, London, UK.

Harvey, E.M. 1987. Optimization of joint photography. B.Sc. Thesis, Department of Earth Sciences, University of Waterloo, 64pp

Hoek, E. V., and Bray, J. 1981. Rock Slope Engineering. Institution of Mining and Metallurgy, London, 358 pp.

Hoppe, H., DeRose, T., Duchamp, T., McDonald, J.A., and Stuetzle, W. 1992. Surface reconstruction from unorganized points. SIGGRAPH 1992: 71-78.

Hudson, J.A. 1989. Rock mechanics principles in engineering practice. Butterworths, London, 72pp.

Hudson, J.A., and Hudson, J.L. 1993. Establishing potential behavioral modes of rock engineering systems by computer simulation of interaction matrix energy flux. International Journal of Rock Mechanics and Mining Sciences and Geomechanics abstract, Vol. 30, 4, pp 457- 468.

Hudson, J.A., and La Pointe. 1980. Printed circuits for studying rock mass permeability. International Journal of Rock Mechanics and Mining Sciences and Geomechanics Abstracts, Technical Note, 17, 5, 297-301.

Hudson, J.A., and Priest, S.D. 1979. Discontinuity and rock mass geometry. International Journal for rock Mechanics and Mining Sciences, vol. 16, pp. 339-362.

Hudson, J.A., and Priest, S.D. 1983. Discontinuity frequency in rock masses. International Journal of Rock Mechanics and Mining Sciences and Geomechanics Abstracts, Vol. 20, pp. 73-89.

Jain, A.K. 1989. Fundamentals of digital Image Processing. Prentice Hall Inc. New Jersey, USA.

Kemeny, J. and R. Post. 2003. Estimating Three-Dimensional Rock Discontinuity Orientation from Digital Images of Fracture Traces, Computers and Geosciences, 29/1, pp. 65-77.

Kemeny, J., Norton, B., Turner, K. 2006. Rock slope stability analysis utilizing ground-based LIDAR and digital image processing. Felsbau v. 24, No. 3, pp 8-15. Split Engineering, 2008. Split-FX Software.

Kemeny, J., Turner., K., and Norton, B. 2006. Hardware, Software, Accuracy, and Best-Practices. Proceedings of American Rock Mechanics Association, June 17-18, Golden, Colorado. 13pp

Kemeny J., and Turner, K. 2008. Ground-Based LiDAr Rock Slope Mapping and Assessment. Publication No. FHWA-CFL/TD-08-006. 113pp

Kersten, R.W.O. 1990. The stress distribution required for fault and joint development. Proc. of the Int. Conf. on Mechanics of Jointed and Faulted Rock, Vienna, Austria, H.P. Rossmanith (ed.), Balkema, Rotterdam, 251-256

Kodak home page. 2012. http://store.kodak.com/store/ekconsus/en_US/pd/Z1275_Zoom_Digital_Camera/productID.146582900

Labourdette, R. and Jones, R.R. 2007. Characterization of fluvial architectural element using a three-dimensional outcrop data set: Escanilla braided system, South–Central Pyrenees, Spain. Geosphere, 3, 422-434.

La Pointe, P.R. and Hudson, J.A. 1985. Characterization and Interpretation of Rock mass jointing patterns. Geological Society of America, Special Paper 199, 1-37.

Lato, J.M. 2010. Geotechnical applications of LiDAR pertaining to geomechanical evaluation and hazard identification. PhD Thesis submitted to the Department of Geological Sciences and Geological Engineering, Queens University, Canada.

Lepist, L., Kunttu, L., Aution, J. 2004. Rock Imaging Classification Using Non Homogenous Textures and Spectra Imaging.

Lim, M., Petley, D.N., Rosser, N.J., Allison, R.J., Long, A.J. and Pybus, D. 2005. Combined digital photogrametry and time-of-flight laser scanning for monitoring cliff evolution. Photogrammetry record, 20, 109-129.

Maerz, N.H. 1990. Photoanalysis of rock fabric. Ph.D Thesis, University of Waterloo, Canada.

Maerz, N. H., Ibarra, J. A., and Franklin, J. A., 1996. Overbreak and underbreak in underground openings. Part 1: Measurement using the light sectioning method and digital image processing. Journal of Geotechnical and Geological Engineering. Vol. 14, pp. 307-323.

Maerz, N. H., and Zhou, W. 1999. Multivariate analysis of bore hole discontinuity data. Rock Mechanics for Industry. In Proceedings of the 37th US Rock Mechanics Symposium, Vail Colorado, June 6-9. Vol. 1, pp. 431-438.

Maerz, N. H., and Zhou, W. 2000. Discontinuity data analysis from oriented boreholes. Pacific Rocks; In Proceedings of the Fourth North American Rock Mechanics Symposium, Seattle, Washington, July 31- Aug.1. pp. 667-674.

Maerz, N. H., 2000. Highway rock cut stability assessment in rock masses not conducive to stability calculations. In Proceedings of the 51st Annual Highway Geology Symposium, Aug. 29-Sept. 1, Seattle, Washington. pp. 249-259.

Maerz, H. H., and Zhou, W. 2005. Multivariate clustering analysis of the ECRB cross drift discontinuities, Yucca Mountain Project. Alaska Rocks, In Proceedings of the 40th US Rock Mechanics Symposium, Anchorage Alaska, June 25-29. 10 pp.

Maerz, N.H., Youssef, A.M., Otoo, J.N., Kassebaum, T.J., Duan, Y. 2012. A Simple Method of Measuring Discontinuity Orienations from Terrestrial LiDAR Images. Submitted to the Journal of Environmental and Engineering Geoscience, 17pp

Maerz, N., Otoo, J., Kassebaum, T., Boyko, K. 2012. Using LiDAR in Highway Rock Cuts. Proceedings of the 63rd Highway Geology Symposium, California, USA.

Mah, J., Samson, C., and Mckinnon, S.D. 2011. 3D Laser Imaging for joint orientation analysis. Int. Journal of Rock Mechanics and Mining Sciences. 10pp.

McCarter, M.K., 1976. Application of plane photogrammetry to open pit mapping. In Proceedings of the US Symposium on rock Mechanics, Snowbird, UT, pp 93-98.

Mikos, M., Vidmar, A., and Brilly, M., 2005. Using a laser measurement system for monitoring morphological changes on the Strug rock fall, Slovenia, Nat. Hazards Earth Syst. Sci., 5, 143–153.

Monte, J.M. 2004. Rock Mass Characterization Using Laser Scanning and Digital Imaging Data Collection Techniques. Master’s Thesis, University of Arizona. USA.

Nasrallah, J., Monte, J. and Kemeny, J. 2004. Rock Mass Characterization for Slope/Catch Bench Design Using 3D Laser and Digital Imaging, Gulf Rocks 2004 (ARMA 2004, Rock Mechanics Symposium and the 6th NARMS) Houston, TX.

Nocolas, D.E., and Sims, D.B. 2001. Collecting and Using Geologic Structure Data for Slope Design. In: Hustrulid, W.A., McCarter, M.K., Van Zyl, D.J.A. (Eds), Slope Stability in Surface Mining. SME Littleton, Co. 11-26.

Otoo, J. N., Maerz, N. H., Duan, Y., and Xiaoling, L., 2011. LiDAR and optical imaging for 3-D fracture orientations. NSF, CMMI, Atlanta, GA, January 4-7, 2011. 8pp.

Otoo, J. N., Maerz, N., H., Xiaoling, L., and Duan, Y., 2011. 3-D discontinuity orientations using combined optical imaging and LiDAR techniques. Proceedings of the 45th US Rock Mechanics Symposium, San Francisco California, June 26-29 2011, 9 pp.

Otoo, J.N., Maerz, N.H., Li, X., and Duan, Y. 2012. Verification of a 3-D LiDAR point cloud viewer for measuring discontinuity orientations. Proceedings of the 46th US Rock Mechanics Symposium, Chicago, Illinois, June 24-27 2012, 9pp.

Parker, J.R. 1997. Algorithms for Image Processing and Computer Vision. Wiley New York, NY, 432 pp.

Pollard, D.D., and Aydin, A. 1988. Progress in understanding jointing during the past century. Geological Society of America Bulletin 100. Pp. 1181-1204.

Post, R. 2001. Characterizing of Joints and Fractures in a Rock Mass Using Digital Image Processing. M.S. Thesis, University of Arizona, Tucson, AZ 105 pp.

Post, R. M., Kemeny, J. M., and Murphy, R., 2001. Image Processing for automatic extraction of rock joint orientation data from digital images. Proceedings of the 38th U.S. Rock Mechanics Symposium, Washington, D.C., July 7-10, 2001, pp. 877-884.

Price, N.J. 1966. Fault and Joint Development in Brittle and Semi-Brittle Rock. Pergamon, Oxford.

Priest, S. D., 1985. Hemispherical Projection Methods in Rock Mechanics. George Alleu & Unwin, London, 124 pp.

Priest, S.D. 1993. Discontinuity Analysis for Rock Engineering. Chapman and Hall, London, 473 pp.

Priest, S.D. and Hudson, J.A. 1981. Estimation of Discontinuity Spacing and Trace Length Using Scanline Surveys. Int. Journal of Rock Mech., Min. Sci. and Geomech. Abstract. Vol 18, pp. 183-197.

Reid, T.R., Harrison, J.P. 2000. A semi-automated methodology for discontinuity trace detection in digital images of rock mass exposures. Int. Journal Rock Mech. Min. Sci. 37, 1073-1089.

Richardson, S. 1975. Internal report, Utah Copper Division, Kennecott Copper Corporation, Geology Department, Bingham canyon, Utah.

Roncella, R., and Forlain, G. 2005. Extraction of planar patches from point clouds to retrieve dips and dip direction of rock discontinuities. ISPRS WG III/3, III/4, V/3 Workshop “Laser scanning 2005”, the Netherlands, September, 12-14, 2005.

Sagy, A., Brodsky, E.E. and Axen, G.J. 2007. Evolution of fault-surface roughness with slip. Geology, 35, 283-286.

Scheidegger, A.E. 1978. The Enigma of Jointing, Rivista Italiana Di Geofisica. Affini, 4pp.

Siefko, S., Hack, R., van Knapen, B., Turner, K, and Kemeny, J. 2005. Method for automated discontinuity analysis of rock slopes with three-dimensional laser scanning. Transportation Research Record, No. 1913, pp. 187-194.

Slob, S., Hack, R., Knapen, B., Turner, K., and Kemeny, J. 2005. A Method for Automated Discontinuity Analysis of Rock Slopes with 3D Laser Scanning. In: Proceedings of the Transportation Research Board 84th Annual Meeting, January 9-13, 2005. Washington, D.C.

Strouth, A, and Eberhard, E., 2006. The use of LIDAR to overcome rock slope hazard data collection challenges at Afternoon Creek, Washington. Methods for Rock Face Characterization workshop, Golden Colorado, June 17-18, 2006, pp. 49-62.

Sturzeinegger, M and Stead, D. 2009. Close-range Terrestrial Digital Photogrammetry and Terrestrial Laser Scanning for Discontinuity Characterization on Rock Cuts.

Split Engineering home Page. 2010. Split-FX. http://www.spliteng.com/downloads/SplitFXBrochure2007.pdf.

Tonon, F., and Kottenstette, J., T. 2006. Summary Paper on the Morrison Field Exercise. Proceedings of the American Rock Mechanics Association, 2006. Denver Colorado. 17pp.

Tsoutrelis C.E. Exadactylous G.E Kapenis A.P. 1990. Study of rock mass discontinuity system using photo analysis. In Rossmanith HP (ed) Mechanics of jointed and faulted rock. Balkema, Rotterdam, pp 103-112.

Van Hise, C.R. 1896. Principles of North American Pre-cambrian Geology: US Geological Survey 16th Annual Report. Pp. 581-874.

Voyat, I., Roncella, R., Forlani, G., and Ferrero, A.M. 2006. Advanced techniques for geostructural surveys in modeling fractured rock masses: application to two Alpine Sites. Proceedings of the American Rock Mechanics Association, June 17-18, 2006, Golden Colorado. 11pp.

Woodbury,N., Brubacher, M., Woodbury, J.R., 1993. Noninvasive tank Gauging with frequency Modulated Laser Ranging sensors, pp 27-31, September, 2003.

Wyllie, D.C., and Mah, C.W. 2004. Rock Slope Engineering, 4th Ed. Taylor and Francis Group, London and New York. 431pp.

Xiaoling, L., Duan, Y., Zeng, W., Maerz, N., Otoo, J., 2011. Integrating optical image with LiDAR for 3D fracture orientation analysis. IEEE, Int. Geo. and Rem. Sensing Symp. YVR, Canada, 24-29 July, 2011.

Zavodni, Z.M., and Mccarter, M.K., 1976. Main Hill Slide zone, Utah Copper Division, Proceedings of 17th Symposium on Rock Mechanics, Salt Lake City.

Zhou, W. and Maerz, N. H. 2001. Multivariate clustering analysis of discontinuity data: implementation and applications. Rock Mechanics in the National Interest. In Proceedings of the 38th U.S. Rock Mechanics Symposium, Washington, D.C., July 7-10, 2001, pp 861-868, 2001.

Zhou, W., and Maerz, N. H. 2002. Implementation of multivariate clustering methods for characterizing discontinuites from oriented boreholes. Computers & Geosciences, v. 28, no. 7, pp. 827-839.

VITA

James Nii Aboh Otoo was born in Accra, Ghana, West Africa. He attended the Kwame Nkrumah University of Science and Technology, Kumasi, Ghana. He obtained a Bachelor of Science honors degree in Geological Engineering in 2002.

After graduation, James worked as an Engineer/Geologist for Geomax Resources Development Limited, a consulting firm in Accra, Ghana. He later joined HydroSearch Consult, another consulting firm in Accra, Ghana. During James's work with these companies, he consulted on several jobs ranging from geophysics to project management. James currently holds a master's degree in Geoscience awarded by the Western Kentucky University, Bowling Green, Kentucky. He worked for the Hoffman Environmental Research Center, Bowling Green, Kentucky from 2007 till 2009 when he left to pursue a PhD in Geological Engineering at the Missouri University of Science and Technology. While at the Missouri University of Science and Technology, he represented the Geological Science and Engineering department on the Council of Graduate students. He also represented graduate students on the university's students appeal committee. James was also a member of the university's first graduate students travel grant committee. Additionally, he was the vice president of the university's student chapter of the society of exploration geophysicts (SEG).

James has won several competitive external awards including, two graduate student fellowships from National Science Foundation for its research and innovation conference, Mack Gipson award from the National Association of Black Geologists and Geophysicts, SEG/Exxon Mobil student award, and AAPG/SEG student award. He received his PhD in December, 2012.